Waterford Institute *of* Technology

Development of Interferometric & Spectroscopic Techniques for High–resolution Spectral Measurements on Fibre Bragg Gratings

Volume II of II (Appendices)

by

Ronan O'Byrne

Submitted for the Degree of

Doctor of Philosophy

to the

School of Science

Waterford Institute of Technology

Supervisors:

D. A. Flavin[1], Dr. C. Keary[1], Dr. P.J. Cregg[1] Dr. S. Sergeyev[1,2] & Prof. J. D. C. Jones[3]

[1]Waterford Institute of Technology, [2]Aston University, Birmingham, U.K., [3]Heriot–Watt University, Edinburgh, U.K.

(Submitted to Waterford Institute of Technology, October 2013)

Declaration

No part of the work described in this thesis, or the thesis itself, has been submitted as an exercise for a degree at this or any other institution.
The work herein has been performed entirely by the author.

Ronan O'Byrne.
October 2013

Dedicated to the memory of

Dónal Flavin (R.I.P.)

Contents

A Maxwell's equations **V.II A-1**
A.1 Energy transfer via electromagnetic radiation . . . . . V.II A-5
A.2 Wave equation solutions . . . . . V.II A-5
A.3 Spherical waves . . . . . V.II A-6
A.4 References . . . . . V.II A-7

B Second order coherence theory **V.II B-1**
B.1 Young's slits experiment . . . . . V.II B-1
B.2 Power spectrum . . . . . V.II B-5
B.3 Coherence time/Coherence length . . . . . V.II B-5
B.4 High– & low–coherence . . . . . V.II B-6
B.5 Interference hyperboloid of revolution . . . . . V.II B-8
B.5.1 Diffraction . . . . . V.II B-10
B.6 References . . . . . V.II B-14

C Analytic signal **V.II C-1**
C.1 References . . . . . V.II C-4

D An information based comparison of FT– and grating based spectroscopy **V.II D-1**
D.1 References . . . . . V.II D-4

E Polarisation overview **V.II E-1**
E.1 Stokes parameters . . . . . V.II E-4
E.2 The Poincaré sphere representation . . . . . V.II E-5
E.3 Geometric phase effects . . . . . V.II E-7
E.4 Mueller calculus . . . . . V.II E-10
E.5 Jones calculus . . . . . V.II E-12
E.6 References . . . . . V.II E-13

F Electromagnetic waves in optical fibres **V.II F-1**
F.1 Total internal reflection . . . . . V.II F-1

F.2 Electromagnetic wave propagation in fibres . . . . . V.II F-3
F.3 References . . . . . V.II F-5

G FBG Inscription mechanism V.II G-1
G.1 FBG classification . . . . . V.II G-2
G.2 Perturbations and Coupled–mode approach . . . . . V.II G-3
G.2.1 Perturbation approach . . . . . V.II G-3
G.2.2 Coupled–mode approach . . . . . V.II G-5
G.3 References . . . . . V.II G-8

H Brief Fourier transform overview V.II H-1
H.1 Properties . . . . . V.II H-2
H.2 References . . . . . V.II H-6

I Assembly of the fibre straining device V.II I-1
I.1 Mounting the fibre onto the mount . . . . . V.II I-1
I.2 Soldering fibre to fibre mount . . . . . V.II I-2

J Exalos ESL1505-2100 SLED V.II J-1

K Theory for geometric aberrations V.II K-1
K.1 Derivation of Seidel Aberrations . . . . . V.II K-1
K.2 Geometric aberrations . . . . . V.II K-5
K.2.1 Spherical Aberration . . . . . V.II K-7
K.2.2 Coma Aberration . . . . . V.II K-8
K.2.3 Field Curvature & Astigmatism Aberration . . . . . V.II K-8
K.2.4 Grating aberrations . . . . . V.II K-10
K.3 SpectroBragg design . . . . . V.II K-11
K.3.1 Angle of diffracted rays at M_2 . . . . . V.II K-11
K.3.2 Čzerny–Turner design considerations . . . . . V.II K-14
K.4 References . . . . . V.II K-17

L Assembly of the SpectroBragg V.II L-1
L.1 Collimation and configuration of radiation into the 75 mm plane . . . V.II L-1
L.2 Drawing alignment marks . . . . . V.II L-3
L.3 Steps required for the assembling of the SpectroBragg . . . . . V.II L-4

M Lyot Depolariser V.II M-1
M.1 References . . . . . V.II M-3

N Polarisation experiments figures **V.II N-1**
N.1 Control Experiment . . . . . V.II N-2
N.2 Lyot depolariser . . . . . V.II N-15
N.3 Lefèvre SOP fixer . . . . . V.II N-26
N.4 Circulator/Faraday mirror SOP fixer . . . . . V.II N-38
N.5 PDL balancing . . . . . V.II N-48
N.6 Azimuthal Equidistant Projection Figures . . . . . V.II N-59
N.7 References . . . . . V.II N-65

O Effect of intensity changes on centroid value **V.II O-1**

P Two–output, π–shifted interferometry **V.II P-1**
P.1 Phase unwrapping . . . . . V.II P-2
P.2 Apodisation or 'windowing' of data . . . . . V.II P-3
P.3 References . . . . . V.II P-6

Q NewFocus receiver **V.II Q-1**
Q.1 NewFocus receiver repair . . . . . V.II Q-1
Q.2 NewFocus receiver configuration . . . . . V.II Q-1

R Variable and fixed interferogram lengths and window sizes **V.II R-1**
R.1 Variable interferogram length centroid approach . . . . . V.II R-1
R.2 Variable length HTT . . . . . V.II R-7
R.3 Peak Wavelength determination: Centroid approach . . . . . V.II R-13
R.4 Peak Wavelength determination: HTT approach . . . . . V.II R-30
R.5 Summary . . . . . V.II R-45

List of Figures

B.1 Young's slits experiment. Screen $\mathcal{A}$ is illuminated by a plane wave, producing coherent secondary wavelets at points P_1 and P_2, which interfere constructively at point Q on screen $\mathcal{B}$. . . . . V.II B-2

B.2 Figurative examples of: (a) high–coherence interferogram, the interference modulation is approximately uniform across the interferogram; and (b) low–coherence interferogram, the interference modulation has a beating of the envelope of the interferogram. . . . . V.II B-7

B.3 Hyperbolic curves of intensity maxima from two points sources (after figure 1.3 in Tolansky [31]). . . . . V.II B-8

B.4 Hyperboloids of revolution showing non–localised standing waves for two sources, clipped by a bounding box(after Tolansky [31]). . . . . V.II B-9

B.5 Illustration of Fresnel–Kirchhoff diffraction formula. After Born & Wolf [40]. . . . . V.II B-11

B.6 (a) A generated example of a cross section of a rectangular diffraction grating. Shown are 60 data points. (b) The FFT of (a) extended to 1000 data points. . . . . V.II B-13

D.1 The information capacity of four spectrometer systems in terms of size required for a fixed information throughput for a given spectral resolution, and ease of direct presentation of the spectrum (after Gebbie [1]). (a) The Spectrometer types discussed; and (b) A block diagram of the process incorporating the spectrometers. . . . . V.II D-2

E.1 Polarisation ellipse describing the locus of resultant vector of propagating $E_x(z,t)$ and $E_y(z,t)$ fields. . . . . V.II E-2

E.2 Poincaré sphere showing projections of point $\mathbf{P}$ onto S_1, S_2 and S_3. . V.II E-6

E.3 Pancharatnam phase from following the closed path, **ABCA**, about the Poincaré sphere. . . . . V.II E-8

E.4 Spin–redirection phase from following the closed path, **ABCA**, about the sphere of directions in momentum space. . . . . V.II E-8

E.5 Topological phases Ω_1 and Ω_2, from following either path $\mathbf{AB_1C}$ or $\mathbf{AB_2C}$, respectively, with the loop completed by the great circle arc between AC, on the Poincaré sphere. B_1 and B_2 are the eigenaxes of a polarisation modifying optical component. . . . . V.II E-9

F.1 Total internal reflection with the geometric reflection, R_G; Goos–Hänchen shifted reflection, R_{GH}; and Imbert–Fedorov shifted reflection, R_{FI_L} and R_{FI_R}, for right and left circular polarisation, respectively. After figure 1.7 of [1] and figure 1 of [2]. . . . . V.II F-2

F.2 Ray diagram of meridional ray and skew ray. . . . . V.II F-3

H.1 A Fourier transform pair example. A signal with two frequencies, $f(t)$, is decomposed into the real part, $\Re\left(F(\nu)\right)$, and imaginary part, $\Im\left(F(\nu)\right)$. . . . . V.II H-2

H.2 A convolution example. An impulse signal $x(t)$, (a), is convolved with the rectangular signal $y(t)$, (b), to give $x(t) * y(t)$, (c). After Brigham [18]. . . . . V.II H-4

H.3 A correlation example. An impulse signal $x(t)$, (a), is correlated with the rectangular signal $y(t)$, (b), to give $x(t) * y(t)$, (c). After Brigham [18]. . . . . V.II H-5

I.1 Unprotected ribbon solder broken during transport. . . . . V.II I-2

I.2 Graphical representation of soldering technique. . . . . V.II I-3

J.1 OSA spectrum of ESL1505-2100 Exalos SLED. . . . . V.II J-1

K.1 Diagram of the configuration used for derivation of Seidel aberrations. V.II K-1

K.2 Spherical aberration. . . . . V.II K-7

K.3 Coma aberration. . . . . V.II K-8

K.4 Astigmatism aberration. . . . . V.II K-9

K.5 Field curvature aberration. . . . . V.II K-9

K.6 Geometric determination of the angle ϕ_d. Using the triangles 1.a–1.c, a relation for ϕ_d is obtained. The triangles 1.a–1.c are separately shown, with their vertices indicated by coloured circles. . . . . V.II K-12

K.7 Continuation of figure K.6. Geometric determination of the angle ϕ_d in terms of known angles, $\theta_d(\lambda_{\text{design}})$, $\Delta\theta_d$ and β. Using the triangles 2.a–2.d, a relation for φ_d is obtained. . . . . V.II K-13

K.8 The SpectroBragg resolution and spectral bandwidth was determined by diffraction grating dispersion and the angle intercepted by the mirror M_2. At position $\underline{\mathbf{r}}_1$, a larger angle is intercepted, and the spectrum occupies half the diode array. At position $\underline{\mathbf{r}}_2$, a smaller angle is intercepted, and the spectrum occupies most of the array but experiences vignetting. . . . . V.II K-14

K.9 The width of the diffracted beam depends upon θ_d as $w\sin(\theta_d)$. The smaller the value of θ_d the wider the diffracted beam. For M_2 centred upon λ_{design}, an asymmetry in the width either side of λ_{design} exists. . V.II K-15

K.10 The SpectroBragg resolution is the observed resolution at the InGaAs array. The SpectroBragg spectral range is denoted by λ_{min}(red circle) and λ_{max}(blue circle). The design wavelength is in the centre of the InGaAs array (green circle). The surface normals of the components are indicated with broken lines. . . . . V.II K-16

K.11 The unfolded path of the diffracted design wavelength, λ_{design}, and the next resolvable wavelength, λ_1. The InGaAs array is oriented so that its surface normal is parallel to path of λ_{design}. The spatial separation at the array is $y_d = R\sin(\Delta\theta_d)$ . . . . . V.II K-16

L.1 (a) Collimating the beam, (b) Aligning the beam in the 75 mm plane. V.II L-2

L.2 Steps for the construction of alignment markings upon the optical bench. . . . . V.II L-3

L.3 TR150/M posts were placed one tapped hole apart, and abut AMA025/M platform against posts, locating the fibre holder centrally. . . . . V.II L-4

L.4 Collimated fibre beam placed in 75 mm plane. MBT616/M and AMA025/M aligned over centre tapped hole. . . . . V.II L-5

L.5 Adjusted the KS2D mirror mounts to have their principal optical axis in the 75 mm plane, and orthogonal to the optical bench. . . . . V.II L-6

L.6 Constructing the mark to indicate alignment of collimating mirror and subsequent components. The AMA025/M was abutted against two TR150/M posts. A microscope slide with orthogonal lines was placed centrally into the diverging beam, along the principal optical axis. The microscope slide was fixed with double–sided adhesive tape. V.II L-8

L.7 Construction to determine proper angle: A computer expansion slot backplate was attached to a right angle adapter (RA90) via a short pillar post (TR50/M). . . . . V.II L-9

L.8 Plan view of alignment target on principal optical axis. Spherical mirror was mounted in KS2D mount so as to reflect back along principal axis. . . . . V.II L-10

L.9 The KS2D was aligned with the perpendicular lines. By moving the point of observation over the KS2D the edge of the KS2D and one of the lines on the bench was colocated. The KS2D was positioned by aligning the edge of the KS2D and the lines on the bench. . . . . V.II L-10
L.10 By aligning the backplate, the projected shadow minimised. When the crossed lines were overlayed on the shadow the centre of the beam fell on edge of the backplate. . . . . V.II L-11
L.11 The collimating mirror was aligned by projecting onto the backplate fixed at the desired angle. . . . . V.II L-11
L.12 A second KS2D mount parallel to the first KS2D but intercepting the collimated beam reflected the beam parallel to the expanding beam axis. The extra distance and alignment with the bench allowed for the collimation to be checked and corrected at the first KS2D. . . . . V.II L-12
L.13 The first KS2D mount was moved towards or away from the AMA025/M mount to obtain a collimated beam, as determined by the location and dimensions of the crossed lines projected from the microscope slide remaining unchanged at target positions (a) and (b). . . . . V.II L-13
L.14 At a point between the two KS2D mounts (and that allows for the placement of subsequent equipment) an angle 2α was marked out relative to the **principal axis 1**. Lines were drawn for the diffraction grating surface normal, alignment lines perpendicular to the grating surface normal and a line parallel to the intended diffracted beam at 1550 nm. . . . . V.II L-15
L.15 The diffraction grating mount was aligned with the lines perpendicular to the drawn surface normal. The diffraction grating needed to intercept the collimated beam as fully as possible to maximise the diffraction for both resolution and visibility purposes. . . . . V.II L-16
L.16 A potential surface normal for the focusing mirror mount was drawn. Alignment lines perpendicular were marked to allow alignment of the focusing mirror's KS2D mount on the bench. Depending upon where focusing mirror intercepted **principal axis 3**, the reflected beam was offset. A series of parallel reflected lines were marked (in green). . . . V.II L-17
L.17 The focusing mirror was placed to intercept **principal axis 3** without obstructing the beam path to preceding components. Additionally the reflected beam were not be obstructed by subsequent components. The actual **principal axis 3** was also determined using the focused beam before (target position (a)) and after the focal point(target position (b)). . . . . V.II L-18

L.18 The photodiode array mount was alinged co–linear with **principal axis 4**. By using the lines drawn parallel to **principal axis 4**, the photodiode array mount was positioned so the centre of the photodiode array was co–linear with **principal axis 4**; aided by using a fixed IR viewing card and a movable IR card. . . . . V.II L-19

L.19 The photodiode array mount was constrained to move parallel to **principal axis 4**. Using the stiff SCSI data cable and kinematic mounts, the photodiode array mount was adjusted for focusing. . . . V.II L-20

L.20 Construction of the prism mount. An RA90 atop a TR150/M pillar post held a perpendicular TR150/M in the 75 mm plane with an RA180 post end clamp at the end ⌀M6 tapped hole. A TR50/M pillar post orthogonal to the TR150/m, but still in the 75 mm plane, held the prism with double–sided adhesive tape. . . . . V.II L-21

L.21 The photodiode array mount and prism mount were adjusted to co–locate the photodiode array and focal plane of the focusing mirror. The photodiode array mount was constrained to move parallel to **principal axis 4**, but the prism mount was not. The prism was roughly aligned by using the brass housing of the window over the photodiode array, and adjusted by observing the captured spectra. . . V.II L-22

L.22 The photodiode array mount was locked into final position with KL02 kinematic positioners at data cable side of mount. . . . . V.II L-23

N.1 Poincaré sphere projections of anisotropic FBG data showing: **(a)** S_2 V. S_3 along S_1 to $-S_1$; **(b)** S_2 V. S_3 along $-S_1$ to S_1; **(c)** S_1 V. S_3 along S_2 to $-S_2$; **(d)** S_1 V. S_3 along $-S_2$ to S_2 ;**(e)** S_2 V. S_1 along S_3 to $-S_3$; and **(f)** S_2 V. S_1 along $-S_3$ to S_3. . . . . V.II N-8

N.2 Poincaré sphere projections of isotropic FBG data showing: **(a)** S_2 V. S_3 along S_1 to $-S_1$; **(b)** S_2 V. S_3 along $-S_1$ to S_1; **(c)** S_1 V. S_3 along S_2 to $-S_2$; **(d)** S_1 V. S_3 along $-S_2$ to S_2 ;**(e)** S_2 V. S_1 along S_3 to $-S_3$; and **(f)** S_2 V. S_1 along $-S_3$ to S_3. . . . . V.II N-9

N.3 Plot of anisotropic FBG data showing **(a)** the data captured on the SpectroBragg; **(b)** the FFT filtered SpectroBragg data; **(c)** the calculated ideal SpectroBragg intensity from the polarimeter data, using a rotation angle of 116°; and **(e)** the cross–correlation, $\mathcal{R}_{\text{Int.}}$, of (b) & (d). . . . . V.II N-10

N.4 Plot of isotropic FBG data showing **(a)** the data captured on the SpectroBragg; **(b)** the FFT filtered SpectroBragg data; **(c)** the calculated ideal SpectroBragg intensity from the polarimeter data, using a rotation angle of 26°; and **(e)** the cross–correlation, $\mathcal{R}_{\text{Int.}}$, of (b) & (d). . . . . V.II N-11
N.5 Plot of **(a)** centroid determined λ_B for the anisotropic FBG data showing; **(b)** the centroid determined λ_B from the FFT filtered SpectroBragg data. . . . . V.II N-12
N.6 Plot of **(a)** centroid determined λ_B for the anisotropic FBG data showing; **(b)** the centroid determined λ_B from the FFT filtered SpectroBragg data. . . . . V.II N-12
N.7 Plot of changing correlation coefficient $\rho_{\text{Int.}}(\theta_{rot}, \phi_{pr})$ for axes rotation $\theta_{rot} = 0 \ldots 180°$ and phase retardation $\phi_{pr} = -90 \ldots 90°$ obtained for idealised SpectroBragg Mueller matrix for anisotropic FBG data. . . V.II N-13
N.8 Cross–sectional plots of figure N.7 which contain the largest value for the correlation coefficient $\rho_{\text{Int.}}(\theta_{rot}, \phi_{pr})$, (a) constant phase retardation ϕ_{pr} and (b) showing constant rotation θ_{rot}. . . . . V.II N-13
N.9 Plot of changing correlation coefficient $\rho_{\text{Int.}}(\theta_{rot}, \phi_{pr})$ for axes rotation $\theta_{rot} = 0 \ldots 180°$ and phase retardation $\phi_{pr} = -90 \ldots 90°$ obtained for idealised SpectroBragg Mueller matrix for isotropic FBG data. . . . . V.II N-14
N.10 Cross–sectional plots of figure N.9 which contain the largest value for the correlation coefficient $\rho_{\text{Int.}}(\theta_{rot}, \phi_{pr})$, (a) constant phase retardation ϕ_{pr} and (b) showing constant rotation θ_{rot}. . . . . V.II N-14
N.11 Channelled spectrum produced by full SLED spectrum through the Lyot depolariser onto the SpectroBragg, with magnified view inset. . V.II N-15
N.12 Poincaré sphere projections of anisotropic FBG data showing: **(a)** S_2 V. S_3 along S_1 to $-S_1$; **(b)** S_2 V. S_3 along $-S_1$ to S_1; **(c)** S_1 V. S_3 along S_2 to $-S_2$; **(d)** S_1 V. S_3 along $-S_2$ to S_2 ;**(e)** S_2 V. S_1 along S_3 to $-S_3$; and **(f)** S_2 V. S_1 along $-S_3$ to S_3. . . . . V.II N-19
N.13 Poincaré sphere projections of isotropic FBG data showing: **(a)** S_2 V. S_3 along S_1 to $-S_1$; **(b)** S_2 V. S_3 along $-S_1$ to S_1; **(c)** S_1 V. S_3 along S_2 to $-S_2$; **(d)** S_1 V. S_3 along $-S_2$ to S_2 ;**(e)** S_2 V. S_1 along S_3 to $-S_3$; and **(f)** S_2 V. S_1 along $-S_3$ to S_3. . . . . V.II N-20
N.14 Plot of anisotropic FBG data showing **(a)** the data captured on the SpectroBragg; **(b)** the FFT filtered SpectroBragg data; **(c)** the calculated ideal SpectroBragg intensity from the polarimeter data, using a rotation angle of 7°; and **(d)** the cross–correlation, $\mathcal{R}_{\text{Int.}}$, of (b) & (c) for Lyot depolariser. . . . . V.II N-21

N.15 Plot of isotropic FBG data showing **(a)** the data captured on the SpectroBragg; **(b)** the FFT filtered SpectroBragg data; **(c)** the calculated ideal SpectroBragg intensity from the polarimeter data, using a rotation angle of 49°; and **(d)** the cross–correlation, $\mathcal{R}_{\text{Int.}}$, of (b) & (c) for Lyot depolariser. . . . . V.II N-22
N.16 Plot of **(a)** centroid determined λ_B for the anisotropic FBG data showing; **(b)** the centroid determined λ_B from the FFT filtered SpectroBragg data. . . . . V.II N-23
N.17 Plot of **(a)** centroid determined λ_B for the anisotropic FBG data showing; **(b)** the centroid determined λ_B from the FFT filtered SpectroBragg data. . . . . V.II N-23
N.18 Plot of changing correlation coefficient $\rho_{\text{Int.}}(\theta_{rot}, \phi_{pr})$ for axes rotation $\theta_{rot} = 0 \ldots 180°$ and phase retardation $\phi_{pr} = -90 \ldots 90°$ obtained for idealised SpectroBragg Mueller matrix for anisotropic FBG data. . . V.II N-24
N.19 Cross–sectional plots of figure N.18 which contain the largest value for the correlation coefficient $\rho_{\text{Int.}}(\theta_{rot}, \phi_{pr})$, (a) constant phase retardation ϕ_{pr} and (b) showing constant rotation θ_{rot}. . . . . V.II N-24
N.20 Plot of changing correlation coefficient $\rho_{\text{Int.}}(\theta_{rot}, \phi_{pr})$ for axes rotation $\theta_{rot} = 0 \ldots 180°$ and phase retardation $\phi_{pr} = -90 \ldots 90°$ obtained for idealised SpectroBragg Mueller matrix for isotropic FBG. . . . . V.II N-25
N.21 Cross–sectional plots of figure N.20 which contain the largest value for the correlation coefficient $\rho_{\text{Int.}}(\theta_{rot}, \phi_{pr})$, (a) constant phase retardation ϕ_{pr} and (b) showing constant rotation θ_{rot}. . . . . V.II N-25
N.22 Poincaré sphere projections of anisotropic FBG data showing: **(a)** S_2 V. S_3 along S_1 to $-S_1$; **(b)** S_2 V. S_3 along $-S_1$ to S_1; **(c)** S_1 V. S_3 along S_2 to $-S_2$; **(d)** S_1 V. S_3 along $-S_2$ to S_2 ;**(e)** S_2 V. S_1 along S_3 to $-S_3$; and **(f)** S_2 V. S_1 along $-S_3$ to S_3. . . . . V.II N-31
N.23 Poincaré sphere projections of isotropic FBG data showing: **(a)** S_2 V. S_3 along S_1 to $-S_1$; **(b)** S_2 V. S_3 along $-S_1$ to S_1; **(c)** S_1 V. S_3 along S_2 to $-S_2$; **(d)** S_1 V. S_3 along $-S_2$ to S_2 ;**(e)** S_2 V. S_1 along S_3 to $-S_3$; and **(f)** S_2 V. S_1 along $-S_3$ to S_3. . . . . V.II N-32
N.24 Plot of anisotropic FBG data showing **(a)** the data captured on the SpectroBragg; **(b)** the FFT filtered SpectroBragg data; **(c)** the calculated ideal SpectroBragg intensity from the polarimeter data, using a rotation angle of 118°; and **(d)** the cross–correlation, $\mathcal{R}_{\text{Int.}}$, of (b) & (c) for Lefèvre controller approach. . . . . V.II N-33

N.25 Plot of isotropic FBG data showing **(a)** the data captured on the SpectroBragg; **(b)** the FFT filtered SpectroBragg data; **(c)** the calculated ideal SpectroBragg intensity from the polarimeter data, using a rotation angle of 16°; and **(d)** the cross–correlation, $\mathcal{R}_{\text{Int.}}$, of (b) & (c) for Lefèvre controller approach. . . . . V.II N-34
N.26 Plot of **(a)** centroid determined λ_B for the anisotropic FBG data showing; **(b)** the centroid determined λ_B from the FFT filtered SpectroBragg data. . . . . V.II N-35
N.27 Plot of **(a)** centroid determined λ_B for the anisotropic FBG data showing; **(b)** the centroid determined λ_B from the FFT filtered SpectroBragg data. . . . . V.II N-35
N.28 Plot of changing correlation coefficient $\rho_{\text{Int.}}(\theta_{rot}, \phi_{pr})$ for axes rotation $\theta_{rot} = 0 \ldots 180°$ and phase retardation $\phi_{pr} = -90 \ldots 90°$ obtained for idealised SpectroBragg Mueller matrix for anisotropic FBG. . . . . V.II N-36
N.29 Cross–sectional plots of figure N.28 which contain the largest value for the correlation coefficient $\rho_{\text{Int.}}(\theta_{rot}, \phi_{pr})$, (a) constant phase retardation ϕ_{pr} and (b) showing constant rotation θ_{rot}. . . . . V.II N-36
N.30 Plot of changing correlation coefficient $\rho_{\text{Int.}}(\theta_{rot}, \phi_{pr})$ for axes rotation $\theta_{rot} = 0 \ldots 180°$ and phase retardation $\phi_{pr} = -90 \ldots 90°$ obtained for idealised SpectroBragg Mueller matrix for isotropic FBG. . . . . V.II N-37
N.31 Cross–sectional plots of figure N.30 which contain the largest value for the correlation coefficient $\rho_{\text{Int.}}(\theta_{rot}, \phi_{pr})$, (a) constant phase retardation ϕ_{pr} and (b) showing constant rotation θ_{rot}. . . . . V.II N-37
N.32 Poincaré sphere projections of anisotropic FBG data showing: **(a)** S_2 V. S_3 along S_1 to $-S_1$; **(b)** S_2 V. S_3 along $-S_1$ to S_1; **(c)** S_1 V. S_3 along S_2 to $-S_2$; **(d)** S_1 V. S_3 along $-S_2$ to S_2 ;**(e)** S_2 V. S_1 along S_3 to $-S_3$; and **(f)** S_2 V. S_1 along $-S_3$ to S_3. . . . . V.II N-41
N.33 Poincaré sphere projections of isotropic FBG data showing: **(a)** S_2 V. S_3 along S_1 to $-S_1$; **(b)** S_2 V. S_3 along $-S_1$ to S_1; **(c)** S_1 V. S_3 along S_2 to $-S_2$; **(d)** S_1 V. S_3 along $-S_2$ to S_2 ;**(e)** S_2 V. S_1 along S_3 to $-S_3$; and **(f)** S_2 V. S_1 along $-S_3$ to S_3. . . . . V.II N-42
N.34 Plot of anisotropic FBG data showing **(a)** the data captured on the SpectroBragg; **(b)** the FFT filtered SpectroBragg data; **(c)** the calculated ideal SpectroBragg intensity from the polarimeter data, using a rotation angle of 57°; and **(d)** the cross–correlation, $\mathcal{R}_{\text{Int.}}$, of (b) & (c) for Circulator/Faraday mirror approach. . . . . V.II N-43

N.35 Plot of isotropic FBG data showing **(a)** the data captured on the SpectroBragg; **(b)** the FFT filtered SpectroBragg data; **(c)** the calculated ideal SpectroBragg intensity from the polarimeter data, using a rotation angle of 120°; and **(d)** the cross–correlation, $\mathcal{R}_{\text{Int.}}$, of (b) & (c) for Circulator/Faraday mirror approach. . . . . V.II N-44
N.36 Plot of **(a)** centroid determined λ_B for the anisotropic FBG data showing; **(b)** the centroid determined λ_B from the FFT filtered SpectroBragg data. . . . . V.II N-45
N.37 Plot of **(a)** centroid determined λ_B for the anisotropic FBG data showing; **(b)** the centroid determined λ_B from the FFT filtered SpectroBragg data. . . . . V.II N-45
N.38 Plot of changing correlation coefficient $\rho_{\text{Int.}}(\theta_{rot}, \phi_{pr})$ for axes rotation $\theta_{rot} = 0 \ldots 180°$ and phase retardation $\phi_{pr} = -90 \ldots 90°$ obtained for idealised SpectroBragg Mueller matrix for anisotropic FBG. . . . . V.II N-46
N.39 Cross–sectional plots of figure N.38 which contain the largest value for the correlation coefficient $\rho_{\text{Int.}}(\theta_{rot}, \phi_{pr})$, (a) constant phase retardation ϕ_{pr} and (b) showing constant rotation θ_{rot}. . . . . V.II N-46
N.40 Plot of changing correlation coefficient $\rho_{\text{Int.}}(\theta_{rot}, \phi_{pr})$ for axes rotation $\theta_{rot} = 0 \ldots 180°$ and phase retardation $\phi_{pr} = -90 \ldots 90°$ obtained for idealised SpectroBragg Mueller matrix for isotropic FBG. . . . . V.II N-47
N.41 Cross–sectional plots of figure N.40 which contain the largest value for the correlation coefficient $\rho_{\text{Int.}}(\theta_{rot}, \phi_{pr})$, (a) constant phase retardation ϕ_{pr} and (b) showing constant rotation θ_{rot}. . . . . V.II N-47
N.42 Poincaré sphere projections of anisotropic FBG data showing: **(a)** S_2 V. S_3 along S_1 to $-S_1$; **(b)** S_2 V. S_3 along $-S_1$ to S_1; **(c)** S_1 V. S_3 along S_2 to $-S_2$; **(d)** S_1 V. S_3 along $-S_2$ to S_2 ;**(e)** S_2 V. S_1 along S_3 to $-S_3$; and **(f)** S_2 V. S_1 along $-S_3$ to S_3. . . . . V.II N-52
N.43 Poincaré sphere projections of isotropic FBG data showing: **(a)** S_2 V. S_3 along S_1 to $-S_1$; **(b)** S_2 V. S_3 along $-S_1$ to S_1; **(c)** S_1 V. S_3 along S_2 to $-S_2$; **(d)** S_1 V. S_3 along $-S_2$ to S_2 ;**(e)** S_2 V. S_1 along S_3 to $-S_3$; and **(f)** S_2 V. S_1 along $-S_3$ to S_3. . . . . V.II N-53
N.44 Plot of anisotropic FBG data showing **(a)** the data captured on the SpectroBragg; **(b)** the FFT filtered SpectroBragg data; **(c)** the calculated ideal SpectroBragg intensity from the polarimeter data, using a rotation angle of 118°; and **(d)** the cross–correlation, $\mathcal{R}_{\text{Int.}}$, of (b) & (c) for PDL compensator. . . . . V.II N-54

N.45 Plot of isotropic FBG data showing **(a)** the data captured on the SpectroBragg; **(b)** the FFT filtered SpectroBragg data; **(c)** the calculated ideal SpectroBragg intensity from the polarimeter data, using a rotation angle of 61°; and **(d)** the cross–correlation, $\mathcal{R}_{\text{Int.}}$, of (b) & (c) for PDL compensator. . . . . V.II N-55
N.46 Plot of **(a)** centroid determined λ_B for the anisotropic FBG data showing; **(b)** the centroid determined λ_B from the FFT filtered SpectroBragg data. . . . . V.II N-56
N.47 Plot of **(a)** centroid determined λ_B for the anisotropic FBG data showing; **(b)** the centroid determined λ_B from the FFT filtered SpectroBragg data. . . . . V.II N-56
N.48 Plot of changing correlation coefficient $\rho_{\text{Int.}}(\theta_{rot}, \phi_{pr})$ for axes rotation $\theta_{rot} = 0 \ldots 180°$ and phase retardation $\phi_{pr} = -90 \ldots 90°$ obtained for idealised SpectroBragg Mueller matrix for anisotropic FBG. . . . . V.II N-57
N.49 Cross–sectional plots of figure N.48 which contain the largest value for the correlation coefficient $\rho_{\text{Int.}}(\theta_{rot}, \phi_{pr})$, (a) constant phase retardation ϕ_{pr} and (b) showing constant rotation θ_{rot}. . . . . V.II N-57
N.50 Plot of changing correlation coefficient $\rho_{\text{Int.}}(\theta_{rot}, \phi_{pr})$ for axes rotation $\theta_{rot} = 0 \ldots 180°$ and phase retardation $\phi_{pr} = -90 \ldots 90°$ obtained for idealised SpectroBragg Mueller matrix for isotropic FBG. . . . . V.II N-58
N.51 Cross–sectional plots of figure N.50 which contain the largest value for the correlation coefficient $\rho_{\text{Int.}}(\theta_{rot}, \phi_{pr})$, (a) constant phase retardation ϕ_{pr} and (b) showing constant rotation θ_{rot}. . . . . V.II N-58
N.52 Control experiment anisotropic FBG Stokes vectors, from figure N.1 (page V.II N-8). . . . . V.II N-60
N.53 Control experiment isotropic FBG Stokes vectors, from figure N.2 (page V.II N-9). . . . . V.II N-60
N.54 Lyot depolariser experiment anisotropic FBG Stokes vectors, from figure N.12 (page V.II N-19). . . . . V.II N-61
N.55 Lyot depolariser experiment isotropic FBG Stokes vectors, from figure N.13 (page V.II N-20). . . . . V.II N-61
N.56 Lefèvre polarisation controller experiment anisotropic FBG Stokes vectors, from figure N.22 (page V.II N-31). . . . . V.II N-62
N.57 Lefèvre polarisation controller experiment isotropic FBG Stokes vectors, from figure N.23 (page V.II N-32). . . . . V.II N-62
N.58 circulator/Faraday mirror experiment anisotropic FBG Stokes vectors, from figure N.32 (page V.II N-41). . . . . V.II N-63
N.59 circulator/Faraday mirror experiment isotropic FBG Stokes vectors, from figure N.33 (page V.II N-42). . . . . V.II N-63

N.60 PDL compensation experiment anisotropic FBG Stokes vectors, from figure N.42 (page V.II N-52). . . . . V.II N-64
N.61 PDL compensation experiment isotropic FBG Stokes vectors, from figure N.43 (page V.II N-53). . . . . V.II N-64

O.1 (a) Dihedral angle between neighbouring SOPs; (b) Intensity observed by SpectroBragg for these changes in SOP; wavelength changes as calculated by centroid calculation for these changes in SOP. . . . . V.II O-2
O.2 (a) Normalised plots of the minimum– and maximum–intensity spectral profiles about the centroid calculated λ_B, shown in figure O.1(b); (b) difference between the maximum (blue) and minimum (green) normalised intensity values. . . . . V.II O-3

P.1 The Hamming and rectangular windows, multiplying all data in the range by 1. . . . . V.II P-5
P.2 The semi–log spectral responses of the Hamming and rectangular windows. . . . . V.II P-5

Q.1 Schematic of the modified NewFocus 2053 receiver. The 2053 photodiode failed and was replaced by a GaP500 photodiode. The failed photodiode was fixed with epoxy into the FC/APC connector supplied on the 2053 and so was unusable. The GaP500 photodiode was soldered onto the circuit board as the failed photodiode had been. Half of an FC/APC mating sleeve was used to provide the FC/APC connection, and the photodiode located within the mating sleeve half. V.II Q-2
Q.2 Photograph of the NewFocus receiver settings. . . . . V.II Q-2

R.1 Centroid rectangular windows for $n_w = 1$, with window length $2n_w + 1$.V.II R-3
R.2 Centroid rectangular windows for $n_w = 20$, with window length $2n_w + 1$. The legend of figure R.1 applies. . . . . V.II R-3
R.3 Overlayed differences in mean centroid determined peak wavelengths, $\Delta_w \overline{\lambda_B}$, as rectangular window width, n_w, is adjusted for temperature sensor and reference FBG. The differences do not converge as the lowest values are at $n'_w = 1 : 3$. . . . . V.II R-4
R.4 Overlayed differences in standard deviation of the centroid determined peak wavelengths, $\Delta_w \delta_{\lambda_B}$, as rectangular window width, n_w, is adjusted for temperature sensor and reference FBG. . . . . V.II R-4
R.5 Linear fit to temperature response slope of temperature signal and reference FBGs as calculated by centroid approach, with rectangular windows of width $2n_w + 1$. . . . . V.II R-5

R.6 Residuals to the linear fits to temperature response slope of temperature signal and reference FBGs shown in figure R.5. . . . . V.II R-5
R.7 Differences in linear fit to temperature response slope of temperature signal and reference FBGs as calculated by centroid approach, n'_w changing. . . . . V.II R-6
R.8 Differences in the residuals to the linear fits to temperature response slopes of figure R.7. . . . . V.II R-6
R.9 HTT Hamming windows for $n_w = 1$, with window length $2n_w + 1$. . . V.II R-8
R.10 HTT Hamming windows for $n_w = 20$, with window length $2n_w + 1$. The legend of figure R.9 applies. . . . . V.II R-8
R.11 Overlayed differences in mean HTT determined peak wavelengths, $\Delta_w \overline{\lambda_B}$, as Hamming window width, n_w, is adjusted for temperature sensor and reference FBG. . . . . V.II R-9
R.12 Overlayed differences in standard deviation of the HTT determined peak wavelengths, $\Delta_w \delta_{\lambda_B}$, as Hamming window width, n_w, is adjusted for temperature sensor and reference FBG. . . . . V.II R-9
R.13 Linear fit to temperature response slope of temperature signal and reference FBGs as calculated by HTT approach, with Hamming windows of width $2n_w + 1$. . . . . V.II R-11
R.14 Residuals to the linear fits to temperature response slope of temperature signal and reference FBGs shown in figure R.13. . . . . V.II R-11
R.15 Differences in linear fit to temperature response slope of temperature signal and reference FBGs as calculated by HTT approach, n'_w changing. V.II R-12
R.16 Differences in the residuals to the linear fits to temperature response slopes of figure R.13. . . . . V.II R-12
R.17 (a)Temperature signal FBG ($\sim$ 1566 nm) and (b) reference FBG ($\sim$ 1560nm) centroid wavelength against temperature. Different window lengths are overlapped at each interferogram length. The wavelength values have been corrected against the reference laser wavelength. . . V.II R-14
R.18 Overlayed differences in mean centroid determined peak wavelengths, $\Delta_w \overline{\lambda_B}$, as rectangular window width, n_w, is adjusted for temperature sensor and reference FBG. The differences do not converge as the lowest values are at $n'_w = 1 \ldots 3$. . . . . V.II R-16
R.19 The n'_w position at which a minimum centroid determined $\Delta_w \overline{\lambda_B}$ is obtained for each temperature step. The average values are 8.9 ± 5.93 and 7.53 ± 5.49 for the temperature sensor and reference FBGs, respectively. . . . . V.II R-16

R.20 Overlayed differences in standard deviation of the centroid determined peak wavelengths, $\Delta_w \delta_{\lambda_B}$, as rectangular window width, n_w, is adjusted for temperature sensor and reference FBG. The differences do not converge as the lowest values are at $n'_w = 1 \ldots 3$. . . . . V.II R-17
R.21 The n'_w position at which a minimum centroid determined $\Delta_w \delta_{\lambda_B}$ is obtained for each temperature step. The average values are 10.38 ± 4.63 and 8.47 ± 4.56 for the temperature sensor and reference FBGs, respectively. . . . . V.II R-17
R.22 Overlayed differences in mean centroid determined peak wavelengths, $\Delta_i \overline{\lambda_B}$, as rectangular window width, n_i, is adjusted for temperature sensor and reference FBG. . . . . V.II R-19
R.23 The n'_i position at which a minimum centroid determined $\Delta_i \overline{\lambda_B}$ is obtained for each temperature step. The average values are 9.64 ± 3.98 and 9.85 ± 4.15 for the temperature sensor and reference FBGs, respectively. . . . . V.II R-19
R.24 Overlayed differences in standard deviation of the centroid determined peak wavelengths, $\Delta_i \delta_{\lambda_B}$, as rectangular window width, n_i, is adjusted for temperature sensor and reference FBG. . . . . V.II R-20
R.25 The n'_i position at which a minimum centroid determined $\Delta_i \delta_{\lambda_B}$ is obtained for each temperature step. The average values are 8.37 ± 4.26 and 8.33 ± 4.03 for the temperature sensor and reference FBGs, respectively. . . . . V.II R-20
R.26 Linear fit to temperature response slope of temperature signal FBG as calculated by centroid approach, with rectangular windows of width $2n_w + 1$ and interferogram length step n_i. . . . . V.II R-21
R.27 Linear fit to temperature response slope of reference FBG as calculated by centroid approach, with rectangular windows for $2n_w + 1$ and interferogram length step n_i. . . . . V.II R-21
R.28 Residuals to the linear fits to temperature response slope of signal FBG shown in figure R.26 (page V.II R-21). . . . . V.II R-23
R.29 Residuals to the linear fits to temperature response slope of reference FBG shown in figure R.27 (page V.II R-21). . . . . V.II R-23
R.30 Differences along n_i of slopes the linear fits to temperature response slope of temperature signal FBG shown in figure R.26 (page V.II R-21). V.II R-24
R.31 Differences along n_i of slopes the linear fits to temperature response slope of reference FBG shown in figure R.27 (page V.II R-21). . . . . V.II R-24
R.32 Temperature signal FBG values of $n_w = 2, 3, 4$ from R.26 (page V.II R-21) indicating oscillation. . . . . V.II R-25

R.33 Reference FBG values of $n_w = 2, 3, 4$ from R.27 (page V.II R-21) indicating oscillation. . . . . V.II R-25
R.34 (a) Temperature signal FBG values of $n_w = 2, 3, 4$ from figure 6.20 (page V.I - 292); (b) corresponding temperature signal FBG values for $n_i = 5$ (lower n_i) ; (c) corresponding temperature signal FBG values for $n_i = 7$ (upper n_i). . . . . V.II R-28
R.35 (a) Reference FBG values of $n_w = 2, 3, 4$ from figure 6.21 (page V.I - 292); (b) corresponding reference FBG values for $n_i = 5$ (lower n_i) ; (c) corresponding reference FBG values for $n_i = 7$ (upper n_i). . . . . V.II R-29
R.36 (a) Temperature signal FBG ($\sim$ 1566 nm) and (b) reference FBG ($\sim$ 1560nm) HTT wavelength against temperature. Different window lengths are overlapped at each interferogram length. The wavelength values have been corrected against the reference laser wavelength. . . V.II R-31
R.37 Overlayed differences in mean HTT determined peak wavelengths, $\Delta_w\overline{\lambda_B}$, as Hamming window width, n_w, is adjusted for temperature sensor and reference FBG. The differences converge until the other FBG begins to enter the window. . . . . V.II R-32
R.38 The n'_w position at which a minimum HTT determined $\Delta_w\overline{\lambda_B}$ is obtained for each temperature step. The average values are 13.61 ± 3.27 and 14.53 ± 3.57 for the temperature sensor and reference FBGs, respectively. . . . . V.II R-32
R.39 Overlayed differences in standard deviation of the HTT determined peak wavelengths, $\Delta_w\delta_{\lambda_B}$, as Hamming window width, n_w, is adjusted for temperature sensor and reference FBG. The differences converge until the other FBG begins to enter the window. . . . . V.II R-33
R.40 The n'_w position at which a minimum HTT determined $\Delta_w\delta_{\lambda_B}$ is obtained for each temperature step. The average values are 12.68 ± 4.39 and 12.44 ± 4.42 for the temperature sensor and reference FBGs, respectively. . . . . V.II R-33
R.41 Overlayed differences in mean HTT determined peak wavelengths, $\Delta_i\overline{\lambda_B}$, as interferogram length, n_i, is adjusted for temperature sensor and reference FBG. The differences show no convergence but a weak periodic oscillation. . . . . V.II R-35
R.42 The n'_i position at which a minimum HTT determined $\Delta_i\overline{\lambda_B}$ is obtained for each temperature step. The average values are 8.88 ± 4.35 and 7.37 ± 4.45 for the temperature sensor and reference FBGs, respectively. . . . . V.II R-35

R.43 Overlayed differences in standard deviation of the HTT determined peak wavelengths, $\Delta_i \delta_{\lambda_B}$, as interferogram length, n_i, is adjusted for temperature sensor and reference FBG. The differences show no obvious convergence. . . . . V.II R-36
R.44 The n_i' position at which a minimum HTT determined $\Delta_i \delta_{\lambda_B}$ is obtained for each temperature step. The average values are 8.02 ± 4.35 and 9.03 ± 4.48 for the temperature sensor and reference FBGs, respectively. . . . . V.II R-36
R.45 Linear fit to temperature response slope of temperature signal FBG as calculated by HTT approach, with rectangular windows of width $2n_w + 1$ and interferogram length step n_i. . . . . V.II R-37
R.46 Linear fit to temperature response slope of reference FBG as calculated by HTT approach, with rectangular windows for $2n_w + 1$ and interferogram length step n_i. . . . . V.II R-37
R.47 Residuals to the linear fits to temperature response slope of signal FBG shown in figure R.45 (page V.II R-37). . . . . V.II R-40
R.48 Residuals to the linear fits to temperature response slope of reference FBG shown in figure R.46 (page V.II R-37). . . . . V.II R-40
R.49 Differences along n_i of slopes the linear fits to temperature response slope of temperature signal FBG shown in figure R.45 (page V.II R-37).V.II R-41
R.50 Differences along n_i of slopes the linear fits to temperature response slope of reference FBG shown in figure R.46 (page V.II R-37). . . . . V.II R-41
R.51 Temperature signal FBG values of $n_w = 13, 14, 15$ from R.45 (page V.II R-37) indicating oscillation. . . . . V.II R-42
R.52 Reference FBG values of $n_w = 13, 14, 15$ from R.46 (page V.II R-37) indicating oscillation. . . . . V.II R-42
R.53 Temperature signal FBG values of $n_w = 1, 2, 3$ and the average value from $n_w = 13, 14, 15$. . . . . V.II R-43
R.54 Reference FBG values of $n_w = 1, 2, 3$ and the average value from $n_w = 13, 14, 15$. . . . . V.II R-43

List of Tables

J.1 From Exalos Measurement report ESL1505-2100-SN:121, and specification ESL1505-2100, Rev:1.0 (30-09-03). . . . . V.II J-2

N.1 Summary of control experiment **(a)** correlation coefficient, $\rho_{\text{Int.}}$, values for correlation between captured SpectroBragg intensity and calculated S_{SB}. In subsequent tables, the rotation and phase retardation angles which produced the value are listed under the $\rho_{\text{Int.}}$ value; **(b)** the FFT filtered and unfiltered (in parentheses) normalised standard deviations, $\sigma_{\text{Int.}}$, for both SpectroBragg and polarimeter data. The values are for the data with and without applied SOP changes (i.e. background); **(c)** the FFT filtered and unfiltered (in parentheses) standard deviation of centroid calculated wavelength, σ_{λ_B}, for the anisotropic and isotropic FBGs; **(d)** the SpectroBragg intensity–centroid λ_B correlation coefficient, ρ_{λ_B}, as a measure of intensity pattern's influence on λ_B. . . . . V.II N-3

N.2 Lyot depolariser approach summary of **(a)** correlation coefficient, $\rho_{\text{Int.}}$, values for correlation between captured SpectroBragg intensity and calculated S_{SB}; **(b)** the FFT filtered and unfiltered (in parentheses) normalised standard deviations, $\sigma_{\text{Int.}}$, for both SpectroBragg and polarimeter data. The values are for the data with applied SOP changes and without applied SOP changes (i.e. background); **(c)** the FFT filtered and unfiltered (in parentheses) standard deviation of centroid calculated wavelength, σ_{λ_B}, for the anisotropic and isotropic FBGs; **(d)** the SpectroBragg intensity–centroid λ_B correlation coefficient, ρ_{λ_B}, as a measure of intensity pattern's influence on λ_B. . . . V.II N-16

N.3 Lefèvre controller mitigation approach summary of **(a)** correlation coefficient, $\rho_{\text{Int.}}$, values for correlation between captured SpectroBragg intensity and calculated S_{SB}; **(b)** the FFT filtered and unfiltered (in parentheses) normalised standard deviations, $\sigma_{\text{Int.}}$, for both SpectroBragg and polarimeter data. The values are for the data with applied SOP changes and without applied SOP changes (i.e. background); **(c)** the FFT filtered and unfiltered (in parentheses) standard deviation of centroid calculated wavelength, σ_{λ_B}, for the anisotropic and isotropic FBGs; **(d)** the SpectroBragg intensity–centroid λ_B correlation coefficient, ρ_{λ_B}, as a measure of intensity pattern's influence on λ_B. . . . . V.II N-27

N.4 Circulator/Faraday mirror mitigation approach summary of **(a)** correlation coefficient, $\rho_{\text{Int.}}$, values for correlation between captured SpectroBragg intensity and calculated S_{SB}; **(b)** the FFT filtered and unfiltered (in parentheses) normalised standard deviations, $\sigma_{\text{Int.}}$, for both SpectroBragg and polarimeter data. The values are for the data with applied SOP changes and without applied SOP changes (i.e. background); **(c)** the FFT filtered and unfiltered (in parentheses) standard deviation of centroid calculated wavelength, σ_{λ_B}, for the anisotropic and isotropic FBGs; **(d)** the SpectroBragg intensity–centroid λ_B correlation coefficient, ρ_{λ_B}, as a measure of intensity pattern's influence on λ_B. . . . . V.II N-40

N.5 PDL balancing mitigation approach summary of **(a)** correlation coefficient, $\rho_{\text{Int.}}$, values for correlation between captured SpectroBragg intensity and calculated S_{SB}; **(b)** the FFT filtered and unfiltered (in parentheses) normalised standard deviations, $\sigma_{\text{Int.}}$, for both SpectroBragg and polarimeter data. The values are for the data with applied SOP changes and without applied SOP changes (i.e. background); **(c)** the FFT filtered and unfiltered (in parentheses) standard deviation of centroid calculated wavelength, σ_{λ_B}, for the anisotropic and isotropic FBGs; **(d)** the SpectroBragg intensity–centroid λ_B correlation coefficient, ρ_{λ_B}, as a measure of intensity pattern's influence on λ_B. . . . . V.II N-51

R.1 Averages of centroid calculated mean values across all n_i for the ranges of n_w. . . . . V.II R-15

R.2 Standard deviations of centroid calculated mean values across all n_i for the ranges of n_w. . . . . V.II R-15

R.3 Mean values of temperature sensor and reference FBGs with changing n'_w and n'_i from figures R.19 (page V.II R-16) and R.23 (page V.II R-19), respectively. . . . . V.II R-18
R.4 Mean values of temperature sensor and reference FBGs with changing n'_w and n'_i from figures R.21 (page V.II R-17) and R.25 (page V.II R-20), respectively. . . . . V.II R-18
R.5 Temperature sensor FBG centroid approach calculated slopes, $\frac{1}{\lambda_B}\frac{\partial\lambda_B}{\partial T}\times 10^{-6}\,{}^\circ\mathrm{C}^{-1}$, for $n_w = 2, 3, 4$ for each n_i, with norm of residuals (nm) in parenthesis. . . . . V.II R-27
R.6 Reference FBG centroid approach calculated slopes, $\frac{1}{\lambda_B}\frac{\partial\lambda_B}{\partial T}\times 10^{-6}{}^\circ\mathrm{C}^{-1}$, for $n_w = 2, 3, 4$ for each n_i, with norm of residuals (nm) in parenthesis. V.II R-27
R.7 Averages of HTT calculated mean values across all n_i for the ranges of n_w. . . . . V.II R-30
R.8 Standard deviations of HTT calculated mean values across all n_i for the ranges of n_w. . . . . V.II R-34
R.9 Mean values of temperature sensor and reference FBGs with changing n'_w and n'_i from figures R.37 (page V.II R-32) and R.41 (page V.II R-35), respectively. . . . . V.II R-38
R.10 Mean values of temperature sensor and reference FBGs with changing n'_w and n'_i from figures R.39 (page V.II R-33) and R.43 (page V.II R-36), respectively. . . . . V.II R-38
R.11 Temperature sensor FBG HTT approach calculated slopes, $\frac{1}{\lambda_B}\frac{\partial\lambda_B}{\partial T}\times 10^{-6}\,{}^\circ\mathrm{C}^{-1}$, for $n_w = 2, 3, 4$ for each n_i, with norm of residuals (nm) in parenthesis. . . . . V.II R-39
R.12 Reference FBG HTT approach calculated slopes, $\frac{1}{\lambda_B}\frac{\partial\lambda_B}{\partial T}\times 10^{-6}\,{}^\circ\mathrm{C}^{-1}$, for $n_w = 2, 3, 4$ for each n_i, with norm of residuals (nm) in parenthesis. V.II R-44
R.13 Optimum n_w values for the centroid and HTT approaches, for both the variable and fixed interferogram length cases. . . . . V.II R-45
R.14 Selected n_i values for the centroid and HTT approaches, based upon minimum difference from average across all n_w and n_i. . . . . V.II R-45

Appendix A

Maxwell's equations

Electromagnetic fields are classically described by Maxwell's equations [1, 2]. Maxwell's equation relates four macroscopic vectorial fields: the electric field, $\underline{\mathbf{E}}(\underline{\mathbf{r}}, t)$; the electric displacement $\underline{\mathbf{D}}(\underline{\mathbf{r}}, t)$; the magnetic induction $\underline{\mathbf{B}}(\underline{\mathbf{r}}, t)$; and the magnetic field $\underline{\mathbf{H}}(\underline{\mathbf{r}}, t)$. $\underline{\mathbf{r}}$ is the spatial position vector in three–dimensional space, $= x\ \underline{\hat{\mathbf{x}}} + y\ \underline{\hat{\mathbf{y}}} + z\ \underline{\hat{\mathbf{z}}}$, defined by the mutually orthonormal unit vectors $\underline{\hat{\mathbf{x}}}$, $\underline{\hat{\mathbf{y}}}$ and $\underline{\hat{\mathbf{z}}}$; and t is the time.

The differential form of Maxwell's equations[1] or Maxwell's postulates [2, 3] is:

$$\underline{\nabla} \bullet \underline{\mathbf{D}}(\underline{\mathbf{r}}, t) = \underline{\boldsymbol{\rho}}(\underline{\mathbf{r}}, t) \tag{A.1a}$$

$$\underline{\nabla} \bullet \underline{\mathbf{B}}(\underline{\mathbf{r}}, t) = 0 \tag{A.1b}$$

$$\underline{\nabla} \times \underline{\mathbf{E}}(\underline{\mathbf{r}}, t) + \frac{\partial \underline{\mathbf{B}}(\underline{\mathbf{r}}, t)}{\partial t} = 0 \tag{A.1c}$$

$$\underline{\nabla} \times \underline{\mathbf{H}}(\underline{\mathbf{r}}, t) - \frac{\partial \underline{\mathbf{D}}(\underline{\mathbf{r}}, t)}{\partial t} = \underline{\mathbf{J}}(\underline{\mathbf{r}}, t) \tag{A.1d}$$

where $\underline{\nabla}$ is the gradient in the co–ordinate system, $\underline{\mathbf{J}}(\underline{\mathbf{r}}, t)$ is the electric current density and $\underline{\boldsymbol{\rho}}(\underline{\mathbf{r}}, t)$ is the electric charge density.

In a material, the *constitutive relations* or material relations [2], express behaviour of the material influenced by the field. In the most general formulation the constitutive relations are [3]:

$$\underline{\mathbf{D}}(\underline{\mathbf{r}}, t) = \mathcal{F}\left(\underline{\mathbf{E}}(\underline{\mathbf{r}}, t), \underline{\mathbf{B}}(\underline{\mathbf{r}}, t)\right) \tag{A.2a}$$

$$\underline{\mathbf{H}}(\underline{\mathbf{r}}, t) = \mathcal{G}\left(\underline{\mathbf{E}}(\underline{\mathbf{r}}, t), \underline{\mathbf{B}}(\underline{\mathbf{r}}, t)\right) \tag{A.2b}$$

[1] Used to describe the behaviour of electromagnetic fields, as opposed to the sum effect at a point, provided by the integral form [3].

where $\mathcal{F}$ and $\mathcal{G}$ are linear/nonlinear functions for linear/nonlinear materials. $\mathcal{F}$ and $\mathcal{G}$ will, in general, contain dyadics[2] relating $\underline{\mathbf{E}}(\underline{\mathbf{r}},t)$ and $\underline{\mathbf{B}}(\underline{\mathbf{r}},t)$ to both $\underline{\mathbf{D}}(\underline{\mathbf{r}},t)$ and $\underline{\mathbf{H}}(\underline{\mathbf{r}},t)$ [3].

In general, the components of $\mathcal{F}$ and $\mathcal{G}$ are tensors, such that $\underline{\mathbf{D}}$ and $\underline{\mathbf{E}}$ are not aligned or $\underline{\mathbf{H}}$ and $\underline{\mathbf{B}}$ are not aligned. To a first order approximation [4],

$$\underline{\mathbf{D}}(\underline{\mathbf{r}},t) = \underline{\mathbf{P}} + \underline{\underline{\boldsymbol{\epsilon}}}_0 \underline{\mathbf{E}}(\underline{\mathbf{r}},t) \tag{A.3a}$$

$$\underline{\mathbf{B}}(\underline{\mathbf{r}},t) = \underline{\underline{\boldsymbol{\mu}}}_0 \left(\underline{\mathbf{M}} + \underline{\mathbf{H}}(\underline{\mathbf{r}},t)\right) \tag{A.3b}$$

where $\underline{\mathbf{P}}$ is the induced polarisation, $\underline{\mathbf{M}}$ is the induced magnetisation, $\underline{\underline{\boldsymbol{\epsilon}}}_0 = \epsilon_0 \underline{\underline{\mathbf{I}}}$ and $\underline{\underline{\boldsymbol{\mu}}}_0 = \mu_0 \underline{\underline{\mathbf{I}}}$ are the permittivity and permeability of free space, respectively, and $\underline{\underline{\mathbf{I}}}$ is the identity second rank matrix.

The polarisation and magnetisation are typically complicated functions, and it is convenient to define the dyadics *electric susceptibility*, $\underline{\underline{\boldsymbol{\chi}}}_e$, and *magnetic susceptibility*, $\underline{\underline{\boldsymbol{\chi}}}_m$, [4, 5]:

$$\underline{\mathbf{P}} = \left(\underline{\underline{\boldsymbol{\epsilon}}}_0 \, \underline{\underline{\boldsymbol{\chi}}}_e \underline{\mathbf{E}}\right) + \underline{\mathbf{P}}_0 \tag{A.4a}$$

$$\underline{\mathbf{M}} = \left(\underline{\underline{\boldsymbol{\chi}}}_m \underline{\mathbf{H}}\right) + \underline{\mathbf{M}}_0 \tag{A.4b}$$

where $\underline{\mathbf{P}}_0$ and $\underline{\mathbf{M}}_0$ are residual polarisation and magnetisation, respectively.

If $\underline{\mathbf{P}}_0 \ll \left(\underline{\underline{\boldsymbol{\epsilon}}}_0 \, \underline{\underline{\boldsymbol{\chi}}}_e \underline{\mathbf{E}}\right)$ and $\underline{\mathbf{M}}_0 \ll \left(\underline{\underline{\boldsymbol{\chi}}}_m \underline{\mathbf{H}}\right)$, then equations (A.4) may be approximated as [2, 4]

$$\underline{\mathbf{D}}(\underline{\mathbf{r}},t) = \underline{\underline{\boldsymbol{\epsilon}}}_0 \left(\underline{\underline{\mathbf{I}}} + \underline{\underline{\boldsymbol{\chi}}}_e\right) \underline{\mathbf{E}}(\underline{\mathbf{r}},t) \equiv \underline{\underline{\boldsymbol{\epsilon}}} \, \underline{\mathbf{E}}(\underline{\mathbf{r}},t) \tag{A.5a}$$

$$\underline{\mathbf{B}}(\underline{\mathbf{r}},t) = \underline{\underline{\boldsymbol{\mu}}}_0 \left(\underline{\underline{\mathbf{I}}} + \underline{\underline{\boldsymbol{\chi}}}_m\right) \underline{\mathbf{H}}(\underline{\mathbf{r}},t) \equiv \underline{\underline{\boldsymbol{\mu}}} \, \underline{\mathbf{H}}(\underline{\mathbf{r}},t) \tag{A.5b}$$

where $\underline{\underline{\mathbf{I}}}$ is the identity matrix.

If the values $\underline{\underline{\boldsymbol{\epsilon}}}$ and $\underline{\underline{\boldsymbol{\mu}}}$ do not depend upon the field strength, the material is termed *linear*; if the values do not depend upon the position the material is termed *homogeneous*; and if the values do not depend upon the orientation of the fields the material is described as *isotropic*[3] [4], i.e. the components of $\mathcal{F}$ and $\mathcal{G}$ are scalars. The symmetry[4] of an isotropic material is highest, as it exhibits arbitrary translation–, inversion– and reflection–symmetry, $\mathsf{C}_{\infty v}$. When $\underline{\mathbf{D}}$ and $\underline{\mathbf{E}}$ or $\underline{\mathbf{H}}$ and $\underline{\mathbf{B}}$ are not aligned, the material is termed *anisotropic*[5] [3].

[2]Second rank tensors.

[3]$\underline{\mathbf{P}} = P\underline{\underline{\mathbf{I}}}$, $\underline{\mathbf{M}} = M\underline{\underline{\mathbf{I}}}$, $\underline{\underline{\boldsymbol{\epsilon}}}_0 = \epsilon_0 \underline{\underline{\mathbf{I}}}$ and $\underline{\underline{\boldsymbol{\mu}}}_0 = \mu_0 \underline{\underline{\mathbf{I}}}$ have no position dependence. As written, there is no temporal dependence, but this is not required for isotropy [2].

[4]The symmetry is important as "*the eigenvalues and eigenfunctions of a system belong to the irreducible representations of the group of symmetry operations of that system*" [6].

[5]Anisotropy may result in dichroism (directional changes in amplitude) or birefringence (direc-

When both $\underline{\mathbf{D}}$ and $\underline{\mathbf{E}}$ are anisotropically coupled to both $\underline{\mathbf{H}}$ and $\underline{\mathbf{B}}$ the material is termed *bianisotropic* [3]. This work will encounter electrical anisotropic effects [8], although bianisotropy may arise in the homogenisation of two or more constituent media [3]. The symmetry of an anisotropy is lower than for isotropy as one rotation is no longer valid. The symmetry will be lower still for bianisotropy.

(An)isotropy, therefore, is a manifestation of the interaction of the incident electromagnetic field with the electronic states of the material. From the definition of a field, when an electromagnetic field interacts with the material, the response time will be finite. Consequently $\underline{\underline{\boldsymbol{\epsilon}}}$ and $\underline{\underline{\boldsymbol{\mu}}}$ depend upon the rate at which the electromagnetic fields vary in time, which is termed *dispersion* [4].

It was experimentally demonstrated that, for non–relativistic speeds, the electric field vector, $\underline{\mathbf{E}}(\underline{\mathbf{r}}, t)$, exerts a greater force on electrons than the magnetic field does. This is the basis of the convention to use $\underline{\mathbf{E}}(\underline{\mathbf{r}}, t)$ to describe the orientation of the electromagnetic radiation [9].

In linear, homogeneous, nondispersive and isotropic materials Maxwell's equations can be readily rearranged to describe propagating electromagnetic fields in a simple form, termed the *wave equation* [2, 4]. Using the approximation of Ohm's law, which is assumed to hold [2, 4],

$$\underline{\mathbf{J}} = \underline{\underline{\boldsymbol{\sigma}}}_{\mathrm{EM}} \underline{\mathbf{E}} \tag{A.6}$$

where $\underline{\underline{\boldsymbol{\sigma}}}_{\mathrm{EM}}$ is the specific conductivity; the electromagnetic wave equations describing a propagating wave are:

$$\underline{\nabla}^2 \underline{\mathbf{E}} - \underline{\underline{\boldsymbol{\mu}}}\, \underline{\underline{\boldsymbol{\epsilon}}} \frac{\partial^2 \underline{\mathbf{E}}}{\partial t^2} - \underline{\underline{\boldsymbol{\mu}}}\, \underline{\underline{\boldsymbol{\sigma}}}_{\mathrm{EM}} \frac{\partial \underline{\mathbf{E}}}{\partial t} = \underline{\nabla} \left(\frac{\underline{\boldsymbol{\rho}}}{\underline{\underline{\boldsymbol{\epsilon}}}} \right) \tag{A.7a}$$

$$\underline{\nabla}^2 \underline{\mathbf{B}} - \underline{\underline{\boldsymbol{\mu}}}\, \underline{\underline{\boldsymbol{\epsilon}}} \frac{\partial^2 \underline{\mathbf{B}}}{\partial t^2} - \underline{\underline{\boldsymbol{\mu}}}\, \underline{\underline{\boldsymbol{\sigma}}}_{\mathrm{EM}} \frac{\partial \underline{\mathbf{B}}}{\partial t} = 0 \tag{A.7b}$$

which, in a vacuum (where $\underline{\boldsymbol{\rho}} = 0$ and $\underline{\underline{\boldsymbol{\sigma}}}_{\mathrm{EM}} = 0$), gives the vacuum wave equations [2, 4]:

$$\underline{\nabla}^2 \underline{\mathbf{E}} - \underline{\underline{\boldsymbol{\mu}}}\, \underline{\underline{\boldsymbol{\epsilon}}} \frac{\partial^2 \underline{\mathbf{E}}}{\partial t^2} = 0 \tag{A.8a}$$

$$\underline{\nabla}^2 \underline{\mathbf{B}} - \underline{\underline{\boldsymbol{\mu}}}\, \underline{\underline{\boldsymbol{\epsilon}}} \frac{\partial^2 \underline{\mathbf{B}}}{\partial t^2} = 0 \tag{A.8b}$$

Equations (A.8) are of the form [2, 10]

$$\underline{\nabla}^2 \underline{\boldsymbol{\psi}} - \frac{1}{\underline{v}^2} \frac{\partial^2 \underline{\boldsymbol{\psi}}}{\partial t^2} = 0 \tag{A.9}$$

tional changes in phase), or combinations of both [7].

which is the equation describing a propagating wave, $\underline{\boldsymbol{\psi}}$, moving at speed $\underline{v}$. For electromagnetic waves in free space,

$$\underline{v} = \frac{1}{\sqrt{\underline{\underline{\boldsymbol{\mu}}}_0 \underline{\underline{\boldsymbol{\epsilon}}}_0}} = \underline{c} \tag{A.10}$$

where $\underline{c}$ is the speed of light times the unit vector. However, in a medium

$$\underline{v} = \frac{1}{\sqrt{\underline{\underline{\boldsymbol{\mu}}}\,\underline{\underline{\boldsymbol{\epsilon}}}}} = \frac{\underline{c}}{\sqrt{\underline{\underline{\boldsymbol{\mu}}}_r\,\underline{\underline{\boldsymbol{\epsilon}}}_r}} < \underline{c} \tag{A.11}$$

where $\underline{\underline{\boldsymbol{\mu}}}_r$ and $\underline{\underline{\boldsymbol{\epsilon}}}_r$ are the ratios of $\underline{\underline{\boldsymbol{\mu}}}$ to $\underline{\underline{\boldsymbol{\mu}}}_0$ and $\underline{\underline{\boldsymbol{\epsilon}}}$ to $\underline{\underline{\boldsymbol{\epsilon}}}_0$ and are termed *the relative permeability* and *permittivity*[6], respectively. Typically, $\underline{\underline{\boldsymbol{\mu}}}_r \equiv 1$ and $\underline{\underline{\boldsymbol{\epsilon}}}_r > 1$ [2]. For this reason $\underline{\mathbf{E}}$ is used more than $\underline{\mathbf{H}}$ in treatments of optics [3, 9]. At optical frequencies, the frequency of electromagnetic radiation oscillates too fast for explicit measurement of the wave frequency [11].

The ratio of the speed of light in vacuo to the speed of light in a material is termed the *absolute refractive index*[7] [2]

$$\underline{\underline{n}} = \frac{\underline{c}}{\underline{v}} = \sqrt{\underline{\underline{\boldsymbol{\mu}}}\,\underline{\underline{\boldsymbol{\epsilon}}}} \tag{A.12}$$

However, dispersion makes the refractive index dependent upon frequency, ν, with which the electromagnetic fields vary in time, so for a material, i:

$$\underline{\underline{n}}_i = \underline{\underline{n}}_i(\nu) \tag{A.13}$$

The refractive index may be extended to incorporate attenuation by replacing the real $\underline{\underline{n}}$ with the complex $\underline{\underline{\tilde{\mathbf{n}}}}$ [13, 14],

$$\underline{\underline{\tilde{\mathbf{n}}}} = \underline{\underline{n}}\left(\underline{\underline{\mathbf{I}}} + i\underline{\underline{\boldsymbol{\kappa}}}_{\text{att}}\right) \tag{A.14}$$

where $\underline{\underline{\mathbf{I}}}$ is the identity matrix and $\underline{\underline{\boldsymbol{\kappa}}}_{\text{att}}$, the *attenuation index* of the material, the components of which are real constants.

[6] Also known as the dielectric tensor.

[7] The refractive index may be described by a vector, as opposed to a matrix, by neglecting bianisotropy. The vectors $\underline{\mathbf{E}}$ and $\underline{\mathbf{S}}$, the Poynting vector (§A.1), are coplanar to $\underline{\mathbf{D}}$ and $\underline{\mathbf{S}}$, reducing the dimensions of $\underline{\underline{n}}$ to $\underline{n}$ [12]. The dyadic version will be retained for the present to preserve orders in equations.

A.1 Energy transfer via electromagnetic radiation

The energy transmitted by an electromagnetic wave is provided by the *Poynting vector* [5],

$$\underline{\mathbf{S}} = \underline{\mathbf{E}} \times \underline{\mathbf{H}}^* \tag{A.15}$$

The Poynting vector describes the radiation intensity, the flux of energy per unit area normal to the direction of that flux. The experimentally observed intensity is a time average over many fluctuations of the electromagnetic field [4],

$$I \propto |\langle \underline{\mathbf{S}} \rangle| \bullet \underline{\hat{\mathbf{r}}} \tag{A.16}$$

where $\underline{\hat{\mathbf{r}}}$ is the unit vector normal to the direction of propagation. When $|\underline{\hat{\mathbf{E}}}|$ and $|\underline{\hat{\mathbf{H}}}|$ are orthogonal and proportional to each other,

$$I \propto \left|\langle \underline{\mathbf{E}} \rangle^2\right| \bullet \underline{\hat{\mathbf{r}}} \propto \left|\langle \underline{\mathbf{H}} \rangle^2\right| \bullet \underline{\hat{\mathbf{r}}} \tag{A.17}$$

A.2 Wave equation solutions

Equations (A.8) have time–varying non–zero solutions [15]. The simplest solution is the uniform monochromatic plane wave[8]. The superposition of plane waves allows the construction of different arbitrary waves [16, 17], and polychromatic fields can be constructed by the superposition of plane waves of different frequency.

The monochromatic plane wave[9] may be described as

$$\underline{\mathbf{E}}(\underline{\mathbf{r}}, t) = E_0 \left[\cos(\phi(\underline{\mathbf{r}}, t))\right] \tag{A.18}$$

where

$$\phi(\underline{\mathbf{r}}, t) = \underline{\mathbf{k}} \bullet \underline{\mathbf{r}} - \omega t, \tag{A.19}$$

and $\underline{\mathbf{k}} = k\underline{\mathbf{s}}$ is the *propagation vector* or *wave vector* in the direction of $\underline{\mathbf{s}}$ [2]:

$$k = nk_0 = \frac{2\pi}{\lambda} = \frac{n\omega}{c} = \frac{\omega}{v} \tag{A.20}$$

where $\omega = 2\pi\nu$ is the *angular frequency* derived from the frequency ν. $n = \underline{n} \bullet \underline{\mathbf{s}}$.

For simplicity, let $\underline{\mathbf{s}}$ be aligned with the unit vector $\underline{\hat{\mathbf{z}}}$, giving

$$E(z, t) = E_0 \left[\cos(kz - \omega t)\right] \tag{A.21}$$

[8] The monochromatic plane wave has a single spatial and temporal frequency, thus making it a basis set for waves which have a Fourier transform. The plane wave has no electric/magnetic field amplitude (hence polarisation) in the direction of propagation.

[9] A plane is defined as a wave with constant phase, i.e. $\underline{\mathbf{k}} \bullet \underline{\mathbf{r}} =$ const., in all planes perpendicular to the direction of propagation [18]. The plane wave is uniform if the amplitude is constant [19].

A point of constant phase moves with the velocity of the wave, termed the *phase velocity* [18],

$$c = \lambda\nu = \frac{\omega}{k} \tag{A.22}$$

Hence, ω and k are not independent when the phase velocity is fixed. This gives rise to the *dispersion relation*, which, for the vacuum, will be simply

$$\omega = ck \tag{A.23}$$

Rewriting equation (A.18) using Euler's formula [18]

$$E(t) = E_0\, \Re\left[\cos(kz - \omega t) + i\sin(kz - \omega t)\right] = E_0\, \Re\left[e^{-i(kz-\omega t)}\right] \tag{A.24}$$

where the real part of (A.24) is denoted by the symbol $\Re$, which is typically omitted in treatments with the understanding that the real part is to be taken.

To simplify the complex quantities further, this quantity may be written as a *phasor*, $f(\underline{\mathbf{r}})$, [20, 21], i.e.

$$f(\underline{\mathbf{r}}, t) = f(\underline{\mathbf{r}})e^{-i\omega t} \tag{A.25}$$

The phasor allows efficient calculation of the spatial components of waveforms independent of the temporal evolution. Equation (A.24) in phasor form gives

$$E(t) = E_0\, e^{-i(kz)} \tag{A.26}$$

A.3 Spherical waves

Another wave solution to equation (A.8) (page V.II A-3) is the spherical wave, obtained by solving in spherical co–ordinates. The Laplacian, $\underline{\nabla}^2$, is

$$\underline{\nabla}^2 = \frac{\partial^2}{\partial r^2} + \frac{2}{r}\frac{\partial}{\partial r} + \frac{1}{r^2\sin^2\varphi}\frac{\partial^2}{\partial\theta^2} + \frac{\cos\varphi}{r^2\sin\varphi}\frac{\partial}{\partial\varphi} + \frac{1}{r^2}\frac{\partial^2}{\partial\varphi^2} \tag{A.27}$$

which, for a spherically symmetric spherical wave, may be reduced to

$$\underline{\nabla}^2 = \frac{\partial^2}{\partial r^2} + \frac{2}{r}\frac{\partial}{\partial r} \tag{A.28}$$

The spherical Laplacian in equation (A.1c) (page V.II A-1) yields the spherical vacuum wave equation

$$\underline{\nabla}^2\underline{\mathbf{E}} - \mu\varepsilon\frac{\partial^2\underline{\mathbf{E}}}{\partial t^2} = \frac{\partial^2\underline{\mathbf{E}}}{\partial r^2} + \frac{2}{r}\frac{\partial\underline{\mathbf{E}}}{\partial r} - \mu\varepsilon\frac{\partial^2\underline{\mathbf{E}}}{\partial t^2} = 0 \tag{A.29}$$

which may be rewritten in a form similar to equation (A.9) (page V.II A-3) by rearranging and multiplying by r as

$$\frac{\partial^2}{\partial r^2}(rE) - \frac{1}{c^2}\frac{\partial^2}{\partial t^2}(rE) = 0 \tag{A.30}$$

Solving the wave equation for the quantity rE gives the spherical wave solution, in the complex phasor form of

$$E(t) = \frac{E}{r}\left[e^{-i(kr)}\right] \tag{A.31}$$

A.4 References

[1] E. Hecht. *Optics*, chapter 3, pages 33–7–8. Addison-Wesley Publishing Company, Inc., Reading, Massachusetts, 2nd edition, 1987.

[2] M. Born and E. Wolf. *Principles of Optics: Electromagnetic Theory of Propagation, Interference and Diffraction of Light*, chapter 1, pages 1–74. Cambridge University Press, Cambridge, 7th edition, 1999. ISBN: 0521642221.

[3] T. G. Mackay and A. Lakhtakia. *Electromagnetic fields in linear bianisotropic mediums*, volume 51 of *Progress in Optics*, chapter 3. Elsevier, Amsterdam, 2008. ISBN: 9780444532114.

[4] J. Shamir. *Optical Systems and Processes*, chapter 2, pages 5–18. SPIE, Bellingham, jul 1999. ISBN: 0819432261.

[5] M. E. Lines. *Physical properties of materials: theoretical overview*, volume 30 of *Handbook of infrared Optical Materials*, chapter 1, pages 1–70. Marcel Dekker, Inc., New York, 1991. ISBN: 0824784685.

[6] C. Bradley and A. Cracknell. *The Mathematical Theory of Symmetry in Solids: Representation Theory for Point Groups and Space Groups*, chapter 1, pages 1–50. Oxford Classic Texts in the Physical Sciences. Oxford University Press, Oxford, 2010. ISBN: 0199582580.

[7] S. N. Savenkov, O. I. Sydoruk, and R. S. Muttiah. Conditions for polarization elements to be dichroic and birefringent. *J. Opt. Soc. Am. A*, 22(7):1447–1452, July 2005.

[8] R. J. Black and L. Gagnon. *Optical Waveguide Modes: Polarization, Coupling and Symmetry*, chapter 1, pages 1–18. McGraw-Hill Companies, Inc., New York, 2010. ISBN: 0071622969.

[9] C. Brosseau. *Polarization and coherence optics: Historical perspective, status, and future directions*, volume 54 of *Progress in Optics*, chapter 3. Elsevier, Amsterdam, 2009. ISBN: 9780444535283.

[10] R. P Feynman, R. B. Leighton, and M. Sands. *The Feynman Lectures on Physics*, volume 2, chapter 18, pages 18.1–18.11. Addison-Wesley, Massachusetts, 1964. ISBN: 020102117x.

[11] J. Pevrina. *Coherence of Light*, chapter 1, pages 9–12. The Modern University Physics Series. Van Nostrand Reinhold Company, London, 1971. ISBN: 0442063423.

[12] R. E. Newnham. *Properties of Materials: Anisotropy, Symmetry, Structure*, chapter 25, pages 274–285. Oxford University Press, jan 2005. ISBN: 019852076X.

[13] M. Born and E. Wolf. *Principles of Optics: Electromagnetic Theory of Propagation, Interference and Diffraction of Light*, chapter 4, pages 142–227. Cambridge University Press, Cambridge, 7th edition, 1999. ISBN: 0521642221.

[14] M. Fox. *Optical Properties of Solids*, chapter 1, pages 1–24. Oxford University Press, Oxford, 2001. ISBN: 0198506120.

[15] L. D. Landau and E. M. Lifshitz. *The Classical Theory of Fields*, volume 2 of *Course of Theoretical Physics*, chapter 6, pages 116–139. Butterworth-Heinemann, Oxford, 4th edition, 1975. ISBN: 0750627689.

[16] W. Lauterborn, T. Kurz, and M. Wiesenfeldt. *Coherent Optics: Fundamentals and Applications*, chapter 9, pages 147–178. Springer-Verlag, Berlin, 1995. ISBN: 3540583726.

[17] R. W. Hamming. *Digital Filters*, chapter 8, pages 164–184. Dover Publications, Inc., New York, 3rd edition, 1998. ISBN: 048665088X.

[18] W. Lauterborn, T. Kurz, and M. Wiesenfeldt. *Coherent Optics: Fundamentals and Applications*, chapter 3, pages 15–29. Springer-Verlag, Berlin, 1995. ISBN: 3540583726.

[19] C.-L. Chen. *Foundations for Guided-Wave Optics*, chapter 1, pages 1–23. John Wiley & Sons, Inc., Hoboken, New Jersey, 2007. ISBN-10: 0471756873.

[20] M. Fox. *Quantum Optics*, chapter 7, pages 126–150. Oxford University Press, Oxford, 2006. ISBN: 0198566735.

[21] B. Maxum. *Field Mathematics for Electromagnetics, Photonics, and Materials Science*, volume TT64, chapter 1, pages 1.1–1.24. SPIE, Bellingham, 2005. ISBN: 0819455237.

Appendix B

Second order coherence theory

Maxwell's equations describe propagation and inter–relation of the classical electromagnetic fields $\underline{\mathbf{E}}$, $\underline{\mathbf{D}}$, $\underline{\mathbf{B}}$, and $\underline{\mathbf{H}}$. The relationship of electromagnetic radiations to other similar radiations, such as the relationship between $\underline{\mathbf{E}}_1 = \underline{\mathbf{E}}(\underline{\mathbf{r}}_1, t_1)$ and $\underline{\mathbf{E}}_2 = \underline{\mathbf{E}}(\underline{\mathbf{r}}_2, t_2)$, which may be from different spatial or temporal origins, is described by *coherence theory* [1,2]. Coherence theory is successful at describing the observed time–averaged intensity measurement of arbitrary waveforms [3,4].

Originally, coherence was the theoretical description of the experimental phenomenon of interference, but now is generalised to coherence properties of an electromagnetic, typically optical, field [5]. Interference is the simplest phenomenon exhibiting the correlations between optical waves, e.g. $\underline{\mathbf{E}}_1$ and $\underline{\mathbf{E}}_2$.

B.1 Young's slits experiment

The Young's slits experiment has had a significant impact upon physics[1] [7], as it readily permits experiments to illustrate the effects of coherence. In the Young's slits experiment, a plane wave illuminates a screen $\mathcal{A}$ with two small apertures, P_1 and P_2, set a distance d apart, as illustrated in figure B.1 (page V.II B-2). The apertures become sources of secondary wavelets as per *Huygens' principle* [8,9]. A second screen, $\mathcal{B}$, is placed a distance z from, and parallel to, screen $\mathcal{A}$. The field at an arbitrary point $Q(\underline{\mathbf{r}}, t)$ is sought. $Q(\underline{\mathbf{r}}, t)$ is a distance $\underline{\mathbf{r}}_1$ from P_1 and a distance $\underline{\mathbf{r}}_2$ from P_2.

The field at Q will be the sum of the fields passed by apertures P_1 and P_2. Neglecting the specific geometry of the two apertures, interference fringes will be

[1] For example, the definition of coherence to observable interference patterns in place of the definition: *coherence is complete dependence of phases, incoherence complete independence of phases.* [6].

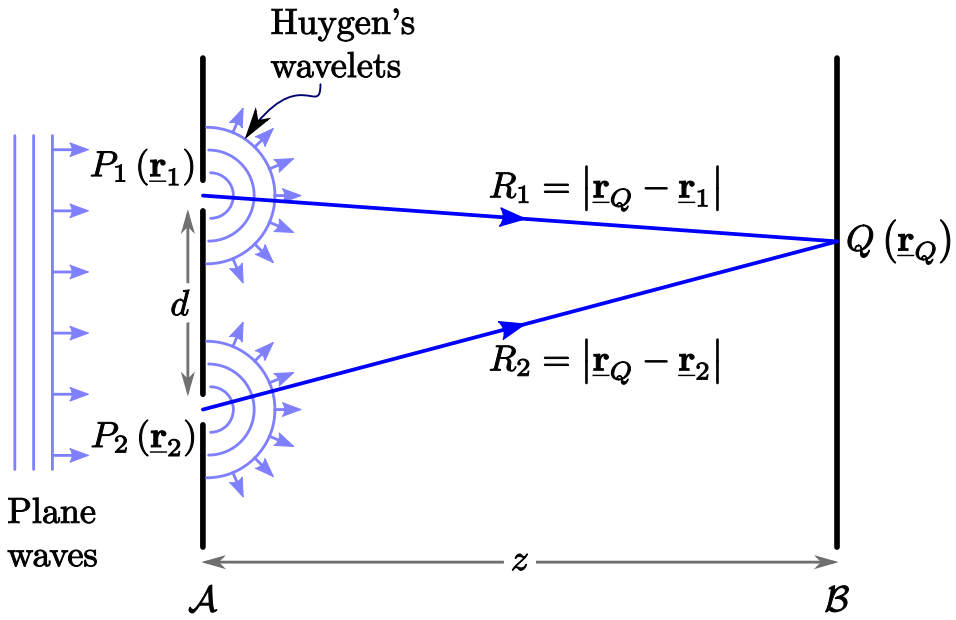

Figure B.1: Young's slits experiment. Screen $\mathcal{A}$ is illuminated by a plane wave, producing coherent secondary wavelets at points P_1 and P_2, which interfere constructively at point Q on screen $\mathcal{B}$.

visible at $\mathcal{B}$ assuming [10, 11]

$$\Delta x \Delta\theta < \overline{\lambda} \tag{B.1}$$

where Δx is the spatial extent of the source, and $2\Delta\theta$ is the angle d subtends at the source. Let the apertures, P_1 and P_2, be illuminated by a quasi–monochromatic plane wave, $\underline{V}(\underline{\mathbf{r}}, t)$, which propagate orthogonally to screen $\mathcal{A}$.

By incorporating the geometry of the two apertures into factors $\underline{\mathbf{K}}_1$ and $\underline{\mathbf{K}}_2$, for apertures P_1 and P_2, respectively,

$$\underline{V}_Q(\underline{\mathbf{r}}_Q, t) = \underline{\mathbf{K}}_1 \underline{V}(\underline{\mathbf{r}}_1, t) + \underline{\mathbf{K}}_2 \underline{V}(\underline{\mathbf{r}}_2, t + \tau) \tag{B.2}$$

where

$$t_1 = t = \frac{c}{R_1} \quad \text{and} \quad t_2 = t + \tau = \frac{c}{R_2} \tag{B.3}$$

and τ is the relative time difference, with R_1 and R_2 shown in figure B.1.

As direct observation of the amplitude of the electric field is not possible, the

intensity, I_Q is observed instead [1]:

$$\begin{aligned} I_Q(\underline{\mathbf{r}}_Q) &= \left\langle \underline{V}_Q^*(\underline{\mathbf{r}}_Q,t) \bullet \underline{V}_Q(\underline{\mathbf{r}}_Q,t) \right\rangle \\ &= |K_1|^2 \left\langle \underline{V}^*(\underline{\mathbf{r}}_1,t_1) \bullet \underline{V}(\underline{\mathbf{r}}_1,t_1) \right\rangle + |K_2|^2 \left\langle \underline{V}^*(\underline{\mathbf{r}}_2,t_2) \bullet \underline{V}(\underline{\mathbf{r}}_2,t_2) \right\rangle \\ &\quad + \Re[|K_1^*||K_2| \left\langle \underline{V}^*(\underline{\mathbf{r}}_1,t_1) \bullet \underline{V}(\underline{\mathbf{r}}_2,t_2) \right\rangle] \\ &\quad + \Re[|K_2^*||K_1| \left\langle \underline{V}^*(\underline{\mathbf{r}}_2,t_2) \bullet \underline{V}(\underline{\mathbf{r}}_1,t_1) \right\rangle] \\ &= |K_1|^2 I_1 + |K_2|^2 I_2 + 2\Re\left[|K_2^*||K_1| \underline{\underline{\mathbf{\Gamma}}}(\underline{\mathbf{r}}_1,\underline{\mathbf{r}}_2,t_1,t_2)\right] \end{aligned} \tag{B.4}$$

where

$$I_1 = \left\langle \underline{V}^*(\underline{\mathbf{r}}_1,t_1) \bullet \underline{V}(\underline{\mathbf{r}}_1,t_1) \right\rangle, \tag{B.5a}$$

$$I_2 = \left\langle \underline{V}^*(\underline{\mathbf{r}}_2,t_2) \bullet \underline{V}(\underline{\mathbf{r}}_2,t_2) \right\rangle, \tag{B.5b}$$

$$\text{and } \left\langle \underline{V}^*(\underline{\mathbf{r}}_2,t_2) \bullet \underline{V}(\underline{\mathbf{r}}_1,t_1) \right\rangle = \left\langle \underline{V}^*(\underline{\mathbf{r}}_1,t_1) \bullet \underline{V}(\underline{\mathbf{r}}_2,t_2) \right\rangle \tag{B.5c}$$

The *cross–correlation function* [11, 12] is

$$\underline{\underline{\mathbf{\Gamma}}}(\underline{\mathbf{r}}_1,\underline{\mathbf{r}}_2,t_1,t_2) = \left\langle \underline{V}^*(\underline{\mathbf{r}}_1,t_1) \underline{V}(\underline{\mathbf{r}}_2,t_2) \right\rangle \tag{B.6}$$

This equation is known as the *mutual coherence function* [13] when $t_2 = t_1 + \tau$ [14], i.e.

$$\underline{\underline{\mathbf{\Gamma}}}(\underline{\mathbf{r}}_1,\underline{\mathbf{r}}_2,\tau) = \lim_{T\to\infty} \frac{1}{2T} \int_{-\infty}^{\infty} \underline{V}^*(\underline{\mathbf{r}}_1,t_1) \underline{V}(\underline{\mathbf{r}}_2,t_1+\tau) d\tau \tag{B.7}$$

The resulting intensity at Q from both P_2 and P_2 is the sum of I_1 and I_2 and the term $2\Re\left[|K_2^*||K_1| \underline{\underline{\mathbf{\Gamma}}}\right]$, which is modulated by $\underline{\underline{\mathbf{\Gamma}}}$, i.e. the superposition of $\underline{V}(\underline{\mathbf{r}}_1,t)$ and $\underline{V}(\underline{\mathbf{r}}_2,t)$ produces *interference* [14]. I_1 is the intensity that would be observed at Q in the absence of P_2 and I_2 is the intensity that would be observed at Q in the absence of P_1.

The use of the relative time difference τ is permitted if the random electromagnetic field, $\underline{V}(\underline{\mathbf{r}},t)$ is *statistically stationary in the wide–sense* [12, 15] [2].

The normalised mutual coherence function is termed the *complex degree of coherence*[3],

$$\gamma(\underline{\mathbf{r}}_1,\underline{\mathbf{r}}_2,\tau) = \frac{\operatorname{Tr} \underline{\underline{\mathbf{\Gamma}}}(\underline{\mathbf{r}}_1,\underline{\mathbf{r}}_2,\tau)}{\sqrt{\underline{\underline{\mathbf{\Gamma}}}(\underline{\mathbf{r}}_1,\underline{\mathbf{r}}_1,0)\, \underline{\underline{\mathbf{\Gamma}}}(\underline{\mathbf{r}}_2,\underline{\mathbf{r}}_2,0)}} \tag{B.8}$$

[2] A statistically stationary process has invariant probability densities under translation of the temporal origin [1].

A process is said to be wide–sense stationary, or second order stationary, if the mean, $\mathbb{E}[X(t)]$, and autocovariance, $R[X(t)]$, of $X(t)$ do not depend on t [16]:

- $\forall t,\tau \in T, \qquad \mathbb{E}[X(t+\tau)] = \mathbb{E}[X(t)]$
- $\forall t_1,t_2,\tau \in T, \quad R[X(t_1+\tau,t_2+\tau)] = R[X(t_1,t_2)]$

where $\mathbb{E}[X(t)] = \int_{\mathbb{E}} X(t) dP_{X(t)}(x)$ and $R[X(t)] = \mathbb{E}[X(t_1)X^*(t_2)] - \mathbb{E}[X(t_1)]\mathbb{E}^*[X(t_2)]$.

[3] A correlation function [17].

where $\underline{\underline{\mathbf{\Gamma}}}(\underline{\mathbf{r}}_1, \underline{\mathbf{r}}_1, 0) = I_1$ and $\underline{\underline{\mathbf{\Gamma}}}(\underline{\mathbf{r}}_2, \underline{\mathbf{r}}_2, 0) = I_2$. For real, non–zero fields, $\underline{V}(\underline{\mathbf{r}}, t)$,

$$0 \leq \gamma(\underline{\mathbf{r}}_1, \underline{\mathbf{r}}_2, \tau) \leq 1 \tag{B.9}$$

The visibility, or contrast function [5], of the interference fringes is a measure of how visibly distinct the fringes are, and was introduced by Michelson [14] as,

$$\mathcal{V}_{\mathcal{Q}} = \frac{\langle I_{max} \rangle - \langle I_{min} \rangle}{\langle I_{max} \rangle + \langle I_{min} \rangle} \tag{B.10}$$

where $\langle I_{max} \rangle$ and $\langle I_{min} \rangle$ are the maximum and minimum averaged intensities at Q, obtained by adding and subtracting the last term in equation (B.4), respectively, to give [14]

$$\mathcal{V}_{\mathcal{Q}} = 2 \frac{1}{\eta(\underline{\mathbf{r}}_Q) + \frac{1}{\eta(\underline{\mathbf{r}}_Q)}} \left| \gamma(\underline{\mathbf{r}}_1, \underline{\mathbf{r}}_2, \tau) \right| \tag{B.11}$$

where

$$\eta(\underline{\mathbf{r}}_Q) = \sqrt{\left(\frac{\langle I_1(\underline{\mathbf{r}}_Q, t) \rangle}{\langle I_2(\underline{\mathbf{r}}_Q, t) \rangle} \right)} \tag{B.12}$$

When $\langle I_1(\underline{\mathbf{r}}_Q, t) \rangle = \langle I_2(\underline{\mathbf{r}}_Q, t) \rangle$ the visibility is then

$$\mathcal{V}_{\mathcal{Q}} = \left| \gamma(\underline{\mathbf{r}}_1, \underline{\mathbf{r}}_2, \tau) \right| \tag{B.13}$$

and so the complex degree of coherence is simply the visibility of the fringes.

When $|\gamma| = 1$, termed *complete coherence*, the interference undergoes the maximum oscillation described by $\underline{\underline{\mathbf{\Gamma}}}$. At the other extreme, when $|\gamma| = 0$, termed *complete incoherence*, no interference is observed[4]. The intermediate case of $0 < |\gamma| < 1$ is termed *partial coherence*. The quasi–monochromatic or polychromatic signal will always be partially coherent due to its component frequencies differing phases.

The utility of coherence theory was expanded by considering equation (B.6) to be not only stationary, but ergodic[5] [11,15,18]. A stationary and ergodic field facilitates time averaging [11]; equation (B.7) is then valid for both temporal averages and ensemble averages.

[4]Complete coherence (correlated) implies linear addition; complete incoherence (uncorrelated) implies quadratic addition [17].

[5]An *ergodic* process is one where every realisation of an ensemble has the same statistical information as any other realisation, and, hence, are interchangeable in time. Different time averages are the same as the ensemble average [18]. An ergodic process is a stricter definition than strict stationary or wide–sense stationary [19].
A process is ergodic if $\forall n \in \mathbb{N}$ and $\forall t_1, \ldots, t_n \in$ time, the limits, if they exist, of sample path integrals of the formulation

- $\frac{1}{2\tau} \int_{-\tau}^{\tau} \phi\left(X(t+t_1), \ldots, X(t+t_n)\right) dt$

are almost surely independent of the sample path of $X(t)$ under consideration, when τ tends towards $+\infty$ [16].

B.2 Power spectrum

Equation (B.7) may also be expressed in the space–frequency domain by assuming $\underline{\underline{\mathbf{\Gamma}}}$ is absolutely integrable in the range $-\infty < \tau < \infty$ and taking the Fourier transform of (B.7) [12], to give the Fourier transform pair:

$$\underline{\underline{\mathbf{W}}}(\underline{\mathbf{r}}_1, \underline{\mathbf{r}}_2, \omega) = \frac{1}{\sqrt{2\pi}} \int_{-\infty}^{\infty} \underline{\underline{\mathbf{\Gamma}}}(\underline{\mathbf{r}}_1, \underline{\mathbf{r}}_2, \tau) e^{i\omega\tau} d\tau \tag{B.14a}$$

$$\underline{\underline{\mathbf{\Gamma}}}(\underline{\mathbf{r}}_1, \underline{\mathbf{r}}_2, \tau) = \frac{1}{\sqrt{2\pi}} \int_{-\infty}^{\infty} \underline{\underline{\mathbf{W}}}(\underline{\mathbf{r}}_1, \underline{\mathbf{r}}_2, \omega) e^{-i\omega\tau} d\omega \tag{B.14b}$$

which is termed the *cross–spectral density function*. When $\underline{\mathbf{r}}_1 = \underline{\mathbf{r}}_2 = \underline{\mathbf{r}}$, then

$$S_W(\underline{\mathbf{r}}, \omega) = \operatorname{Tr} \underline{\underline{\mathbf{W}}}(\underline{\mathbf{r}}, \underline{\mathbf{r}}, \omega) \tag{B.15}$$

where $S_W(\underline{\mathbf{r}}, \omega)$ is termed the *power spectral density* [19] or *spectral density*[6] [14]. The Fourier transform of an autocorrelation, in general, gives the spectral density function. This relationship is termed the *Wiener–Khinchin theorem* [19, 21–24] or the *Wiener–Khintchine theorem* [3,11,18,25,26]. The importance of equation (B.14) is that knowing the autocorrelation function allows the power spectral density to be determined.

$\underline{\underline{\mathbf{W}}}(\underline{\mathbf{r}}_1, \underline{\mathbf{r}}_2, \omega)$ can be normalised to give the *spectral degree of coherence* at frequency ω

$$\mu_W(\underline{\mathbf{r}}_1, \underline{\mathbf{r}}_2, \omega) = \frac{\operatorname{Tr} \underline{\underline{\mathbf{W}}}(\underline{\mathbf{r}}_1, \underline{\mathbf{r}}_2, \omega)}{\sqrt{S_W(\underline{\mathbf{r}}_1, \omega) S_W(\underline{\mathbf{r}}_2, \omega)}} \tag{B.16}$$

B.3 Coherence time/Coherence length

The signal at Q from P_1 and P_2 depends upon their mutual coherence or cross–correlation. Except for strictly monochromatic waves, the cross–correlation will change as the wavefronts propagate. The *coherence time*, τ_c, is introduced to characterise the decay of the visibility [5],

$$\mathcal{V}(\tau_c) = |\gamma(\underline{\mathbf{r}}_1, \underline{\mathbf{r}}_2, \tau_c)| = \frac{1}{e} \tag{B.17}$$

i.e. when the fringes for the wavelengths in the range, $\delta\lambda$, cancel out [10]. The coherence time is the normalised R.M.S. width of $\underline{\underline{\mathbf{\Gamma}}}^2(\underline{\mathbf{r}}_1, \underline{\mathbf{r}}_2, \tau)$,

$$\tau_c = \sqrt{\frac{\int_{-\infty}^{\infty} \tau^2 \left|\underline{\underline{\mathbf{\Gamma}}}(\underline{\mathbf{r}}_1, \underline{\mathbf{r}}_2, \tau)\right|^2}{\int_{-\infty}^{\infty} \left|\underline{\underline{\mathbf{\Gamma}}}(\underline{\mathbf{r}}_1, \underline{\mathbf{r}}_2, \tau)\right|^2}} \tag{B.18}$$

[6] A spectrum is a plot of the dependent variable energy against the independent variable ω [20].

as the average value of an even function will be zero [14].

The *effective spectral width*, $\Delta\omega$, *the bandwidth*, of the quasi–monochromatic wave $\underline{V}_Q(\underline{\mathbf{r}}_Q, t)$ is

$$\Delta\omega = \sqrt{\frac{\int_0^\infty (\omega - \overline{\omega})^2 S_W^2(\underline{\mathbf{r}}, \omega) d\omega}{\int_0^\infty S_W^2(\underline{\mathbf{r}}, \omega) d\omega}} \tag{B.19}$$

where

$$\overline{\omega} = \frac{\int_0^\infty \omega S_W^2(\underline{\mathbf{r}}, \omega) d\omega}{\int_0^\infty S_W^2(\underline{\mathbf{r}}, \omega) d\omega} \tag{B.20}$$

is the mean frequency of $\underline{V}_Q(\underline{\mathbf{r}}_Q, t)$ [14].

$\Delta\overline{\omega}$ depends upon the distribution profile of $S_W(\underline{\mathbf{r}}, \omega)$ and τ_c depends upon $\underline{\underline{\mathbf{\Gamma}}}(\underline{\mathbf{r}}, \underline{\mathbf{r}}, \tau)$ [27]. The relation between τ_c and $\Delta\omega$ depends upon the line shape and, for a Gaussian profile, is [14]

$$\tau_c \Delta\omega \geq \frac{1}{4\pi} \tag{B.21}$$

which is $\sim \frac{1}{4\pi}$ when $\overline{\omega} \gg \Delta\omega$ and the profile of $S_W(\underline{\mathbf{r}}, \omega)$ is approximately Gaussian.

As the speed of propagation of the wave is $\underline{v} = \underline{n}c$, a *coherence length* is defined as [28]

$$\underline{l}_c = \underline{v}\tau_c \sim \frac{c}{\Delta\omega} = \frac{\lambda_0^2}{\Delta\lambda_0} \tag{B.22}$$

The concept of coherence times and lengths present no difficulties for monotonously decaying visibility. The decay of the visibility does not need to be monotonously decaying, and may be periodic, such as for two monochromatic waves producing frequency beating [5], where

$$\mathcal{V}_Q(\tau) = \left| \cos\left(\frac{\omega_1 - \omega_2}{2}\right)\tau \right| \tag{B.23}$$

Typical values for the coherence time of a thermal source are $\sim 10^{-8}$ s to $\sim 10^{-4}$ s for a well stabilised laser. Typical detection times are $\sim 10^{-3}$ s [25].

The coherence length is also termed the *detuning* or *dephasing* length of the signal. Detuning is generally described in terms of high– and low–coherence.

B.4 High– & low–coherence

Optical sources may be grouped in terms of their coherence properties as *high–coherence*, *low–coherence*, and *thermal* or *white–light* sources. The concept of high– and low– is relative, analogous to a high–pass filter and low–pass filter. In this case the comparison is made with the observable coherence length of the system, i.e. the largest path delay introduced. For the purposes of this work, the largest path delay will be that introduced by the Michelson interferometer.

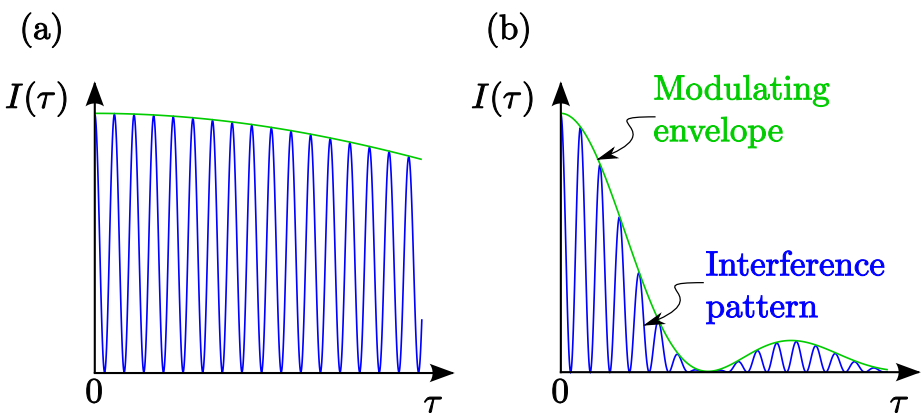

Figure B.2: Figurative examples of: (a) high–coherence interferogram, the interference modulation is approximately uniform across the interferogram; and (b) low–coherence interferogram, the interference modulation has a beating of the envelope of the interferogram.

High–coherence sources are those, such as lasers, which have comparatively long coherence lengths, illustrated in figure B.2(a). The coherence length of a high–coherence source may well exceed the length of the interferometer scan [29].

Low–coherence sources are those which have shorter, but still observable coherence lengths, illustrated in figure B.2(b). The coherence length is on the scale of the interferometer.

Thermal sources are effectively random sources, with coherence lengths of the order of microns or less, below that observable by the apparatus used in this work. The white–light terms arises as, when Fourier transformed, all random sources return the set of all frequencies with random phases [30]. Thermal sources are often grouped in with low–coherence sources.The high–stability telecomms laser used in this work has a quoted spectral linewidth of < 10 MHz, or < 0.1 pm. Unless the resolution of the system exceeds 0.1 pm, this laser appears as a single frequency source.

The spectrum from an FBG will be broader, typically ~ 100 GHz or ~ 1 nm. The FBG spectrum will not appear as a single frequency source unless the demodulation system resolution is lower than ~ 1 nm. High–coherence sources and low–coherence sources have different advantages. The visibility of a high–coherence source will be consistent for the interferogram, however, at the expense of the zero–OPD point of the interferogram not being unambiguous. A low–coherence source will provide an unambiguous zero–OPD point, at the expense of a limited interferogram, and hence recoverable information[7].

[7]The limited interferogram provides limited information as, once the interferogram goes to zero or the DC level, a longer interferogram will not provide more information.

Additionally, low–coherence sources can be cheaper than high–coherence sources.

B.5 Interference hyperboloid of revolution

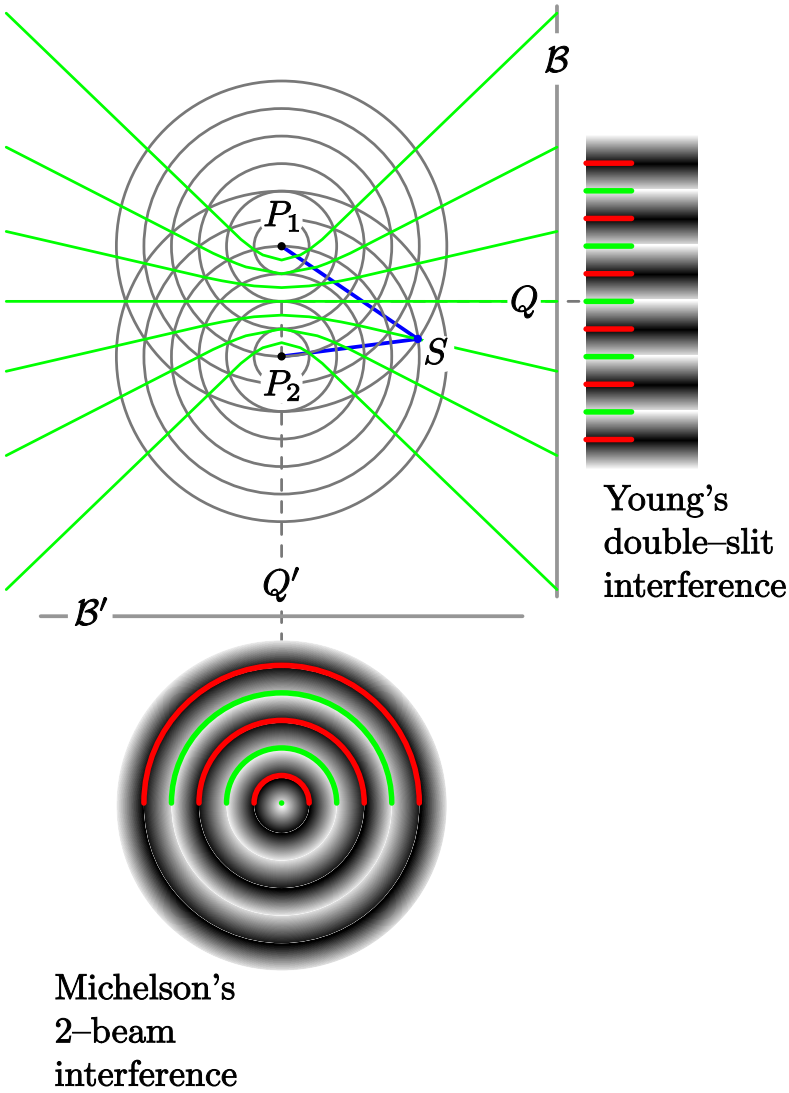

Figure B.3: Hyperbolic curves of intensity maxima from two points sources (after figure 1.3 in Tolansky [31]).

The intensity pattern produced on the screen $\mathcal{B}$ in figure B.3, is described by equation (B.4) (page V.II B-3) as $\underline{\mathbf{r}}_1$ and $\underline{\mathbf{r}}_2$ change to cover $\mathcal{B}$. As shown in figure B.3, the locations where the waves are in phase (the overlapping circles), follow curves. The point S has a maximum when [31]

$$\left|\underline{\mathbf{r}}_{P_2} - \underline{\mathbf{r}}_S\right| - \left|\underline{\mathbf{r}}_{P_1} - \underline{\mathbf{r}}_S\right| = m\lambda \tag{B.24}$$

For a given m, equation (B.24) describes a hyperbola, shown as the green lines on figure B.3. The order occurring at Q is termed the *zero order fringe*[8], with the orders increasing with n [31].

In three–dimensions, spherical waves emanate from P_1 and P_2 and hyperboloids of revolution are obtained by rotating the pattern about the line P_1P_2.

A figurative representation of the interference patterns produced at screens $\mathcal{B}$ and $\mathcal{B}'$ is shown in figure B.3. The Young's slits experiment is observed at screen $\mathcal{B}$. When placed at a distance greater than $\left|\underline{\mathbf{r}}_{P_2} - \underline{\mathbf{r}}_{P_1}\right|$ the fringe hyperbola are effectively parallel lines [31]. The Michelson experiment is observed at screen $\mathcal{B}'$. The intersection of the hyperboloids of revolution will produce circular fringes. Screens at other orientations will produce arcs of varying curvature. Figure B.4 shows a figurative representation of the hyperboloids of revolution, where the red and green surfaces correspond to the red and green lines on the Young's slits and Michelson interference patterns shown in figure B.3.

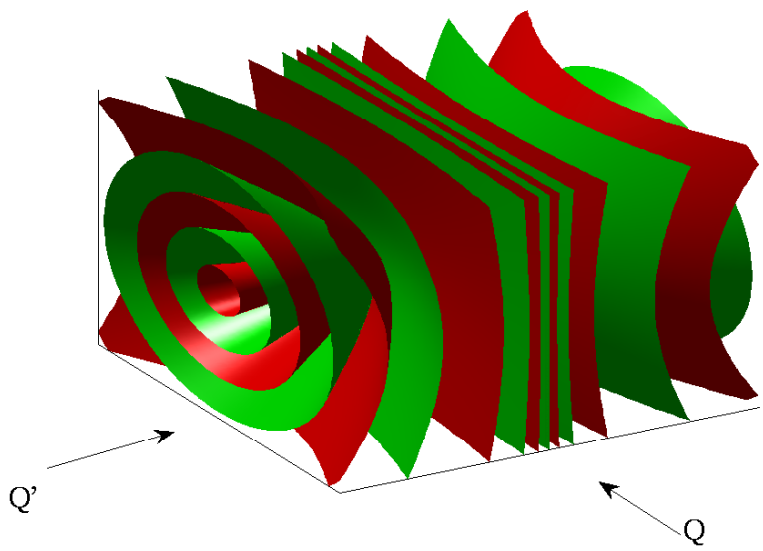

Figure B.4: Hyperboloids of revolution showing non–localised standing waves for two sources, clipped by a bounding box(after Tolansky [31]).

The theory deduced from the Young's slits experiment applies to the Michelson experiment. Instead of the point Q being at varying distances from points P_1 and P_2, dependent upon the angle, the points P_1 and P_2 are on the same line separated by a distance $c\tau$. This is achieved by splitting the incident signal via a beam–splitter

[8]Fringes are also known as *non–localised standing waves*, as their appearance is not restricted to a specific location [31].

and placing mirrors at P_1 and P_2 [9]. When the intensities of P_1 and P_2 are equal, they appear as a single point, P_0, temporally separated by τ. The intensity modulation at Q' will be

$$I_{Q'}(\underline{\mathbf{r}}_{Q'}, \tau) = 2|K_0|^2 I_0 + 2\Re\left[|K_0|^2 \underline{\underline{\mathbf{\Gamma}}}(\tau)\right] \tag{B.25}$$

where

$$I_0 = \langle \underline{V}^*(\underline{\mathbf{r}}_0, \tau) \bullet \underline{V}(\underline{\mathbf{r}}_0, \tau) \rangle \tag{B.26}$$

Similarly, the Mach–Zehnder experiment is a modified version of the Michelson experiment. Instead of the reflected waves passing back along their paths, the mirrors are angled at $\pi/4$ to reflect the signals towards a second beam–splitter. The advantage of the Mach–Zehnder apparatus is the ready availability of the complementary output signals, and a single pass through the interferometer paths.

From the visibility, $\gamma(\underline{\mathbf{r}}_1, \underline{\mathbf{r}}_2, \tau)$ can be measured at either screen $\mathcal{B}$ or $\mathcal{B}'$.

B.5.1 Diffraction

The phenomenon of diffraction is the deviation from linear propagation of radiation which is not due to the processes of reflection or refraction [33]. When a wave[10] encounters an opaque obstacle it undergoes diffraction at the obstacle boundaries [34]. The effect of diffraction is most noticeable when the scale of the obstacle, or the distance between obstacles, is of the order of the wavelength of the incident radiation [35].

Diffraction and interference have no substantive differences [36], the distinction being of historical origin. Currently, interference is considered the intentional combination of two or more waves while diffraction refers to the obstruction of a single wave [36]. The geometry of the apertures was ignored during the derivations thus far, e.g. in equation (B.2) (page V.II B-2). The effects of the aperture geometry are described by diffraction.

The rigorous theoretical treatment of diffraction, vector diffraction, involves the use of Maxwell's equations and appropriate boundary *conditions* [33, 37]. Scalar diffraction, with appropriate boundary *values* is used in preference as it enables easier computation of the effects of diffraction and agrees very well with the results obtained from vector diffraction, where available [38].

The electromagnetic fields are vector fields described by the vector equations (A.1) (page V.II A-1), and satisfy the wave equation (A.7) (page V.II A-3). When dealing with unpolarised radiation or radiation with a fixed state of polarisation,

[9] The Young's slits experiment is a *wavefront division* experiment, and the Michelson is an *amplitude division* experiment. [32]

[10] Any wave, be it mechanical, acoustic or electromagnetic, exhibits diffraction by an opaque edge.

a scalar field may be used [39]. Scalar diffraction theory is based upon Huygens' principle [33, 35, 38, 40–42], which interprets each point on a wavefront as a source of secondary wavefronts.

The following argument is based on [40]. In a homogeneous and isotropic medium the secondary wavefronts are spherical [42]. Any future position, P, of the wavefront is determined by the addition of all the generated secondary spherical wavefront contributions, the envelope, to that position P. Fresnel took Huygens' principle and added to it the superposition due to mutual interference of these secondary wavefronts to describe the diffraction pattern obtained [40]. The observed intensity is then the square of the resultant amplitudes [42].

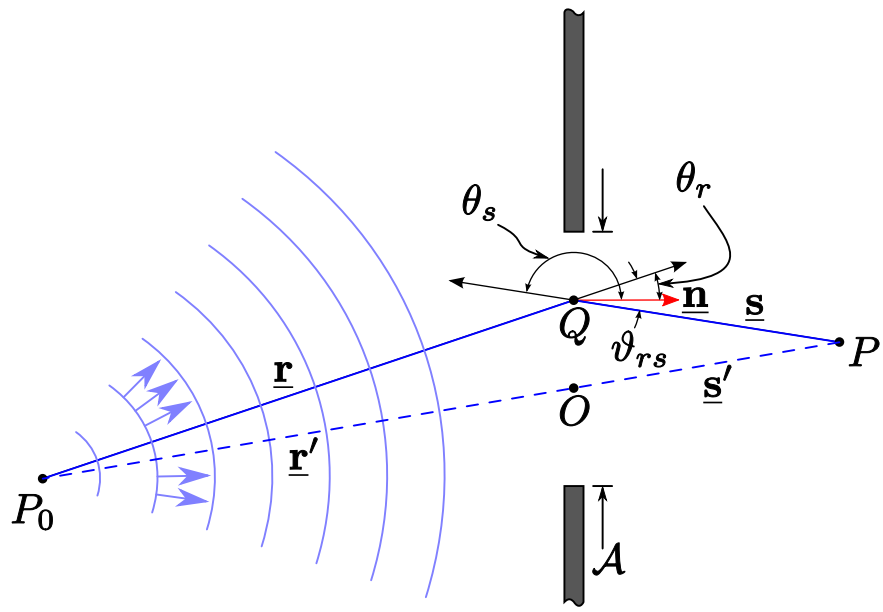

Figure B.5: Illustration of Fresnel–Kirchhoff diffraction formula. After Born & Wolf [40].

Kirchhoff formalised the Huygens–Fresnel principle by showing that it was an approximation of an integral theorem derived by von Helmholtz, termed *the Fresnel–Kirchhoff diffraction integral* [40]:

$$U(P) = -\frac{iV_U}{2\lambda} \iint_{\mathcal{A}} \frac{e^{-ik(\underline{\mathbf{r}}+\underline{\mathbf{s}})}}{\underline{\mathbf{r}}\,\underline{\mathbf{s}}} \left[\cos(\theta_r) - \cos(\theta_s)\right] dS \tag{B.27}$$

where U is the amplitude of the field at P, which is a point in image space, $\mathcal{A}$ is the function describing the aperture or edge of obstacle, V_U is the amplitude of the incident wave, $\underline{\mathbf{r}}$ is the OPD vector from the source to the aperture, $\underline{\mathbf{s}}$ is the OPD

vector from the aperture to the image point, as defined in figure B.5, and dS is an infinitesimal area element in $\mathcal{A}$.

Kirchhoff's approach also supplied the *obliquity factor* or *inclination factor*, $K(\chi)$, which Fresnel's approach had required to prevent backward travelling diffraction arising due to the spherical symmetry of the secondary wavefronts [36, 40]:

$$K(\vartheta_{rs}) = -\frac{i}{2\lambda}\left(1 + \cos\vartheta_{rs}\right) \tag{B.28}$$

The obliquity factor describes changes in amplitude with direction of the secondary wavefronts and describes the observed intensity distribution [40].

By taking the co–ordinates of $P_0 = (x_0, y_0, z_0)$, $P = (x, y, z)$ and $Q = (\xi, \eta)$ by setting O as the origin, and using appropriate expansions [40], the integral governing Fraunhofer diffraction can be written as [40]

$$U(P) = C \iint_{\mathcal{A}} e^{-ik(p\xi+q\eta)} d\xi d\eta \tag{B.29}$$

where

$$C = -\frac{i\cos\delta}{\lambda}\frac{V_U e^{-ik(r'+s')}}{r's'} \qquad = \text{ constant;} \tag{B.30}$$

$$p = l - l_0, \quad q = m - m_0; \tag{B.31}$$

and

$$l_0 = -\frac{x_0}{r'}, \quad l = \frac{x}{s'}, \tag{B.32a}$$

$$m_0 = -\frac{y_0}{r'}, \quad m = \frac{y}{s'}, \tag{B.32b}$$

are the first two direction cosines[11]. Equation (B.29) may be rewritten as

$$U(p, q) = \iint G(\xi, \eta) e^{-\frac{2\pi i}{\lambda}(p\xi+q\eta)} d\xi d\eta \tag{B.33}$$

where the pupil function $G(\xi, \eta)$ is given by

$$G(\xi, \eta) = \begin{cases} \text{constant } (C) & \text{at points in the aperture} \\ 0 & \text{at points outside the opening} \end{cases} \tag{B.34}$$

Thus the far–field or Fraunhofer diffraction pattern, $U(p, q)$, is the two–dimensional Fourier transform of the aperture function, $\mathcal{A}$ [40]. For the cleaved end face of the fibre the emitted beam is a *Bessel function* [43] of revolution about the fibre axis,

[11] The direction cosines are equivalent to the Cartesian co–ordinates of a unit vector, the direction vector $\hat{v}$, e.g. $\alpha \equiv \cos(x, v) \equiv v \bullet \hat{x}/|v|$, and equivalently for y and z[12].

which is the Fourier transform of the circular aperture described by the core. In the case of a linear obstacle, the diffracted pattern is in one dimension. For a diffraction grating the transmitted or reflected radiation is the sum of the obstacles making up the diffraction grating, which is shown figuratively in figure B.6.

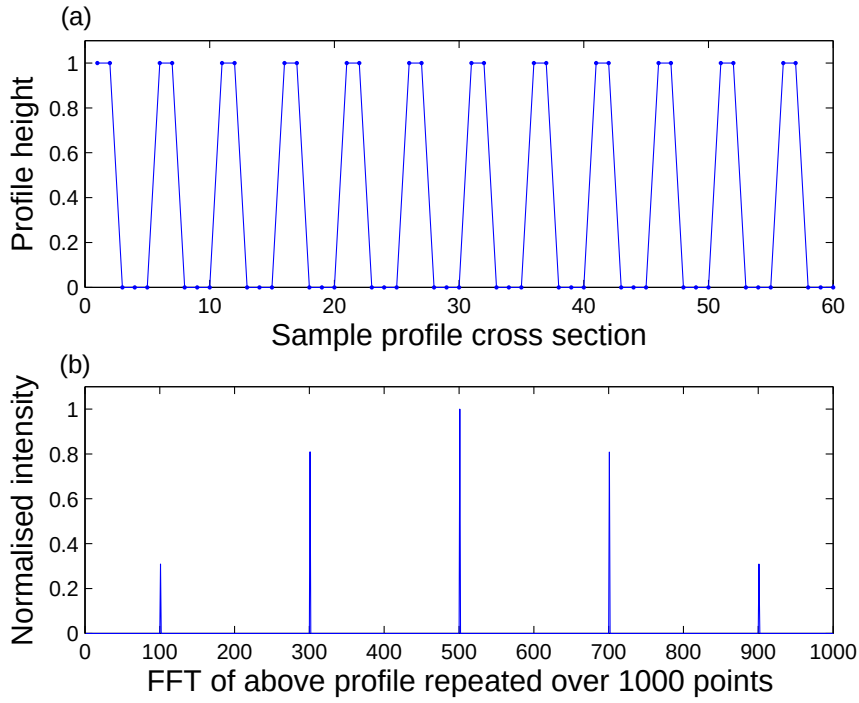

Figure B.6: (a) A generated example of a cross section of a rectangular diffraction grating. Shown are 60 data points. (b) The FFT of (a) extended to 1000 data points.

B.6 References

[1] E. Wolf. *Introduction to the Theory of Coherence and Polarization of Light*, chapter 3, pages 31–59. Cambridge University Press, Cambridge, 2007. ISBN: 9780521822114.

[2] L. Mandel and E. Wolf. *Optical Coherence and Quantum Optics*, chapter 6, pages 340–374. Cambridge University Press, New York, sep 1995. ISBN: 0521417112.

[3] W. H. Carter. *Coherence Theory*, volume 1 of *Handbook of Optics*, chapter 5. McGraw-Hill Companies, Inc., New York, 3 edition, 2010. ISBN: 0071498893.

[4] G. Bennett, W. T. Rhodes, and J. C. James. *Coherence Theory: Tools and Applications*, volume 1 of *Handbook of Optics*, chapter 6. McGraw-Hill Companies, Inc., New York, 3 edition, 2010. ISBN: 0071498893.

[5] W. Lauterborn, T. Kurz, and M. Wiesenfeldt. *Coherent Optics: Fundamentals and Applications*, chapter 4, pages 31–57. Springer-Verlag, Berlin, 1995. ISBN: 3540583726.

[6] F. Zernike. The concept of degree of coherence and its application to optical problems. In L. Mandel and E. Wolf, editors, *Selected Papers on Coherence and Fluctuations of Light*, volume 1, pages 100–110. Dover Publications, Inc., New York, 1970. ISBN: 0486625702.

[7] E. Wolf. *The influence of Young's interference experiment on the development of statistical optics*, volume 50 of *Progress in Optics*, chapter 7. North–Holland Publishing Co., Amsterdam, 2007. ISBN: 9780444530233.

[8] W. Lauterborn, T. Kurz, and M. Wiesenfeldt. *Coherent Optics: Fundamentals and Applications*, chapter 3, pages 15–29. Springer-Verlag, Berlin, 1995. ISBN: 3540583726.

[9] M. Franccon. *Diffraction: Coherence in Optics*, chapter 1, pages 1–13. Pergamon Press Ltd., Oxford, 1966.

[10] E. Wolf. *Introduction to the Theory of Coherence and Polarization of Light*, chapter 1, pages 1–10. Cambridge University Press, Cambridge, 2007. ISBN: 9780521822114.

[11] J. Pevrina. *Coherence of Light*, chapter 2, pages 13–31. The Modern University Physics Series. Van Nostrand Reinhold Company, London, 1971. ISBN: 0442063423.

[12] A. S. Ostrovsky. *Coherent-Mode Representations in Optics*, chapter 1, pages 1–14. SPIE Press, Bellingham, 2006. ISBN: 0819463507.

[13] E. Wolf. A macroscopic theory of interference and diffraction of light from finite sources. II. Fields with a spectral range of arbitrary width. *P. Roy. Soc. Lond. A Mat.*, 230(1181):pp. 246–265, 1955.

[14] L. Mandel and E. Wolf. *Optical Coherence and Quantum Optics*, chapter 4, pages 147–228. Cambridge University Press, New York, sep 1995. ISBN: 0521417112.

[15] E. Wolf. *Introduction to the Theory of Coherence and Polarization of Light*, chapter 2, pages 11–30. Cambridge University Press, Cambridge, 2007. ISBN: 9780521822114.

[16] T Chonavel. *Statistical Signal Processing*, chapter 2, pages 9–21. Advanced Textbooks in Control andSignal Processing. Springer-Verlag Ltd., London, 2002. ISBN: 1852333855.

[17] A. van der Ziel. *Noise*, chapter 1, pages 1–7. Prentice-Hall, Inc., Englewood Cliffs, N. J., 1954.

[18] L. Mandel and E. Wolf. *Optical Coherence and Quantum Optics*, chapter 2, pages 41–91. Cambridge University Press, New York, sep 1995. ISBN: 0521417112.

[19] J. W. Goodman. *Statistical Optics*, chapter 3, pages 60–115. Wiley Classics Library. John Wiley & Sons, Inc., New York, 2000. ISBN: 0471399167.

[20] H. A. Gebbie. Fourier transform versus grating spectroscopy. *Appl. Opt.*, 8(3):501, 1969.

[21] W. Lauterborn, T. Kurz, and M. Wiesenfeldt. *Coherent Optics: Fundamentals and Applications*, chapter Appendix A.1.3, pages 251–252. Springer-Verlag, Berlin, 1995. ISBN: 3540583726.

[22] L. Cohen. *Time Frequency Analysis: Theory and Applications*, chapter 1, pages 1–26. Prentice-Hall, Inc., New Jersey, 1995. ISBN: 0135945321.

[23] E. L. O'Neill. *Introduction to Statistical Optics*. Dover Publications, Inc., New York, 2003. ISBN: 0486435784.

[24] S. G. Lipson, H. Lipson, and D. S. Tannhauser. *Optical Physics*, chapter 4, pages 71–98. Cambridge University Press, Cambridge, 3rd edition, 1995. ISBN: 0521436311.

[25] C. Brosseau. *Fundamentals of Polarized Light: A Statistical Optics Approach*, chapter 3.1, pages 69–122. John Wiley & Sons, Inc., New York, 1998. ISBN: 0471143022.

[26] E. G. Steward. *Fourier Optics: an Introduction*, chapter 4, pages 71–98. Dover Publications, Inc., New York, 2nd edition, 2004. ISBN: 0486435040.

[27] J. W. Goodman. *Statistical Optics*, chapter 5, pages 157–236. Wiley Classics Library. John Wiley & Sons, Inc., New York, 2000. ISBN: 0471399167.

[28] M. Born and E. Wolf. *Principles of Optics: Electromagnetic Theory of Propagation, Interference and Diffraction of Light*, chapter 7, pages 286–411. Cambridge University Press, Cambridge, 7th edition, 1999. ISBN: 0521642221.

[29] A. Mabrouki, M. Gadonna, and R. Le Naour. Polarization characterization of a Mach—Zehnder interferometer. *Appl. Opt.*, 35(19):3591–3596, July 1996.

[30] S. G. Lipson, H. Lipson, and D. S. Tannhauser. *Optical Physics*, chapter 11, pages 290–326. Cambridge University Press, Cambridge, 3rd edition, 1995. ISBN: 0521436311.

[31] S. Tolansky. *An Introduction to Interferometry*, chapter 1, pages 1–9. Longmans, Green And Co., London, 1955.

[32] P. Hariharan. *Basics of Interferometry*, chapter 3, pages 13–22. Academic Press, Inc., New York, 2nd edition, 2007. ISBN: 0123735890.

[33] H. Gross, W. Singer, and M. Totzeck. *Physical Image Formation*, volume 2 of *Handbook of Optical Systems*, chapter 18, pages 41–97. Wiley-VCH Verlag GmbH & Co. KGaA, Weinheim, 2005. ISBN: 3527403787.

[34] G. Chartier. *Introduction to Optics*, chapter 1, pages 1–56. Advanced Texts in Physics. Springer Science+Business Media, Inc., New York, 2005. ISBN: 0387403469.

[35] G. Chartier. *Introduction to Optics*, chapter 8, pages 299–342. Advanced Texts in Physics. Springer Science+Business Media, Inc., New York, 2005. ISBN: 0387403469.

[36] R. Guenther. *Modern Optics*, chapter 9, pages 323–360. John Wiley & Sons, Inc., New York, 1990. ISBN: 0471512885.

[37] M. Born and E. Wolf. *Principles of Optics: Electromagnetic Theory of Propagation, Interference and Diffraction of Light*, chapter 11, pages 633–673. Cambridge University Press, Cambridge, 7th edition, 1999. ISBN: 0521642221.

[38] F. T. S. Yu. *Entropy and Information Optics*, volume 68 of *Optical Engineering*, chapter 2, pages 35–74. Marcel Dekker, Inc., New York, 2000. ISBN: 0824703634.

[39] M. Born and E. Wolf. *Principles of Optics: Electromagnetic Theory of Propagation, Interference and Diffraction of Light*, chapter 2, pages 75–115. Cambridge University Press, Cambridge, 7th edition, 1999. ISBN: 0521642221.

[40] M. Born and E. Wolf. *Principles of Optics: Electromagnetic Theory of Propagation, Interference and Diffraction of Light*, chapter 8, pages 412–516. Cambridge University Press, Cambridge, 7th edition, 1999. ISBN: 0521642221.

[41] E. Hecht. *Optics*, chapter 4, pages 79–127. Addison-Wesley Publishing Company, Inc., Reading, Massachusetts, 2nd edition, 1987.

[42] A. Walther. *Diffraction*, volume 1 of *Applied Optics and Optical Engineering*, chapter 7. Academic Press, Inc., New York, 1965.

[43] F. W. J. Oliver, D. W. Lozier, R. F. Boisvert, and C. W. Clark. *NIST Handbook of Mathematical Functions*, chapter 10, pages 215–286. Cambridge University Press, Cambridge, 1st edition, may 2010. ISBN: 0521140633.

Appendix C

Analytic signal

In 1946 Gabor introduced the analytic signal[1] representation in optics to efficiently represent polychromatic fields [2, 3]. The analytic signal is the generalised version of equation (A.24) (page V.II A-6) [4].

A strictly monochromatic wave has a single frequency. The continuous Fourier transform of a single frequency is a wave of infinite extent. This precludes any real wave being described completely by a monochromatic wave, as a real wave necessarily has a finite epoch. Additionally, when the Fourier transform represents a signal in either its temporal representation or its frequency representation it cannot deal with time–varying frequency components. As the unit of frequency is Hz= s^{-1}, i.e. a constant, the temporal derivative $\frac{\partial}{\partial t}(\mathrm{Hz})$ is zero. Thus, a strictly monochromatic wave cannot be observed, nor can it carry information [5].

This is the advantage of the analytic signal, allowing the physically familiar idea of changing frequencies, e.g. the Doppler shift, and constraining a signal to a temporal or frequency range, an *epoch* and *bandwidth*, respectively [2].

The analytic signal, $\underline{V}(\underline{\mathbf{r}}, t)$, consists of real and imaginary terms that are the Hilbert transform of each other. The Fourier representation of a real non–monochromatic vibration is

$$\underline{V}^{\Re}(\underline{\mathbf{r}}, t) = \int_0^\infty \underline{b}(\underline{\mathbf{r}}, \omega) \cos(\omega t - \Phi(t)) d\omega \tag{C.1}$$

where $\underline{b}(\underline{\mathbf{r}}, \omega)$ is the amplitude, e.g. a Cartesian component of the electric vector [6], and $\Phi(t)$ is the temporal phase. Both $\underline{b}(\underline{\mathbf{r}}, \omega)$ and $\Phi(t)$ are real, and, by causality, $\underline{V}^{\Re}(\underline{\mathbf{r}}, t)$ contains only positive frequencies. A second real vibration is associated

[1] The term *analytic signal* refers to the signal being free of negative frequencies and singularities [1].

with equation (C.1):

$$\underline{V}^{\Im}(\underline{\mathbf{r}},t) = \int_0^\infty \underline{b}(\underline{\mathbf{r}},\omega)\sin(\omega t - \Phi(\omega))d\omega \tag{C.2}$$

Equations (C.1) and (C.2) are combined using Euler's formula to give [4]

$$\underline{V}(\underline{\mathbf{r}},t) = \underline{V}^{\Re}(\underline{\mathbf{r}},t) + i\underline{V}^{\Im}(\underline{\mathbf{r}},t) = \int_0^\infty \underline{b}(\underline{\mathbf{r}},\omega)e^{i(\omega t-\Phi(t))}d\omega \tag{C.3}$$

$\underline{V}(\underline{\mathbf{r}},t)$ is the analytic signal associated with the real signal $\underline{V}^{\Re}(\underline{\mathbf{r}},t)$ [4], which is the quantity obtained from a detector during an experiment. $\underline{V}^{\Re}(\underline{\mathbf{r}},t)$ and $\underline{V}^{\Im}(\underline{\mathbf{r}},t)$ are Hilbert transforms [7–9] of each other [10, 11]:

$$\underline{V}^{\Im}(\underline{\mathbf{r}},t) = \frac{1}{\pi}\mathscr{P}\int_{-\infty}^{\infty}\frac{\underline{V}^{\Re}(\underline{\mathbf{r}},t')}{t'-t}dt', \tag{C.4a}$$

$$\underline{V}^{\Re}(\underline{\mathbf{r}},t) = -\frac{1}{\pi}\mathscr{P}\int_{-\infty}^{\infty}\frac{\underline{V}^{\Im}(\underline{\mathbf{r}},t')}{t'-t}dt' \tag{C.4b}$$

where $\mathscr{P}$ denotes the Cauchy principal value[2] at $t' = t$.

The analytic signal is used in preference to $\underline{V}^{\Re}(\underline{\mathbf{r}},t)$ as it is single–sided and, once the analytic signal is known in one region, it is known everywhere else the signal is analytic [12].

Using the Fourier representation of $\underline{V}^{\Re}(\underline{\mathbf{r}},t)$,

$$\underline{V}^{\Re}(\underline{\mathbf{r}},t) = \int_{-\infty}^{\infty}\underline{\boldsymbol{\upsilon}}(\underline{\mathbf{r}},\omega)e^{i\omega t}d\omega \tag{C.5}$$

where $\underline{\boldsymbol{\upsilon}}(\underline{\mathbf{r}},\omega)$ and $\underline{V}^{\Re}(\underline{\mathbf{r}},t)$ are a Fourier transform pair, and $\underline{\boldsymbol{\upsilon}}(\underline{\mathbf{r}},-\omega) = \underline{\boldsymbol{\upsilon}}^*(\underline{\mathbf{r}},\omega)$[3], which allows equation (C.3) to be expressed in the form of equation (C.1) to give [4, 10]

$$\underline{\boldsymbol{\upsilon}}(\underline{\mathbf{r}},\omega) = \frac{1}{2}\underline{b}(\underline{\mathbf{r}},\omega)e^{i\Phi(\omega)}, \qquad \omega \geqq 0. \tag{C.6}$$

The analytic signal $\underline{V}(\underline{\mathbf{r}},t)$ can now be written as

$$\underline{V}(\underline{\mathbf{r}},t) = 2\int_0^\infty \underline{\boldsymbol{\upsilon}}(\underline{\mathbf{r}},\omega)e^{-i\omega t}d\omega \tag{C.7}$$

Equation (C.7) is the Fourier formulation of the analytic signal used in the analysis here. The analytic signal can be obtained by calculating the Fourier transform of the captured real signal, $\underline{V}^{\Re}(\underline{\mathbf{r}},t)$, suppressing the negative and zero frequency

[2] At the root $t' = t$ the denominator in the Hilbert transform becomes zero. The Cauchy principal value takes the average of a region about the root as representing the non–zero value at the root.

[3] '$*$' denotes the complex conjugate.

terms, multiplying by 2 and then inverse Fourier transforming. The analytic signal is therefore generally a complex signal when $\underline{V}^{\Re}(\underline{\mathbf{r}}, t)$ is real.

Using the analytic signal to describe a polychromatic signal, of mean frequency $\overline{\omega}$ and width $\delta\omega$ (small compared to $\overline{\omega}$),

$$\underline{V}(\underline{\mathbf{r}}, t) = \underline{A}(\underline{\mathbf{r}}, t)e^{i[\Phi(t)-\overline{\omega}t]} \tag{C.8}$$

where amplitude $A \geqslant 0$, and phase Φ are real functions of t [10]. Equating (C.7) and (C.8) gives

$$\underline{A}(\underline{\mathbf{r}}, t)e^{i\Phi(t)} = 2\int_0^\infty \underline{\boldsymbol{\upsilon}}(\underline{\mathbf{r}}, \omega)e^{i(\overline{\omega}-\omega)t}d\omega \tag{C.9}$$

Defining $\underline{g}(\mu) = \underline{\boldsymbol{\upsilon}}(\overline{\omega} + \mu)$ gives [10]

$$\underline{A}(\underline{\mathbf{r}}, t)e^{i\Phi(t)} = 2\int_{-\overline{\omega}}^\infty \underline{g}(\mu)e^{i\mu t}d\mu \tag{C.10}$$

which is of the same form as equation (C.7), but offset by $\overline{\omega}$, i.e. centred on the mean frequency, $\overline{\omega}$. $\underline{\boldsymbol{A}}(\underline{\mathbf{r}}, t)$ and $\Phi(t)$ vary slowly compared to $e^{i\mu t}$.The two extreme cases for the experimentally captured modulation, $\underline{V}(\underline{\mathbf{r}}, t)$, can be derived from the analytic representation:

$$\begin{cases} \underline{V}(\underline{\mathbf{r}}, t) = \underline{A}(\underline{\mathbf{r}}, t)e^{i\mu t} & \underline{A}(\underline{\mathbf{r}}, t) \text{ modulation only,} \\ \underline{V}(\underline{\mathbf{r}}, t) = \underline{A}(\underline{\mathbf{r}})e^{i(\Phi(t)+\mu t)} & \Phi(t) \text{ modulation only.} \end{cases} \tag{C.11}$$

It can be shown that both limiting cases are expressible in terms of the other, and in terms of the general form in equation (C.10) [5]. In terms of equation (C.8)

$$\underline{V}^{\Re}(\underline{\mathbf{r}}, t) = \underline{A}(\underline{\mathbf{r}}, t)\cos\left(\Phi(t) - \overline{\omega}t\right) \tag{C.12}$$

which is of the same form as equation (A.24) (page V.II A-6), but expressed in terms of the mean frequency of the polychromatic signal. The phase can be written as [10]

$$\Phi(t) = \overline{\omega}t + \tan^{-1}\left(\frac{\underline{V}^{\Im}(\underline{\mathbf{r}}, t)}{\underline{V}^{\Re}(\underline{\mathbf{r}}, t)}\right) \tag{C.13}$$

The amplitude can be written as

$$\underline{A}(t) = \sqrt{\left(\underline{V}^{\Re}(\underline{\mathbf{r}}, t)\right)^2 + \left(\underline{V}^{\Im}(\underline{\mathbf{r}}, t)\right)^2} \tag{C.14}$$

$\underline{A}(\underline{\mathbf{r}}, t)$ is termed the instantaneous amplitude and $d\Phi(t)/dt$ the instantaneous frequency of the signal.

The total phase modulation is

$$\Phi(t) - \overline{\omega}t = \varphi(t) \tag{C.15}$$

The phase of a signal $\underline{\mathbf{V}}(t)$ is important because it carries most of the information of a signal [13] and allows the full signal to be reconstructed [14]. The phase is important to know in any process of Fourier synthesis or analysis.

Phase is a property of the wave, and not directly measurable at optical frequencies. The value will be between the *phase principal values*, $\pm\pi$. This is termed the *wrapped phase* in the interval $(-\pi, \pi]$.

C.1 References

[1] C. Brosseau. *Fundamentals of Polarized Light: A Statistical Optics Approach*, chapter 3.1, pages 69–122. John Wiley & Sons, Inc., New York, 1998. ISBN: 0471143022.

[2] D. Gabor. Theory of communication. *J. IEE (London)*, 93(26):429–457, November 1946.

[3] C. Brosseau. *Polarization and coherence optics: Historical perspective, status, and future directions*, volume 54 of *Progress in Optics*, chapter 3. Elsevier, Amsterdam, 2009. ISBN: 9780444535283.

[4] M. Franccon. *Optical Interferometry*, chapter 1, pages 1–34. Academic Press, Inc., New York, 1966. ISBN-10: 0122663500.

[5] B. Picinbono. On instantaneous amplitude and phase of signals. *IEEE T. Signal Proces.*, 45:552–560, March 1997.

[6] M. Born and E. Wolf. *Principles of Optics: Electromagnetic Theory of Propagation, Interference and Diffraction of Light*, chapter 1, pages 1–74. Cambridge University Press, Cambridge, 7th edition, 1999. ISBN: 0521642221.

[7] R. N. Bracewell. *The Fourier Transform and its Application*, chapter 13, pages 329–379. The McGraw-Hill Companies, Inc., New York, 3rd edition, 1999. ISBN: 0073039381.

[8] J. S. Bendat and A. G. Piersol. *Random Data Analysis and Measurement Procedures*, chapter 13, pages 518–549. John Wiley & Sons, Inc., New York, 3rd edition, 2000. ISBN: 0471317330.

[9] S. L. Hahn. *Hilbert Transform in Signal Processing*, chapter 1, pages 3–53. Signal Processing Library. Artech House, Inc, Boston, 1996. ISBN: 0890068860.

[10] M. Born and E. Wolf. *Principles of Optics: Electromagnetic Theory of Propagation, Interference and Diffraction of Light*, chapter 10, pages 554–632. Cambridge University Press, Cambridge, 7th edition, 1999. ISBN: 0521642221.

[11] E. Wolf. *Introduction to the Theory of Coherence and Polarization of Light*, chapter 2, pages 11–30. Cambridge University Press, Cambridge, 2007. ISBN: 9780521822114.

[12] P. Dennery and A. Krzywicki. *Mathematics for Physicists*, chapter 1, pages 1–101. Dover Publications, Inc., New York, 1996. ISBN: 0486691934.

[13] D. C. Ghiglia and M. D. Pritt. *Two-Dimensional Phase Unwrapping: Theory, Algorithms, and Software*, chapter 1, pages 1–30. John Wiley & Sons, Inc., New York, 1998. ISBN: 0471249351.

[14] J. Pevrina. *Coherence of Light*, chapter 3, pages 32–46. The Modern University Physics Series. Van Nostrand Reinhold Company, London, 1971. ISBN: 0442063423.

Appendix D

An information based comparison of FT– and grating based spectroscopy

The following discussion is based upon the essay by Gebbie [1].

The four phase based spectrometer systems considered in figure D.1(a) are the prism, diffraction grating, Fabry-Pérot and Michelson apparatus. Each system separates the incoming signal into a number of separate beams, applies a systematic delay between the beams and the output is the superposition of the delayed beams. This is schematically shown in figure D.1(b).

The pattern produced by the superposition of beams is determined by the frequency composition of the input signal and, using knowledge of the spectrometer's operation, can return the spectrum.

The tuning factor of each spectrometer system is the delay between beams introduced, which determines the limit of the spectral resolution of the interferometer [2]. The spectrometer systems can be arranged on a scale [1], according to the number of beams in the superposition, shown in figure D.1. The minimum number of beams must be two, i.e. the Michelson/Mach–Zehnder, and the maximum number of beams is infinite[1], i.e. the prism.

The diffraction grating and Fabry–Pérot systems are intermediate on the scale, and, as the Young's slits and Michelson can be considered interchangeable in terms of the superposition of beams at Q and Q'(figure B.3 (page V.II B-8), the diffraction grating and Fabry-Pérot can be considered as the multiple–beam interferometer equivalents in the directions Q and Q', respectively.

[1]Assuming the prism is a continuum, by ignoring the atomic structure of the material.

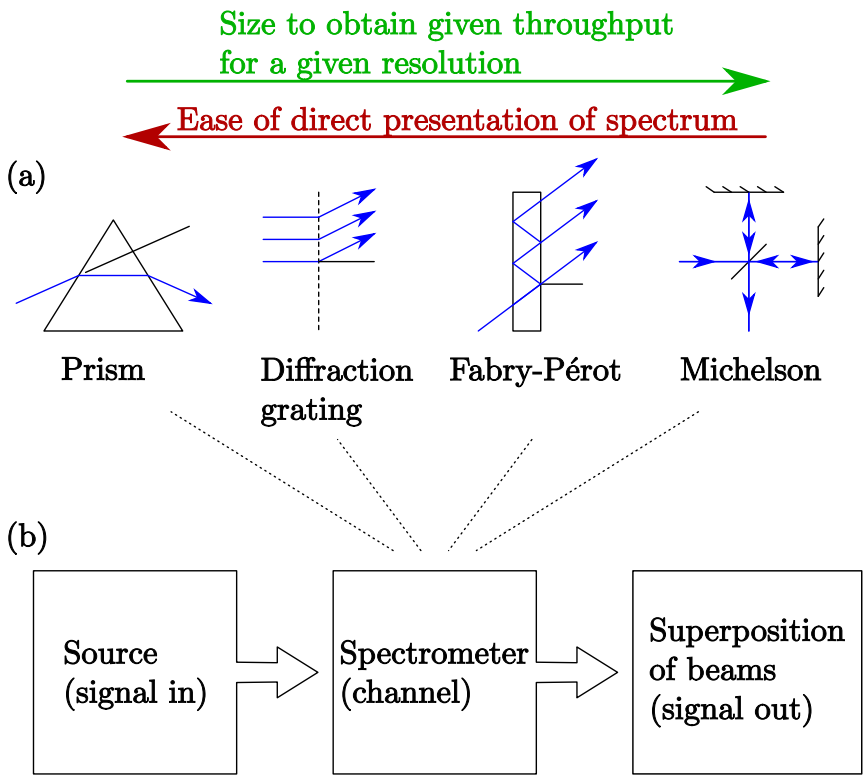

Figure D.1: The information capacity of four spectrometer systems in terms of size required for a fixed information throughput for a given spectral resolution, and ease of direct presentation of the spectrum (after Gebbie [1]). (a) The Spectrometer types discussed; and (b) A block diagram of the process incorporating the spectrometers.

The prism not only analyses the input signal, but also directs each frequency into a unique angle, due to dispersion, giving a unique direct presentation of the spectrum. The diffraction grating distributes the energy over a number of orders for each frequency, and so the free-spectral range is reduced. A complicated spectrum may have overlapping orders from different frequencies, and a unique direct presentation is not guaranteed. The Michelson spectrometer is worst in terms of direct presentation, as the whole spectrum is presented in terms of co–sinusoidal oscillations at Q', an indirect process of presentation [2].

However, when the spectrometer systems are compared for throughput of information for size of the spectrometer system at a given spectral resolution, the order is reversed. For a given throughput there is an increase of greater than an order of magnitude in resolution between the prism, diffraction grating and Fabry–Perót.

The increase in resolution between the Fabry–Perót and Michelson interferometer is less than an order of magnitude [3]. The difference in ordering can be explained by considering the *analysis* and *presentation* of the spectrum as two different functions. The prism and diffraction grating must perform both functions, where the Michelson interferometer performs only one.

For a given spectrum, I_ν against ν, ΔI_ν and $\Delta\nu$ denote the ranges of I_ν and ν, respectively. For all other values of ν outside the range $\Delta\nu$, $I_\nu = 0$. I_ν and ν will be obtained by a spectrometer, with respective accuracies δI_ν and $\delta\nu$. $\delta\nu$ will be determined by the spectral resolution of the spectrometer. δI_ν will be ideally determined only by the noise level of the detector(s) of the spectrometer, i.e. no phase or interferometric instrument noise.

The total amount of information (measured in bits) is [1]

$$I_{inf} = \frac{\Delta\nu\Delta I_\nu}{\delta\nu\delta I_\nu} \tag{D.1}$$

The fixed channel capacity, I_{inf}, of the instrument must be shared by *analysis* and *presentation* for the diffraction grating and prism. The more channel space required for *presentation*, the less available for *analysis*. The Michelson interferometer devotes its channel capacity to a single function. The output of the Michelson interferometer is then digitised into a digital computer, removing the time constraints of the analog computer. The simultaneous recording of all frequencies by the Michelson interferometer gives a time advantage[2] in data capture, termed the *Fellgett advantage* [4]. This is of significant benefit in detector noise limited systems. The system then divides the noise amongst the spectral features present, reducing the individual relative noise level.

However, if the spectrum is needed faster than can be processed for the output of a Michelson interferometer based spectrometer, or if the spectrum changes faster than the scan time of the Michelson interferometer, a trade–off in terms of information throughput against total processing time must be made. The scaling of the respective systems in figure D.1 gives an indication of the optimal spectrographic system, in this case.

The systems can also be compared by ease of assembly. The Michelson interferometer is easier to assemble than the diffraction grating or prism spectrometer, where the input signal often needs to be collimated, the angles need to be calibrated and the energy focused. The Michelson interferometer is, by comparison, self referencing, as the beams must travel back along their incident paths. The effort required in the alignment of the optics in a Fabry–Perót, and the combined optics

[2]The time taken, for a given accuracy, will be $\sqrt{\frac{N}{2}}$ shorter than for a scanning diffraction grating or prism monochromator [2].

for diffraction grating based systems, typically exceeds that required for a Michelson interferometer.

D.1 References

[1] H. A. Gebbie. Fourier transform versus grating spectroscopy. *Appl. Opt.*, 8(3):501, 1969.

[2] L. Mertz. *Transformations in Optics*, chapter 1, pages 1–43. John Wiley & Sons, Inc., New York, 1965.

[3] H. Gross, F. Blechinger, and B. Achtner. *Survey of Optical Instruments*, volume 4 of *Handbook of Optical Systems*, chapter 45, pages 941–1055. Wiley-VCH Verlag GmbH & Co. KGaA, Weinheim, 2008. ISBN: 3527403806.

[4] P. B. Fellgett. The nature and origin of multiplex Fourier spectrometry. *Notes Rec. Roy. Soc.*, 60(1):91–93, 2006.

Appendix E

Polarisation overview

The vectorial representations of $\underline{\mathbf{E}}$, $\underline{\mathbf{H}}$, $\underline{\mathbf{D}}$ and $\underline{\mathbf{B}}$ group the individual, orthogonal, components of the fields, but do not describe the internal structure of those fields. The coherence and diffraction treatments, described in appendix B (page V.II B-1), have implicitly presumed that the interfering vector components of the different were not orthogonal.

In general[1] and particularly when anisotropic materials are used, the internal structure, the polarisation of the field, cannot be ignored.

Assuming the electric field[2] is transverse to the z direction of propagation, i.e. no z polarisation [2]

$$\underline{\mathbf{E}}(z,t) = \begin{pmatrix} E_x(z,t) \\ E_y(z,t) \end{pmatrix} = \begin{pmatrix} E_{0x}\cos(\tau + \Phi_x) \\ E_{0y}\cos(\tau + \Phi_y) \end{pmatrix} \tag{E.1}$$

where $\tau = \omega t - kz$ is the propagating term and Φ_x and Φ_y are the respective phases in the x and y orientation. The amplitude will be the vector sum of the orthogonal components. For quasi–monochromatic light $E_x(z,t)$ and $E_y(z,t)$ are separately described by analytic signals [3].

As the field propagates, the components $E_x(z,t)$ and $E_y(z,t)$ produce a resultant vector, the locus of which describes an ellipse in space. The resultant vector is termed the *state of polarisation*, SOP[3] [3].

Using the trigonometric identity, $\cos(x \pm y) = \cos x \cos y \mp \sin x \sin y$, to rewrite

[1] By which is meant that polarisation is known not to be a factor.

[2] As mentioned previously, $\underline{\mathbf{E}}$ is of greater influence than $\underline{\mathbf{H}}$ [1], and hence anisotropy will be influenced more by $\underline{\mathbf{P}}$ than by $\underline{\mathbf{M}}$.

[3] The SOP is also defined as the length of the principal axis and orientation of the polarisation ellipse together with the degree of polarisation [4].

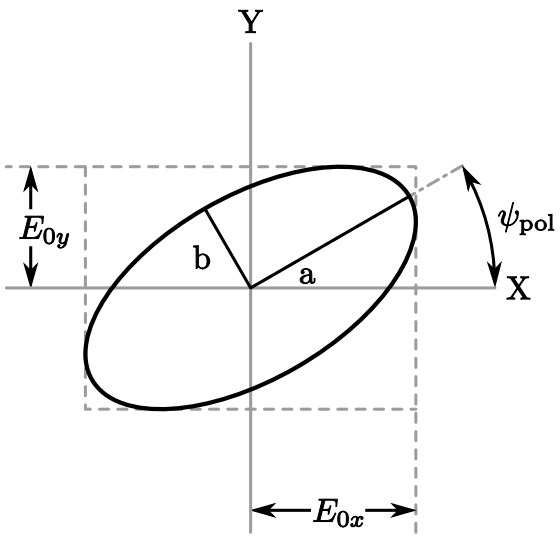

Figure E.1: Polarisation ellipse describing the locus of resultant vector of propagating $E_x(z,t)$ and $E_y(z,t)$ fields.

equation (E.1) and separating, gives

$$\frac{E_x}{E_{0x}} = \cos\tau\cos\Phi_x - \sin\tau\sin\Phi_x \tag{E.2a}$$

$$\frac{E_y}{E_{0y}} = \cos\tau\cos\Phi_y - \sin\tau\sin\Phi_y \tag{E.2b}$$

Hence,

$$\frac{E_x}{E_{0x}}\sin\Phi_y - \frac{E_y}{E_{0y}}\sin\Phi_x = \cos\tau\sin(\Phi_y - \Phi_x) \tag{E.3a}$$

$$\frac{E_x}{E_{0x}}\cos\Phi_y - \frac{E_y}{E_{0y}}\cos\Phi_x = \sin\tau\sin(\Phi_y - \Phi_x) \tag{E.3b}$$

Squaring equation (E.3) and adding gives

$$\frac{E_x^2}{E_{0x}^2} + \frac{E_y^2}{E_{0y}^2} - 2\frac{E_x}{E_{0x}}\frac{E_y}{E_{0y}}\cos\Phi_{\text{pol}} = \sin^2(\Phi_{\text{pol}}) \tag{E.4}$$

where

$$\Phi_{\text{pol}} = \Phi_y - \Phi_x \tag{E.5}$$

Equation (E.4) is the equation of the *polarisation ellipse*.

Figure E.1 shows the ellipse inscribed within a rectangle of side lengths $2E_{0x}$ and $2E_{0y}$. The azimuthal angle, ψ_{pol}, and the *ellipticity*, χ_{pol}, are obtained from the

ellipse using [2]

$$\tan 2\psi_{\text{pol}} = (\tan 2\alpha_{\text{pol}}) \cos \Phi_{\text{pol}} \qquad o \leq \psi_{\text{pol}} \leq \pi \tag{E.6a}$$

$$\sin 2\chi_{\text{pol}} = (\sin 2\alpha_{\text{pol}}) \sin \Phi_{\text{pol}} \qquad -\tfrac{\pi}{4} < \chi_{\text{pol}} \leq \tfrac{\pi}{4} \tag{E.6b}$$

where

$$\tan \alpha_{\text{pol}} = \frac{E_{0y}}{E_{0x}} \qquad 0 \leq \alpha_{\text{pol}} \leq \tfrac{\pi}{2} \tag{E.7a}$$

$$\tan \chi_{\text{pol}} = \pm \frac{b}{a} \tag{E.7b}$$

and $a^2 + b^2 = E_{0x}^2 + E_{0y}^2$.

Four general states can be obtained from equation (E.4) [2]:

1. When $\Phi_{\text{pol}} = \frac{\pi}{2}$ or $\frac{3\pi}{2}$ equation (E.4) becomes,

$$\frac{E_x^2}{E_{0x}^2} + \frac{E_y^2}{E_{0y}^2} = 1 \tag{E.8}$$

   which is the standard equation of an ellipse.

2. When $E_{0x} = E_{0y} = E_0$ and $\Phi_{\text{pol}} = \frac{\pi}{2}$ or $\frac{3\pi}{2}$, equation (E.4) becomes

$$\frac{E_x^2}{E_0^2} + \frac{E_y^2}{E_0^2} = 1 \tag{E.9}$$

   which describes a circle. $\Phi_{\text{pol}} = \frac{\pi}{2}$ and $\frac{3\pi}{2}$ describe *right circularly polarised*, RCP, and *left circularly polarised*, LCP, light, respectively.

3. When $E_{0x} = 0$ or $E_{0y} = 0$, then there is only one direction in which the field oscillates; these are termed *linear vertical polarisation*, LVP, and *linear horizontal polarisation*, LHP, respectively.

4. When $\Phi_{\text{pol}} = 0$ or π, equation (E.4) becomes

$$\frac{E_x^2}{E_{0x}^2} + \frac{E_y^2}{E_{0y}^2} \pm 2\frac{E_x}{E_{0x}}\frac{E_y}{E_{0y}} = 0$$
$$\Rightarrow \left(\frac{E_x}{E_{0x}} \pm \frac{E_y}{E_{0y}}\right)^2 = 0$$

   and so

$$E_y = \pm \left(\frac{E_{0y}}{E_{0x}}\right) E_x \tag{E.10}$$

   which is the equation of a line, i.e. linearly polarised light with slope $\pm\,(E_{0y}/E_{0x})$. When $\Phi_{\text{pol}} = 0$ the slope is negative, and when $\Phi_{\text{pol}} = \pi$ the slope is positive. When $E_{0x} = E_{0y}$ then $E_y = \pm E_x$ with the positive value termed *linear* $+45°$

polarised light, L+45P, and the negative value termed *linear* $-45°$ polarised light, L−45P.

These are the degenerate forms of completely polarised light. However, unpolarised light and partially polarised light are also encountered, which cannot be as neatly described. Partially polarised light may be considered as consisting of a sum of unpolarised and polarised light. The polarisation ellipse cannot be directly observed either, as the propagation terms oscillate at optical frequencies $\sim 10^{14}$ Hz.

Shurcliff operationally defined unpolarised light as: light which, '*when operated on by any elementary kind of energy–conserving device that divides the beam into two completely polarised subbeams, yields subbeams that have equal power (in a time interval long enough to permit the powers be measured)*' [5]. Stokes adopted the experimental definition: unpolarised light is light whose intensity is unaffected when a polariser is rotated or by the presence of a retarder of any retardance value [6].

The term unpolarised light is typically reserved for naturally occurring unpolarised light, e.g. sunlight [7]. The amplitudes E_y and E_x and relative phase Φ_{pol} are random. These terms change at the frequency of the propagating light, and so, when observed by a detector, effectively occupy all values of E_y, E_x and Φ_{pol}.

The term *depolarised light* is used to refer to polarised or partially polarised light that has been disordered to be unpolarised. Light diffusion by powders, ground optical surfaces, or opal glasses provides true depolarisation, i.e. random phase differences, at the expense of a wide scattering angle [8].

The term *pseudo–depolarised light* is used to refer to light that appears to become depolarised to a detector, i.e. is mathematically equivalent to unpolarised light for that detector[4]. In this work the use of the word depolariser will refer to a pseudo–depolariser, for brevity.

E.1 Stokes parameters

In 1852, Sir G. G. Stokes published a representation scheme which allowed for the representation of all polarisation states from completely polarised light to completely unpolarised light, using experimentally observable parameters. These are termed *the Stokes parameters*. The value of this work was not recognised for nearly a century until S. Chandrasekhar [10] used Stokes parameters to describe radiative transfer equations for partially polarised light [1, 6]. The Stokes parameters are obtained from experimentally obtained quantities.

[4]The SOP is varied rapidly with respect to a variable that is not specified in the experiment [9].

The Stokes parameters are

$$S_0 = \langle E_x E_x^* + E_y E_y^* \rangle = E_{0x}^2 + E_{0y}^2 \tag{E.11a}$$

$$S_1 = \langle E_x E_x^* - E_y E_y^* \rangle = E_{0x}^2 - E_{0y}^2 \tag{E.11b}$$

$$S_2 = \langle E_x E_y^* + E_y E_x^* \rangle = 2E_{0x}E_{0y}\cos\Phi_{\text{pol}} \tag{E.11c}$$

$$S_3 = \langle i(E_x E_y^* - E_y E_x^*) \rangle = 2E_{0x}E_{0y}\sin\Phi_{\text{pol}} \tag{E.11d}$$

The Stokes parameters are alternatively labelled as $(S_0, S_1, S_2, S_3) = (I, M, C, S) = (I, Q, U, V)$ [11].

The Stokes parameters allow the definition of the *degree of polarisation*, DOP, as [12]

$$\mathcal{P} = \frac{I_{pol}}{I_{tot}} = \frac{\sqrt{S_1^2 + S_2^2 + S_3^2}}{S_0} \qquad 0 \leq \mathcal{P} \leq 1 \tag{E.12}$$

where I_{pol} is the sum of the intensity of the polarised components and I_{tot} is the total sum of the intensity of the beam. Partially polarised light can thus be represented as a sum of unpolarised light and completely polarised light[5]

$$\underline{\mathbf{S}} = \begin{pmatrix} S_0 \\ S_1 \\ S_2 \\ S_3 \end{pmatrix} = (1-\mathcal{P}) \begin{pmatrix} S_0 \\ 0 \\ 0 \\ 0 \end{pmatrix}_{unpol} + \mathcal{P} \begin{pmatrix} S_0 \\ S_1 \\ S_2 \\ S_3 \end{pmatrix}_{pol}, \qquad 0 \leq \mathcal{P} \leq 1 \tag{E.13}$$

where the Stokes parameters are arranged into what is termed, by convention, the *Stokes vector*, although it is a column matrix [6].

E.2 The Poincaré sphere representation

The Stokes vector may be represented graphically using the Poincaré sphere as shown in figure E.2 [11,14,15]. The ranges of $-\pi \leq 2\psi \leq \pi$ and $-\frac{\pi}{2} \leq 2\chi \leq \frac{\pi}{2}$ cover the entire sphere. The normalised[6] Stokes parameters S_1, S_2 and S_3 are plotted upon the axes of an xyz–coordinate system. The radius of the sphere is 1. A point $\mathbf{P}$ has a vector of length $\sqrt{S_1^2 + S_2^2 + S_3^2}$. Completely polarised light is represented by a point upon the sphere surface, as $S_0 = \sqrt{S_1^2 + S_2^2 + S_3^2}$. Partially polarised light is represented by a distribution of points, which are not at the surface, but within the sphere, as $S_0 > \sqrt{S_1^2 + S_2^2 + S_3^2}$ [16]. The distance, $\sqrt{S_1^2 + S_2^2 + S_3^2}$, of the partially polarised point between the centre and surface, S_0, gives the degree of

[5]Wolf has qualified this assertion by stating that this is only true if, and only if, the cross–spectral density matrix, equation (2.17) (page V.I - 19), can be so decomposed into a sum of completely polarised and completely unpolarised at the origin [13].

[6]Normalised by dividing by S_0.

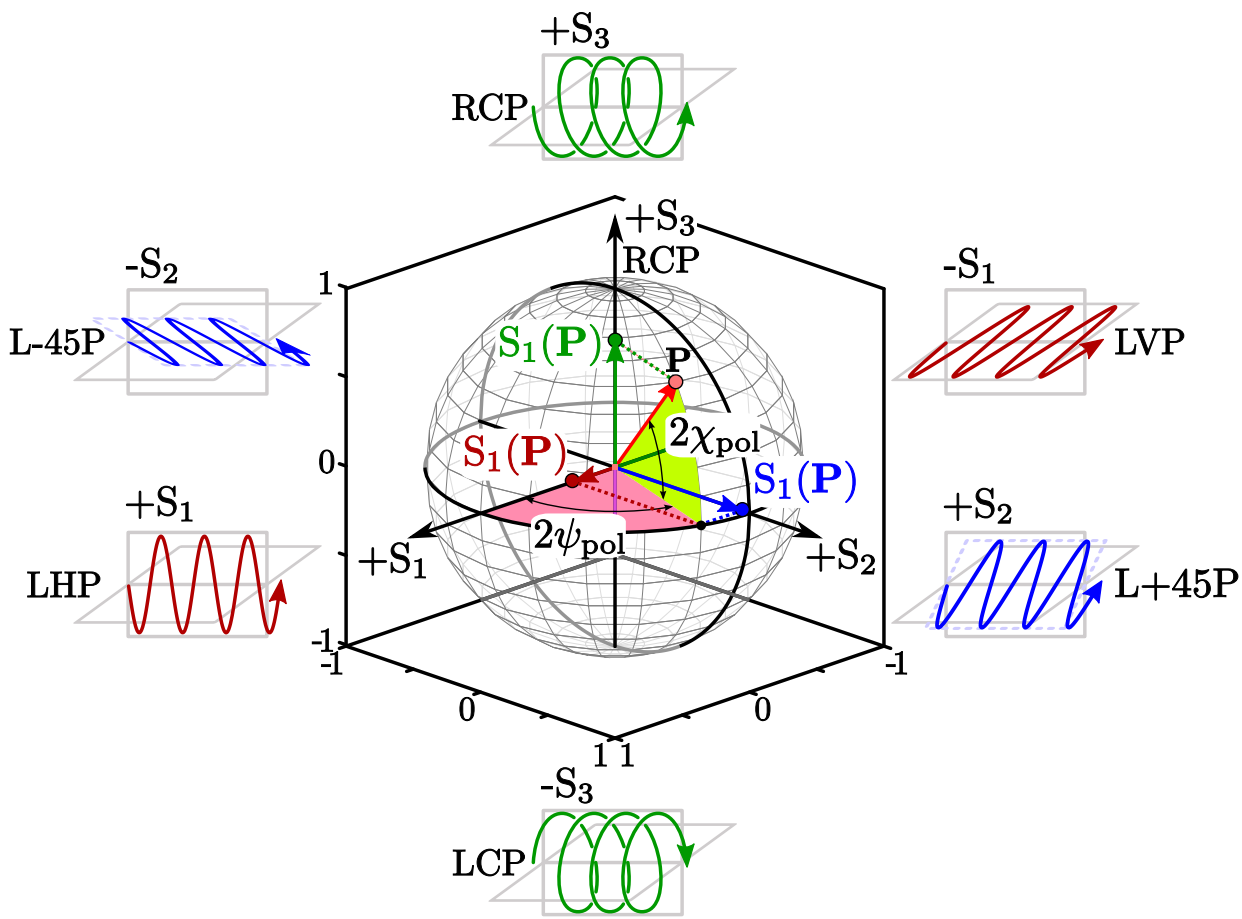

Figure E.2: Poincaré sphere showing projections of point **P** onto S_1, S_2 and S_3.

polarisation. Unpolarised light is represented by the origin, as the Stokes vector for unpolarised light is $(S_0, 0, 0, 0)$.

Circularly polarised SOPs are at the poles, linear SOPs at the equator and elliptical SOPs at intermediate locations. Right–hand SOPs occupy the upper half–space, and left–handed SOPs the lower half space. Orthogonal SOPs are represented by diametrically opposite points.

The relationship between the polarisation ellipse and the Poincaré sphere is given by [11, 15]

$$S_1 = \cos(2\chi_{\text{pol}})\cos(2\psi_{\text{pol}}) \tag{E.14}$$

$$S_2 = \cos(2\chi_{\text{pol}})\sin(2\psi_{\text{pol}}) \tag{E.15}$$

$$S_3 = \sin(2\chi_{\text{pol}}) \tag{E.16}$$

In order to represent SOPs graphically the completely polarised component of partially polarised light is extended to intercept the surface of the sphere and there indicated. This prevents confusion arising, for example, from neighbouring points

being at the surface and beneath the surface of the sphere when the SOP evolves from completely to partially polarised. The polarimeter data used in this work will show the completely polarised component of the SOP.

Generally it is assumed the linear SOPs will be represented at the equator; however, modified versions are used [17].

E.3 Geometric phase effects

When the SOP of a light beam is made to follow a closed path on the Poincaré sphere, i,e, the initial and final SOPs are the same, a phase shift of topological origin is acquired [18,19], which is termed the *Pancharatnam phase* or *Pancharatnam–Berry phase*. This is distinct from the introduced phase shift from birefringence, polarising element thickness or polarising eigenaxes orientation, which may be considered as a *dynamical* phase shift [20].

The phase shift, Φ_{GP}, is equal to half the solid angle, Ω, subtended at the centre of the Poincaré sphere by the path $ABCA$ on the surface [21], as shown in figure E.3,

$$\Phi_{GP} = \pm\frac{\Omega}{2} \tag{E.17}$$

Out–of–plane optical paths similarly introduce phase shifts via closed circuits upon the sphere of directions in momentum space, termed *spin–redirection phase* [22].

The momentum vector, $\underline{\mathbf{k}}$, is normal to the surface of the sphere and the electric vector, $\underline{\mathbf{E}}$, is a tangent to the surface at the momentum vector, shown in figure E.4. The electric vector can therefore occupy any direction, i.e. polarisation orientation, while remaining a tangent to the surface [21]. The effect is to rotate the state of polarisation, as the momentum vector follows the path $ABCA$, with the associated electric vector $\underline{\mathbf{E}}_A$ and $\underline{\mathbf{E}}_{A'}$ at the start and at the end, respectively. Spin–redirection phase has an effect in fibre based polarisation rotators [22].

When light, consisting of left– and right–circularly polarised light, traverses a coiled fibre, or even a curved fibre, the two orientations acquire opposite phase shifts, which are again equal to the solid angle subtended by the path in momentum space [21,23].

The cases of a fixed propagation direction and closed loop changes in SOP, and fixed SOP and closed loop changes in the direction of propagation [24] are complementary. These phase terms arise when any parameter describing a property of the system undergoes a cyclic evolution in state space, e.g. the geodesic triangle on the Poincaré sphere or sphere of directions in momentum space [1].

In general the effects arise as 2×2 matrices commute but 3×3 do not commute

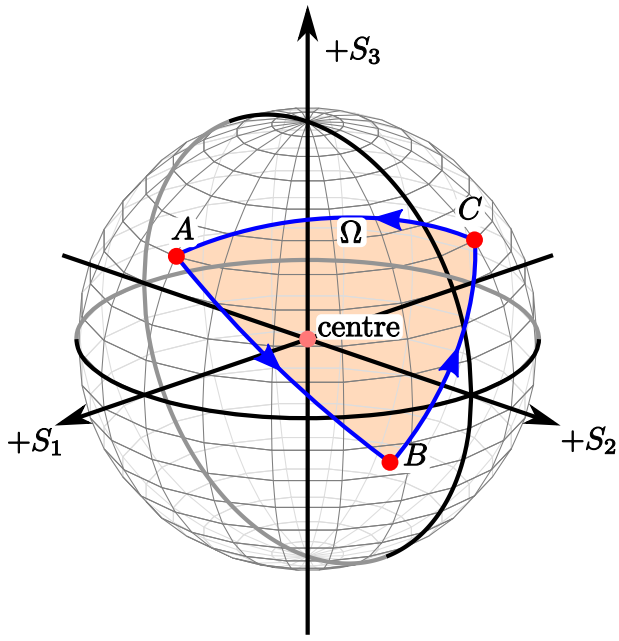

Figure E.3: Pancharatnam phase from following the closed path, **ABCA**, about the Poincaré sphere.

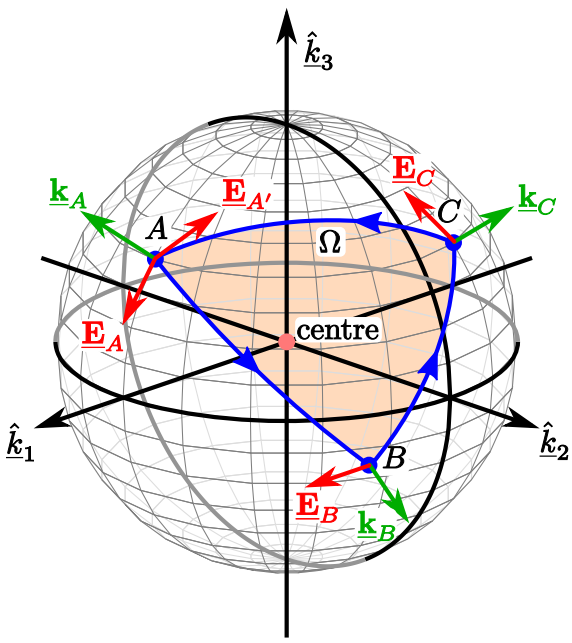

Figure E.4: Spin–redirection phase from following the closed path, **ABCA**, about the sphere of directions in momentum space.

[21]. Being topological in nature, the effects are independent of wavelength.

A geometric phase shift also arises when the path does not return to its original state [20, 25]. The effect of geometric phase shifts should be considered where the phase of a signal is employed for measurement, and there exists an anisotropic element in the apparatus [20]. By using the eigenaxes of a polarising element, B_1 and B_2, a triangular path can be defined in conjunction with the direct[7] arc AC. For example, from figure E.5, the vertices of the triangular path are initial SOP A, the medium's fast or slow eigenaxes[8] SOPs, B_1 and B_2, and the final SOP $C \neq A$ [25]. The solid angles subtended by these triangles, AB_1C and AB_2C, are Ω_1 and Ω_2, respectively, and are given by equation (E.17).

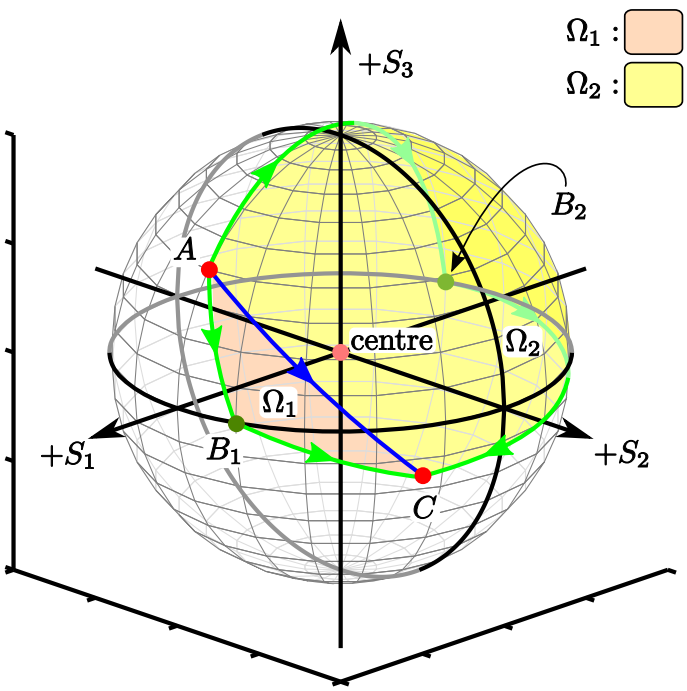

Figure E.5: Topological phases Ω_1 and Ω_2, from following either path $\mathbf{AB_1C}$ or $\mathbf{AB_2C}$, respectively, with the loop completed by the great circle arc between AC, on the Poincaré sphere. B_1 and B_2 are the eigenaxes of a polarisation modifying optical component.

This approach was extended to incorporate both the fast and slow axes, $n_{f,s}$ [20]. For a Mach–Zehnder interferometer, with a birefringent element of thickness d in

[7] The geodesic arc AC on the great circle containing A and C.

[8] The polarising medium's fast and slow eigenaxes are presumed orthogonal, and hence antipodal on the Poincaré sphere.

one arm[9], the phase shift is

$$\begin{aligned}\Phi_{\text{total}} &= \Phi_D &+ \quad \Phi_G \\ &= \tfrac{\Phi_f+\Phi_s}{2} &+ \quad \tan^{-1}\left[\tan\left(\tfrac{\gamma_\Phi}{2}\right) \bullet \cos(2\psi_{\text{pol}})\right]\end{aligned} \tag{E.18}$$

where the first term is the dynamical phase shift due to birefringence, with $\Phi_{f,s} = k_{f,s}d$, $k_{f,s} = n_{f,s}k_0$[10] being the phases of the fast and slow axes, respectively; and the second term is the geometrical phase shift, with $\gamma_\Phi = \Phi_f - \Phi_s$ and azimuthal angle ψ_{pol}.

Rewriting the second term in a form similar to equation (E.17),

$$\Phi_G = \frac{\frac{\Omega_s}{2} - \frac{\Omega_f}{2}}{2} \tag{E.19}$$

where $\Omega_{f,s}$ are the solid angles subtended at the centre of the Poincaré sphere by the paths between the initial SOP, fast and slow axes, respectively, and final SOP.

The geometric phase, in general, will shift the interference pattern produced by interfering beams such that the zero OPD between the arms will not coincide with an intensity maximum. In the case of non–identical initial and final SOPs, the geometric phase term contains a dependence upon the birefringence and, hence, will have a wavelength dependence.

E.4 Mueller calculus

The Stokes parameters allow the SOP of light to be characterised, but do not predict or explain how the SOP was arrived at. It is assumed the final SOP, $\underline{\mathbf{S}}_{\text{out}}$, is a linear combination of the initial SOP[11], $\underline{\mathbf{S}}_{\text{in}}$ [26, 27]. The relation between $\underline{\mathbf{S}}_{\text{out}}$ and $\underline{\mathbf{S}}_{\text{in}}$ is a 4×4 matrix, the *Mueller matrix*,

$$\underline{\mathbf{S}}_{\text{out}} = \underline{\underline{\mathbf{M}}}_{\text{sys}}\,\underline{\mathbf{S}}_{\text{in}} \tag{E.20}$$

where

$$\underline{\underline{\mathbf{M}}}_{\text{sys}} = \begin{pmatrix} m_{11} & m_{12} & m_{13} & m_{14} \\ m_{21} & m_{22} & m_{23} & m_{24} \\ m_{31} & m_{32} & m_{33} & m_{34} \\ m_{41} & m_{42} & m_{43} & m_{44} \end{pmatrix} = \underline{\underline{\mathbf{M}}}_N\,\underline{\underline{\mathbf{M}}}_{N-1}\cdots\underline{\underline{\mathbf{M}}}_1 \tag{E.21}$$

and $\underline{\underline{\mathbf{M}}}_{\text{sys}}$ is the Mueller matrix of the system. $\underline{\underline{\mathbf{M}}}_{\text{sys}}$ may be composed of N separate polarising elements $\underline{\underline{\mathbf{M}}}_N\,\underline{\underline{\mathbf{M}}}_{N-1}\cdots\underline{\underline{\mathbf{M}}}_1$, where the N matrices are in reverse order

[9] If the interferometer has birefringent elements in both arms, the difference between the birefringent elements can be described, equivalently, by a single birefringent element in one arm.

[10] As in equation (A.20) (page V.II A-5).

[11] The SOPs and the calculus have an implicitly defined co–ordinate system.

to the N polarising elements encountered, i.e. $\underline{\underline{\mathbf{M}}}_1$ is for the first polarising element encountered.

The elements of the Mueller matrix are characteristic of the optical medium, and independent of each other. Symmetry conditions, imposed or arising from the optical properties of the polarising element, reduce the number of independent elements [27], making some elements equal or zero. Additionally [27],

$$|m_{kl}| \leq m_{11} \leq 1 \tag{E.22}$$

where k, l are the row and column indices.

Mueller matrices for LHP and LVP polarisers are, respectively,

$$\underline{\underline{\mathbf{M}}}_{\mathrm{LHP}} = \frac{1}{2}\begin{pmatrix} 1 & 1 & 0 & 0 \\ 1 & 1 & 0 & 0 \\ 0 & 0 & 0 & 0 \\ 0 & 0 & 0 & 0 \end{pmatrix} \tag{E.23}$$

and

$$\underline{\underline{\mathbf{M}}}_{\mathrm{LVP}} = \frac{1}{2}\begin{pmatrix} 1 & -1 & 0 & 0 \\ -1 & 1 & 0 & 0 \\ 0 & 0 & 0 & 0 \\ 0 & 0 & 0 & 0 \end{pmatrix} \tag{E.24}$$

Mueller matrices for a general quarter–waveplate, half–waveplate and depolariser are, respectively,

$$\underline{\underline{\mathbf{M}}}_{\mathrm{QWP}} = \frac{1}{2}\begin{pmatrix} 1 & 0 & 0 & 0 \\ 0 & 1 & 0 & 0 \\ 0 & 0 & 0 & 1 \\ 0 & 0 & -1 & 0 \end{pmatrix} \tag{E.25}$$

$$\underline{\underline{\mathbf{M}}}_{\mathrm{HWP}} = \frac{1}{2}\begin{pmatrix} 1 & 0 & 0 & 0 \\ 0 & 1 & 0 & 0 \\ 0 & 0 & -1 & 0 \\ 0 & 0 & 0 & -1 \end{pmatrix} \tag{E.26}$$

$$\underline{\underline{\mathbf{M}}}_{\mathrm{DePol}} = \frac{1}{2}\begin{pmatrix} 1 & 0 & 0 & 0 \\ 0 & 0 & 0 & 0 \\ 0 & 0 & 0 & 0 \\ 0 & 0 & 0 & 0 \end{pmatrix} \tag{E.27}$$

E.5 Jones calculus

The Stokes parameters and the Mueller matrix calculus can describe all states of polarisation and polarising elements. However, the use of the optical intensity restricts the Stokes parameters and Mueller matrices to single beams or multiple incoherently added beams, i.e. where no phase or amplitude relationship exists between the component beams [28].

Any interferometric device which has an OPD within the coherence length of the light under consideration will not be accurately described by the Stokes parameters or Mueller matrices, as they will not incorporate the interference term. The difficulties in using the amplitude term through multiple polarising elements led R. Clark Jones to introduce what are now termed the *Jones matrix calculus* [26, 28–36].

The *Jones vector* consists of the orthogonal Cartesian co–ordinates of the electric vector

$$\underline{\mathbf{E}}(z,t) = \begin{pmatrix} E_x(z,t) \\ E_y(z,t) \end{pmatrix} \qquad (E.1)$$

The Jones vector can only describe completely polarised light, which is a disadvantage in describing real systems where partially polarised light is frequently encountered, and the system itself may depolarise the light as it traverses it. To represent unpolarised light two orthogonal Jones vectors with half the amplitude are added.

When $E_x = 0$ the Jones vector describes light in the LVP SOP, and when $E_y = 0$ it describes the LHP SOP [37]. Polarising elements are represented by a 2×2 *Jones matrix*[12]

$$\underline{\mathbf{E}}_{out} = \underline{\underline{\mathbf{J}}}_{\text{sys}}\, \underline{\mathbf{E}}_{in} \qquad \text{(E.28a)}$$

$$\text{where } \underline{\underline{\mathbf{J}}}_{\text{sys}} = \begin{pmatrix} j_{11} & j_{12} \\ j_{21} & j_{22} \end{pmatrix} = \underline{\underline{\mathbf{J}}}_N \underline{\underline{\mathbf{J}}}_{N-1} \cdots \underline{\underline{\mathbf{J}}}_1 \qquad \text{(E.28b)}$$

and where $\underline{\underline{\mathbf{J}}}_{\text{sys}}$ is the Mueller matrix of the system, which may be composed of N separate polarising elements $\underline{\underline{\mathbf{J}}}_N \underline{\underline{\mathbf{J}}}_{N-1} \cdots \underline{\underline{\mathbf{J}}}_1$, where the N matrices are in reverse order to the order the N polarising elements are encountered by the light.

For subsequent use in this work, the Jones matrices for linear horizontal and

[12] The Jones matrix would be a 3×3 matrix to the 3×1 Jones vector if a plane wave propagating along a co–ordinate axes had not been chosen [27].

linear vertical polarisations are, respectively

$$\underline{\underline{\mathbf{J}}}_{\mathrm{LHP}} = \begin{pmatrix} 1 & 0 \\ 0 & 0 \end{pmatrix} \tag{E.29a}$$

$$\underline{\underline{\mathbf{J}}}_{\mathrm{LVP}} = \begin{pmatrix} 0 & 0 \\ 0 & 1 \end{pmatrix} \tag{E.29b}$$

$$\tag{E.29c}$$

E.6 References

[1] C. Brosseau. *Polarization and coherence optics: Historical perspective, status, and future directions*, volume 54 of *Progress in Optics*, chapter 3. Elsevier, Amsterdam, 2009. ISBN: 9780444535283.

[2] D. Goldstein. *Polarized Light*, volume 83 of *Optical Engineering*, chapter 3, pages 21–30. Marcel Dekker, Inc., New York, 2 edition, 2003. ISBN: 082474053X.

[3] C. Brosseau. *Fundamentals of Polarized Light: A Statistical Optics Approach*, chapter 3.1, pages 69–122. John Wiley & Sons, Inc., New York, 1998. ISBN: 0471143022.

[4] E. Wolf. *Introduction to the Theory of Coherence and Polarization of Light*, chapter 8, pages 154–173. Cambridge University Press, Cambridge, 2007. ISBN: 9780521822114.

[5] W. A. Shurcliff. *Polarized Light: Production and Use*, chapter 1, pages 1–14. Harvard University Press, Massachusetts, 1966.

[6] D. Goldstein. *Polarized Light*, volume 83 of *Optical Engineering*, chapter 4, pages 31–64. Marcel Dekker, Inc., New York, 2 edition, 2003. ISBN: 082474053X.

[7] M. Born and E. Wolf. *Principles of Optics: Electromagnetic Theory of Propagation, Interference and Diffraction of Light*, chapter 10, pages 554–632. Cambridge University Press, Cambridge, 7th edition, 1999. ISBN: 0521642221.

[8] S. Huard. *Polarization of Light*, chapter 5, pages 179–242. John Wiley & Sons, Ltd., London, feb 1997. ISBN: 0471965367.

[9] D. S. Kliger, J. W. Lewis, and C. E. Randall. *Polarized Light in Optics and Spectroscopy*, chapter 3, pages 27–58. Academic Press, Inc., Boston, 1990. ISBN: 0124149758.

[10] S. Chandrasekhar. *Radiative Transfer*, chapter 1, pages 1–53. Dover Books on Physics Series. Dover Publications, New York, 1960. ISBN: 0486605906.

[11] W. A. Shurcliff. *Polarized Light: Production and Use*, chapter 2, pages 15–31. Harvard University Press, Massachusetts, 1966.

[12] E. Collett. *Polarized Light in Fiber Optics*, chapter 5, pages 55–76. SPIE Press/Polawave Group, New Jersey, nov 2004. ISBN: 0819457612.

[13] E. Wolf. Can a light beam be considered to be the sum of a completely polarized and a completely unpolarized beam? *Opt. Lett.*, 33(7):642–644, April 2008.

[14] D. Goldstein. *Polarized Light*, volume 83 of *Optical Engineering*, chapter 12, pages 241–274. Marcel Dekker, Inc., New York, 2 edition, 2003. ISBN: 082474053X.

[15] E. Collett. *Polarized Light in Fiber Optics*, chapter 7, pages 115–148. SPIE Press/Polawave Group, New Jersey, nov 2004. ISBN: 0819457612.

[16] P. Hernday. *Fiber Optic Test and Measurement*, chapter 6, pages 220–245. Prentice Hall, Inc., New Jersey, 1998. ISBN: 0135343305.

[17] R. J. Espejo and S. D. Dyer. Transverse-stress fiber Bragg grating sensor with high spatial resolution and temperature stability. *J. Lightwave Technol.*, 25(7):1777–1785, July 2007.

[18] S. Pancharatnam. Generalized theory of interference, and its applications, Part I. Coherent pencils. *P. Indian Acad. Sci. A*, 44:247–262, 1956. 10.1007/BF03046050.

[19] C. Brosseau. *Fundamentals of Polarized Light: A Statistical Optics Approach*, chapter 3.2, pages 123–137. John Wiley & Sons, Inc., New York, 1998. ISBN: 0471143022.

[20] P. Kurzynowski, W. A. Woźniak, and M. Szarycz. Geometric phase: two triangles on the Poincaré sphere. *J. Opt. Soc. Am. A*, 28(3):475–482, March 2011.

[21] P. D. C. Hobbs. *Building Electro–Optical Systems*, chapter 6, pages 208–232. John Wiley & Sons, Inc., Hoboken, New Jersey, 2nd edition, 2009. ISBN: 9780470402290.

[22] P. Hariharan. *The geometric phase*, volume 48 of *Progress in Optics*, chapter 4. Elsevier, Amsterdam, 2005. ISBN: 9780444520388.

[23] A. Tomita and R. Y. Chiao. Observation of Berry's topological phase by use of an optical fiber. *Phys. Rev. Lett.*, 57(8):937–940, August 1986.

[24] S. G. Lipson, H. Lipson, and D. S. Tannhauser. *Optical Physics*, chapter 9, pages 220–262. Cambridge University Press, Cambridge, 3rd edition, 1995. ISBN: 0521436311.

[25] J. Courtial. Wave plates and the Pancharatnam phase. *Opt. Commun.*, 171(4-6):179–183, 1999.

[26] W. A. Shurcliff. *Polarized Light: Production and Use*, chapter 8, pages 109–123. Harvard University Press, Massachusetts, 1966.

[27] C. Brosseau. *Fundamentals of Polarized Light: A Statistical Optics Approach*, chapter 4.1, pages 181–243. John Wiley & Sons, Inc., New York, 1998. ISBN: 0471143022.

[28] D. Goldstein. *Polarized Light*, volume 83 of *Optical Engineering*, chapter 11, pages 211–240. Marcel Dekker, Inc., New York, 2 edition, 2003. ISBN: 082474053X.

[29] R. C. Jones. A new calculus for the treatment of optical systems. I. Description and discussion of the calculus. *J. Opt. Soc. Am.*, 31(7):488–493, 1941.

[30] H. Hurwitz Jr. and R. C. Jones. A new calculus for the treatment of optical systems. II. Proof of three general equivalence theorems. *J. Opt. Soc. Am.*, 31(7):493–495, 1941.

[31] R. C. Jones. A new calculus for the treatment of optical systems. III. The Sohncke theory of optical activity. *J. Opt. Soc. Am.*, 31(7):500–503, 1941.

[32] R. C. Jones. A new calculus for the treatment of optical systems. IV. *J. Opt. Soc. Am.*, 32(8):486–493, 1942.

[33] R. C. Jones. A new calculus for the treatment of optical systems V. A more general formulation, and description of another calculus. *J. Opt. Soc. Am.*, 37(2):107, 1947.

[34] R. C. Jones. A new calculus for the treatment of optical systems VI. Experimental determination of the matrix. *J. Opt. Soc. Am.*, 37(2):110, 1947.

[35] R. C. Jones. A new calculus for the treatment of optical systems. VII. Properties of the N-matrices. *J. Opt. Soc. Am.*, 38(8):671–683, 1948.

[36] R. C. Jones. New calculus for the treatment of optical systems. VIII. Electromagnetic theory. *J. Opt. Soc. Am.*, 46(2):126–131, 1956.

[37] E. Hecht. *Optics*, chapter 8, pages 270–332. Addison-Wesley Publishing Company, Inc., Reading, Massachusetts, 2nd edition, 1987.

Appendix F

Electromagnetic waves in optical fibres

F.1 Total internal reflection

Geometric reflection and refraction occur in the same plane. Geometric refraction is described by Snell's law,

$$n_1 \sin\theta_1 = n_2 \sin\theta_2 \tag{F.1}$$

where n_1, n_2 and θ_1, θ_2 are the refractive index and angle of propagation for media 1 and 2 in the plane defined by θ_1, θ_2, respectively. Snell's law is derived from the continuity of the phase velocity at the interface between the media [3].

For $n_2 > n_1$, the *critical angle*, θ_c, is defined, for a ray direction from medium 2 to medium 1, as $\sin\theta_1 = 1$. Equation (F.1) is then

$$n_2 \sin\theta_c = n_1 \tag{F.2}$$

For $\theta_2 > \theta_c$, the geometrical refracted ray is reflected back into medium 2. This is termed *total internal reflection*, TIR.

The geometric TIR from the ray approach does not describe the longitudinal and lateral shifts of the totally internally reflected beam, which is due to the evanescent wave "tunnelling" through medium 1. Wave theory is required for a full description of the longitudinal shift, which occurs only for linearly polarised light, and is termed the *Goos–Hänchen* effect [1,4,5]. The lateral shift, which occurs for all other SOPs, but is largest for circularly polarised light, is termed the *Imbert–Fedorov effect* [1, 2,6–8]. The Imbert–Fedorov shift is typically an order of magnitude less than the

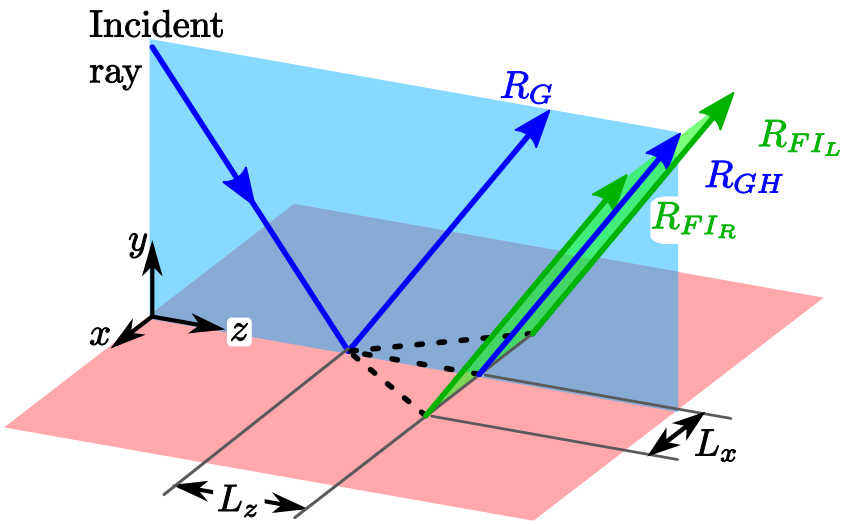

Figure F.1: Total internal reflection with the geometric reflection, R_G; Goos–Hänchen shifted reflection, R_{GH}; and Imbert–Fedorov shifted reflection, R_{FI_L} and R_{FI_R}, for right and left circular polarisation, respectively. After figure 1.7 of [1] and figure 1 of [2].

Goos–Hänchen shift. The beam that is reflected is the superposition of the geometric and shifted beam components [9]. The largest beam shifts occur when the phase–matching condition between the geometric and shift beams is met.

In developing the theory of guided radiation, electromagnetic radiation is typically launched into an optical fibre, as opposed to originating there, i.e. there are no sources. In an optical fibre medium 2 is termed *the core*, and medium 1 *the cladding*. The normalised difference between the refractive indices of the core and cladding, $\underline{n}_{co}$ and $\underline{n}_{cl}$, is

$$\Delta\underline{n} = \frac{\underline{n}_{co} - \underline{n}_{cl}}{\underline{n}_{cl}} \tag{F.3}$$

and is usually described as a percentage. For SMF-28 fibre, $|\Delta n| = 0.36\%$[1], and in general is $< 1\%$. [3]

The critical angle within the fibre limits the range of angles that may be launched into the fibre. The refractive index of the medium external to the fibre is n_0, so the acceptance angle, ϕ_c, is given by

$$\underline{n}_0 \sin\phi_c = \underline{n}_{co} \sin(\frac{\pi}{2} - \theta_c) \tag{F.4}$$

[1]From *Corning SMF-28e optical fiber product information*, Corning Inc. (http://www.corning.com/assets/0/433/573/583/09573389-147D-4CBC-B55F-18C817D5F800.pdf).

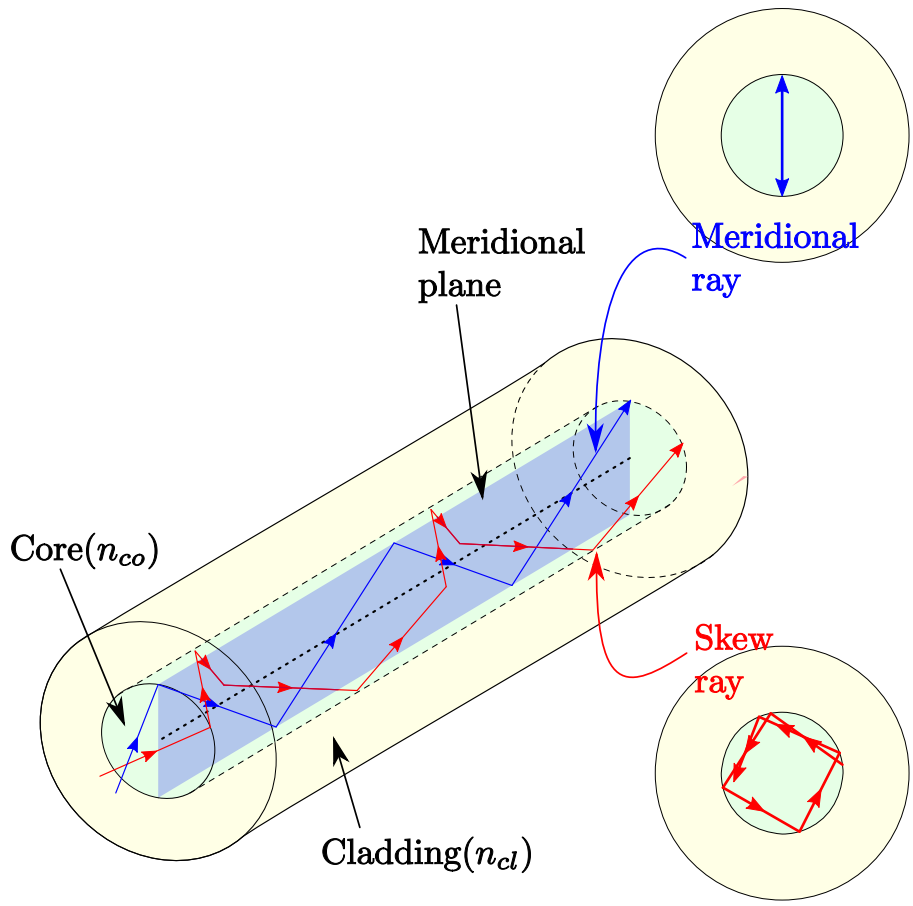

Figure F.2: Ray diagram of meridional ray and skew ray.

which, combined with equation (F.2) gives

$$\mathrm{NA} = \underline{n}_0 \sin\phi_c = \sqrt{\underline{n}_1^2 - \underline{n}_2^2} \tag{F.5}$$

where $\underline{n}_0 \sin\phi_c$ is termed the *numerical aperture*[2], NA, of the fibre [11].

F.2 Electromagnetic wave propagation in fibres

Cylindrical geometry is used to describe electromagnetic wave propagation in an optical fibre. The refractive index, $\underline{n} = n(r)$, is presumed to be independent of ϕ or z. A step index is presumed[3], as in SMF-28[4],

[2]Or, more precisely, the *meridional numerical aperture* [10]. Skew numerical aperture is slightly larger.

[3]Due to the different dispersion characteristics of the doped core and 'pure' cladding, *profile dispersion* will arise [12].

[4]From *Corning SMF-28e optical fiber product information*, Corning Inc. (http://www.corning.com/assets/0/433/573/583/09573389-147D-4CBC-B55F-18C817D5F800.pdf).

$$\underline{n} = \begin{cases} \underline{n}_{co} & 0 \leq \underline{\mathbf{r}} \leq \underline{\mathbf{r}}_{co} \\ \underline{n}_{cl} & \underline{\mathbf{r}} > \underline{\mathbf{r}}_{co} \end{cases} \tag{F.6}$$

where $\underline{\mathbf{r}}_{co}$ is the core radius. The fibre is also presumed to be homogeneous and free of electromagnetic sources, i.e. $\underline{\mathbf{B}} = \underline{\underline{\boldsymbol{\mu}}}_0 \, \underline{\mathbf{H}} = \mu_0 \underline{\mathbf{H}}$ and $\underline{\mathbf{D}} \equiv \varepsilon_0 \underline{n}^2 \underline{\mathbf{E}}$ [5].

The plane wave electromagnetic phasors [13–16], in cylindrical co–ordinates and propagating in the $+z$ direction with propagation constant $\underline{\boldsymbol{\beta}}(z)$ [6], may be separated into longitudinal and transverse components as [13]

$$\begin{Bmatrix} \underline{\mathbf{E}}(\underline{\mathbf{r}}, z) \\ \underline{\mathbf{H}}(\underline{\mathbf{r}}, z) \end{Bmatrix} = \left(\begin{Bmatrix} \underline{\mathbf{E}}_t(\underline{\mathbf{r}}) \\ \underline{\mathbf{H}}_t(\underline{\mathbf{r}}) \end{Bmatrix} + \begin{Bmatrix} E_z(\underline{\mathbf{r}})\underline{\hat{\mathbf{z}}} \\ H_z(\underline{\mathbf{r}})\underline{\hat{\mathbf{z}}} \end{Bmatrix} \right) e^{-i\underline{\boldsymbol{\beta}} z} \tag{F.7}$$

where $\underline{\mathbf{r}} = (r, \phi)$ and $\underline{\hat{\mathbf{z}}}$ is the unit vector in the z–direction.

When substituted into equation (A.8) (page V.II A-3) [13, 14, 16]

$$\frac{\partial^2}{\partial r^2} \begin{Bmatrix} \underline{\mathbf{E}}_t(\underline{\mathbf{r}}) \\ \underline{\mathbf{H}}_t(\underline{\mathbf{r}}) \end{Bmatrix} + \frac{1}{r}\frac{\partial}{\partial r} \begin{Bmatrix} \underline{\mathbf{E}}_t(\underline{\mathbf{r}}) \\ \underline{\mathbf{H}}_t(\underline{\mathbf{r}}) \end{Bmatrix} + \frac{1}{r^2}\frac{\partial^2}{\partial \phi^2} \begin{Bmatrix} \underline{\mathbf{E}}_t(\underline{\mathbf{r}}) \\ \underline{\mathbf{H}}_t(\underline{\mathbf{r}}) \end{Bmatrix} + \left[\underline{\mathbf{k}}^2 \underline{n}(r)^2 - \underline{\boldsymbol{\beta}}^2\right] \begin{Bmatrix} \underline{\mathbf{E}}_t(\underline{\mathbf{r}}) \\ \underline{\mathbf{H}}_t(\underline{\mathbf{r}}) \end{Bmatrix} = 0 \tag{F.8}$$

The solutions in the three co–ordinates are not independent, with $\underline{\mathbf{r}}$ depending upon z. The transverse electromagnetic equations are related to E_z and H_z as [14,17]

$$E_r = -\frac{i}{\underline{\mathbf{p}}(r)} \left(\underline{\boldsymbol{\beta}} \frac{\partial E_z}{\partial r} + \frac{\omega \mu_0}{r} \frac{\partial H_z}{\partial \phi} \right) \tag{F.9a}$$

$$E_\phi = -\frac{i}{\underline{\mathbf{p}}(r)} \left(-\omega \mu_0 \frac{\partial H_z}{\partial r} + \frac{\underline{\boldsymbol{\beta}}}{r} \frac{\partial E_z}{\partial \phi} \right) \tag{F.9b}$$

$$H_r = -\frac{i}{\underline{\mathbf{p}}(r)} \left(\underline{\boldsymbol{\beta}} \frac{\partial H_z}{\partial r} - \frac{\omega \varepsilon_0 \underline{n}(r)^2}{r} \frac{\partial E_z}{\partial \phi} \right) \tag{F.9c}$$

$$H_\phi = -\frac{i}{\underline{\mathbf{p}}(r)} \left(\omega \varepsilon_0 \underline{n}(r)^2 \frac{\partial E_z}{\partial r} + \frac{\underline{\boldsymbol{\beta}}}{r} \frac{\partial H_z}{\partial \phi} \right) \tag{F.9d}$$

where [14, 16]

$$\underline{\mathbf{p}}^2(r) = \underline{\boldsymbol{\beta}}^2 - \underline{\mathbf{k}}^2 \underline{n}(r)^2 \tag{F.10}$$

Using a periodic azimuthal, ϕ, dependency of the propagating fields [16, 17][7]:

$$\begin{Bmatrix} \underline{\mathbf{E}}_\phi \\ \underline{\mathbf{H}}_\phi \end{Bmatrix} E_\phi = e^{\pm i(l\phi + \psi)} \tag{F.11}$$

[5] The fibre is presumed to be magnetically isotropic, with possible electrical anisotropy.
[6] The wave's phase velocity is $\underline{v} = \frac{\omega}{\underline{\boldsymbol{\beta}}}$ [16].
[7] Or, equivalently, by using $\cos(l\phi + \psi)$ or $\sin(l\phi + \psi)$ [17].

where ψ denotes the phase and $l = 0, \pm 1, \pm 2, \ldots; l \in \mathbb{Z}$ [17], gives the wave solution

$$\begin{Bmatrix} \underline{\mathbf{E}} \\ \underline{\mathbf{H}} \end{Bmatrix} (r, \phi, z) = \begin{Bmatrix} E_r \\ H_r \end{Bmatrix} e^{il\phi} e^{-i\beta_z z} \tag{F.12}$$

with which equation (F.8) reduces to [16, 17]:

$$\frac{\partial^2}{\partial r^2} \begin{Bmatrix} E_r \\ H_r \end{Bmatrix} + \frac{1}{r} \frac{\partial}{\partial r} \begin{Bmatrix} E_r \\ H_r \end{Bmatrix} + \left(\underline{\mathbf{q}}^2(r) - \frac{l^2}{r^2} \right) \begin{Bmatrix} E_r \\ H_r \end{Bmatrix} = 0 \tag{F.13}$$

where

$$\underline{\mathbf{q}}^2(r) = \underline{\mathbf{k}}^2 \underline{n}(r)^2 - \underline{\boldsymbol{\beta}}^2 \tag{F.14}$$

Equation (F.13) is a *Bessel equation* as its solutions can be expressed as Bessel functions [3, 16–18].

F.3 References

[1] F. de Fornel. *Evanescent Waves: From Newtonian Optics to Atomic Optics*, chapter 1, pages 5–29. Springer-Verlag, Berlin, 2001. ISBN: 3540658459.

[2] F. Pillon, H. Gilles, and S. Girard. Experimental observation of the Imbert-Fedorov transverse displacement after a single total reflection. *Appl. Opt.*, 43(9):1863–1869, March 2004.

[3] R. Hui and M. O'Sullivan. *Fiber Optic Measurement Techniques*, chapter 1, pages 1–128. Academic Press, New York, 2009. ISBN: 0123738652.

[4] K. Iizuka. *Elements of Photonics*, volume 1, chapter 2, pages 110–165. John Wiley & Sons, Inc., New York, 2002. ISBN: 0471839388.

[5] A. Rogers. *Polarization in Optical Fibers*, chapter 1, pages 1–40. Artech House, Inc., Boston, 2008. ISBN: 1580535348.

[6] A. V. Novitsky and L. M. Barkovsky. Total internal reflection of vector Bessel beams: Imbert–Fedorov shift and intensity transformation. *J. Opt. A-Pure Appl. Op.*, 10(7):075006, 2008.

[7] O. Bryngdahl. *Evanescent waves in optical imaging*, volume 11 of *Progress in Optics*, chapter 4, pages 167–221. North–Holland Publishing Co., Amsterdam, 1973.

[8] F. Pillon, H. Gilles, S. Girard, M. Laroche, R. Kaiser, and A. Gazibegovic. Goos-Hänchen and Imbert-Fedorov shifts for leaky guided modes. *J. Opt. Soc. Am. B*, 22(6):1290–1299, June 2005.

[9] T. Tamir and H. L. Bertoni. Lateral displacement of optical beams at multilayered and periodic structures. *J. Opt. Soc. Am.*, 61(10):1397–1413, October 1971.

[10] R. Drougard and R. J. Potter. *Fiber Optics*, chapter 11. Advanced Optical Techniques. North–Holland Publishing Co., Amsterdam, 1967.

[11] K. Iizuka. *Elements of Photonics*, volume 2, chapter 11, pages 692–796. John Wiley & Sons, Inc., New York, 2002. ISBN: 0471408158.

[12] V. A. Henderek. *Foundations of optical fiber technology*, chapter 2, pages 45–84. Optical Fiber Sensor Technology: Fundamentals. Kluwer Academic Publishers, Dordrecht, 2000. ISBN: 0792378520.

[13] R. J. Black and L. Gagnon. *Optical Waveguide Modes: Polarization, Coupling and Symmetry*, chapter 2, pages 19–34. McGraw-Hill Companies, Inc., New York, 2010. ISBN: 0071622969.

[14] S. Huard. *Polarization of Light*, chapter 6, pages 243–296. John Wiley & Sons, Ltd., London, feb 1997. ISBN: 0471965367.

[15] K. Okamoto. *Fundamentals of Optical Waveguides*, chapter 1, pages 1–12. Academic Press, Amsterdam, 2nd edition, 2006. ISBN: 0125250967.

[16] A. Rogers. *Polarization in Optical Fibers*, chapter 2, pages 41–74. Artech House, Inc., Boston, 2008. ISBN: 1580535348.

[17] K. Okamoto. *Fundamentals of Optical Waveguides*, chapter 3, pages 57–158. Academic Press, Amsterdam, 2nd edition, 2006. ISBN: 0125250967.

[18] F. W. J. Oliver, D. W. Lozier, R. F. Boisvert, and C. W. Clark. *NIST Handbook of Mathematical Functions*, chapter 10, pages 215–286. Cambridge University Press, Cambridge, 1st edition, may 2010. ISBN: 0521140633.

Appendix G

FBG Inscription mechanism

A full understanding of the inscription process has not yet been established [1–4]. The observed dependencies suggest a multi–process or multi–parameter process which must incorporate different sufficient, but not required, techniques to generate the refractive index change [1,3]. Two processes that are expected to make significant contributions to the refractive index change are [2, 3, 5, 6]:

- GeO colour centre [7] defects, where a Ge atom is co–ordinated with another Ge or Si atom, which produces the 240 nm absorption peak[1];
- Structural rearrangement of the glass network/matrix, increasing densification (i.e. it becomes more crystalline–like) [8, 9]. Pre–straining the fibre prior to inscription improves the inscription process and the final refractive index [10]. For hydrogenated SMF-28 FBGs inscribed by 264 nm irradiation, no compaction was observed. The same fibres without hydrogenation exhibited compaction [11].

Other processes have been suggested building upon these [5]. Frequently used inscription sources are KrF (at 248 nm) and ArF (at 193 nm) excimer[2] lasers. These lasers use a single–photon process and can inscribe FBGs with a positive $\Delta n \sim 10^{-5}$ to 10^{-4} in Ge–doped SMF [5].

Continuous wave irradiation requires stability of the inscription system of the order of minutes, for both interferometric and phase mask techniques. Pulsed inscription requires stability times equal to the duration of pulses needed for inscription. For single pulse (low–reflectivity) FBGs, the stability time can be of the order of tens of nanoseconds, which can allow the FBGs to be inscribed when the fibre

[1] Photorefractivity is observed in Ge:SiO_2 fibres, but also in Ge free fibres [2, 3, 6].

[2] An *excimer* is an excited dimer, so KrF and ArF strictly form an *exciplex*, or excited complex. However, the term *excimer* is standard for these lasers.

is being drawn [12]. This inscription process can mechanically weaken the fibre by physically damaging the fibre surface, as material is ablated from the outer cladding with the period of the phase mask [13].

Inscription irregularities may arise if the stripped fibre section isn't clean or is damaged after the buffer stripping [12]. The inscription techniques assume a uniform interface and flux, with the modulation arising from the interference only. When the fibre is not clean or is damaged, the uniformity of the interface and flux are unlikely to be maintained.

G.1 FBG classification

The following categories of FBGs are recognised, dependent upon the inscription energy/ hydrogenation/ material response [14]:

- Type I: Irradiation intensity $100 - 1000\,\mathrm{mJ/cm^2}$ [5]: The initial FBG structure exhibits a monotonic increase in the (positive) refractive index change. The inscription process is related to local electronic defects [5] and compaction [15].

- Type II: Irradiation intensity $> 1\ \mathrm{J/cm^2}$ [3] or $> 0.5\ \mathrm{J/cm^2}$: At high fluence the fibre experiences high–energy–density physical damage by densification, i.e. fusion of the glass matrix [16, 17].

- Type IIa[3]: When a non–hydrogenated fibre is illuminated by the transverse UV flux, a Type I FBG is observed being generated and rises to a maximum reflectivity. As the flux is maintained, the FBG begins to diminish as the minima of the index modulation are filled and the ratio of AC to DC index changes drops. The Type I FBG is eventually erased, and a second FBG is written with reduced core stresses and negative refractive index change, blue–shifted with respect to the Type I FBG [18].

- Type Ia form in hydrogenated fibres only [18–20]. Similar to the Type IIa FBG, a second FBG then appears, with a large red–shift with respect to the Type I FBG [21], with a negative refractive index change.

The narrower the FBG bandwidth, the greater the accuracy with which the wavelength shift can be determined [22]. Narrower bandwidths are achieved with longer gratings (more reflecting planes). The spatial resolution of the sensing element thus has an inverse relationship to the accuracy with which the change at the sensing element can be determined.

[3] Also known as Type III [2].

However, the bandwidth tends to broaden with increasingly greater reflectivity (large refractive index changes), termed flat–top FBGs. Once the central peak reaches saturation, its reflectivity cannot increase. The neighbouring wavelengths then reach saturation and the saturated region broadens. In this case the illuminating signal from this FBG may be fully reflected before the furthest planes are illuminated, reducing the gauge length. This situation can also lead to spectrally distinct FBGs depending upon which side is illuminated.

Typically, the reflected signal spectrum is understood as the integrated reflectivity of all the planes. If only a subset of the planes are addressed, and they are not symmetric with respect to the centre of the FBG, the integrated reflectivities from opposite sides need not result in identical spectra.

G.2 Perturbations and Coupled–mode approach

G.2.1 Perturbation approach

For many physical problems exact solutions are difficult to obtain due to nonlinearities, inhomogeneities and general boundary conditions [23]. Approximate solutions can be obtained by numerical approaches (e.g finite element methods) or analytical approaches (e.g. perturbation methods).

A *nondimentionalised*[4] variable is frequently the best to use in these approaches. This allows the magnitude of the expanded components to be determined in terms of the physical problem, indicating which terms can be ignored as their magnitude is negligible compared to other terms.

In general, a problem involving the function $u(x, \zeta)$, represented mathematically by the differential equation $L(u, x, \zeta) = 0$ and the boundary condition $B(u, \zeta) = 0$, does not have an exact solution [24]. x is an independent variable and ζ is a parameter.

However, an approximate solution may be obtained using perturbation methods if there exists an $\zeta = \zeta_0$ for which a solution can be obtained. The approximate solution may be sought by expanding ζ, usually in the binomial or Taylor expansion [23], and retaining the first few terms.

Expanding in powers of ζ

$$u(x, \zeta) = u_0(x) + \zeta u_1(x) + \zeta^2 u_2(x) + \dots \tag{G.1}$$

where u_n is independent of ζ and $u_0(x)$ is the solution for $\zeta = 0$.

[4]Nondimentionalisation is achieved by dividing the variable(s) by a characteristic quantity of the same dimension [23].

As an example of the perturbation method, the refractive index modulation in an FBG is modelled as a perturbation of the refractive index in an unmodified fibre core, $\underline{n}_{co}$. Although the change in refractive index, $\Delta\underline{n}_{co}$, is larger than for those causing Rayleigh scattering, the changes are, at their largest, of the order of 10^{-2} for an FBG, and more typically $10^{-5} - 10^{-3}$. Following [6], let $u = \underline{\mathbf{P}}$, $x = \underline{\mathbf{E}}_{\text{app}}$, $\zeta = \underline{\underline{\boldsymbol{\chi}}}_e$, and using equation (A.4a) (page V.II A-2),

$$\underline{\mathbf{P}} = \left(\underline{\underline{\boldsymbol{\epsilon}}}_0\, \underline{\underline{\boldsymbol{\chi}}}_e \underline{\mathbf{E}}_{\text{app}}\right) + \underline{\mathbf{P}}_0 \qquad \text{(A.4a)}$$

which is expanded, in powers of the applied electric field $\underline{\mathbf{E}}_{\text{app}}$, to give [6, 25, 26],

$$\underline{\mathbf{P}} = \underline{\underline{\boldsymbol{\epsilon}}}_0 \left[\underline{\underline{\boldsymbol{\chi}}}_e^{(1)} \underline{\mathbf{E}}_{\text{app}} + \underline{\underline{\underline{\boldsymbol{\chi}}}}_e^{(2)} \underline{\mathbf{E}}^*_{\text{app}} \underline{\mathbf{E}}_{\text{app}} + \underline{\underline{\underline{\underline{\boldsymbol{\chi}}}}}_e^{(3)} (\underline{\mathbf{E}}^*_{\text{app}} \underline{\mathbf{E}}_{\text{app}})^* \underline{\mathbf{E}}_{\text{app}} + \ldots\right] + \underline{\mathbf{P}}_0 \qquad \text{(G.2)}$$

where (m) in $\boldsymbol{\chi}_e^{(m)}$ is the mth order (non)linear susceptibility [27]. The linear (first order) term returns equation (A.5a)[5] (page V.II A-2).

For fused silica the intrinsic polarisation, $\underline{\mathbf{P}}_0 = 0$, so, grouping the higher order terms in equation (G.2) and inserting and rearranging equation (A.5a) (page V.II A-2), gives

$$\begin{aligned}
\underline{\underline{\boldsymbol{\epsilon}}}_{\text{total}} &= \frac{\underline{\mathbf{D}}}{\underline{\underline{\boldsymbol{\epsilon}}}_0 \underline{\mathbf{E}}_{\text{app}}} = \underline{\underline{\boldsymbol{\epsilon}}}_r + \underline{\underline{\underline{\boldsymbol{\chi}}}}_e^{(2)} \underline{\mathbf{E}}_{\text{app}} + \underline{\underline{\underline{\underline{\boldsymbol{\chi}}}}}_e^{(3)} \underline{\mathbf{E}}^*_{\text{app}} \underline{\mathbf{E}}_{\text{app}} + \ldots \\
&= \underline{\underline{\boldsymbol{\epsilon}}}_r + \Delta\underline{\underline{\boldsymbol{\epsilon}}} \\
&= \underline{\underline{n}}^2_{\text{eff}} \qquad \ldots \text{from equation (A.12)} \\
&= \left(\underline{\underline{n}}_{co} + \Delta\underline{\underline{n}}_{co}\right)^2 \\
&\approx \underline{n}^2_{co} + 2\underline{n}_{co}\Delta\underline{n}_{co}
\end{aligned} \qquad \text{(G.3)}$$

where the anisotropic refractive index is described by a vector and $(\Delta\underline{n}_{co})^2 \ll 1$ [6]. Rearranging (G.3) in terms of $\Delta\underline{n}_{co}$ gives (equation (2.101) (page V.I - 66))

$$\Delta\underline{n}_{co} = \frac{1}{2\underline{n}_{co}} \left[\underline{\underline{\underline{\boldsymbol{\chi}}}}_e^{(2)} \underline{\mathbf{E}}_{\text{app}} + \underline{\underline{\underline{\underline{\boldsymbol{\chi}}}}}_e^{(3)} \underline{\mathbf{E}}^*_{\text{app}} \underline{\mathbf{E}}_{\text{app}} + \ldots\right] \qquad \text{(G.4)}$$

The second order term, $\underline{\underline{\underline{\boldsymbol{\chi}}}}_e^{(2)}$, describes *photorefractivity*, which is typically zero in amorphous materials. The third order terms, $\underline{\underline{\underline{\underline{\boldsymbol{\chi}}}}}_e^{(3)}$, are found in all Curie groups [28]. $\underline{\underline{\underline{\underline{\boldsymbol{\chi}}}}}_e^{(3)}$ is not large, $\sim 10^{-7}$, and so does not produce the larger refractive index changes observed in FBGs, $\sim 10^{-3}$.

Thus, the approximate solution is simplified. The terms of the expansion that need to be retained for a given physical problem can be selected, with the remaining

[5] The linear relationships used in the Heckmann diagram, figure 2.6 (page V.I - 33), are similarly obtained.

terms omitted. For fibres, perturbation methods are used to describe Rayleigh scattering and weakly guided approximation anisotropy [29] in terms of thermodynamic density fluctuations in the core and to model the mode coupling components such as couplers and FBGs [30].

G.2.2 Coupled–mode approach

The coupled–mode approach to understanding the operation of the FBG [30–33] describes the FBG as a perturbation of the refractive index [30,34]. The longitudinal, z–axis, refractive index profile of the fibre containing the FBG is described as [32]

$$\underline{n}_{\text{eff}}(z) = \begin{cases} \underline{n}_{co} + \Delta\underline{n}\cos\left(\frac{2\pi z}{\Lambda} + \varphi(z)\right) & \ldots\text{within FBG} \\ \underline{n}_{co} & \ldots\text{outside FBG} \end{cases} \tag{G.5}$$

where $\underline{n}_{co}$ is the core refractive index outside the FBG, $\Delta\underline{n}$ is the amplitude of the index modulation, Λ is the period of the modulation, as in figure 2.18 (page V.I - 62)(c), and $\varphi(z)$ is possible chirping of Λ. The region outside the FBG is assumed to be described as per section §F.2 (page V.II F-3), i.e. the perturbation is confined to the FBG.

Coupled–mode theory uses combinations of the unperturbed modes of section §F.2 (page V.II F-3) as the basis to describe the modes in perturbed region; hence the name. The solution to the wave cylindrical equation (F.8) (page V.II F-4) within the FBG, using the weakly guiding approximation, is a linear superposition of the expanded m transverse core modes described in equation (F.7) (page V.II F-4) [31, 32, 35]:

$$\begin{Bmatrix} \underline{\mathbf{E}}_{\text{FBG}}(\underline{\mathbf{r}}, z) \\ \underline{\mathbf{H}}_{\text{FBG}}(\underline{\mathbf{r}}, z) \end{Bmatrix} = \sum_{m=1}^{N} \begin{Bmatrix} (A_m + B_m)\,\underline{\mathbf{E}}(\underline{\mathbf{r}}, z) \\ (C_m + D_m)\,\underline{\mathbf{H}}(\underline{\mathbf{r}}, z) \end{Bmatrix} e^{-i\underline{\boldsymbol{\beta}}_m z} \tag{G.6}$$

where N is the number of modes supported by the fibre, A_m, C_m and B_m, D_m are the mode amplitudes for the forward, $+z$, and backward, $-z$ propagating modes, for $\underline{\mathbf{E}}_{\text{FBG}}$,$\underline{\mathbf{H}}_{\text{FBG}}$, respectively.

Directional fibre couplers may be described using the same theoretical approach, but the number of modes in the region of overlap of their cores will not necessarily be 1. Instead of reversing direction, the mode amplitudes of the forward propagating coupled–modes determine the eventual ratio of $\underline{\mathbf{E}}$ and $\underline{\mathbf{H}}$ in the output fibres of the coupler.

B_m and D_m are assumed to vary slowly with respect to the wavelength of inter-

est[6], λ_B [31, 32, 35]. The coupling of the modes along z evolves as

$$\frac{d}{dz}\begin{Bmatrix} A_m \\ C_m \end{Bmatrix} = i\sum_{q=1}^{N}\begin{Bmatrix} A_Q \\ C_Q \end{Bmatrix}\left(C^t_{qm}+C^z_{qm}\right)e^{i(\underline{\boldsymbol{\beta}}_q-\underline{\boldsymbol{\beta}}_m)z} + i\sum_{q=1}^{N}\begin{Bmatrix} B_Q \\ D_Q \end{Bmatrix}\left(C^t_{qm}-C^z_{qm}\right)e^{-i(\underline{\boldsymbol{\beta}}_q+\underline{\boldsymbol{\beta}}_m)z} \tag{G.7a}$$

$$\frac{d}{dz}\begin{Bmatrix} B_m \\ D_m \end{Bmatrix} = -i\sum_{q=1}^{N}\begin{Bmatrix} A_Q \\ C_Q \end{Bmatrix}\left(C^t_{qm}-C^z_{qm}\right)e^{i(\underline{\boldsymbol{\beta}}_q+\underline{\boldsymbol{\beta}}_m)z} - i\sum_{q=1}^{N}\begin{Bmatrix} B_Q \\ D_Q \end{Bmatrix}\left(C^t_{qm}+C^z_{qm}\right)e^{-i(\underline{\boldsymbol{\beta}}_q-\underline{\boldsymbol{\beta}}_m)z} \tag{G.7b}$$

where C^t_{qm} and C^z_{qm} are the transverse and longitudinal coupling coefficients [32],

$$C^t_{qm}(z) = \frac{\omega}{4}\iint_{-\infty}^{\infty}\Delta\underline{\underline{\boldsymbol{\epsilon}}}(\underline{\mathbf{r}},z)\begin{Bmatrix} \underline{\mathbf{E}}^*_{\mathrm{FBG}\,Q}(\underline{\mathbf{r}}) \\ \underline{\mathbf{H}}^*_{\mathrm{FBG}\,Q}(\underline{\mathbf{r}}) \end{Bmatrix}\bullet\begin{Bmatrix} \underline{\mathbf{E}}_{\mathrm{FBG}_m}(\underline{\mathbf{r}}) \\ \underline{\mathbf{H}}_{\mathrm{FBG}_m}(\underline{\mathbf{r}}) \end{Bmatrix}dxdy \tag{G.8}$$

where $\Delta\underline{\underline{\boldsymbol{\epsilon}}} \approx 2\underline{n}_{co}\Delta\underline{n}; \Delta\underline{n} \ll \underline{n}_{co}$. C^z_{qm} is defined similarly to $C^t_{qm}(z)$ but is typically neglected as $C^z_{qm} \ll C^t_{qm}$.

Taking an isotropic FBG profile, with no modulation in the cladding, the core index can be described by defining two coefficients [32]

$$\sigma_{\mathrm{CM}_{mq}}(z) = \frac{\omega\underline{n}_{\mathrm{eff}}}{2}\overline{\Delta\underline{n}}_{\mathrm{eff}}(z)\iint_{core}\begin{Bmatrix} \underline{\mathbf{E}}^*_{\mathrm{FBG}\,Q}(\underline{\mathbf{r}}) \\ \underline{\mathbf{H}}^*_{\mathrm{FBG}\,Q}(\underline{\mathbf{r}}) \end{Bmatrix}\bullet\begin{Bmatrix} \underline{\mathbf{E}}_{\mathrm{FBG}_m}(\underline{\mathbf{r}}) \\ \underline{\mathbf{H}}_{\mathrm{FBG}_m}(\underline{\mathbf{r}}) \end{Bmatrix}dxdy \tag{G.9a}$$

$$\kappa_{\mathrm{CM}_{mq}}(z) = \frac{\mathcal{V}_{UV}}{2}\sigma_{\mathrm{CM}_{mq}}(z) \tag{G.9b}$$

where $\overline{\Delta\underline{n}}_{\mathrm{eff}}(z)$ is the averaged, "DC", index change over Λ, $\sigma_{\mathrm{CM}_{mq}}(z)$ describes the averaged, "DC", coupling coefficient and $\kappa_{\mathrm{CM}_{mq}}(z)$ is the oscillating, "AC", coupling coefficient. Where $\sigma_{\mathrm{CM}_{11}}(z) \neq \sigma_{\mathrm{CM}_{22}}(z)$, the modes exhibit a relative detuning or removal of degeneracy and polarisation dependent coupling arises. The components $\sigma_{\mathrm{CM}_{12}}(z)$ and $\sigma_{\mathrm{CM}_{21}}(z)$[7] describes the mutual coupling of these non–degenerate modes, resulting in the exchange of power between polarisations [36].

Equation (G.8) can then be rewritten in terms of $\sigma_{\mathrm{CM}_{mq}}(z)$ and $\kappa_{\mathrm{CM}_{mq}}(z)$ as

$$C^t_{qm}(z) = \sigma_{\mathrm{CM}_{mq}}(z) + 2\kappa_{\mathrm{CM}_{mq}}(z)\cos\left(\frac{2\pi z}{\Lambda}+\varphi(z)\right) \tag{G.10}$$

For an FBG, where the forward single–mode is coupled into the identical counter–

[6] And all wavelengths close to λ_B.

[7] In the absence of absorption, $\sigma_{\mathrm{CM}_{12}}(z) = \sigma^*_{\mathrm{CM}_{21}}(z)$ [36].

propagating single–mode, equations (G.7) reduce to [32]

$$\frac{d}{dz}R = i\sigma_{\text{FBG}}R(z) + i\kappa_{\text{CM}}S(z) \tag{G.11a}$$

$$\frac{d}{dz}S = -i\sigma_{\text{FBG}}S(z) - i\kappa_{\text{CM}}{}^{*}R(z) \tag{G.11b}$$

where R and S are

$$R(z) \equiv A(z)e^{i\delta\lambda_{\text{CM}}z-\frac{\phi}{2}} \tag{G.12a}$$

$$S(z) \equiv B(z)e^{-i\delta\lambda_{\text{CM}}z+\frac{\phi}{2}} \tag{G.12b}$$

where σ_{FBG} is a general "DC" self–coupling coefficient [32]

$$\sigma_{\text{FBG}} \equiv \delta\lambda_{\text{CM}}(z) + \sigma_{\text{CM}} - \frac{1}{2}\frac{d\phi}{dz} \tag{G.13}$$

and the *detuning*[8] $\delta\lambda_{\text{CM}}$ is given by

$$\delta\lambda_{\text{CM}} \equiv \beta - \frac{\pi}{\Lambda} = 2\pi\underline{n}_{\text{eff}}\left(\frac{1}{\lambda} - \frac{1}{\lambda_B}\right) \tag{G.14}$$

$\frac{d\phi}{dz}$ describes possible chirping of the FBG.

For single–mode FBGs, $\sigma_{\text{CM}}$and κ_{CM} take the form

$$\sigma_{\text{CM}} = \frac{2\pi}{\lambda}\overline{\Delta\underline{n}}_{\text{eff}} \tag{G.15a}$$

$$\text{and } \kappa_{\text{CM}} = \kappa_{\text{CM}}{}^{*} = \frac{\pi}{\lambda}\mathcal{V}_{UV}\overline{\Delta\underline{n}}_{\text{eff}} \tag{G.15b}$$

For uniform FBGs, without a chirp, σ_{CM}, σ_{FBG} and κ_{CM} are constants.

The reflectivity of the FBG is given as [22, 32, 37]

$$\mathcal{R}_{\text{FBG}} = \tanh^2\left(\kappa_{\text{CM}}L_{\text{FBG}}\right) \approx \tanh^2\left(\pi\underline{n}_{\text{eff}}\frac{L_{\text{FBG}}}{\lambda_B}\mathcal{V}_{UV}\eta_{\text{FBG}}(V)\right) \tag{G.16}$$

where $\eta_{\text{FBG}}(V)$ is the fraction of integrated fundamental mode intensity contained in the core and V is the normalised frequency defined in equation (2.29) (page V.I - 24). Explicitly, the reflectivity is proportional to the length of the FBG and the strength of the index modulation.

Refractive index changes of 0.02 in FBGs have been reported [38]. A sharp subpeak on the short wavelength side is observed for strongly reflecting FBGs [39][9].

[8] The deviation from Bragg condition [2].

[9] In non–linear cases, a Kerr effect induced modulation instability can produce resonances to the sides of the central peak [40, 41]. The conditions described in this thesis are all in the linear regime.

This arises from self–chirping of $\Delta \underline{n}_{\text{eff}}(z)$, which is absent if the average index change is held constant or adjusted with a second UV exposure [39]. The more strongly reflecting the FBG, the shorter its effective spatial extent[10], as the transmitted signal at λ_B is depleted by reflection [39].

The bandwidth of the FBGs may be described by the full–width at half–maximum[11], FWHM, or by the difference in λ between the first minima on either side of the main peak[12].

The FWHM bandwidth is [22]

$$\delta\lambda_{B\text{FWHM}} = \frac{\delta\lambda}{\lambda_B} = s_{\text{FBG}} \sqrt{\left(\frac{\mathcal{V}_{UV}}{\overline{\underline{n}}_{\text{eff}}}\right)^2 + \left(\frac{1}{N_{\text{FBG}}}\right)^2} \tag{G.17}$$

where N_{FBG} is the number of grating planes and $s_{\text{FBG}} \sim 1$ for strong gratings and ~ 0.5 for weak gratings.

The bandwidth between minima is [32]

$$\delta\lambda_{Bmin} = \frac{\delta\lambda}{\lambda_B} = \frac{\mathcal{V}_{UV}\overline{\Delta \underline{n}}_{\text{eff}}}{\overline{\underline{n}}_{\text{eff}}} \sqrt{1 + \left(\frac{\lambda_B}{\mathcal{V}_{UV}\overline{\Delta \underline{n}}_{\text{eff}} L_{\text{FBG}}}\right)^2} \tag{G.18}$$

Side lobe structure will arise from Fabry–Perót type resonances within the FBG, which are more noticeable in stronger reflectivity FBGs [32].

As the spectral profile of an FBG is a quasi–monochromatic signal with a non–negligible bandwidth, it is represented by an analytic signal, with the phase given by equation (C.13) (page V.II C-3), rather than a monochromatic wave [44–46]. For the spectroscopic instruments used in this work, the FBGs are low–coherence signals, i.e. are broader than the minimum spectral resolution, and are treated as quasi–monochromatic signals.

G.3 References

[1] R. Kashyap. *Fiber Bragg Gratings*, chapter 1, pages 1–12. Academic Press, San Diego, 1999. ISBN: 0124005608.

[2] P. St. J. Russell and J. L. Archambault. *Fiber Gratings*, volume 3 of *Optoelectronics Library*, chapter 2. Artech House, Inc., Boston, 1997. ISBN: 0890069328.

[10] As a sensor, the stronger FBG will have a shorter gauge length. The gauge factor is defined as [42]:

$$K = \left(\frac{\Delta\lambda_B}{X\lambda_B}\right)$$

for quantity X.

[11] Also termed the 3 dB point.

[12] Effectively the coherence length of the reflected FBG signal [43].

[3] K. O. Hill. *Fiber Bragg gratings*, volume 5 of *Handbook of Optics*, chapter 17. McGraw-Hill Companies, Inc., New York, 3 edition, 2010. ISBN: 0071633138.

[4] B. Poumellec and F. Kherbouche. The photorefractive Bragg gratings in the fibers for telecommunications. *J. Phys. III*, 6:1595–1624, December 1996.

[5] A. Othonos and K. Kalli. *Fiber Bragg Gratings : Fundamentals and Applications in Telecommunications and Sensing*, chapter 2, pages 9–94. Optoelectronics Library. Artech House, Inc., Boston, 1999. ISBN: 0890063443.

[6] R. Kashyap. *Fiber Bragg Gratings*, chapter 2, pages 13–54. Academic Press, San Diego, 1999. ISBN: 0124005608.

[7] K. Nassau. *The Physics and Chemistry of Color*, chapter 9, pages 187–204. Wiley Series in Pure and Appl. Opt. Wiley-Interscience, New York, 2nd edition, 2001. ISBN: 0471391069.

[8] B. Poumellec, P. Niay, M. Douay, and J. F. Bayon. The UV-induced refractive index grating in Ge: SiO2 preforms: additional CW experiments and the macroscopic origin of the change in index. *J. Phys. D Appl. Phys.*, 29(7):1842, 1996.

[9] C. Y. Wei, C. C. Ye, S. W. James, P. E. Irving, and R. P. Tatam. AFM observation of surface topography of fibre Bragg gratings fabricated in germanium-boron codoped fibres and hydrogen- loaded fibres. *Opt. Mater.*, 20(4):283–294, 2002.

[10] E. Salik, D. S. Starodubov, and J. Feinberg. Increase of photosensitivity in Ge-doped fibers under strain. *Opt. Lett.*, 25(16):1147–1149, August 2000.

[11] H. G. Limberger, C. Ban, R. P. Salathé, S. A. Slattery, and D. N. Nikogosyan. Absence of UV-induced stress in Bragg gratings recorded by high-intensity 264 nm laser pulses in a hydrogenated standard telecom fiber. *Opt. Express*, 15(9):5610–5615, 2007.

[12] C. G. Askins, M. A. Putnam, G. M. Williams, and E. J. Friebele. Stepped-wavelength optical-fiber Bragg grating arrays fabricated in line on a draw tower. *Opt. Lett.*, 19(2):147–149, January 1994.

[13] C. Y. Wei, C. C. Ye, S. W. James, R. P. Tatam, and P. E. Irving. The influence of hydrogen loading and the fabrication process on the mechanical strength of optical fibre bragg gratings. *Opt. Mater.*, 20(4):241–251, 2002.

[14] D. N. Nikogosyan. Multi-photon high-excitation-energy approach to fibre grating inscription. *Meas. Sci. Technol.*, 18(1):R1–R29, January 2007.

[15] N. H. Ky, H. G. Limberger, R. P. Salath'e, F. Cochet, and L. Dong. UV-irradiation induced stress and index changes during the growth of type-I and type-IIA fiber gratings. *Opt. Commun.*, 225(4-6):313–318, 2003.

[16] R. Kashyap. *Fiber Bragg Gratings*, chapter 3, pages 55–118. Academic Press, San Diego, 1999. ISBN: 0124005608.

[17] A. Othonos and K. Kalli. *Fiber Bragg Gratings : Fundamentals and Applications in Telecommunications and Sensing*, chapter 3, pages 95–147. Optoelectronics Library. Artech House, Inc., Boston, 1999. ISBN: 0890063443.

[18] Y. Liu, J. A. R. Williams, L. Zhang, and I. Bennion. Abnormal spectral evolution of fiber Bragg gratings in hydrogenated fibers. *Opt. Lett.*, 27(8):586–588, April 2002.

[19] K. Kalli, A. G. Simpson, K. Zhou, L. Zhang, D. Birkin, T. Ellingham, and I. Bennion. Spectral modification of type IA fibre Bragg gratings by high-power near-infrared lasers. *Meas. Sci. Technol.*, 17(5):968, 2006.

[20] K. Kalli, A. G. Simpson, K. Zhou, L. Zhang, and I. Bennion. Tailoring the temperature and strain coefficients of Type I and Type IA dual grating sensorsthe impact of hydrogenation conditions. *Meas. Sci. Technol.*, 17(5):949, 2006.

[21] K. Kalli, G. Simpson, K. Zhou, L. Zhang, and I. Bennion. Dependence of type IA FBG growth on inscription intensity. In *Nonlinear Photonics*, page JWA36. Optical Society of America, 2007.

[22] Y. J. Rao. In-fibre Bragg grating sensors. *Meas. Sci. Technol.*, 8(4):355–375, April 1997.

[23] A. H. Nayfeh. *Introduction to Perturbation Techniques*, chapter 1, pages 1–27. Wiley-VCH Verlag GmbH & Co. KGaA, Weinheim, 2004. ISBN: 0471310131.

[24] A. H. Nayfeh. *Perturbation Methods*, chapter 1, pages 1–22. Wiley-VCH Verlag GmbH & Co. KGaA, Weinheim, 2004. ISBN: 0471399175.

[25] L. D. Landau, E. M. Lifshitz, and L. P. Pitaevskii. *Electrodynamics of Continuous Media*, volume 8 of *Course of Theoretical Physics*, chapter 13, pages 372–393. Butterworth-Heinemann, Oxford, 2nd edition, 1984. ISBN: 0750626348.

[26] J.-P. Goure and I. Verrier. *Optical Fibre Devices*, chapter 5, pages 165–220. Optics and Optoelectronics. IOP Publishing Ltd., Bristol, 2002. ISBN: 0750308117.

[27] R. W. Boyd. *Nonlinear Optics*, chapter 1, pages 1–65. Academic Press, 2nd edition, 2003. ISBN: 0121216829.

[28] R. E. Newnham. *Properties of Materials: Anisotropy, Symmetry, Structure*, chapter 29, pages 313–324. Oxford University Press, jan 2005. ISBN: 019852076X.

[29] R. J. Black and L. Gagnon. *Optical Waveguide Modes: Polarization, Coupling and Symmetry*, chapter 2, pages 19–34. McGraw-Hill Companies, Inc., New York, 2010. ISBN: 0071622969.

[30] K. Okamoto. *Fundamentals of Optical Waveguides*, chapter 4, pages 159–208. Academic Press, Amsterdam, 2nd edition, 2006. ISBN: 0125250967.

[31] A. Othonos and K. Kalli. *Fiber Bragg Gratings : Fundamentals and Applications in Telecommunications and Sensing*, chapter 5, pages 189–222. Optoelectronics Library. Artech House, Inc., Boston, 1999. ISBN: 0890063443.

[32] T. Erdogan. Fiber grating spectra. *J. Lightwave Technol.*, 15(8):1277–1294, August 1997.

[33] D. K. W. Lam and B. K. Garside. Characterization of single-mode optical fiber filters. *Appl. Opt.*, 20(3):440, 1981.

[34] A. W. Snyder and J. D. Love. *Optical Waveguide Theory*, chapter 27, pages 542–552. Chapman & Hall, Ltd., London, 1983. ISBN: 0412242508.

[35] R. Kashyap. *Fiber Bragg Gratings*, chapter 4, pages 119–193. Academic Press, San Diego, 1999. ISBN: 0124005608.

[36] R. Ulrich and A. Simon. Polarization optics of twisted single-mode fibers. *Appl. Opt.*, 18(13):2241–2251, July 1979.

[37] P. St. J. Russell, J.-L. Archambault, and L. Reekie. Fibre gratings. *Phys. World*, pages 41–48, October 1993.

[38] E. G. Loewen and E. Popov. *Diffraction Gratings and Applications*, volume 58 of *Optical Engineering*, chapter 9, pages 323–365. Marcel Dekker, Inc., New York, 1997. ISBN: 0824799232.

[39] K. O. Hill and G. Meltz. Fiber Bragg grating technology fundamentals and overview. *J. Lightwave Technol.*, 15(8):1263–1276, August 1997.

[40] C. Martijn de Sterke. Theory of modulational instability in fiber Bragg gratings. *J. Opt. Soc. Am. B*, 15(11):2660–2667, November 1998.

[41] F. K. Abdullaev, S. A. Darmanyan, and J. Garnier. *Modulation instability of electromagnetic waves in inhomogeneous and in discrete media*, volume 44 of *Progress in Optics*, chapter 5. Elsevier, Amsterdam, 2002. ISBN: 0444511482.

[42] R. A. Collacott. *Structural Integrity Monitoring*, chapter 8, pages 286–311. Chapman & Hall Ltd., London, 1985. ISBN: 0412219204.

[43] W. Lauterborn, T. Kurz, and M. Wiesenfeldt. *Coherent Optics: Fundamentals and Applications*, chapter 4, pages 31–57. Springer-Verlag, Berlin, 1995. ISBN: 3540583726.

[44] M. A. Muriel and A. Carballar. Phase reconstruction from reflectivity in uniform fiber Bragg gratings. *Opt. Lett.*, 22(2):93–95, 1997.

[45] D. A. Flavin, R. McBride, and J. D. C. Jones. Short optical path scan interferometric interrogation of a fibre Bragg grating embedded in a composite. *Electron. Lett.*, 33(4):319–321, 1997.

[46] S. D. Dyer, J. D. Kofler, R. J. Espejo, and S. M. Etzel. Stability of fiber Bragg grating wavelength calibration references. In *Bragg Gratings, Photosensitivity, and Poling in Glass Waveguides*, page MD1. Optical Society of America, 2003.

Appendix H

Brief Fourier transform overview

The Fourier transform is an important mathematical tool for the analysis of optical problems. The ubiquitous *Fourier transform*, FT, is of major importance in optics. The FT provides for the decomposition of a spatially or temporally varying real signal, such as that captured by an optical detector, in terms of single frequency sinusoids [1–8]. It provides a representation of the signal in the frequency domain [9].

A complicated signal, not easily amenable to analysis in the temporal or spatial domain, may be significantly easier to analyse in the frequency domain [4, 10]. Generally, a real signal will produce a complex frequency representation.

A simple example of a two–component signal and its Fourier transform is given in figure H.1. The Fourier transform is separated into the real, $\Re$, and imaginary, $\Im$, parts for clarity.

Temporal signals will be used hereafter, but may be replaced by spatial signals, equivalently.

A Fourier transform and its associated inverse Fourier transform are termed a *Fourier transform pair*:

$$F(\nu) = \int_{-\infty}^{\infty} f(t) e^{-i2\pi t\nu} dt \qquad -\infty > t > \infty \tag{H.1a}$$

$$f(t) = \int_{-\infty}^{\infty} F(\nu) e^{i2\pi t\nu} d\nu \qquad -\infty > \nu > \infty \tag{H.1b}$$

Equation (H.1a) is the Fourier transform and equation (H.1b) is the inverse Fourier transform. A signal may then be equivalently described by $F(\nu)$ or $f(t)$, to allow ease of analysis in terms of either frequency, ν, or time, t. In this work the Fourier transform pairing is denoted as

$$F(\nu) \Leftrightarrow f(t) \tag{H.2}$$

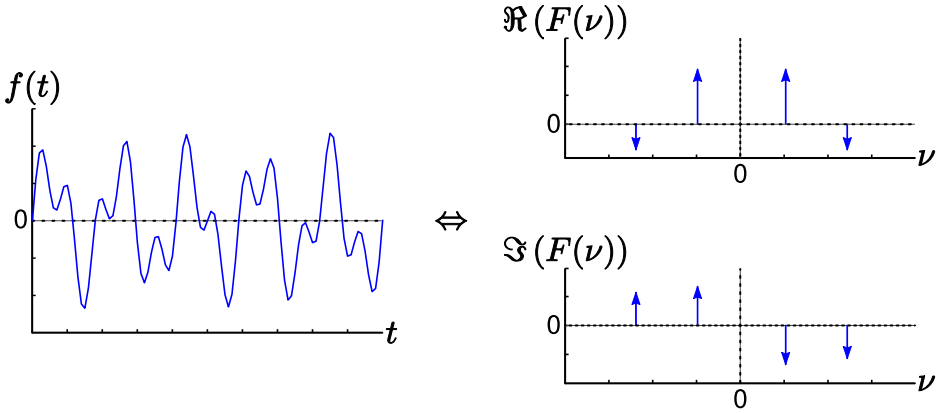

Figure H.1: A Fourier transform pair example. A signal with two frequencies, $f(t)$, is decomposed into the real part, $\Re(F(\nu))$, and imaginary part, $\Im(F(\nu))$.

H.1 Properties

The Fourier transform has several important properties of which many are used in this work. The following discussion follows that laid out by Brigham [11], but incorporates information from [12–17].

Linearity

The linearity of the Fourier transform facilitates the analysis of linear systems using the Fourier transform

$$x(t) + y(t) \Leftrightarrow X(\nu) + Y(\nu) \tag{H.3}$$

as long as $x(t) \Leftrightarrow X(\nu)$ and $y(t) \Leftrightarrow Y(\nu)$. This allows a captured signal with multiple component sub-signals to be analysed.

Symmetry

If $x(t) \Leftrightarrow X(\nu)$ then, by symmetry,

$$X(t) \Leftrightarrow x(-\nu) \tag{H.4}$$

The symmetry property indicates that the application of the Fourier transform is not restricted to a specific domain, e.g. time or space only.

Time– and frequency–scaling

The time– or frequency–scaling property is

$$x(kt) \Leftrightarrow \frac{1}{|k|} X\left(\frac{\nu}{k}\right) \tag{H.5a}$$

$$\frac{1}{|k|} h\left(\frac{t}{k}\right) \Leftrightarrow X(k\nu) \tag{H.5b}$$

This indicates that compressing (expanding) one variable expands (compresses) the other, i.e. as $t \to 0$ then $\nu \to \infty$, and vice versa.

Time– and frequency–shifting

The time– and frequency–shifting property is

$$x(t - t_0) \Leftrightarrow X(\nu) e^{-i2\pi\nu t_0} \tag{H.6a}$$

$$x(t) e^{i2\pi\nu_0 t} \Leftrightarrow X(\nu - \nu_0) \tag{H.6b}$$

By applying an offset to either t or ν, e.g. $t' = t - t_0$ or $\nu' = \nu - \nu_0$, data can be moved with respect to the origin to simplify analysis or manipulation of the data.

Even and odd functions

The function $x_e(t)$ is even if $x_e(t) = x_e(-t)$; then the Fourier transform is an even function and real

$$x_e(t) \Leftrightarrow \Re(\nu) = \int_{-\infty}^{\infty} x_e(t) \cos(2\pi\nu t)\, dt \tag{H.7}$$

The function $x_o(t)$ is odd if $x_o(t) = -x_o(-t)$; then the Fourier transform is odd and imaginary

$$x_o(t) \Leftrightarrow i\Im(\nu) = -i \int_{-\infty}^{\infty} x_o(t) \sin(2\pi\nu t)\, dt \tag{H.8}$$

Convolution

A very important property is that of convolution [18, 19], denoted by '$*$'. Convolution is the process by which the windowing of data is explained, both in terms of the finiteness of an interferogram[1] and the application of 'corrective' windows, as discussed in appendix section P.2 (page V.II P-3) in terms of the signal processing for the experimental chapters.

The convolution property is defined as

$$z(t) = \int_{-\infty}^{\infty} x(\tau) y(t - \tau) d\tau = \int_{-\infty}^{\infty} x(t - \tau) y(\tau) d\tau = x(t) * y(t) \tag{H.9}$$

[1] By the time– and frequency–scaling property, a finite interferogram cannot have an infinitely narrow spectral resolution.

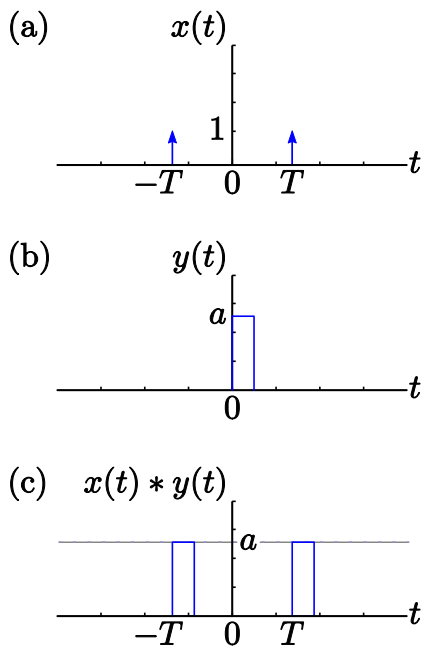

Figure H.2: A convolution example. An impulse signal $x(t)$, (a), is convolved with the rectangular signal $y(t)$, (b), to give $x(t) * y(t)$, (c). After Brigham [18].

which forms the convolution–multiplication Fourier transform pair

$$x(t)y(t) \Leftrightarrow X(\nu) * Y(\nu) \tag{H.10a}$$

$$x(t) * y(t) \Leftrightarrow X(\nu)Y(\nu) \tag{H.10b}$$

Convolution is also associative and distributive [19]

$$x * (y * z) = (x * y) * z \qquad \text{(associative)} \tag{H.11a}$$

$$x * (y + z) = x * y + x * z \qquad \text{(distributive)} \tag{H.11b}$$

A simplified example of the convolution of a rectangular function with two unit impulse functions is provided in figure H.2 [18].

Correlation

The correlation function, denoted by '$\star$', of $x(t)$ and $y(t)$ is defined as

$$z(t) = \int_{-\infty}^{\infty} x(\tau)y(t+\tau)d\tau = x(t) \star y(t) \tag{H.12}$$

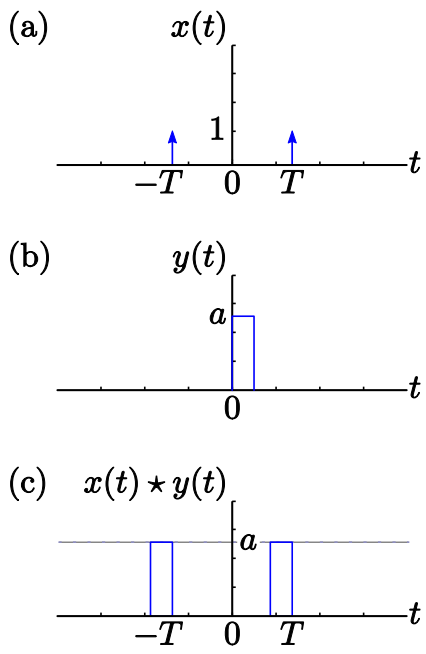

Figure H.3: A correlation example. An impulse signal $x(t)$, (a), is correlated with the rectangular signal $y(t)$, (b), to give $x(t) * y(t)$, (c). After Brigham [18].

A simplified example, after the convolution example, of the correlation of a rectangular function with two unit impulse functions is provided in figure H.3 [18]. The Fourier transform pair for the correlation function is

$$x(t) \star y(t) \Leftrightarrow X(\nu)Y^*(\nu) \tag{H.13}$$

Correlation is not commutative

$$x \star y \neq y \star x \tag{H.14}$$

Convolution is related to correlation by [19]

$$x * y = x(-) \star h \tag{H.15}$$

where $x(-)$ refers to the negative of the variable, i.e. by setting $t \to -t$.

Power spectrum

The power or energy spectrum is defined as $|F(\nu)|^2$ of a function $f(t)$, i.e. the squared modulus of the Fourier transform. When $x(t)$ is correlated with itself,

termed the autocorrelation,

$$|X(\nu)|^2 = x(t) \star x(t) \tag{H.16}$$

returns the power spectrum. This is used in interferometry to obtain the power spectrum of interferograms, termed the *Wiener–Khinchin theorem* or the *Wiener–Khintchine theorem*, as mentioned in appendix section B.2 .

DFT & FFT

To use the Fourier transform in a digital computer the *Discrete Fourier transform*, DFT, is used [20]

$$F(\nu) = \frac{1}{N} \sum_{\tau=0}^{N-1} f(\tau) e^{-i2\pi\left(\frac{\nu}{N}\right)\tau} \tag{H.17}$$

The inverse DFT is

$$f(\tau) = \sum_{\nu=0}^{N-1} F(\nu) e^{i2\pi\left(\frac{\nu}{N}\right)\tau} \tag{H.18}$$

The DFT of a signal with N samples takes of the order of N^2 calculations to perform. The *fast Fourier transform*, FFT, is an optimised algorithm reducing the computation to the order of $N \log(N)$ calculations [21]. The Matlab functions `fft` and `ifft` are used in this work for the Fourier transform and inverse Fourier transform, respectively.

H.2 References

[1] E. C. Titchmarsh. *Introduction to the Theory of Fourier Integrals*, chapter 1, pages 1–49. Oxford University Press, Oxford, 1937.

[2] F. W. J. Oliver, D. W. Lozier, R. F. Boisvert, and C. W. Clark. *NIST Handbook of Mathematical Functions*, chapter 1, pages 1–39. Cambridge University Press, Cambridge, 1st edition, may 2010. ISBN: 0521140633.

[3] E. G. Steward. *Fourier Optics: an Introduction*, chapter 4, pages 71–98. Dover Publications, Inc., New York, 2nd edition, 2004. ISBN: 0486435040.

[4] R. N. Bracewell. *The Fourier Transform and its Application*, chapter 1, pages 1–4. The McGraw-Hill Companies, Inc., New York, 3rd edition, 1999. ISBN: 0073039381.

[5] E. O. Brigham. *The Fast Fourier Transform and its Applications*, chapter 1, pages 1–8. Prentice Hall, Inc., New Jersey, 1988. ISBN: 0133075052.

[6] S. G. Lipson, H. Lipson, and D. S. Tannhauser. *Optical Physics*, chapter 4, pages 71–98. Cambridge University Press, Cambridge, 3rd edition, 1995. ISBN: 0521436311.

[7] E. Hecht. *Optics*, chapter 7, pages 242–269. Addison-Wesley Publishing Company, Inc., Reading, Massachusetts, 2nd edition, 1987.

[8] A. V. Oppenheim, R. W. Schafer, and J. R. Buck. *Discrete-Time Signal Processing*, chapter 2, pages 8–93. Prentice-Hall, Inc., New Jersey, 2 edition, 1999. ISBN: 0137549202.

[9] D. Gabor. Theory of communication. *J. IEE (London)*, 93(26):429–457, November 1946.

[10] L. Cohen. *Time Frequency Analysis: Theory and Applications*, chapter 1, pages 1–26. Prentice-Hall, Inc., New Jersey, 1995. ISBN: 0135945321.

[11] E. O. Brigham. *The Fast Fourier Transform and its Applications*, chapter 3, pages 30–49. Prentice Hall, Inc., New Jersey, 1988. ISBN: 0133075052.

[12] E. O. Brigham. *The Fast Fourier Transform*, chapter 3, pages 31–49. Prentice-Hall, Inc., New Jersey, 1974. ISBN: 013307496X.

[13] W. H. Steel. *Interferometry*, chapter 2, pages 12–25. Cambridge Studies in Modern Optics. Cambridge University Press, Cambridge, 2 edition, 1983. ISBN: 0521311624.

[14] P. R. Griffiths and J. A. de Haseth. *Fourier Transform Infrared Spectrometry*, chapter 4, pages 75–95. Chemical Analysis. John Wiley & Sons, Inc., New York, 2nd edition, 2007. ISBN: 9780471194040.

[15] S. Davis, M. C. Abrams, and J. W. Brault. *Fourier Transform Spectrometry*, chapter 4, pages 41–66. Academic Press, San Diego, 2001. ISBN: 9780120425105.

[16] R. N. Bracewell. *The Fourier Transform and its Application*. The McGraw-Hill Companies, Inc., New York, 3rd edition, 1999. ISBN: 0073039381.

[17] L. Mertz. *Transformations in Optics*, chapter 1, pages 1–43. John Wiley & Sons, Inc., New York, 1965.

[18] E. O. Brigham. *The Fast Fourier Transform and its Applications*, chapter 4, pages 50–73. Prentice Hall, Inc., New Jersey, 1988. ISBN: 0133075052.

[19] R. N. Bracewell. *The Fourier Transform and its Application*, chapter 3, pages 24–54. The McGraw-Hill Companies, Inc., New York, 3rd edition, 1999. ISBN: 0073039381.

[20] R. N. Bracewell. *The Fourier Transform and its Application*, chapter 11, pages 258–292. The McGraw-Hill Companies, Inc., New York, 3rd edition, 1999. ISBN: 0073039381.

[21] E. O. Brigham. *The Fast Fourier Transform and its Applications*, chapter 8, pages 131–166. Prentice Hall, Inc., New Jersey, 1988. ISBN: 0133075052.

Appendix I

Assembly of the fibre straining device

This appendix covers the attachment of the fibre to the fibre straining apparatus, built for the work reported in chapter 4. The glass solder employed is first discussed, then the steps used to successfully complete[1] the soldering are described.

The recommended means of melting the solder is via an oven, and not a soldering iron. An oven would have needed to be built to accomodate the glass slide used, and was thus ruled out. The soldering iron was adequate for the task, although it was necessary to obtain one which could provide the correct solder melting temperature.

I.1 Glass solder used for attachment

The first batch of glass solder received did not have padding to prevent damage, as shown in figure 4.5 (page V.I - 181). Much of the ribbon was broken into sections like that shown in figure I.1. This turned out to be of great benefit, as the circular solder preforms were difficult to place onto the fibre, tended to wet more to the soldering iron than the glass plate and provided a very small surface area for contact. The broken section could be placed alongside the fibre to be fixed, heated and spread alongside the fibre, making it easier to complete the soldering.

[1] It is very easy to solder the fibre to the mount in such a way that the subsequent application of strain breaks the fibre at the solder.

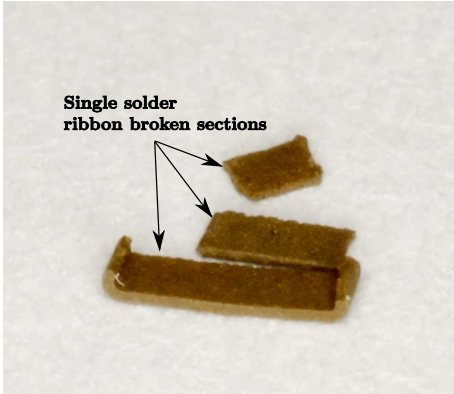

Figure I.1: Unprotected ribbon solder broken during transport.

I.2 Soldering fibre to fibre mount

The folowing are the steps, illustrated in figure I.2, used to successfully attach the fibre to the strain rig with glass solder.

(a). To prevent the fibre being soldered at an angle to the direction of applied strain, the fibre was fixed in place with scotch tape. In figure I.2, a piece of magnetic strip was used, on both sides, to keep the fibre at the level of the glass slide.

(b). Glass solder was placed beside the fibre where the solder attachment was to be made.

(c). The soldering iron was placed directly over broken ribbon preforms, and moved down to solder to begin melting.

(d). The iron was carefully moved along fibre, in the direction away from FBG.

(e). The iron was moved alongside fibre allowing a smooth melt along fibre (without touching fibre itself if possible). Adhesion to fibre should occur.

(f). The iron was moved to other side and steps (c)–(e) repeated. The sides were alternated until a length of fibre ~ 2 mm was covered by solder.

(g). The solder was left to cool for approximately a minute. Given the quantity of solder and the surface area, the solder should, in general, cool quickly.

(h). The scotch tape was carefully removed to avoid breaking fibre[2].

[2]It may not be necessary to remove the scotch tape from the side of the attachment not experiencing strain.

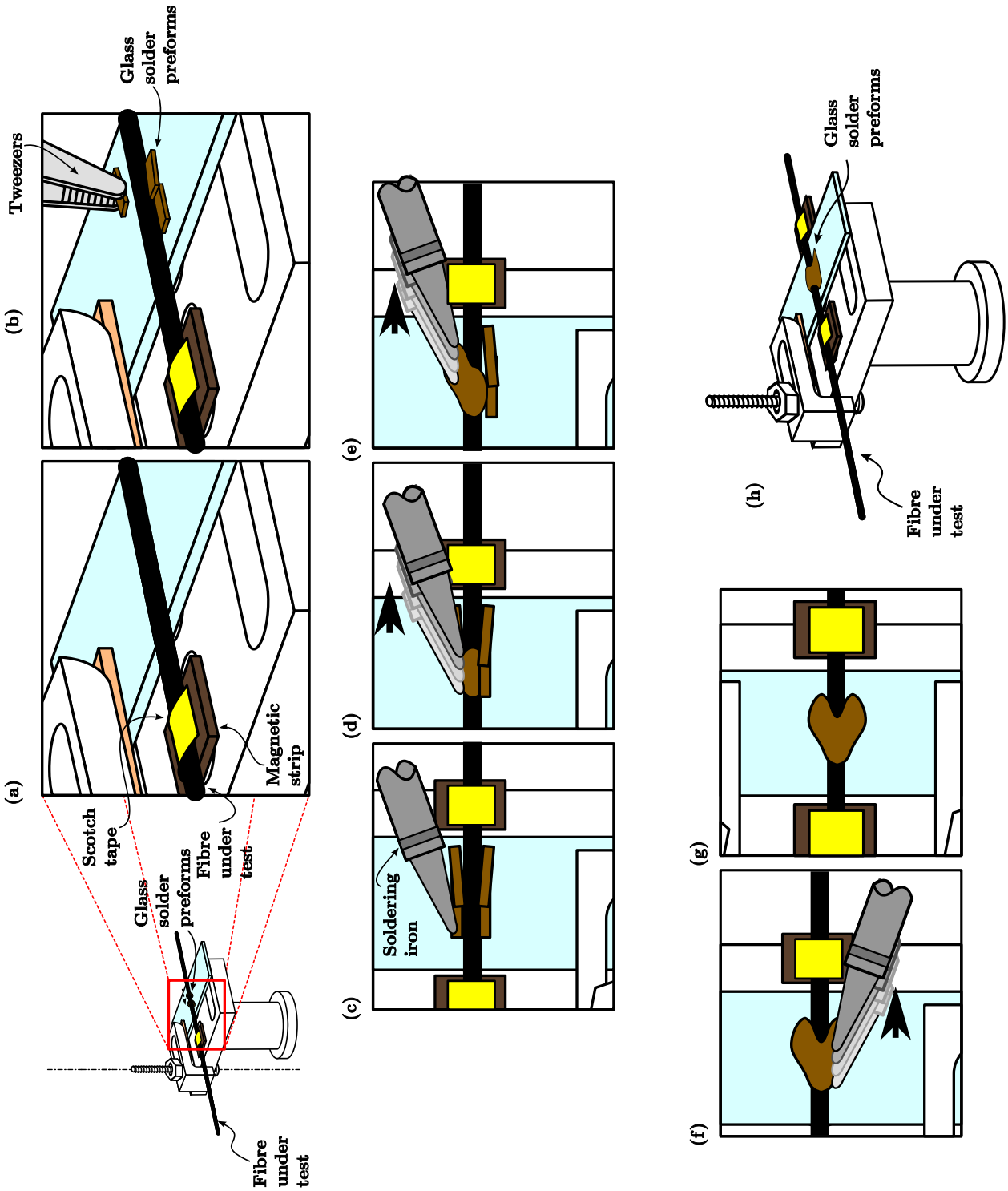

Figure I.2: Graphical representation of soldering technique.

Appendix J

Exalos ESL1505-2100 SLED

The following are the spectrum, obtained with the Ando AQ6317B OSA, and the specifications, from the Exalos measurement report, for the SLED used in this work.

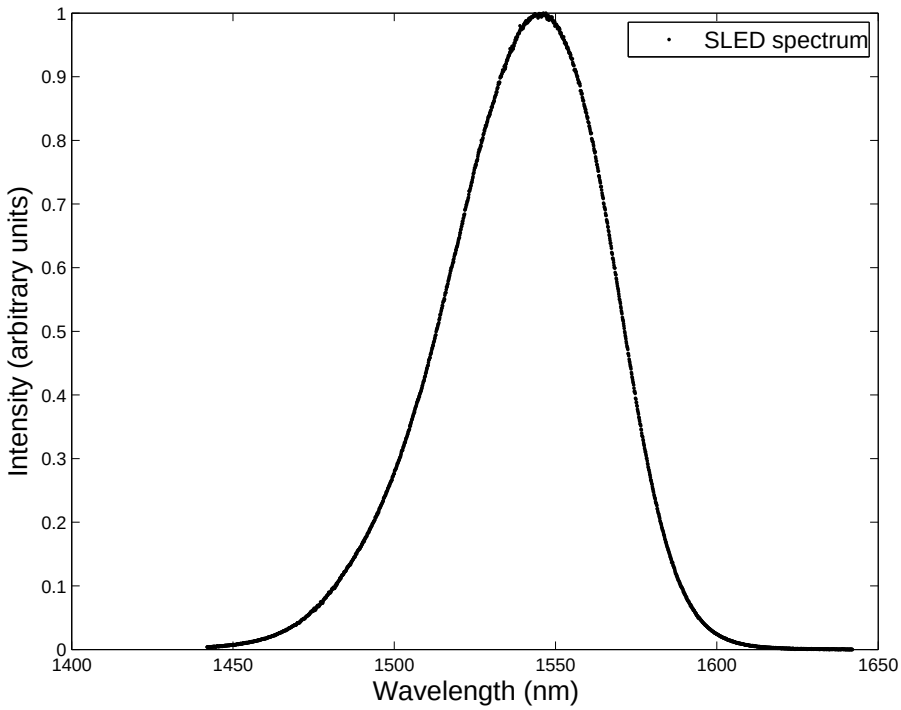

Figure J.1: OSA spectrum of ESL1505-2100 Exalos SLED.

Max. Power	2.35 mW
Peak Wavelength	1543.2 nm
Central Wavelength	1542.7 nm
Bandwidth	59.4 nm
ASE ripple	0.04 dB
$V_i@I_s$	1.92 V
T_{th}	20.0 °C
I_{tec}	0.13 A
I_s	180.0 mA
T_{case}	20.0 °C
V_{tec}	0.20 V

Table J.1: From Exalos Measurement report ESL1505-2100-SN:121, and specification ESL1505-2100, Rev:1.0 (30-09-03).

Appendix K

Theory for geometric aberrations

K.1 Derivation of Seidel Aberrations

Following the treatment in [1], the general characteristics for third–order geometric aberrations of reflective and refractive systems are the same [2], and so refractive diagrams are used below for clarity of presentation [3]. The stigmatic ideal in the ray optics representation converts a point source to a point image or, for parallel radiation at infinity, to a point dependent upon the angle of the parallel radiation. The wave representation is obtained by considering equal distances from the source point as representing waves with the same phase. For stigmatic focusing, the wavefronts are a series of concentric circles centred on the stigmatic focal point. Thus, the non–ideal focusing of real focusing elements appear as wavefront deviations from the ideal concentric wavefronts.

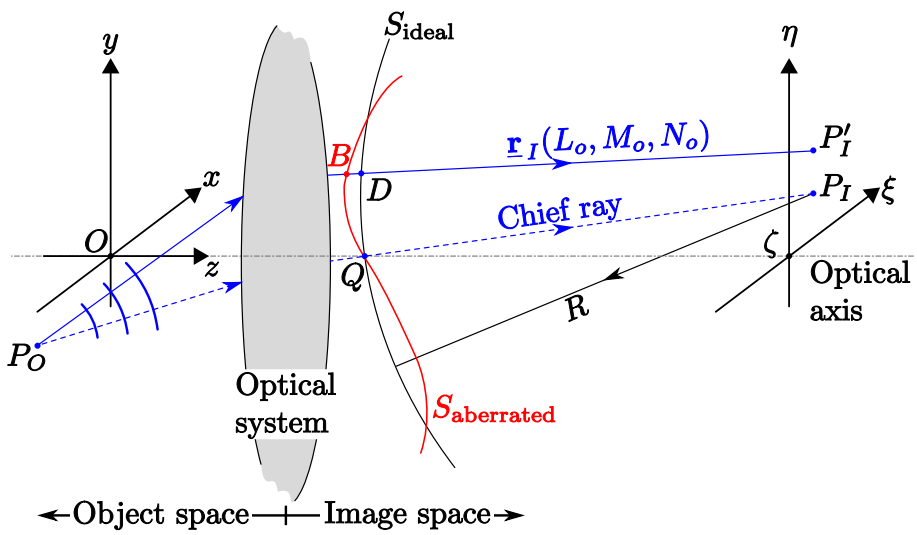

Figure K.1: Diagram of the configuration used for derivation of Seidel aberrations.

To describe the aberrations, let P_I be the stigmatic image of a point P_O, as in figure K.1. Hamilton's point characteristic function, or Hamiltonian, V_H, is defined as the optical length along the stigmatic path P_O to P_I and V_H is a function of the co–ordinate system. $\underline{\hat{\mathbf{r}}}_{\mathrm{O}}$ and $\underline{\hat{\mathbf{r}}}_{\mathrm{I}}$ are unit vectors on the ray through P_O and P_I, respectively. The position vectors $\underline{\mathbf{a}}_{\mathrm{O}}$ and $\underline{\mathbf{a}}_{\mathrm{I}}$ define the points P_O and P_I. Letting P_I' be a neighbouring point with position vector $\underline{\mathbf{a}}_{\mathrm{I}} + \underline{\delta\mathbf{a}}_{\mathrm{I}}$,

$$V_H(\underline{\mathbf{a}}_{\mathrm{I}} + \underline{\delta\mathbf{a}}_{\mathrm{I}}, \underline{\mathbf{a}}) - V_H(\underline{\mathbf{a}}_{\mathrm{I}}, \underline{\mathbf{a}}) = \underline{\delta\mathbf{a}}_{\mathrm{I}} \bullet \underline{\nabla} V_H \tag{K.1}$$

The left hand side of equation K.1 is the OPD between the two wavefronts S_{ideal} and $S_{\mathrm{aberrated}}$, and, hence,

$$V_H(\underline{\mathbf{a}}_{\mathrm{I}} + \underline{\delta\mathbf{a}}_{\mathrm{I}}, \underline{\mathbf{a}}) - V_H(\underline{\mathbf{a}}_{\mathrm{I}}, \underline{\mathbf{a}}) = n^{'} \underline{\delta\mathbf{a}}_{\mathrm{I}} \bullet \underline{\hat{\mathbf{r}}}_{\mathrm{I}} \tag{K.2}$$

where $n^{'}$ is the refractive index of the medium.
Substituting (K.2) into (K.1) gives

$$n^{'} \underline{\delta\mathbf{a}}_{\mathrm{I}} \bullet \underline{\hat{\mathbf{r}}}_{\mathrm{I}} = \underline{\delta\mathbf{a}}_{\mathrm{I}} \bullet \underline{\nabla} V_H \tag{K.3}$$

As $\underline{\delta\mathbf{a}}_{\mathrm{I}}$ is an arbitrary increment, we have $n^{'} \underline{\hat{\mathbf{r}}}_{\mathrm{I}} = \underline{\nabla} V_H$ and, therefore

$$\left.\begin{aligned} n^{'} L_I &= \frac{\partial V_H}{\partial \xi} \\ n^{'} M_I &= \frac{\partial V_H}{\partial \eta} \\ n^{'} N_I &= \frac{\partial V_H}{\partial \zeta} \end{aligned}\right\} \tag{K.4}$$

which are refraction invariants [4], where L_I, M_I, N_I are the direction cosines of the wavefront surface normals (tangents to the ray). Similarly, in object space

$$\left.\begin{aligned} nL_O &= \frac{\partial V_H}{\partial x} \\ nM_O &= \frac{\partial V_H}{\partial y} \\ nN_O &= \frac{\partial V_H}{\partial z} \end{aligned}\right\} \tag{K.5}$$

Closely related to the characteristic equation is the *Eikonal*, defined as

$$E_H(\underline{\mathbf{r}}_{\mathrm{O}}, \underline{\mathbf{r}}_{\mathrm{I}}) = V_H(\underline{\mathbf{a}}_{\mathrm{O}}, \underline{\mathbf{a}}_{\mathrm{I}}) - n^{'} \underline{\mathbf{a}}_{\mathrm{I}} \bullet \underline{\mathbf{r}}_{\mathrm{I}} + n \underline{\mathbf{a}}_{\mathrm{O}} \bullet \underline{\mathbf{r}}_{\mathrm{O}} \tag{K.6}$$

which, by differentiating with respect to L_I gives

$$\frac{\partial E_H}{\partial L_I} = \frac{\partial V_H}{\partial \xi}\frac{\partial \xi}{\partial L_I} + \frac{\partial V_H}{\partial \eta}\frac{\partial \eta}{\partial L_I} - n^{'}\xi - n^{'}L_I\frac{\partial \xi}{\partial L_I} - n^{'}M_I\frac{\partial \eta}{\partial L_I} \tag{K.7}$$

Using the first two equations of (K.4) gives

$$\frac{\partial E_H}{\partial L_I} = -n^{'}\xi \tag{K.8}$$

Similarly, differentiating with respect to M_I, gives

$$\frac{\partial E_H}{\partial M_I} = -n^{'}\eta \tag{K.9}$$

Equations (K.8) and (K.9) are the two dimensional versions of (K.4), by assuming there is no z dependence, i.e. in the image plane only. There are similar equations for object space. Equations (K.8) and (K.9) yield the transverse ray aberrations.

The wave aberration can be obtained from the transverse ray aberration. The optical path length from P_O to D is $V_H(P_O, D)$ so the aberration function W is

$$\begin{aligned} W(x,y) &= V_H(P_O, B) - V_H(P_O, D) \\ &= V_H(P_O, Q) - V_H(P_O, D) \end{aligned} \tag{K.10}$$

As B and Q are on the same wavefront, $V_H(P_O, Q) = V_H(P_O, B)$. Differentiating W with respect to x and y gives

$$\frac{\partial W}{\partial x} = -\frac{\partial V_H}{\partial x} - \frac{\partial V_H}{\partial z} \bullet \frac{\partial z}{\partial x} \tag{K.11a}$$

$$\frac{\partial W}{\partial y} = -\frac{\partial V_H}{\partial y} - \frac{\partial V_H}{\partial z} \bullet \frac{\partial z}{\partial y} \tag{K.11b}$$

The optical systems have axial symmetry and z coincides with this axis of symmetry. The point angle eikonal is, therefore, only a function of four rotationally invariant variables [5]

$$V_H(\xi, \eta, L_I, M_I) = V_H(u_1, u_2, u_3)$$

where

$$u_1 = \frac{1}{2}\left(x^2 + y^2\right), \tag{K.12a}$$

$$u_2 = xL_I + yM_I, \tag{K.12b}$$

$$u_3 = \frac{1}{2}\left(L_I^2 + M_I^2\right) \tag{K.12c}$$

For a perfect system

$$V_H = -\beta_{\mathrm{A}} u_2 + f(u_1), \tag{K.13}$$

where β_{A} is the magnification and the paraxial form is

$$V_H = -\beta_{\mathrm{A}} u_2 - a\beta_{\mathrm{A}} u_1 \tag{K.14}$$

where a is the paraxial power[1] of the system.

For a real, imperfect, focusing element

$$\begin{aligned} V_H = \; & -a\beta_{\mathrm{A}} u_1 - \beta_{\mathrm{A}} u_2 \\ & -\tfrac{1}{2}\left[K_{11}u_1^2 + 2K_{12}u_1u_2 + K_{22}u_2^2 + 2K_{13}u_1u_3 + 2K_{23}u_2u_3 + K_{33}u_3^2\right] \\ & + [\cdots] \end{aligned} \tag{K.15}$$

Limiting the expansion to third order aberrations, errors due to the terms of V_H are quadratic in u_i. Differentiating equation (K.15) with respect to L_O and M_O yields

$$\begin{pmatrix} \xi \\ \eta \end{pmatrix} = \beta_{\mathrm{A}} \begin{pmatrix} x \\ y \end{pmatrix} + (K_{12}u_1 + K_{22}u_2 + K_{23}u_3) \begin{pmatrix} x \\ y \end{pmatrix} + (K_{13}u_1 + K_{23}u_2 + K_{33}u_3) \begin{pmatrix} n' L_I \\ n' M_I \end{pmatrix} \tag{K.16}$$

By using the axial symmetry and choosing the tangential plane to be aligned with the x axis ($y = 0$), equation (K.12) may be rewritten as

$$\begin{aligned} u_1 &= \tfrac{1}{2}x^2, \\ u_2 &= n' x L_I, \\ u_3 &= \tfrac{1}{2}n'^2 \left(L_I^2 + M_I^2\right) \end{aligned} \tag{K.17}$$

which, when substituted into equation (K.16), yields

$$\left.\begin{aligned} \xi =& \beta_{\mathrm{A}} x + \frac{1}{2}K_{12}x^3 + \frac{1}{2}\left(K_{13} + 2K_{22}\right)x^2 L_I + \frac{1}{2}K_{23}\left(3L_I^2 + M_I^2\right)x \\ & + \frac{1}{2}K_{33}\left(L_I^2 + M_I^2\right)L_I \\ \eta =& \frac{1}{2}K_{13}x^2 M_I + K_{23}L_I M_I x + \frac{1}{2}K_{33}\left(L_I^2 + M_I^2\right)M_I \end{aligned}\right\} \tag{K.18}$$

Equation (K.18) allows the Seidel aberrations to be considered. Taking only third order terms and grouping these terms by the powers of their respective co–ordinates, the Seidel sums are obtained, describing the *primary aberrations*: **Spher-**

[1] The paraxial or Gaussian power of a single refracting surface is $(n' - n)C_{\mathrm{surface}}$, where C_{surface} is the curvature of the surface and n and n' are the refractive indices of the media on either side of the surface. For a reflecting surface $n' \equiv n$. The concept of the power of a system is only defined for the paraxial approximation [6].

ical, **Coma**, **Astigmatism**, **Field Curvature**, and **Distortion** [4].

Distortion does not affect a point source as it refers to the geometrical modification of similarity of the object and image [4]. The exact definitions of coma, astigmatism and field curvature are not standardised [4]. They will be defined here using equation (K.18). Figures K.3 (page V.II K-8), K.4 (page V.II K-9) and K.5 (page V.II K-9) show the effects of coma, astigmatism and field curvature, respectively.

K.2 Geometric aberrations

The basic principal of image formation is that the paths of rays[2] from a point on an object to its conjugate image point should all have the same optical path length [3].

The ideal spectral measuring device would be stigmatic, where a monochromatic single point source produces a single point output at the appropriate angle for that wavelength. In practice, stigmatic spectrometers are rarely achieved [5, 8]. Spectrometers using transmitting components can suffer from wavelength dependent absorption[3] and dispersion as the radiation under test passes through the components, thus altering the produced spectrum.

To remove chromatic aberrations and increase the efficiency of the spectrometer reflective elements are used in preference to transmitting elements. The focusing elements are mirrors and the diffraction grating operates in reflection. The mirrors' increased optical throughput comes at the expense of loss of alignment of the optical axis and the geometric axis of symmetry of the focusing element[4]. In order for the source not to obstruct the collimated beam, the mirror must reflect the collimated radiation away from the entrance aperture. Unless the aperture is small, or very long focal lengths are used, the angle at which the collimated radiation emerges from the mirror, with respect to the incident radiation, will poorly approximate the paraxial condition. Conveniently, the confinement of the signal within the fibre waveguide, and the use of the fibre end–face as the aperture, provides the small aperture condition without the loss of energy present using an aperture stop to shape the beam.

Focusing elements are required to convert spherical wave fronts (from an effectively isotropically radiating point source[5]) to plane wave fronts (for the diffraction grating) and back to spherical waves (to the point image). Geometric aberrations

[2]Optical rays are considered to be the surface normal, at the ray, of the optical wavefront [7].

[3]The wavelength absorption arises, not from geometric aberrations, but from material efficiencies upon transmission (e.g. refraction and absorption efficiencies).

[4]The use of mirrors at an angle means that the axial symmetry is broken for incident and reflected radiation. There is only a plane of symmetry, in general, so Cartesian co–ordinates are used.

[5]The focusing element has no apertures or stops between it and the point source.

are introduced for skew–rays, that is, radiation not close to the optical axis. The dispersion of the radiation into various angles limits the paraxial approximation to a narrow wavelength range. This can be mitigated by the use of a rotating focusing system for the detector so that the radiation at the detector always satisfies the paraxial approximation [8].

Such an arrangement is a scanning device; the spectrum is only measured at one angular setting at a time. The limitation to this approach is the measurement accuracy and precision [9] of the angle of the focusing arm, and the temporal spectral stability of the source being examined.

Geometric monochromatic focusing to a point requires a paraboloid focusing element (usually a mirror) illuminated by plane waves perpendicular to the optical axis [10], as a spherical focusing element does not bring a plane wavefront to a single focal point or generate a plane wave from spherical waves emanating from a single focal point[6].

Monochromatic deviations from the stigmatic ideal are termed geometrical aberrations [5, 7, 11–13]. The effect of these aberrations is to locate energy at a detector element, from a given diffracted wavelength, into neighbouring detector elements or away from any detecting element. In the first case, this distorts the neighbouring spectral values (a systematic error), and, in the second, the signal strength is diminished.

Geometrical aberrations can have positive or negative sign [14], and may be mitigated by the arrangement of multiple focusing elements as a system so as to have the aberrations introduced by one focusing element compensate for the aberrations introduced by other focusing elements.

Aberrations are usually described by the effect of the focusing element on incident plane waves at an angle to the focusing elements optical axis. The inability to bring the rays to a common focus describes the aberration. The reverse process also holds: a 'point source' would need to have the same spatial distribution to produce plane waves at that angle to the focusing elements optical axis. As the work reported here has the cleaved end–face of a fibre as the 'point source', the radiation incident onto the diffraction grating will not be strictly collimated due to these aberrations.

Aberrations are described using two approximation systems: Seidel sums and Zernike Polynomials [15, 16]. Zernike surface polynomials describe the aberrations produced from the surface of the focusing element using orthogonal polynomials, and may require many terms for complicated surfaces. Zernike polynomials provide a more accurate calculation of the aberrations in a system and readily facilitate determination of diffraction effects but at greater computational expense. Aberrations

[6]Geometrically, the surface described by equal distances from a planar surface (called the directrix) and a focal point is a parabola of revolution.

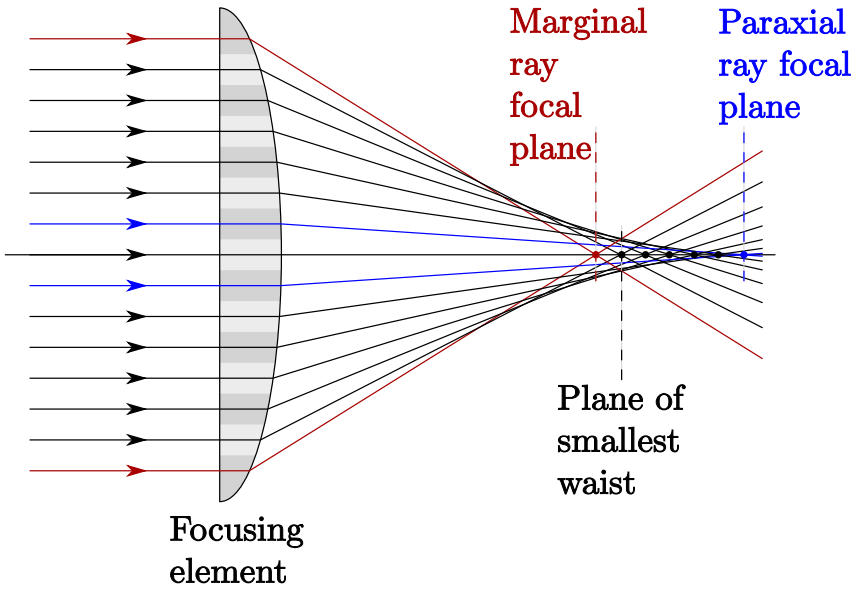

Figure K.2: Spherical aberration.

from smooth surfaces can be described by as few as thirty six polynomials [15].

The *Seidel aberrations*, or sums, are determined by the sum of the contributions of approximations to the incident radiation from all parts of the focusing element [17]. The Gaussian or paraxial approximation is the linear theory, e.g. where $\sin(\theta) \approx \theta$. Seidel theory uses only the next terms in the Taylor expansion, e.g. where [18],

$$\sin(\theta) \simeq \theta - \frac{\theta^3}{3!} + \cdots$$

The Seidel sums do not, by definition, incorporate higher order terms[7].

K.2.1 Spherical Aberration

The following aberration terms are described in appendix section K.1 (page V.II K-1). The aberrations are described in terms of the image plane co–ordinates ξ and η. The values of ξ and η are functions of the object plane co–ordinates x and y and the direction cosines L_I and M_I.

When K_{33} is the only non–zero coefficient, equation (K.18) (page V.II K-4) becomes

$$\left.\begin{aligned} \xi &= \beta_{\mathrm{A}} x + \frac{1}{2} K_{33} \left(L_I^2 + M_I^2\right) L_I \\ \eta &= \frac{1}{2} K_{33} \left(L_I^2 + M_I^2\right) M_I \end{aligned}\right\} \tag{K.19}$$

[7]The higher order terms can provide a more accurate description of the aberrations, but at the expense of mixing what are conceptually separate aberrations using the Seidel approach. [6]

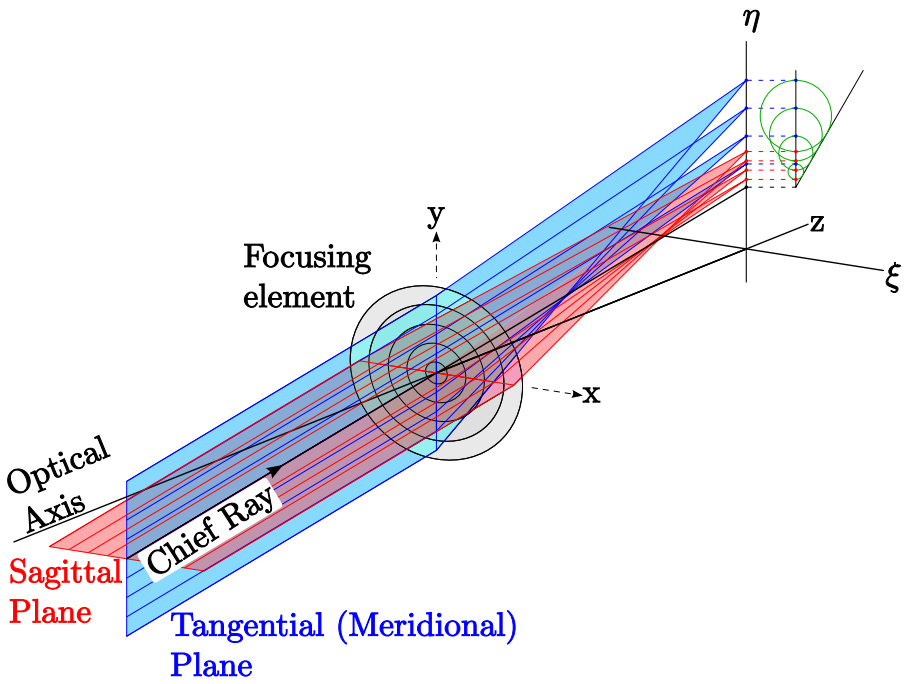

Figure K.3: Coma aberration.

K.2.2 Coma Aberration

Coma derives its name from its comet–like appearance on images. Point sources appear as spatially extended images, with the 'comet tail' radiating from the optical axis for positive coma and radiating towards the optical axis for negative coma [19]. The tangential and sagittal comas are illustrated in figure K.3. Parallel rays incident on a focusing element experience different focal points depending upon the distance from the centre of the focusing element. This is illustrated in figure K.3 as the different zones on the lens which have different tangential and sagittal focal points. The aberration from sagittal coma is two thirds that of tangential coma [15].

Allowing only K_{23} to be non–zero, equation (K.18) (page V.II K-4) becomes

$$\left.\begin{aligned} \xi = \beta_{\mathrm{A}} x + \frac{1}{2} K_{23} \left(3L_I^2 + M_I^2\right) x \\ \eta = K_{23} L_I M_I x \end{aligned}\right\} \tag{K.20}$$

K.2.3 Field Curvature & Astigmatism Aberration

Astigmatism occurs when rays incident on a focusing element have different focal points in the tangential (meridional) and sagittal directions [15]. The tangential and sagittal rays experience different surface curvatures; the tangential surface curvature is in the (x, y) plane only whereas the sagittal surface curvature is in the (y, z) plane. The tangential or meridional plane contains the chief skew ray and optical

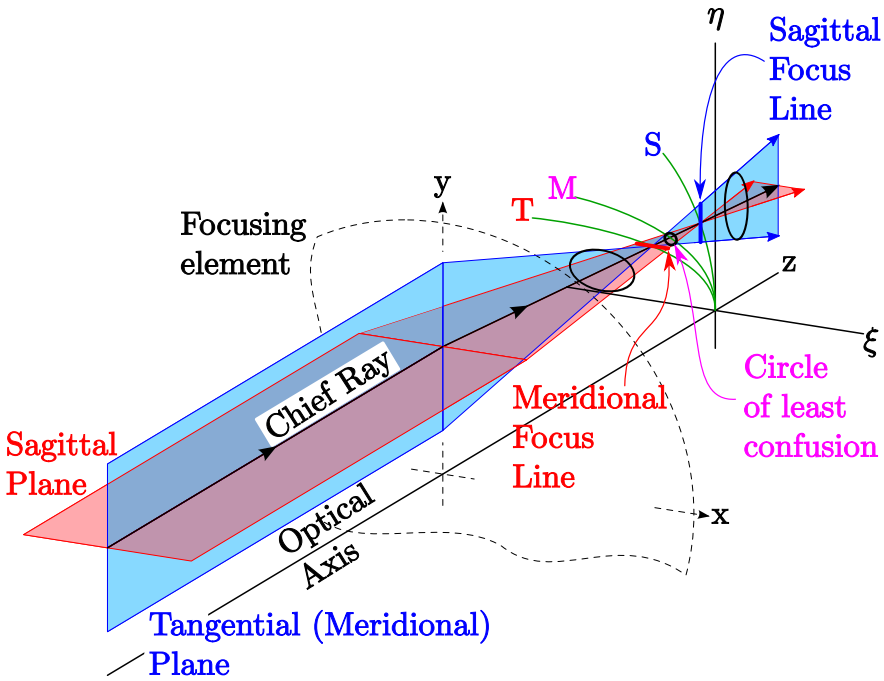

Figure K.4: Astigmatism aberration.

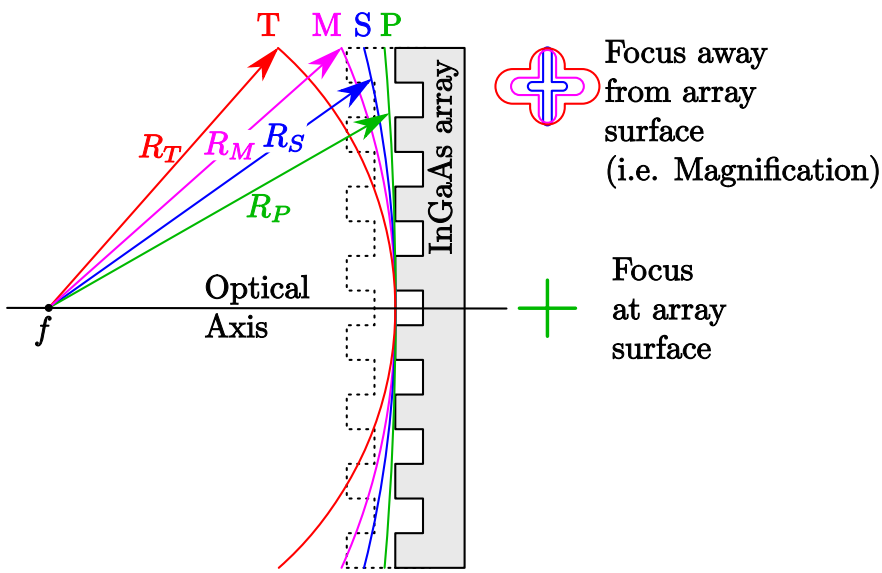

Figure K.5: Field curvature aberration.

axis of the focusing element. The sagittal plane contains the chief skew ray and is normal to the tangential plane. The effect of astigmatism is to produce two mutually perpendicular images at different focal distances [20], as illustrated in figure K.4. The energy of the image is spread out along the extended line, reducing visibility. Between the tangential and sagittal focal points lies the circle of least confusion, where the combined focal cones are minimised.

Field curvature, illustrated in figure K.5, occurs when the focal points for skew rays do not lie in the plane normal to the optical axis at the focal length. The surface described by the ideal focal points is the Petzval surface [15]. The astigmatic surfaces are shown relative to the linear InGaAs array of the spectrometer. The distance to the tangential surface from the Petzval surface is three times the distance of the sagittal surface from the Petzval surface. The circle of least confusion, as described in figure K.4, describes the mean surface.

The definitions of field curvature and astigmatism are not mutually exclusive. The effect of both on a spectrometer is to alter the magnification (and hence energy density on the array) as a function of angle and, hence, wavelength. The circle of least confusion provides the greatest energy density for the spectrometer. The linear array can either be placed at the intersection of the optical axis and the mean surface (the linear array as a tangent), or have the mean surface intersect the linear array at two points (the linear array as a secant line).

Setting K_{13} and K_{22} to be non–zero, equation (K.18) (page V.II K-4) becomes

$$\left.\begin{aligned} \xi &= \beta_{\mathrm{A}} x + \frac{1}{2}\left(K_{13} + 2K_{22}\right) x^2 L_I \\ \eta &= \frac{1}{2} K_{13} x^2 M_I \end{aligned}\right\} \tag{K.21}$$

K.2.4 Grating aberrations

When non–collimated radiation is incident upon a plane grating, the plane wave representation does not apply. The grating response is still linear, i.e. a superposition of the diffracted radiation from each obstacle groove, but the resulting pattern may be shifted, widened or narrowed or made asymmetrical with respect to the incident profile [21].

For a plane grating, which produces diffraction in the x, z plane, the aberration from the grating is [22]

$$\xi = \tfrac{1}{2} y L^2 \left(\sin\theta_i + \sin\theta_d\right) \tag{K.22}$$

which produces a coma term in non–collimated radiation, which only vanishes at $\theta_i = -\theta_d$.

K.3 SpectroBragg design

K.3.1 Angle of diffracted rays at M_2

The angles at which the non–design wavelengths are reflected, ϕ_d, is obtained by using the triangle relations shown in figures K.6 and K.7. The resulting equations are shown in the red boxes. From figure K.6, $\phi_d(\lambda)$ is obtained in terms of known quantities and φ_d, which is unknown.

$$\phi_d(\lambda) = \Delta\theta_d - \varphi_d + \beta \tag{K.23}$$

Figure K.7 allows φ_d to be determined, in terms of known quantities, as

$$\varphi_d = 3\beta + 2\theta_d(\lambda_{\text{design}}) - \pi \tag{K.24}$$

And so equation (K.23) can be written in terms of known quantities

$$\phi_d(\lambda) = \Delta\theta_d(\lambda) - 2\beta - 2\theta_d(\lambda_{\text{design}}) + \pi \tag{K.25}$$

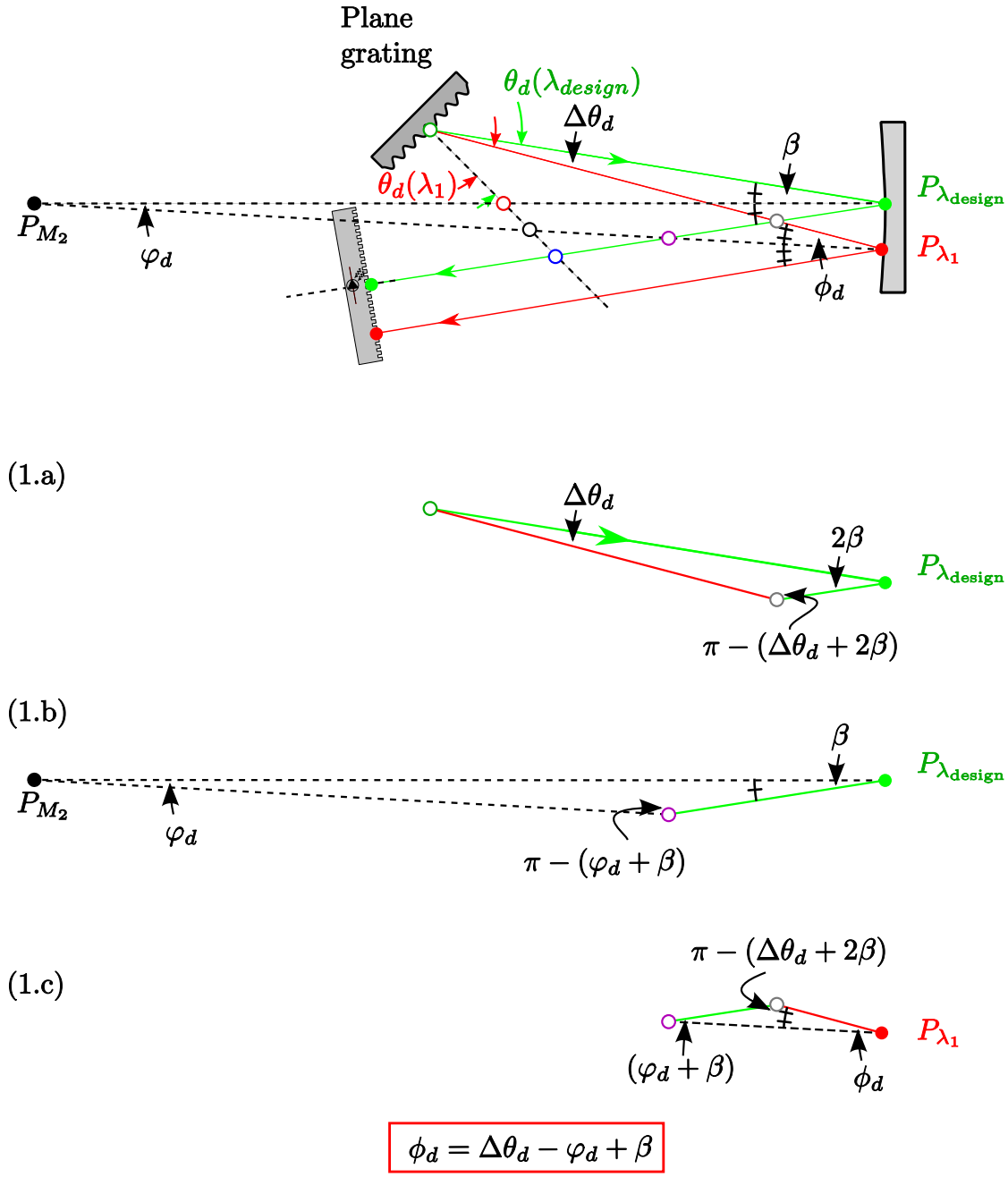

$$\boxed{\phi_d = \Delta\theta_d - \varphi_d + \beta}$$

Figure K.6: Geometric determination of the angle ϕ_d. Using the triangles 1.a–1.c, a relation for ϕ_d is obtained. The triangles 1.a–1.c are separately shown, with their vertices indicated by coloured circles.

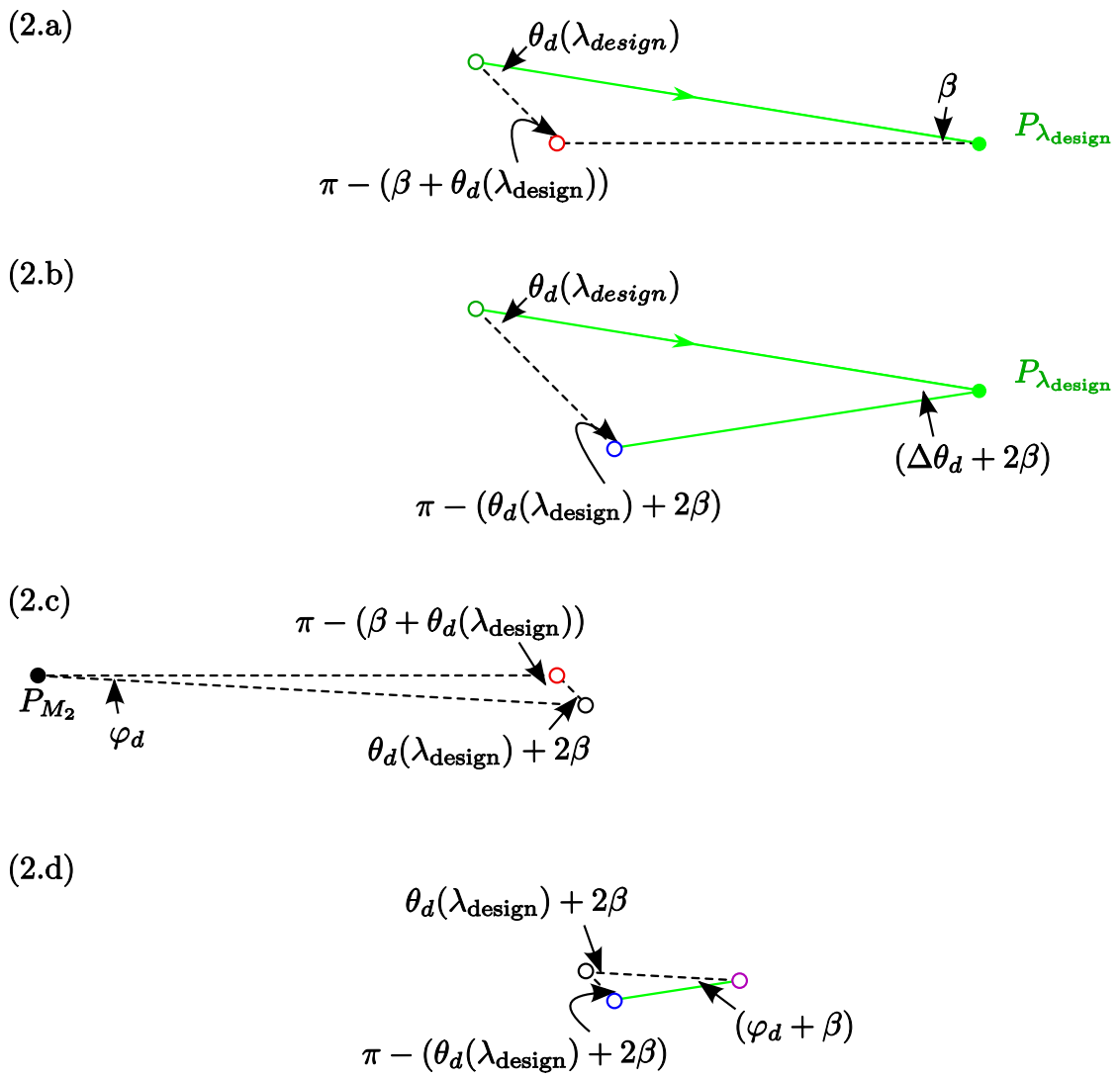

$$\boxed{\begin{aligned} \varphi_d &= 3\beta + 2\theta_d(\lambda_{\text{design}}) - \pi \\ \phi_d &= \Delta\theta_d - 2\beta - 2\theta_d(\lambda_{\text{design}}) + \pi \end{aligned}}$$

Figure K.7: Continuation of figure K.6. Geometric determination of the angle ϕ_d in terms of known angles, $\theta_d(\lambda_{\text{design}})$, $\Delta\theta_d$ and β. Using the triangles 2.a–2.d, a relation for φ_d is obtained.

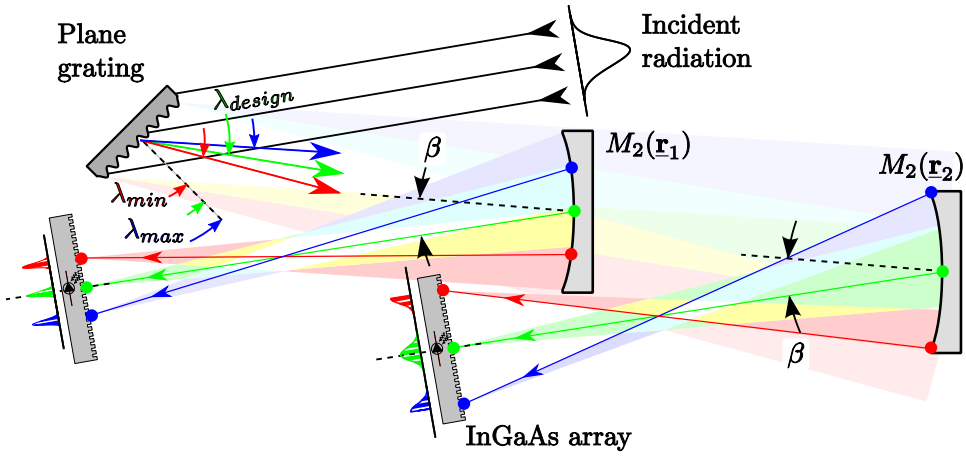

Figure K.8: The SpectroBragg resolution and spectral bandwidth was determined by diffraction grating dispersion and the angle intercepted by the mirror M_2. At position $\underline{\mathbf{r}}_1$, a larger angle is intercepted, and the spectrum occupies half the diode array. At position $\underline{\mathbf{r}}_2$, a smaller angle is intercepted, and the spectrum occupies most of the array but experiences vignetting.

K.3.2 Čzerny–Turner design considerations

The resolution of a Čzerny–Turner type spectrometer is determined by the diffraction grating and the focusing mirror, M_2. The principal ray[8] at the design wavelength is used for the alignment of the components [23], and so the mirrors M_1 and M_2, and the diffraction grating are centred with respect to the design wavelength. The maximum attainable spectral resolution is provided by the diffraction grating[9]. M_2 may concentrate too much spectral detail onto a single detector element so that the maximum attainable resolution is not achieved. Alternatively, M_2 may spread the spectral detail over more detector elements than are required, oversampling the diffraction grating resolution.

The position at which M_2 intercepts the diffracted radiation determines the effect of M_2 on the diffraction grating resolution, as illustrated in figure K.8. The spectral bandwidth has an inverse relationship to the resolution. The spectral bandwidth may be unnecessarily limited when oversampling the spectrum by placing M_2 far from the diffraction grating.

The spectral range is delimited by wavelengths λ_{min} and λ_{max}. Wavelengths outside this band will experience vignetting as the diffracted radiation is not fully intercepted by M_2, as illustrated in figure K.8.

The apparent width of the diffracted radiation is illustrated in figure K.9, and is

[8]The principal ray is the ray from the centre of the grating. It's use is recommended for initial spectrometer design [23].

[9]The aberrations inherent in the Čzerny–Turner design are ignored at this stage of the discussion.

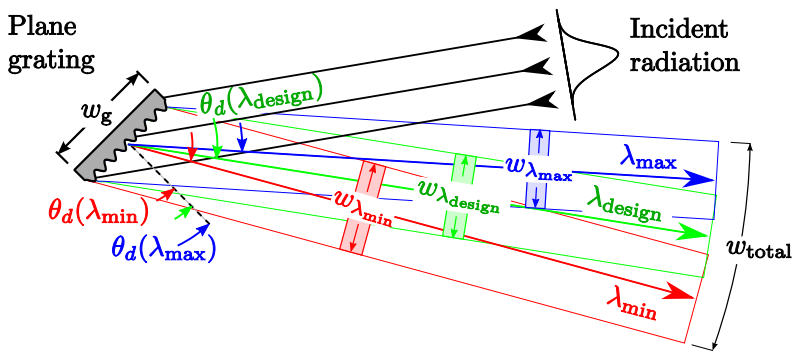

Figure K.9: The width of the diffracted beam depends upon θ_d as $w\sin(\theta_d)$. The smaller the value of θ_d the wider the diffracted beam. For M_2 centred upon λ_{design}, an asymmetry in the width either side of λ_{design} exists.

given by

$$w_\lambda = w\sin(\theta_d) \tag{K.26}$$

The apparent width is wider for smaller θ_d, so the width to be intercepted will be slightly asymmetric with respect to the design wavelength. With respect to the design wavelength ray, the width that the mirror must intercept is then

$$\begin{aligned} w_{\text{total}} = \quad & r\sin(\Delta\theta_{d\text{max}}) + r\sin(\Delta\theta_{d\text{min}}) \\ & +\tfrac{1}{2}w_{\lambda_{\text{max}}}\cos(\Delta\theta_{d\text{max}}) \\ & +\tfrac{1}{2}w_{\lambda_{\text{min}}}\cos(\Delta\theta_{d\text{min}}) \end{aligned} \tag{K.27}$$

where r is the distance from the diffraction grating to M_2 and

$$\Delta\theta_{d\text{max}} = \theta_d(\lambda_{\text{max}}) - \theta_d(\lambda_{\text{design}}) \tag{K.28a}$$

$$\Delta\theta_{d\text{min}} = \theta_d(\lambda_{\text{min}}) - \theta_d(\lambda_{\text{design}}) \tag{K.28b}$$

The first term in equation (K.27) is the orthogonal distance from the design wavelength principal ray for the principal λ_{max} and λ_{min} rays. The second and third terms in equation (K.27) are half the apparent width of diffraction grating projected onto the design wavelength principal ray.

Spherical mirrors are typically manufactured from a blank that is ground and polished into shape before the reflective surface is added. The diffracted beams intercepted by M_2 can be effectively obtained by a rectangle equivalent to the blank dimensions. The mirror is placed at an angle β to the design wavelength principal ray, obtained from equation 3.18 (page V.I - 132).

The radiation at the design wavelength is centred upon the array. The array surface normal is parallel with the principal ray at the design wavelength, as shown

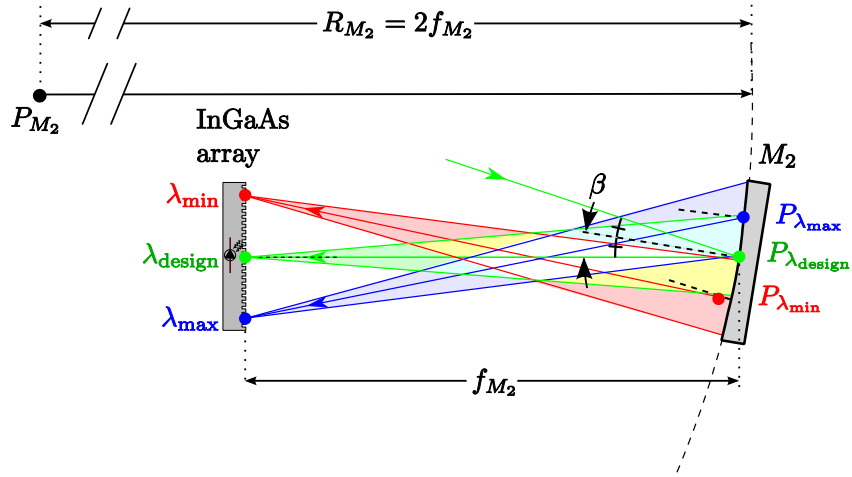

Figure K.10: The SpectroBragg resolution is the observed resolution at the InGaAs array. The SpectroBragg spectral range is denoted by λ_{min}(red circle) and λ_{max}(blue circle). The design wavelength is in the centre of the InGaAs array (green circle). The surface normals of the components are indicated with broken lines.

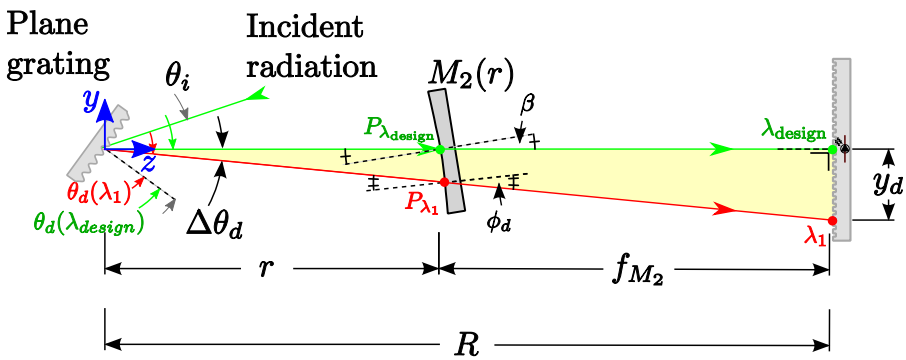

Figure K.11: The unfolded path of the diffracted design wavelength, λ_{design}, and the next resolvable wavelength, λ_1. The InGaAs array is oriented so that its surface normal is parallel to path of λ_{design}. The spatial separation at the array is $y_d = R \sin(\Delta\theta_d)$

in figure K.10. The array is situated at the focal point of M_2, f_{M_2}, at the design wavelength. The design wavelength is reflected from M_2 at an angle β.

The M_2 intercept positions of the principal rays at design wavelength λ_{design} and the spectral range delimiting wavelengths λ_{min} and λ_{max}, $P_{\lambda_{\text{design}}}$, $P_{\lambda_{\text{min}}}$ and $P_{\lambda_{\text{max}}}$, respectively, determine the position of the components. The optical paths shown in figures K.8 to K.10 are unfolded to produce a straight line for λ_{design} in figure K.11. The array is therefore a distance

$$R = r + f_{M_2} \tag{K.29}$$

from the diffraction grating, via mirror M_2.

The angular difference between the principal rays of λ_{design} and λ_1 is, as in equations (K.28), $\Delta\theta_{d1}$. The spatial separation, at the InGaAs array, is then

$$y_d = R \tan(\Delta\theta_{d1}) \tag{K.30}$$

K.4 References

[1] W. T. Welford. *Aberrations of optical systems*, chapter 7, pages 92–129. The Adam Hilger series on optics and electronics. Adam Hilger, Ltd., Bristol, 1986. ISBN: 0852745648.

[2] D. Korsch. *Reflective Optics*, chapter 6, pages 105–135. Academic Press, Inc., Boston, 1991. ISBN: 0124211704.

[3] J. F. James. *Spectrograph Design Fundamentals*, chapter 3, pages 10–27. Cambridge University Press, Cambridge, 2007. ISBN: 0521864631.

[4] D. S. Goodman. *General principles of geometrical optics*, volume 1 of *Handbook of Optics*, chapter 1. McGraw-Hill Companies, Inc., New York, 3 edition, 2010. ISBN: 0071498893.

[5] W. Brouwer and A. Walther. *Geometrical Optics*, chapter 16. Advanced Optical Techniques. North–Holland Publishing Co., Amsterdam, 1967.

[6] W. T. Welford. *Optical Calculations and Optical Instruments, an Introduction*, volume 29 of *Handbuch der Physik (Encyclopedia of Physics)*, chapter 1. Springer-Verlag, 1967.

[7] M. Born and E. Wolf. *Principles of Optics: Electromagnetic Theory of Propagation, Interference and Diffraction of Light*, chapter 5, pages 228–260. Cambridge University Press, Cambridge, 7th edition, 1999. ISBN: 0521642221.

[8] E. G. Loewen and E. Popov. *Diffraction Gratings and Applications*, volume 58 of *Optical Engineering*, chapter 12, pages 437–480. Marcel Dekker, Inc., New York, 1997. ISBN: 0824799232.

[9] BIPM JCGM 200:2008. International vocabulary of metrology - Basic and general concepts and associated terms (VIM), 2008.

[10] H. Gross. *Fundamentals of Technical Optics*, volume 1 of *Handbook of Optical Systems*, chapter 15, pages 759–813. Wiley-VCH Verlag GmbH & Co. KGaA, Weinheim, 2005. ISBN: 3527403779.

[11] H. H. Hopkins. *Wave Theory of Aberrations*, chapter 1, pages 1–20. Monographs on the Physics and Chemistry of Materials. Clarendon Press, Oxford, 1950.

[12] H. Gross, H. Zugge, M. Peschka, and F. Blechinger. *Aberration Theory and Correction of Optical Systems*, volume 3 of *Handbook of Optical Systems*, chapter 34, pages 431–593. Wiley-VCH Verlag GmbH & Co. KGaA, Weinheim, 2007. ISBN: 3527403795.

[13] D. Korsch. *Reflective Optics*, chapter 4, pages 63–83. Academic Press, Inc., Boston, 1991. ISBN: 0124211704.

[14] D. Korsch. *Reflective Optics*, chapter 8, pages 151–205. Academic Press, Inc., Boston, 1991. ISBN: 0124211704.

[15] H. Gross. *Fundamentals of Technical Optics*, volume 1 of *Handbook of Optical Systems*, chapter 11, pages 485–521. Wiley-VCH Verlag GmbH & Co. KGaA, Weinheim, 2005. ISBN: 3527403779.

[16] M. Born and E. Wolf. *Principles of Optics: Electromagnetic Theory of Propagation, Interference and Diffraction of Light*, chapter 9, pages 517–553. Cambridge University Press, Cambridge, 7th edition, 1999. ISBN: 0521642221.

[17] W. T. Welford. *Aberrations of optical systems*, chapter 8, pages 130–161. The Adam Hilger series on optics and electronics. Adam Hilger, Ltd., Bristol, 1986. ISBN: 0852745648.

[18] J. F. James. *Spectrograph Design Fundamentals*, chapter 4, pages 28–40. Cambridge University Press, Cambridge, 2007. ISBN: 0521864631.

[19] F. A. Jenkins and H. E. White. *Fundamentals of Optics*, chapter 9, pages 149–187. Physics Series. McGraw-Hill, 4 edition, 2001. ISBN: 0072561912.

[20] F. A. Jenkins and H. E. White. *Fundamentals of Optics*, chapter 6, pages 98–114. Physics Series. McGraw-Hill, 4 edition, 2001. ISBN: 0072561912.

[21] E. G. Loewen and E. Popov. *Diffraction Gratings and Applications*, volume 58 of *Optical Engineering*, chapter 2, pages 25–55. Marcel Dekker, Inc., New York, 1997. ISBN: 0824799232.

[22] W. T. Welford. *Aberration theory of gratings and grating mountings*, volume 4 of *Progress in Optics*, chapter 6. North–Holland Publishing Co., Amsterdam, 1965.

[23] J. F. James. *Spectrograph Design Fundamentals*, chapter 17, pages 172–174. Cambridge University Press, Cambridge, 2007. ISBN: 0521864631.

Appendix L

Assembly of the SpectroBragg

L.1 Collimation and configuration of radiation into the 75 mm plane

Collimation of the beam: Adjusted the longitudinal position of the fibre holder using the 3–axis micro–positioned to obtain spots of equal size at target positions (a) and (b), as measured using a graduated target.
Place in plane: Adjusted the vertical and lateral transverse position to locate the beam in the 75 mm plane. Using target position (b) made adjustments to target position (a) which produced faster convergence, due to the greater transverse displacement for a given angle at target position (b).

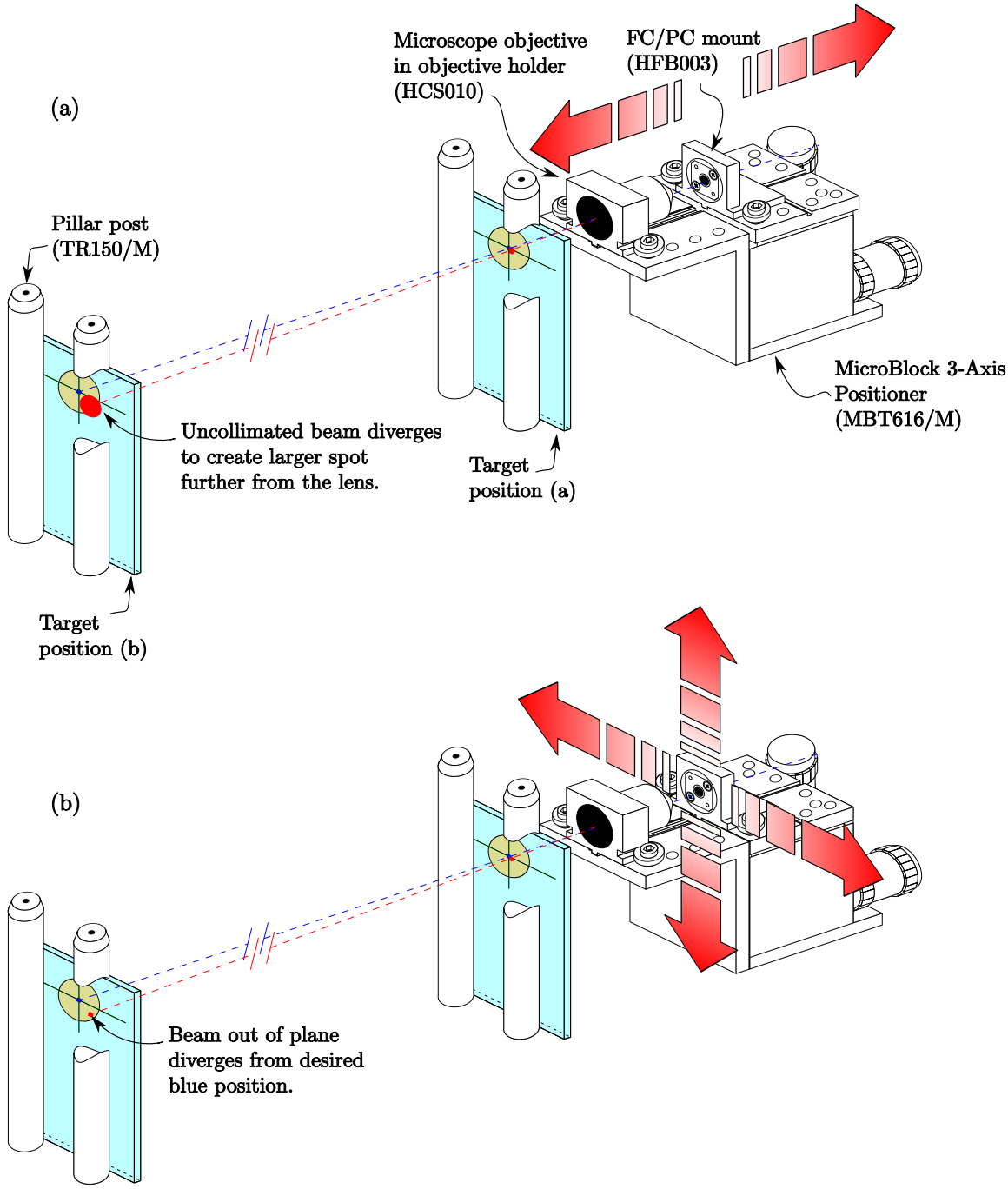

Figure L.1: (a) Collimating the beam, (b) Aligning the beam in the 75 mm plane.

L.2 Drawing alignment marks

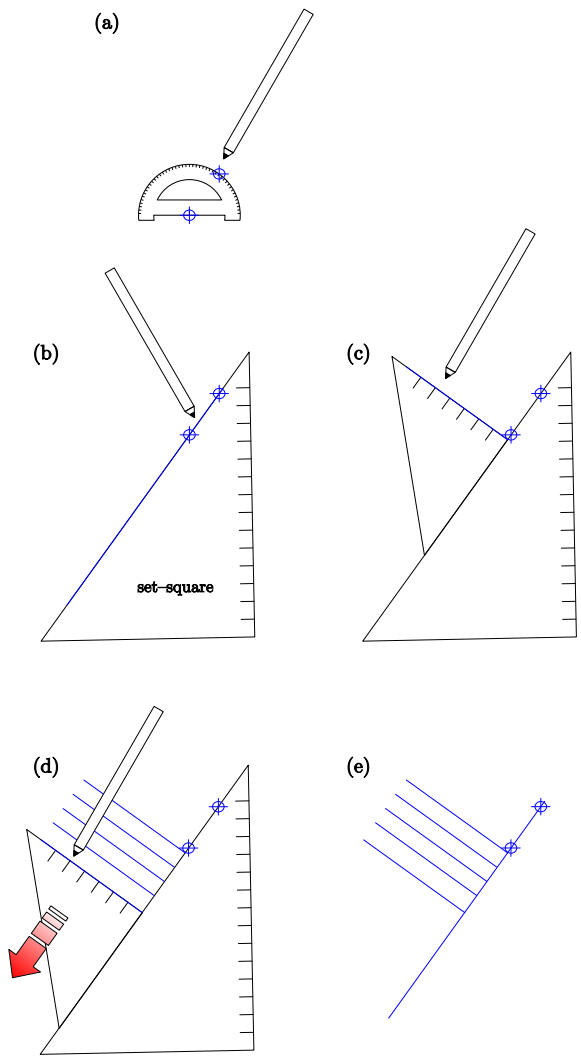

Figure L.2: Steps for the construction of alignment markings upon the optical bench.

a) Marked two points in the direction of the intended angle.
b) Placed set–square against two points, and marked line containing two points.
c) Placed second right–angle set–square along first set–square and marked orthogonal line.
d) Moved second set–square along edge of first set–square, and marked orthogonal lines at appropriate intervals.
e) The orthogonal lines were checked for accuracy with a protractor.

L.3 Steps required for the assembling of the SpectroBragg

Step 1. The SpectroBragg consisted of an FC/PC fibre mounted at the focal distance of a spherical mirror which collimated the radiation emitted from the fibre. The collimated radiation was reflected onto the diffraction grating. The diffracted radiation was focused by a second spherical mirror onto the *Hamamatsu G9214512S InGaAs array*.

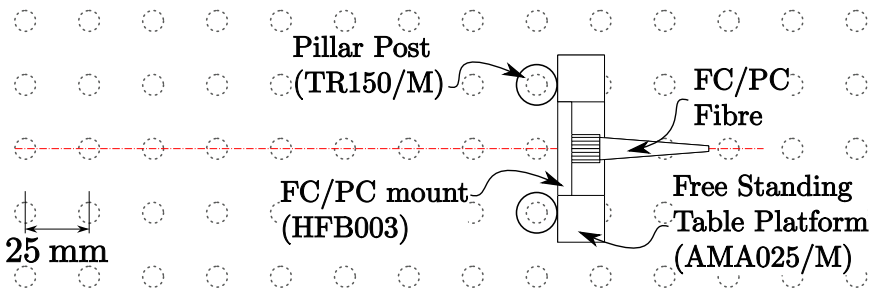

Figure L.3: TR150/M posts were placed one tapped hole apart, and abut AMA025/M platform against posts, locating the fibre holder centrally.

The principal optical plane of the apparatus was 75 mm above and parallel to the optical bench. The first step was to orient the *Thorlabs KS2D* mounts for ⌀50 mm optics[1] orthogonally to the optical bench. The regular square grid of tapped holes on the optical bench are used as the basis for the geometrical positioning, as indicated in figure L.3.

Two *Thorlabs TR150/M* pillar posts were placed one tapped hole apart. A *Thorlabs AMA025/M* free standing table platform with a *Thorlabs HFB003* FC/PC fibre mount flush with the left edge of the platform was abutted to the pillar posts, as illustrated in figure L.3. The AMA025/M was crudely entered by visual inspection at this stage.

Step 2. A previously collimated and 75 mm planed[2] *Thorlabs MBT616/M* 3–axis micro positioner with the FC/PC fibre was abutted against the AMA025/M, as illustrated in figure L.4. Either HeNe radiation at 632 nm or IR radiation at 1550 nm can be used at this stage of the assembly. The 632 nm does not require a converter but does go multi–mode in the SMF–28 fibre, producing intensity changes across the beam diameter. The 1550 nm stays single–mode but requires a converter card to be viewed. The accuracy of the collimation

[1] The KS2D is designed for ⌀2″ ≈ 50.2 mm optics.
[2] Following the instructions in appendix section L.1

should be checked with 1550 nm, as this is the operational centre frequency, if 632 nm is used.

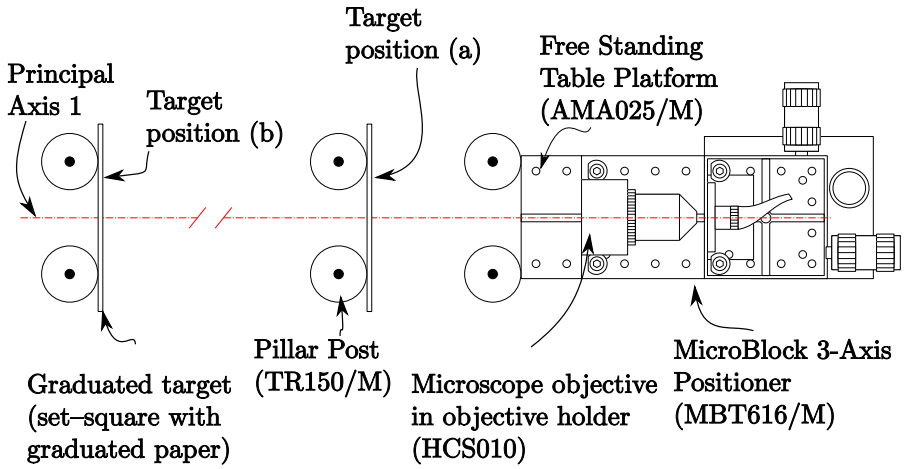

Figure L.4: Collimated fibre beam placed in 75 mm plane. MBT616/M and AMA025/M aligned over centre tapped hole.

Two sets of two TR150/M posts (one tapped hole apart) were positioned parallel to the first set of posts. The locations were labelled 'Target position (a)' and 'Target position (b)'. Target position (a) was close to the first set of posts, and Target position (b) was as far from the first set as possible, given the available space.

The MBT616/M was moved along the AMA025/M until it centred between the two posts, which was measured using a graduated target alternately at target positions (a) and (b). The MBT616/M was then fixed to the bench. The AMA025/M was then aligned with the MBT616/M using the channel on the MBT616/M and the AMA025/M (when aligned, the collimated beam from the MBT616/M will pass through the fibre mount hole of the HFB003). When the AMA025/M was aligned, it was fixed to the bench. The AMA025/M and MBT616/M specified the principal optical axis[3] for radiation into the eventual spectrometer in the 75mm plane, **principal axis 1**. The **principal axis 1** was marked on the bench by noting the location of the radiation on the graduated target, and marking the point on the bench directly below. A line through the marks at target positions (a) and (b) gave the vertical projection of **principal axis 1** onto the bench.

Step 3. The posts at target positions (a) and (b) were removed. A KS2D mount was fitted with a *Thorlabs PF*20-03-*P*01 50 mm plane mirror and placed into

[3]The axis of rotational symmetry of the expanding beam.

principal axis 1. As illustrated in figure L.5 the two sets of posts were placed orthogonally to **principal axis 1** to create new target positions (a) and (b). The KS2D was positioned so as to reflect radiation along **principal axis 1** onto target positions (a) and (b). By adjusting the KS2D, the reflected beam was made to lie in the 75 mm plane. The plane mirror was removed and placed into a second KS2D. The procedure was repeated to align the second KS2D. The two KS2Ds were then parallel to each other and perpendicular to the 75 mm plane. The KS2Ds held the collimating and focusing mirrors for the Čzerny–Turner mount. The posts at target positions (a) and (b) were removed.

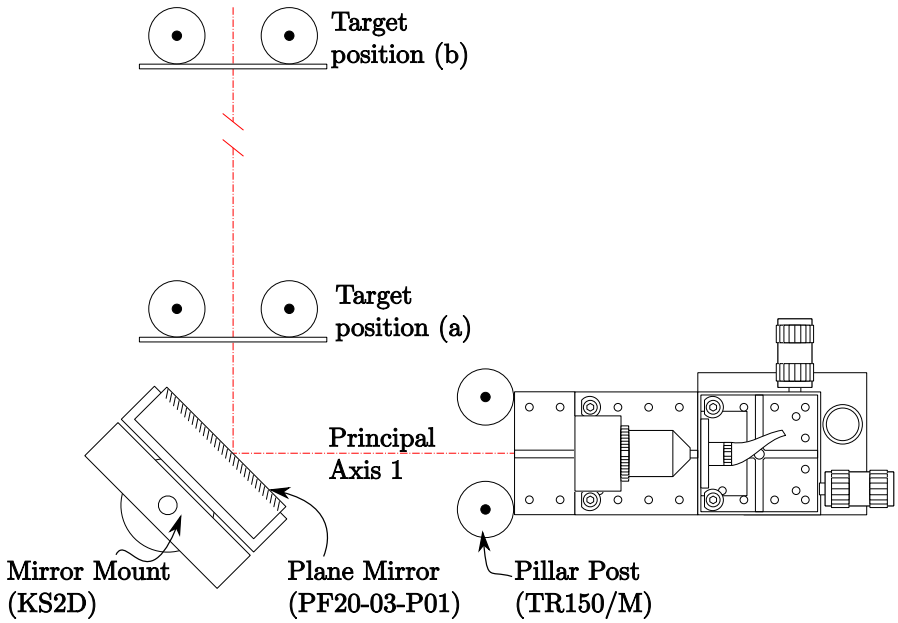

Figure L.5: Adjusted the KS2D mirror mounts to have their principal optical axis in the 75 mm plane, and orthogonal to the optical bench.

Step 4. The positioning of the spherical mirrors was the difficult part of the assembly for the collimating mirror. The alignment was constrained to the region of **principal axis 1** and the focal length of the mirror. A temporary construction facilitated the alignment of the collimating mirror and subsequent components. Two crossing, orthogonal lines[4] of equal length were drawn on a clean microscope slide, as illustrated in figure L.6 (page V.II L-8) and L.8 (page V.II L-10). The microscope slide was positioned so that the intersection of the crossed lines lay on **principal axis 1**. This was easily achieved by using

[4]The lines were drawn with a Compact Disc(CD) labelling pen ⌀0.7 mm.

the collimated radiation from the MBT616/M. The slide was fixed to the posts using double–sided adhesive tape.

Following the procedure outlined in appendix section L.2 (page V.II L-3), starting from approximately one focal length from the AMA025/M, a line (and perpendicular lines to this line) was drawn at the angle of the desired surface normal, as determined in section §3.2.2.1 (page V.I - 131). The perpendicular lines were parallel to the end position of the KS2D mount.

Step 5. The fibre was mounted into the HFB003 flush with the left edge of the AMA025/M, and the MBT616/M was removed. A *Thorlabs CM*508-150-*G*01 spherical mirror of focal length 15 cm was used as the collimating mirror. The CM508-150-G01 was mounted into one of the prepared KS2D mounts and positioned as illustrated in figure L.8 (page V.II L-10), to reflect radiation back along **principal axis 1**. When the collimating mirror surface had the FC/PC fibre aperture at its focal point, the radiation was collimated, and the size of the projected crossed lines at any distance was constant.

The fibre as mounted into the HFB003 flush with the left edge of the AMA025/M, and the MBT616/M was removed. A *Thorlabs CM*508-150-*G*01 spherical mirror of focal length 15 cm was used as the collimating mirror. The CM508-150-G01 was mounted into one of the prepared KS2D mounts and positioned as illustrated in figure L.8 (page V.II L-10), to reflect radiation back along **principal axis 1**. When the collimating mirror surface had the FC/PC fibre aperture at its focal point, the radiation was collimated, and the size of the projected crossed lines at any distance was constant.

Step 6. Figure L.7 shows the construction of the apparatus used to obtain the correct angle. The edge of the backplate 'L' was used to line up with a drawn line at the intended angle. The drawn line was aligned with the backplate by looking at the backplate at an angle such that the top and bottom of the backplate was aligned with the line at the base.

Step 7. The KS2D mirror was initially aligned with the perpendicular lines on the bench by moving one's point of observation back and forward over the KS2D until the edge of the KS2D overlapped one of the lines on the bench, as illustrated in figure L.9 (page V.II L-10).

The projected shadow of the backplate was minimised when the radiation fell on the edge only, as illustrated in figure L.10 (page V.II L-11). When the shadow was overlayed with the crossed lines from the microscope slide, the centre of the expanded beam was aligned on that angle, as illustrated in figure L.11, and for collimated radiation would be the width of the backplate. This

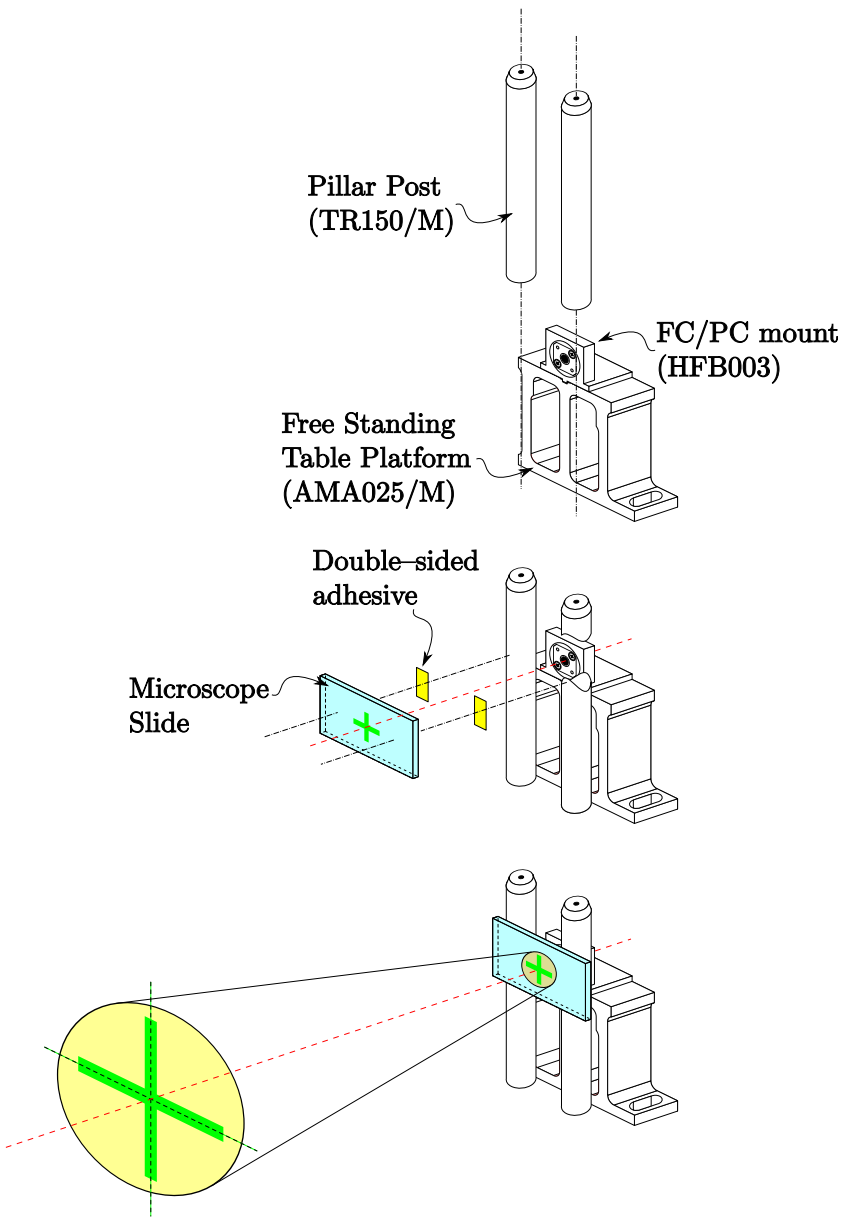

Figure L.6: Constructing the mark to indicate alignment of collimating mirror and subsequent components. The AMA025/M was abutted against two TR150/M posts. A microscope slide with orthogonal lines was placed centrally into the diverging beam, along the principal optical axis. The microscope slide was fixed with double–sided adhesive tape.

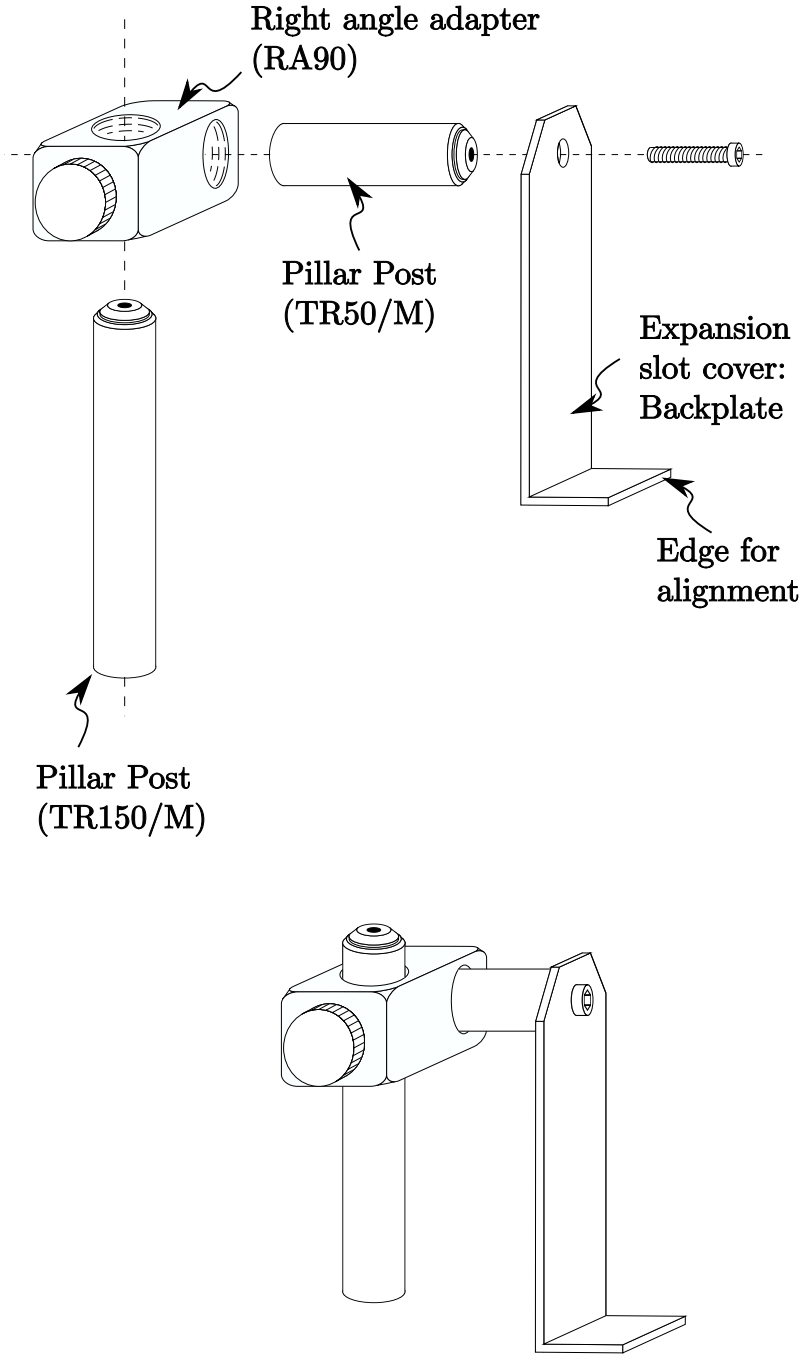

Figure L.7: Construction to determine proper angle: A computer expansion slot backplate was attached to a right angle adapter (RA90) via a short pillar post (TR50/M).

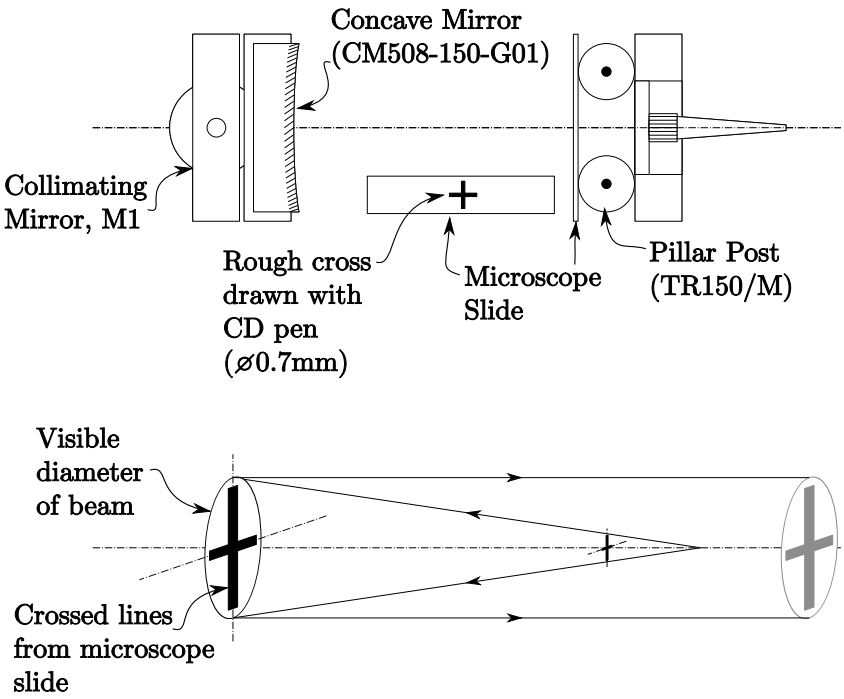

Figure L.8: Plan view of alignment target on principal optical axis. Spherical mirror was mounted in KS2D mount so as to reflect back along principal axis.

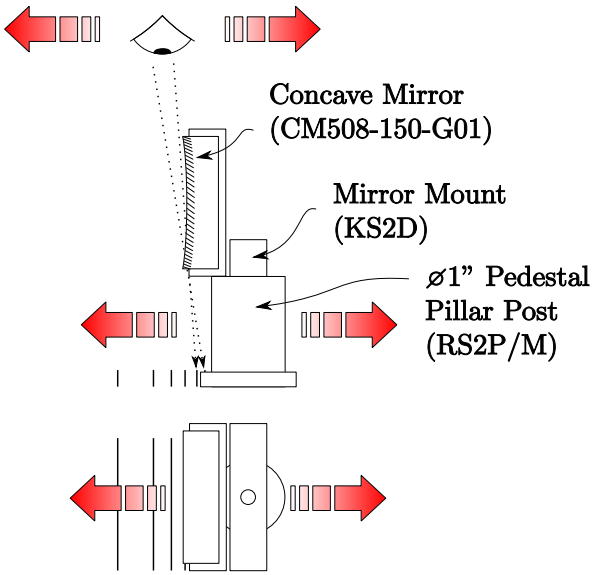

Figure L.9: The KS2D was aligned with the perpendicular lines. By moving the point of observation over the KS2D the edge of the KS2D and one of the lines on the bench was colocated. The KS2D was positioned by aligning the edge of the KS2D and the lines on the bench.

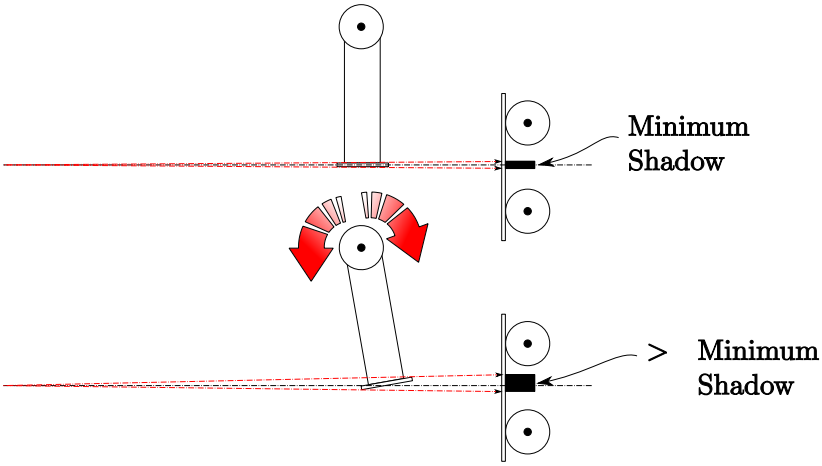

Figure L.10: By aligning the backplate, the projected shadow minimised. When the crossed lines were overlayed on the shadow the centre of the beam fell on edge of the backplate.

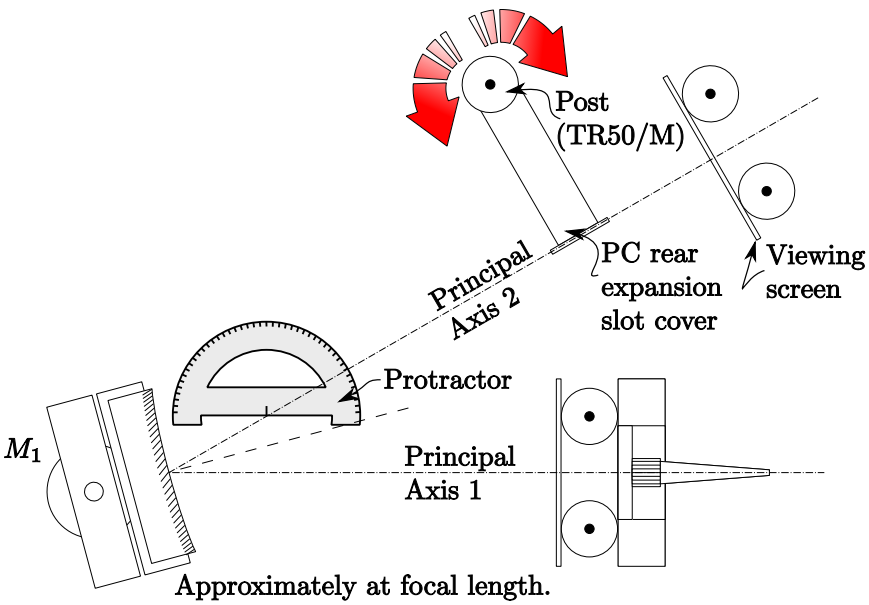

Figure L.11: The collimating mirror was aligned by projecting onto the backplate fixed at the desired angle.

step allowed a crude alignment of the mirror, but with no effective check on its collimation[5].

Step 8. The collimation of the KS2D was determined by placing the second KS2D with the PF20-03-P01 plane mirror to reflect the approximately 'collimated' beam parallel to **principal axis 1**, as illustrated in figure L.12. The second KS2D mount was oriented with respect to the first KS2D by the same procedure as illustrated in figure L.9.

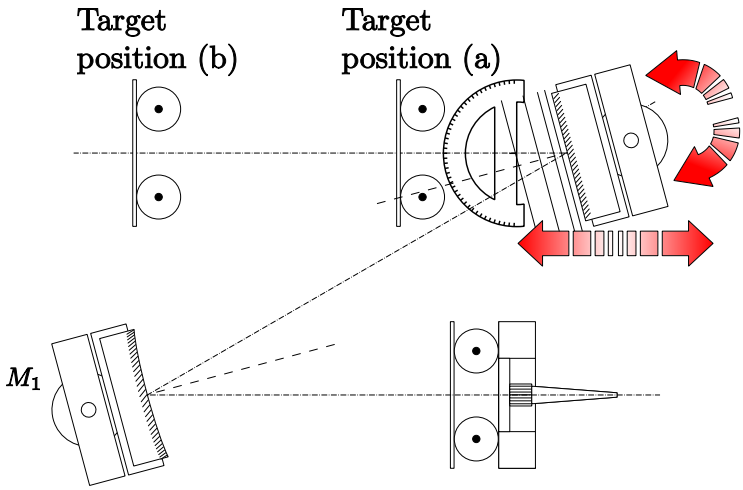

Figure L.12: A second KS2D mount parallel to the first KS2D but intercepting the collimated beam reflected the beam parallel to the expanding beam axis. The extra distance and alignment with the bench allowed for the collimation to be checked and corrected at the first KS2D.

For a collimated beam, it does not matter where it is intercepted by the second KS2D, as the radiation would be parallel. If the beam were nearly collimated, then the beam would expand or contract. By placing the two sets of posts at target positions (a) and (b), as indicated in figure L.12, the geometry of the bench holes allowed for alignment and collimation to be checked[6]. The reflected beam arrangement provides greater distance and, hence, larger deviations from collimation are apparent. The greater the distance the more accurate the collimation. By keeping the angle as constant as possible, collimation can be attained by moving the KS2D mount toward or away from the AMA025/M platform, as illustrated in figure L.13. The beam may be said to

[5]The PF20-03-P01 and CM508-150-G01 mirrors are manufactured from identical blank pieces of glass ground and polished into shape. The centre of the CM508-150-G01 is therefore recessed from the centre of the PF20-03-P01 by the need to curve the mirror surface. Simply replacing the PF20-03-P01 with the CM508-150-G01 does not produce equal results.

[6]This assumes that the two KS2D mounts are parallel, which may not be perfectly achieved.

be as close to collimation as possible when the location and dimensions of the crossed lines projected from the microscope slide do not change when observed from target positions (a) and (b)[7].

Step 9. It must be noted that, whether using the HeNe radiation at 632 nm or IR radiation at 1550 nm, the expanded beam is significantly darker than the collimated spot from the MBT616/M arrangement. This requires the use of near dark conditions, which makes accurate placement more challenging, considering the need to check alignment of the KS2D mounts with the lines on the bench. A distant (or dim) radiation source at, or barely above, the level of the bench was found to be the least worst solution. By looking vertically down onto the bench the radiation source did not interfere with observations, while at lower (nearer to horizontal) observer angles the low radiation provided enough contrast between the dark lines and brushed aluminium of the bench surface.

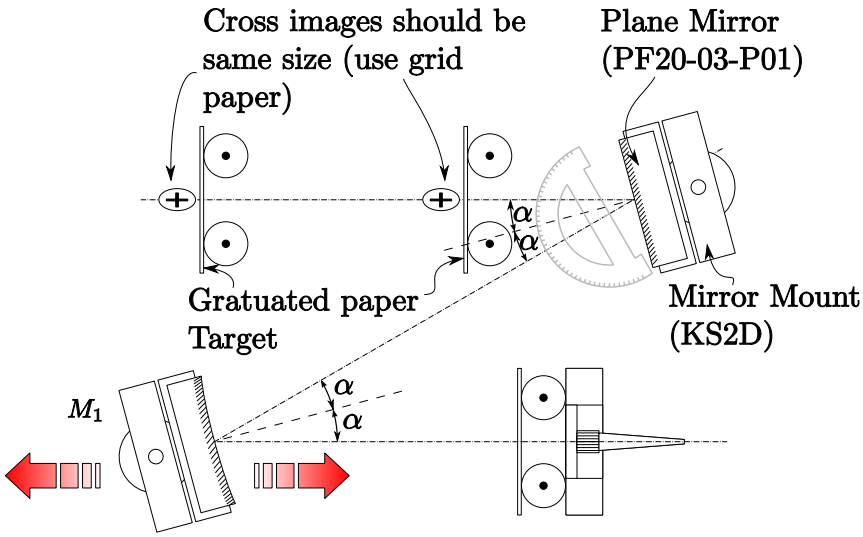

Figure L.13: The first KS2D mount was moved towards or away from the AMA025/M mount to obtain a collimated beam, as determined by the location and dimensions of the crossed lines projected from the microscope slide remaining unchanged at target positions (a) and (b).

There was no significant wavelength dependence[8] at this stage between the 632 nm HeNe or 1550 nm IR radiation for alignment; however, the diffraction

[7]Ideally a Fizeau interferometer would have been used to determine collimation, as is standard. A Fizeau interferometer was not available for the apparatus build and may not have had sufficient illumination to improve the collimation appreciably.

[8]Apart from the index of refraction difference at the fibre core/air boundary.

suffered by the 1550 nm IR radiation as it passed the crossed lines on the microscope slide produced a finer central dark region, that allowed for greater measurement of collimation. This was offset by the need to use an IR viewing card that saturated quickly and needed to be exposed to bright radiation prior to use to fluoresce under the low expanded beam. The exposure of the viewing card to bright radiation temporarily impaired low–light vision, which negated the benefit of the finer crossed line pattern. The eventual solution was to close one's eyes and illuminate the card under the optical bench with a torch held close to the IR viewing card.

The limitations on the apparatus build thus far have been the accuracy of the protractor determining angles and the need to align the components by reference to lines drawn on the optical bench. The protractor was the most limiting factor, as the alignment with the lines drawn on the bench proved to be effective at allowing repeatable positioning of components to high accuracy when the component moved during fixing to the bench. The angle limitation resulted in a deviation from the optimal aberration–correcting setup as calculated by the Rosendahl $\cos^3$ formula from the first KS2D mount onwards.

The **principal axis 2** was obtained by using the backplate to find the collimated beam angle. When the beam and backplate were aligned, a short line was drawn using the bottom of edge of the backplate. A line drawn parallel to this, and at a distance equal to the width of the bottom part of the backplate, provided the line parallel to the projected shadow. The **principal axis 2** was drawn on the optical bench.

Step 10. The next step was to place the diffraction grating mount with the diffraction grating into the collimated beam. The diffraction gratings quoted operational specifications were for collimated radiation, so every care was taken to obtain the best effort at collimation[9].

Bearing in mind the placement of subsequent components, both in terms of their physical volume, space needed for alignment and the need to obtain a small device footprint, a suitable location along **principal axis 2**, between the two KS2Ds was chosen. The surface normal of the diffraction gratings desired angle, mount alignment lines perpendicular to the normal, and the intended diffraction angle of 1550 nm radiation, **principal axis 3**, were drawn as illustrated in figure L.14.

Step 11. The backplate was aligned with **principal axis 3** so that the desired

[9]The Rosendahl $\cos^3$ formula (section §3.2.2.1 (page V.I - 131)) minimises the astigmatism and coma aberrations from the spectrometer as a whole, so aberrated radiation illuminates the diffraction grating even under 'ideal' circumstances.

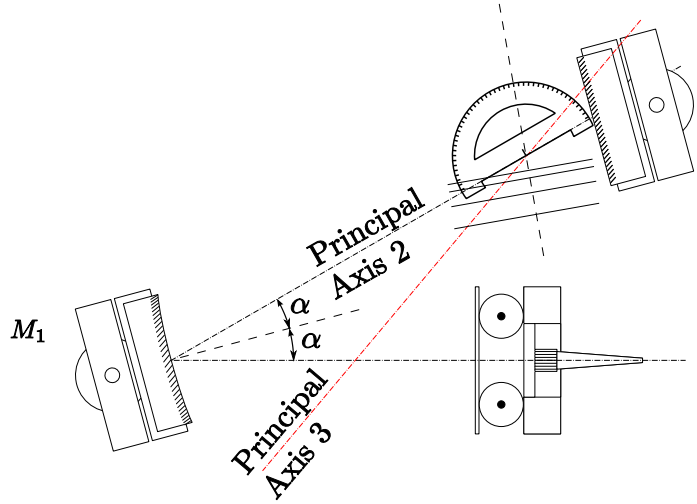

Figure L.14: At a point between the two KS2D mounts (and that allows for the placement of subsequent equipment) an angle 2α was marked out relative to the **principal axis 1**. Lines were drawn for the diffraction grating surface normal, alignment lines perpendicular to the grating surface normal and a line parallel to the intended diffracted beam at 1550 nm.

diffracted radiation would cast the minimum shadow onto target position (a). From this step onward only 1550nm[10] IR radiation could be used for alignment. The diffraction grating mount was placed to intercept **principal axis 2**, with the mount parallel to the alignment lines as illustrated in figure L.15. For a given diffraction grating only one position should satisfy both the alignment and diffraction line conditions. This allows for accurate placement of the diffraction grating mount.

The diffracted beam was not of the same geometry as the collimated beam it intercepted. As illustrated in figure L.15, the crossed lines in the approximately circular beam along **principal axis 2** were compressed in the 75 mm plane along **principal axis 3**, as a result of the angle at which the radiation intercepted the diffraction grating. The width of the crossed line parallel to the backplate was thus reduced, while the visibility was enhanced.

Step 12. With the diffraction grating mount in place, the alignment of the second KS2D, holding the focusing mirror was the next step. The positioning of the focusing mirror was not only constrained by the preceding components but also by the photodiode array mount, which occupied more bench space than

[10] Or the design central wavelength.

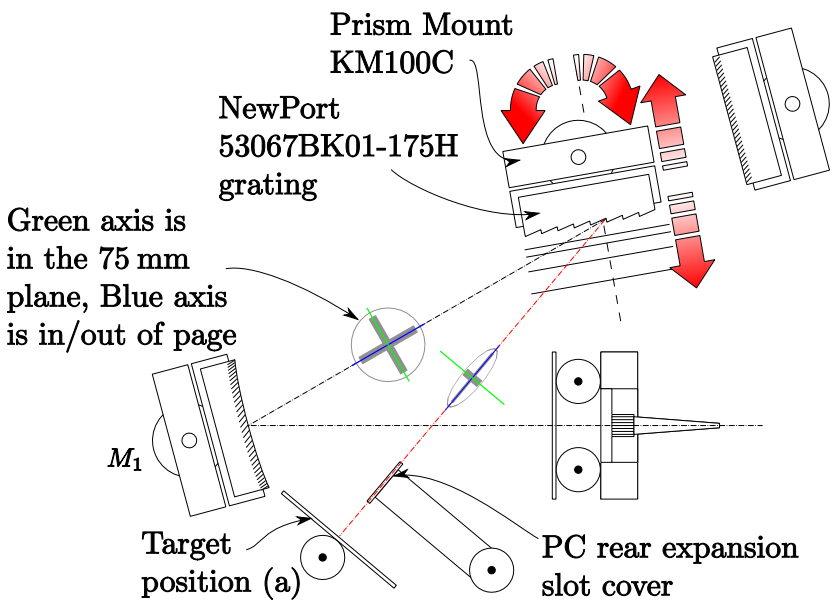

Figure L.15: The diffraction grating mount was aligned with the lines perpendicular to the drawn surface normal. The diffraction grating needed to intercept the collimated beam as fully as possible to maximise the diffraction for both resolution and visibility purposes.

any other single component. As the diffracted beam was still collimated (for a single wavelength), the focusing mirror was freely placed to facilitate the spectrometer design[11].

To provide the maximum flexibility, several potential KS2D surface normals were drawn on the bench, with perpendicular mount alignment lines and several potential **principal axis 4**s were drawn, as illustrated in figure L.16. With the restricted space available for both components and operator hands and tools, the drawn potential **principal axis 4**s were made as long as possible.

The Čzerny–Turner mount being constructed was not of a crossed Čzerny–Turner design. However, the angles at which the components needed to be placed in an uncrossed Čzerny–Turner layout here appear crossed. In a crossed Čzerny–Turner the focusing mirror would have reflected back toward the AMA025/m platform.

Step 13. With the preceding warnings about the placement of the photodiode array mount in mind, the focusing mirror KS2D was placed into **principal axis 3** as illustrated in figure L.17. The actual **principal axis 4** was located using the backplate and the focused beam both before and after the focal point where the

[11] By which is meant that focusing mirror locations which obstruct the beam are not considered.

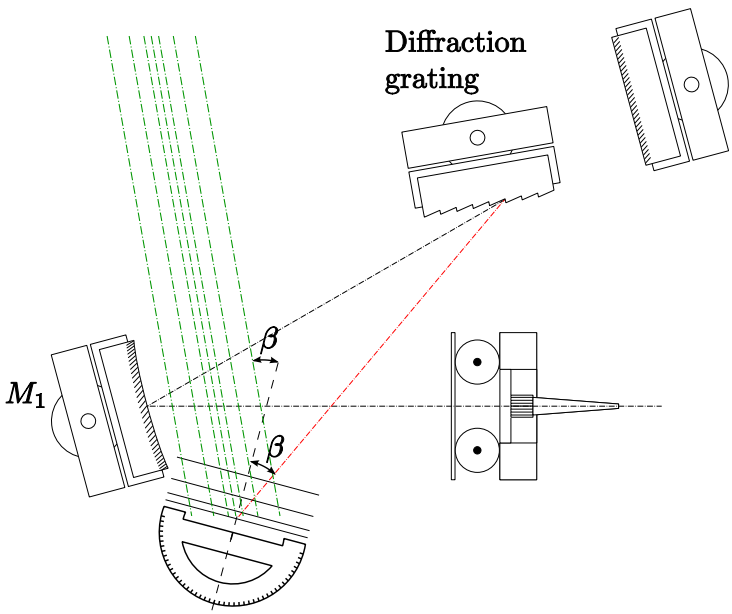

Figure L.16: A potential surface normal for the focusing mirror mount was drawn. Alignment lines perpendicular were marked to allow alignment of the focusing mirror's KS2D mount on the bench. Depending upon where focusing mirror intercepted **principal axis 3**, the reflected beam was offset. A series of parallel reflected lines were marked (in green).

beam expands again, using the same procedure as used to determine **principal axis 2**. On figure L.17, the focal point would be between target positions (a) and (b). By drawing the potential **principal axis 4** line long the alignment can be checked where the visibility of the focused beam is optimum.

The last step was to align the photodiode mount and the prism that reflected the beam 90° towards the bench. The photodiode mount did not allow the photodiode array to be placed into the 75 mm plane. Adjusting the other components up to the plane provided by the photodiode array would not have been possible with the components available. Additionally, fixing the photodiode array vertically to the bench would have been very difficult. The heat sinks along the edges did not provide good purchase for clamps, and the SCSI[12] cable that connected the photodiode array mount to the control electronics case was stiff enough to dislodge the photodiode array mount from any clamps available if the control electronics case or the SCSI cable were moved.

It was thus necessary for both optical and construction purposes to mount

[12]SCSI: Small Computer System Interface. The data communications were unlikely to have been SCSI protocols, but the cable was a SCSI cable.

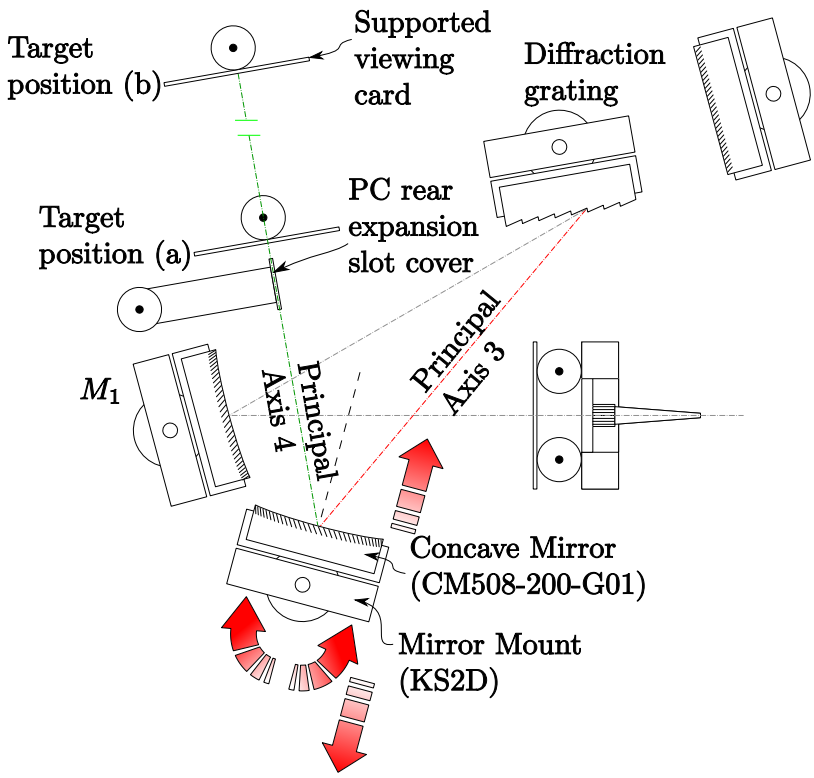

Figure L.17: The focusing mirror was placed to intercept **principal axis 3** without obstructing the beam path to preceding components. Additionally the reflected beam were not be obstructed by subsequent components. The actual **principal axis 3** was also determined using the focused beam before (target position (a)) and after the focal point(target position (b)).

the photodiode array parallel to, but offset from the 75 mm plane. A prism reflected the radiation perpendicular to the 75 mm plane by total internal reflection.

Step 14. To align the photodiode array perpendicular to **principal axis 4**, the potential **principal axis 4** lines were of use. The photodiode array was aligned so that **principal axis 4** passed over the photodiode array window, and the photodiode array mount was parallel to one of the potential **principal axis 4** lines, as illustrated in figure L.18.

Step 15. The photodiode array was now limited to movement along the **principal axis 4**, by using two *Thorlabs KL*02 adjustable kinematic locators. The KL02 used a screw driven ball bearing to fix components, allowing for more precise positioning than likely with bench clamps. The SCSI cable's tension was used to push against the KL02 clamps and kept the photodiode array mount in place, as illustrated in figure L.19.

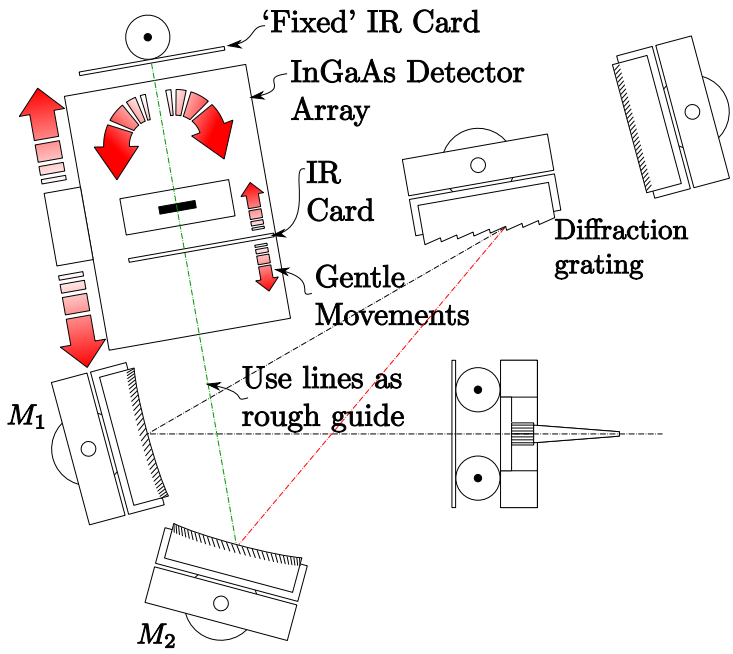

Figure L.18: The photodiode array mount was alinged co–linear with **principal axis 4**. By using the lines drawn parallel to **principal axis 4**, the photodiode array mount was positioned so the centre of the photodiode array was co–linear with **principal axis 4**; aided by using a fixed IR viewing card and a movable IR card.

Step 16. The prism was mounted on a cantilever based mount as shown in figure L.20. The location of the SCSI data cable connector on the side of the photodiode array mount and the location of the diffraction grating mount on the other side prevented the prism mount coming in from the side where one post would be sufficient. The space limitations were evident in the finished apparatus, shown in figure 3.10 (page V.I - 149).

Although the double cantilever approach was not ideal due to possible unsuppressed acoustic resonances, the RA90 and RA180 clamp were sufficient to suppress all but direct impacts with the optical bench. The weight of the platform and prism was not significant with respect to the weight of the TR150/M. A benefit of this arrangement was the elimination of most unwanted scattered radiation that may have been in the system, and which would appear as noise. Except for the array, the other components were in the 75 mm plane. Radiation that may have been scattered by these components would have had to be reflected by the prism onto the array.

Step 17. The prism mount was placed at the far end of the photodiode array mount, as illustrated in figure L.21. The prism and photodiode were moved together

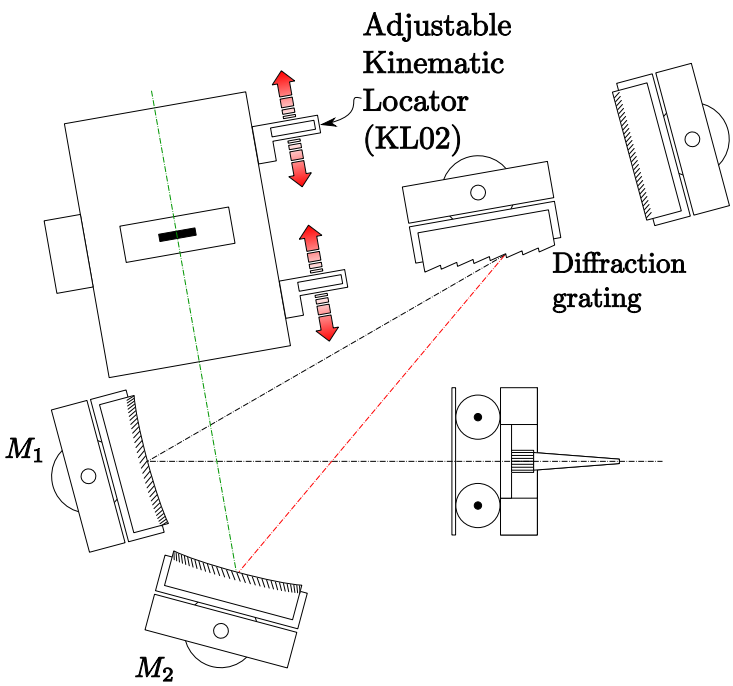

Figure L.19: The photodiode array mount was constrained to move parallel to **principal axis 4**. Using the stiff SCSI data cable and kinematic mounts, the photodiode array mount was adjusted for focusing.

to get the focal plane to coincide with the photodiode array.

The Rosendahl $\cos^3$ equation minimises astigmatism and coma aberrations; it does not remove them. As this formula is derived from assuming near paraxial incidence of the components, the setup here deviates from the theoretical ideal. Additionally, the small device footprint requirement means that the deviations are exacerbated. As such the whole photodiode does not lie in the focal 'plane' of the focusing mirror. These departures from the ideal case are one of the reasons for high resolution spectrographs being of the order of tens of meters and using a curved film holder to record the spectra, achieving better agreement with the theoretical limits. The differences in the SpectroBragg astigmatic focal planes was of the order of ~ 1 cm.

The dynamic range of a single FBG sensor demodulated in the SpectroBragg was such that it would not exhibit these optical aberrations as the measurand changed, so the SpectroBragg may be considered locally linear in response, despite being non–linear by design.

Step 18. With the prism mount correctly positioned over the photodiode array mount, the photodiode array was fixed into position, as illustrated in figure L.22. Two KL02 kinematic positioners were placed at the corners of the pho-

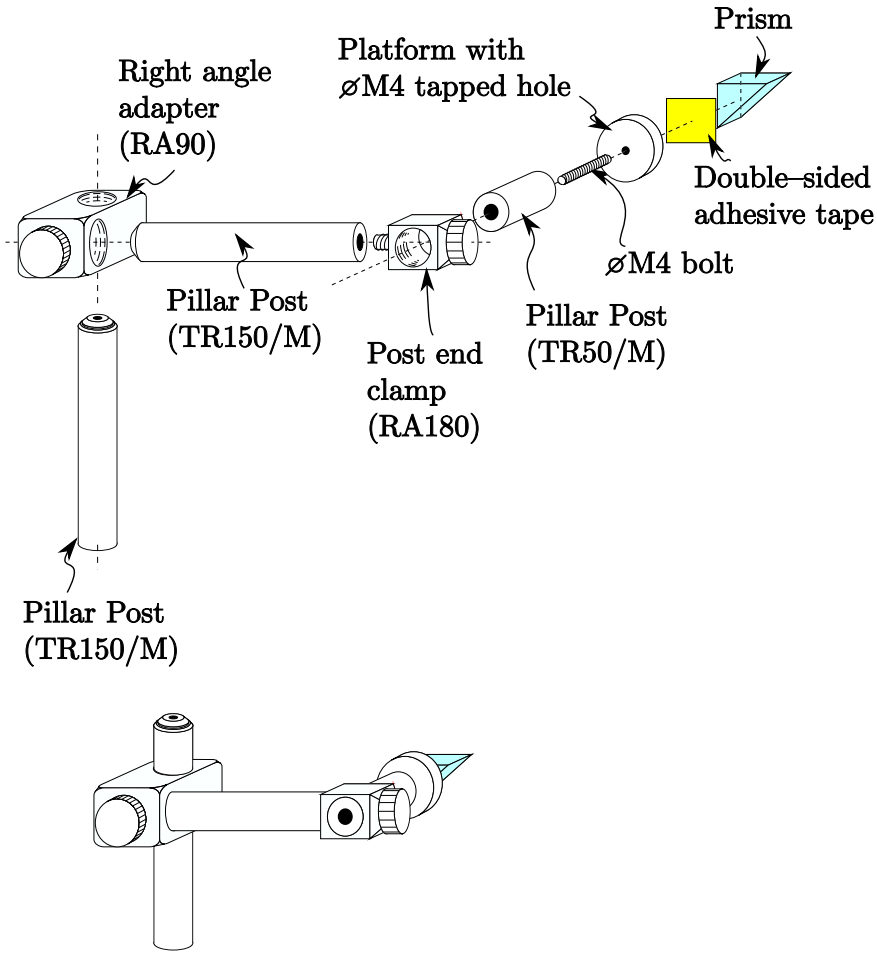

Figure L.20: Construction of the prism mount. An RA90 atop a TR150/M pillar post held a perpendicular TR150/M in the 75 mm plane with an RA180 post end clamp at the end ⌀M6 tapped hole. A TR50/M pillar post orthogonal to the TR150/m, but still in the 75 mm plane, held the prism with double–sided adhesive tape.

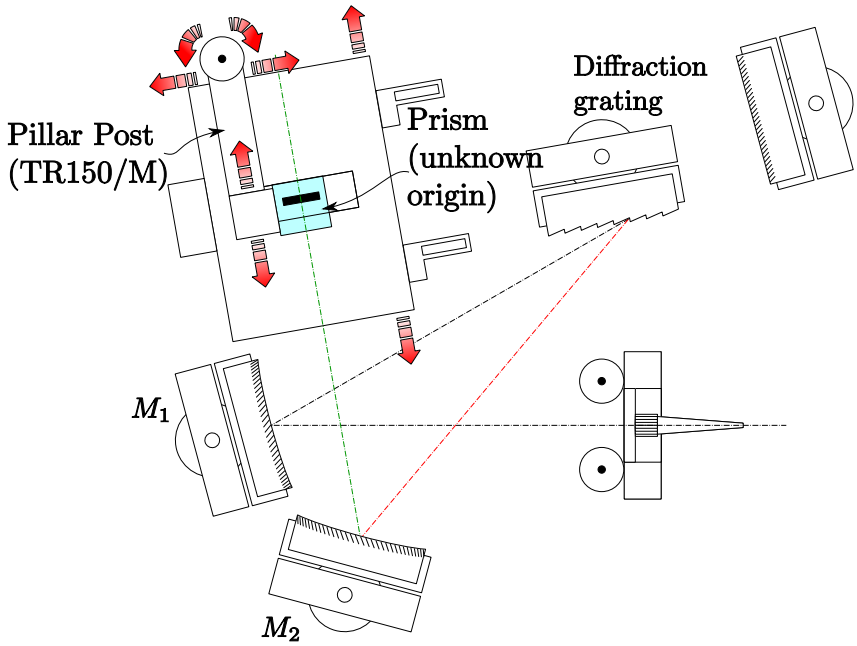

Figure L.21: The photodiode array mount and prism mount were adjusted to co–locate the photodiode array and focal plane of the focusing mirror. The photodiode array mount was constrained to move parallel to **principal axis 4**, but the prism mount was not. The prism was roughly aligned by using the brass housing of the window over the photodiode array, and adjusted by observing the captured spectra.

todiode array mount to prevent movement in the plane of the bench. The SpectroBragg construction was completed with this final step.

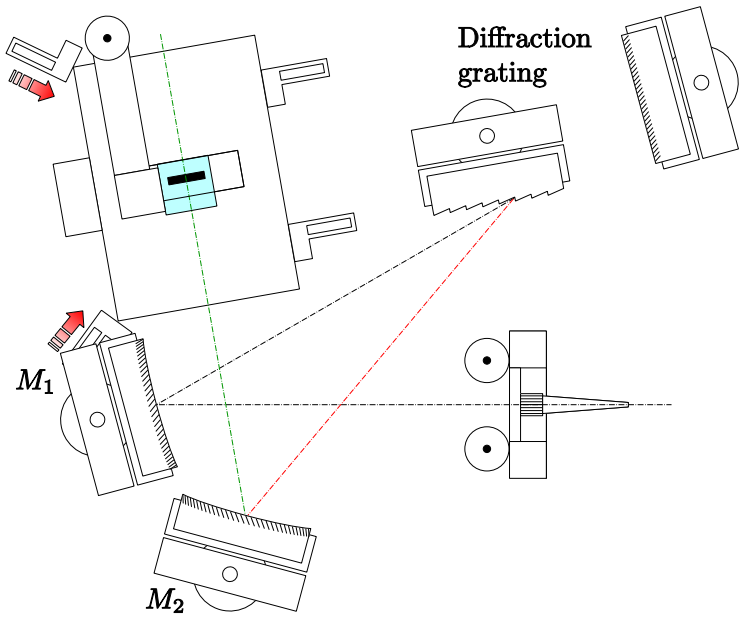

Figure L.22: The photodiode array mount was locked into final position with KL02 kinematic positioners at data cable side of mount.

Appendix M

Lyot Depolariser

A depolariser is a device which produces depolarised or pseudo–depolarised light which is mathematically equivalent to unpolarised light for the system in which it is being used. The Mueller matrix for a depolariser is [1]

$$\underline{\underline{\mathbf{M}}}_{\text{depolariser}} = \begin{pmatrix} m_{00} & 0 & 0 & 0 \\ 0 & 0 & 0 & 0 \\ 0 & 0 & 0 & 0 \\ 0 & 0 & 0 & 0 \end{pmatrix} \tag{M.1}$$

As is evident from the Mueller matrix for an ideal depolariser, where $m_{00} = 1$, the output will have the maximum intensity and a DOP= 0. For any S_{in}, the output Stokes vector will be

$$\begin{aligned} \underline{\mathbf{S}}_{\text{out}} &= \underline{\underline{\mathbf{M}}}_{\text{depolariser}} \underline{\mathbf{S}}_{\text{in}} \\ \underline{\mathbf{S}}_{\text{out}} &= \begin{pmatrix} m_{00} S_{in_0} \\ 0 \\ 0 \\ 0 \end{pmatrix} \end{aligned} \tag{M.2}$$

The vectorial nature of electromagnetic waves is suppressed, i.e. any polarisation–sensitive detector, or analyser, will not experience an intensity change in different orientations. This can be achieved if the input Stokes parameters, S_1, S_2 and S_3, change faster than the detector can follow, i.e. by time averaging [1]

$$S_i \frac{1}{T} \int_0^T m_{ij}(t) dt = 0 \qquad i, j = 0, 1, 2, 3;\ i \neq j = 0 \tag{M.3}$$

Two types of pseudo–depolariser are typically encountered in fibre optic systems. The first is termed a polarisation scrambler, and can depolarise monochromatic light, but over a minimum temporal window. For detection times greater than the tempo-

ral window, the light appears depolarised. Billings was the first to describe this type of monochromatic depolariser [2] using rotating retardation plates, and subsequent developments have used different temporally modulated effects (e.g. piezo–electrical, electro–optical) to achieve the desired result [1].

The second type depolarises light as fast as the radiation traverses the device, but over a minimum spectral window. For detector wavelength resolution in excess of the depolariser's spectral window, the light appears depolarised.

In 1928 Lyot reported a depolariser for astronomy and remote sensing of planetary surfaces [3]. The Lyot depolariser consists of two retardation plates oriented at $\pi/4$ to each other with relative retardations of $1:2$. When the same retarder material is used the physical lengths are in a $1:2$ ratio. The retardation of the plates is determined by the spectral bandwidth to be depolarised. The Lyot depolariser rotates the linear SOP through 2π linearly with λ, about the axis of propagation [1].

Similarly to equation (M.3), the spectral averaging of the SOPs satisfies [1]

$$S_i \int_{\lambda_1}^{\lambda_2} m_{ij}(\lambda) d\lambda = 0 \qquad i,j = 0,1,2,3; \quad i \neq j = 0 \tag{M.4}$$

The angle covered over the limits of the integral in equations (M.3) and (M.4) must be 2π[1] to provide depolarisation.

Equation (M.2) does not specify how to assemble the depolariser, only what the total effect must achieve [1]. The Lyot is amongst the simplest arrangements to satisfy equation (M.2).

The two retardation plates have retardances of δ_1 and δ_2, respectively. The combined Mueller matrix for both plates is [4]

$$\underline{\underline{\mathbf{M}}}_{\mathrm{Lyot}}(\theta, \Delta\phi_1, \Delta\phi_2) = \underline{\underline{\mathbf{M}}}_{\mathrm{WP}_2}(\Delta\phi_2, \theta = \pi/4)\, \underline{\underline{\mathbf{M}}}_{\mathrm{WP}_1}(\Delta\phi_1, \theta = 0) \tag{M.5}$$

$$= \begin{pmatrix} 1 & 0 & 0 & 0 \\ 0 & \cos 2\Delta\phi & \sin 2\Delta\phi \sin\Delta\phi & \sin 2\Delta\phi \cos\Delta\phi \\ 0 & 0 & \cos\Delta\phi & -\sin\Delta\phi \\ 0 & -\sin 2\Delta\phi & \cos 2\Delta\phi \sin\Delta\phi & \cos 2\Delta\phi \cos\Delta\phi \end{pmatrix} \tag{M.6}$$

where $\underline{\underline{\mathbf{M}}}_{\mathrm{WP}_i}$ is the Mueller matrix for retarding waveplate i, $\Delta\phi_i = \ell_i \Delta n = \ell_i(n_f - n_s)$ is the optical path difference between the retarder plate's orthogonal polarisation axes, Δn is the difference in refractive index and ℓ_i is the physical thickness of retarder i. θ refers to the angle of the waveplates eigenaxes with respect to the eigenaxes of the first retarder.

The retardance value of the second waveplate is twice that of the first waveplate,

[1] $2\pi = \omega T$, which gives $T \sim 5 \times 10^{-15}$ s [1].

$\Delta\phi_2 = 2\Delta\phi_1$, and [4]

$$\Delta\phi_1 > L_c, \qquad \Delta\phi_2 > L_c, \qquad |\Delta\phi_1 \pm \Delta\phi_2| > L_c \tag{M.7}$$

where L_c is either the coherence length of the signal, or the equivalent coherence length of the smallest spectral element observed by the detector, if smaller than the input signal.

If the pseudo–depolarised light is passed through a second identical Lyot, oriented at $\pi/2$ to the first Lyot, the original SOP can be recovered [4]. This is why the signal is pseudo–depolarised and not depolarised. The light only appears to be depolarised when appropriately observed. Using an inappropriate detection system may result in worse total system performance as phase and polarisation intensity modulation can arise, instead of only polarisation intensity modulation.

The Lyot depolariser decoheres the signal during the depolarisation, as the orthogonal axes are delayed by the retarding waveplates. From equation (B.22) (page V.II B-6), the decoherence will result in a spectral broadening when compared to the incident signal. Assuming the mean wavelength, λ_0, remains unchanged, the change in coherence length of the output signal is

$$\frac{\partial \Delta_{\lambda_0}}{\partial L_c} = \frac{\partial}{\partial L_c}\left(\frac{\lambda_0^2}{L_c}\right) = -\frac{\lambda_0^2}{L_c^2} \tag{M.8}$$

M.1 References

[1] E. Collett. *Polarized Light in Fiber Optics*, chapter 12, pages 319–354. SPIE Press/Polawave Group, New Jersey, nov 2004. ISBN: 0819457612.

[2] B. H. Billings. Monochromatic depolarizer. *J. Opt. Soc. Am.*, 41(12):966–975, 1951.

[3] C. Brosseau. *Polarization and coherence optics: Historical perspective, status, and future directions*, volume 54 of *Progress in Optics*, chapter 3. Elsevier, Amsterdam, 2009. ISBN: 9780444535283.

[4] S. Huard. *Polarization of Light*, chapter 5, pages 179–242. John Wiley & Sons, Ltd., London, feb 1997. ISBN: 0471965367.

Appendix N

Polarisation experiments figures

This appendix contains the more fully developed results for the various polarisation mitigation approaches examined in chapter 5 (page V.I - 218), §5.4.5 (page V.I - 249). This material, summarised in table 5.1 (page V.I - 248), is lengthy and so separated into subsections that deal only with the approach under consideration.

The results consist of tables comparing the control experiment and the polarisation mitigation approach under consideration, in terms of two quantities for both the signal intensity, $\rho_{\text{Int.}}$ & $\sigma_{\text{Int.}}$, and centroid calculated wavelength, ρ_{λ_B} & σ_{λ_B}, as described in §5.4.4.2 (page V.I - 246).

The cross–correlation coefficient, $\rho_{\text{Int.}}$ is used as a measure of the preservation of the pattern of changing SOP. As the SpectroBragg and Polarimeter had different absolute intensity level readings, and different sensitivities to changing SOP, the direct comparison of the different SpectroBragg data and polarimeter data was facilitated by normalising the standard deviations of the data by dividing by their mean intensity level, $\sigma_{\text{Int.}}$.

The motivation for the use of $\rho_{\text{Int.}}$ is that the polarisation mitigation devices are designed to remove the effects of changing SOP from the eventual signal recovered, and even where the normalisation process apparently enhances the oscillation magnitude, the ideal performance of the polarisation mitigation approach under test would be to reduce this correlation and oscillation magnitude.

The SpectroBragg provided a peak wavelength value, λ_B, when used with the centroid algorithm[1]. The effect of the applied SOP changes upon λ_B is quantified in terms of the normalised standard deviation σ_{λ_B}, using the same approach as for $\sigma_{\text{Int.}}$.

The second quantity, the correlation coefficient ρ_{λ_B}, is more speculative, as there is not a linear relationship between the centroid calculated value and the maximum intensity. The non–linearity of this relationship is briefly discussed in appendix

[1] λ_B was calculated using a window width $2n_w + 1; n_w = 7$.

O (page V.II O-1). Hence, a large correlation coefficient would indicate that the applied SOP changes dominate the centroid calculation, while a low correlation merely indicates that the centroid calculation is not dominated by the applied SOP changes. It does not infer improved performance.

The original and filtered SpectroBragg captured data and the polarimeter data are presented for the integer rotation and phase retardation angles, θ_{rot} & ϕ_{pr} respectively, which returned the largest $\rho_{\text{Int.}}$ [2] and are shown in both figures and tables.

The temporal cross–correlation, $\mathcal{R}_{\text{Int.}}$, of the unfiltered and filtered SpectroBragg and the polarimeter data is also plotted. The centroid calculated λ_B values for the original and filtered SpectroBragg data, as used in calculating ρ_{λ_B} & σ_{λ_B}, are also plotted.

The FFT filtering of the data has, on occasion, made the background level larger by introducing Gibbs effect oscillations. These have been left as is, and used in the comparison, as similar Gibbs effect oscillations may occur in the data and the removal from the background quantity but not from the applied SOP changes quantity could not be justified.

Finally, the Poincaré sphere representations of the different Stokes vectors are plotted[3]. As the Poincaré sphere is a three–dimensional structure, the Poincaré sphere is shown along the positive and negative Stokes parameter axes[4].

N.1 Control Experiment

In the following discussions of the various depolarisation approaches, the polarimeter data should exhibit no substantial change if the SOP changes applied were equivalent. Ideally, the SpectroBragg data should show reduced sensitivity to the SOP changes with the polarisation mitigation approaches.

Both the intensity values, $\rho_{\text{Int.}}$ & $\sigma_{\text{Int.}}$, and centroid determined wavelength values,

[2] Restating, equations (5.25) (page V.I - 239) & (5.29) (page V.I - 240), the modelled Stokes vector at the SpectroBragg is

$$\underline{\mathbf{S}}_{\text{SB}} = \left[\underline{\underline{\mathbf{M}}}_{\text{TE}} + \underline{\underline{\mathbf{M}}}_{\text{TM}}\right] \underline{\mathbf{S}}_{\text{in}}; \qquad \underline{\mathbf{S}}_{\text{in}} = \underline{\underline{\mathbf{M}}}_{\text{rot}}\, \underline{\underline{\mathbf{M}}}_{\text{pr}}\, \underline{\mathbf{S}}_{\text{pol}}$$

where $\underline{\underline{\mathbf{M}}}_{\text{TE}}$ and $\underline{\underline{\mathbf{M}}}_{\text{TM}}$ are the Mueller matrices for orthogonal linear polarisers, describing the idealised diffraction grating, and $\underline{\underline{\mathbf{M}}}_{\text{TE}} = \frac{1}{2}\underline{\underline{\mathbf{M}}}_{\text{TM}}$; $\underline{\mathbf{S}}_{\text{pol}}$ is the Stokes vector captured by the polarimeter; $\underline{\underline{\mathbf{M}}}_{\text{rot}}(\theta_{\text{rot}})$ is the Mueller matrix describing a rotation of the axes by angle θ_{rot}; and $\underline{\underline{\mathbf{M}}}_{\text{pr}}(\phi_{\text{pr}})$ is the Mueller matrix describing a phase retardation of the orthogonal components by the phase angle ϕ_{pr}.

[3] The Thorlabs IPM5300 polarimeter double normalised S_1, S_2, S_3 such that they always equal one, irrespective of the actual DOP.

[4] An additional representation, using the azimuthal equidistant projection, is shown in §N.6 (page V.II N-59). This allows for a comparison of the Poincaré sphere coverage achieved by the different datasets.

ρ_{λ_B} & σ_{λ_B}, are tabulated for the systems under test for the anisotropic and isotropic FBGs, in table N.1. These are the values against which the effectiveness of the different polarisation mitigation schemes will be compared.

Quantity	FBG			Control	
(a) $\rho_{\text{Int.}}$	Aniso.		$\lvert\rho_{\text{Int.}}\rvert$	0.22	(0.28)
			θ_{rot}	125°	
			ϕ_{pr}	−50°	
	Iso.		$\lvert\rho_{\text{Int.}}\rvert$	0.20	(0.18)
			θ_{rot}	130°	
			ϕ_{pr}	72°	
(b) $\sigma_{\text{Int.}}$ (pm)	Aniso.	SB.	w. ΔSOP	0.25	(0.56)
			background	0.07	(0.03)
		Pol.	w. ΔSOP	0.38	(0.56)
			background	0.04	(0.03)
	Iso.	SB.	w. ΔSOP	0.13	(0.18)
			background	0.03	(0.001)
		Pol.	w. ΔSOP	0.50	(0.55)
			background	0.07	(0.18)
(c) σ_{λ_B} (pm)	Aniso.		w. ΔSOP	5.80	(7.41)
			background	0.25	(0.07)
	Iso.		w. ΔSOP	0.88	(1.05)
			background	0.88	(0.28)
(d) $\lvert\rho_{\lambda_B}\rvert$	Aniso.			0.24	(0.40)
	Iso.			0.46	(0.46)

Table N.1: Summary of control experiment **(a)** correlation coefficient, $\rho_{\text{Int.}}$, values for correlation between captured SpectroBragg intensity and calculated S_{SB}. In subsequent tables, the rotation and phase retardation angles which produced the value are listed under the $\rho_{\text{Int.}}$ value; **(b)** the FFT filtered and unfiltered (in parentheses) normalised standard deviations, $\sigma_{\text{Int.}}$, for both SpectroBragg and polarimeter data. The values are for the data with and without applied SOP changes (i.e. background); **(c)** the FFT filtered and unfiltered (in parentheses) standard deviation of centroid calculated wavelength, σ_{λ_B}, for the anisotropic and isotropic FBGs; **(d)** the SpectroBragg intensity–centroid λ_B correlation coefficient, ρ_{λ_B}, as a measure of intensity pattern's influence on λ_B.

The cross–correlation coefficient, $\rho_{\text{Int.}}$, values for the SOPs changes for both the anisotropic and isotropic FBGs are shown in table N.1(a). The anisotropic FBG $\rho_{\text{Int.}}$ value is $\sim$ 110% the isotropic FBG value. This is as expected, as the anisotropic FBG signal is a polarising reflector in addition to experiencing the polarisation changes in the fibre leads which are common to the isotropic FBG signal.

It should be noted that the $\rho_{\text{Int.}}$ values are not close to one, i.e. a very good correlation. The fibre leads between the polarimeter and the SpectroBragg are unlikely to have only acted as ideal SOP phase retarders and rotators. The SpectroBragg is both phase and polarisation–sensitive, whereas the polarimeter measured the SOP only[5].

The normalised standard deviation values, $\sigma_{\text{Int.}}$, for the SpectroBragg data and polarimeter data, for both the anisotropic and isotropic FBGs are shown in table N.1(b). The polarimeter only returns the polarised component of a signal. The degree of polarisations for all the data reported were approximately equivalent[6] for the different mitigation approaches.

The standard deviation of the centroid calculated wavelength, σ_{λ_B}, of the original data and the FFT filtered data are shown in table N.1(c). The two values are presented for completeness. These are the standard deviations for the data plotted in figures N.5 (page V.II N-12) and N.6 (page V.II N-12). Reductions in these values represents an improvement in the quantity ultimately measured by the SpectroBragg.

Also shown are the σ_{λ_B} values in the absence of the applied SOP changes, i.e. the background σ_{λ_B} value. For the filtered σ_{λ_B} values, this provides a figure to compare the magnitude of the introduced Gibbs effect. The anisotropic FBG, as is evident in figure N.5 (page V.II N-12), exhibits an increase in σ_{λ_B} when the SOP changes are applied, whereas the isotropic FBG begins with a comparatively large σ_{λ_B} and remains at that value.

Finally, $|\rho_{\lambda_B}|$, shown in N.1(d), is the SpectroBragg data intensity–λ_B correlation coefficient, to give an indication as to how similar the centroid calculated λ_B values are to the intensity values. If the oscillation in intensity corresponds to the oscillations in λ_B, then the applied SOP changes appear as wavelength changes of the sensor FBGs. Low values do not infer an improved situation, as the respective σ_{λ_B} may still be large. However, it does indicate that the applied SOP changes are not directly correlated with the centroid λ_B value.

Figures N.1 (page V.II N-8) & N.2 (page V.II N-9) show the Poincaré sphere representations of the SOPs for the anisotropic and isotropic FBGs, respectively. The views are along the $\pm S_1$, $\pm S_2$ and $\pm S_3$ axes, as foreground points may mask background points. Figures N.3 (page V.II N-10) to N.6 (page V.II N-12) show the data used in these calculations. Figure N.3(a) (page V.II N-10) shows the data captured by the SpectroBragg. This data should not have contained phase noise from the sources encountered later as there was no Mach–Zehnder interferometer

[5]The phase retardance between orthogonal components at the SpectroBragg detector would add incoherently, so the phase sensitivity of the SpectroBragg refers to interferometrically coupled phase, from the diffraction grating, in the same orientation.

[6]The standard deviation of the DOP was within ±4%.

or phase noise introducing apparatus present. A low frequency modulation was observed, however, and was removed to facilitate comparison with the following datasets, where the FFT filtering did remove interferometrically coupled phase noise.

The FFT filtered version of the SpectroBragg data is shown in figure N.3(b) (page V.II N-10). A Gibbs effect oscillation is observed at the beginning of N.3(b) (page V.II N-10) and windowing was not used to remove it due to the greater distortion this would introduce during the cross–correlation calculation[7].

Figure N.3(c) (page V.II N-10) shows the calculated output from the polarimeter data after passing through the idealised phase retardation/rotation/diffraction grating Mueller matrix. Figure N.3(d) (page V.II N-10) shows the FFT filtered version of N.3(c) (page V.II N-10), which again exhibits a Gibbs effect oscillation at the beginning of the data.

Figure N.3(e) shows the temporal cross–correlation, $\mathcal{R}_{\text{Int.}}$, of figures N.3(b) (page V.II N-10) and N.3(d) (page V.II N-10) [8]. Figure N.3(e) (page V.II N-10) provides a visual indication of how much the changes in the pattern of intensity at the polarimeter are preserved as intensity change patterns at the SpectroBragg.

The absence of any prominent features, indicates that the FFT filtering has removed the low frequency phase noise related oscillations. The slightly asymmetric and broad peak, however, indicates that the cross–correlated features are temporally shifted with respect to each other.

This may be due to a synchronisation error in the datasets, or the slight one period oscillation that N.3(b) (page V.II N-10) and N.3(d) (page V.II N-10) appear to exhibit. As these one period oscillations are roughly π out of phase, the broad peak may be an artefact of this oscillation. It is likely that the FFT filtering may have introduced this one period oscillation.

Figure N.4 (page V.II N-11) shows the corresponding data for the isotropic FBG. Figure N.4(e) (page V.II N-11) is more symmetric and featureless than for the anisotropic FBG. The absence of the one period oscillation in N.4(b) (page V.II N-11) and N.4(d) (page V.II N-11) corresponds with the cross–correlation peak being symmetrical and narrower.

Figures N.5 (page V.II N-12) and N.6 (page V.II N-12) show the calculated centroid wavelength λ_B from the SpectroBragg data. Figure N.5(a) (page V.II N-12) shows the original, unfiltered centroid calculated wavelength, λ_B, and N.5(b) (page V.II N-12) shows the FFT filtered centroid wavelength of the SpectroBragg data. The standard deviations of the background and the applied SOP changes are listed in

[7] For example, correlating the applied Hamming window profiles.

[8] Figure N.3(e) (page V.II N-10) differs from the correlation coefficient presented in table N.1(a) in that it shows the cross–correlation of all the data plotted in figure N.3(b) (page V.II N-10) and N.3(c) (page V.II N-10). The correlation coefficient is calculated for the changing SOP part of the dataset only.

table N.1 (page V.II N-3) with the correlation coefficient of the centroid calculated SpectroBragg λ_B from N.5(c) (page V.II N-12) and SpectroBragg intensity from N.3(d) (page V.II N-10).

The same presentation of information is applied for all the polarisation mitigation approaches discussed subsequently.

As expected, the anisotropic FBG λ_B exhibits greater changes than the isotropic FBG λ_B. These values of λ_B for FBGs experiencing nominally stable laboratory conditions would limit the use of FBGs as sensors, but the applied SOPs changes are unlikely to be encountered intentionally[9]. Where the fibre leads to an FBG sensor are generally considered passive and non–contributory to the desired measurand, figures N.5 (page V.II N-12) and N.6 (page V.II N-12) may lead to incorrect readings or the assumption that the sensor is unusable.

This provided the motivation for the work in chapter 5. An effective polarisation mitigation scheme could assist in determining the existance and extent of non–polarisation based problems, while allowing greater sensitivity to be achieved where polarisation based problems occur.

Figures N.7 (page V.II N-13) and N.9 (page V.II N-14) show the correlation coefficient, $\rho_{\text{Int.}}$, as a function of changing θ_{rot} and ϕ_{pr}, for the anisotropic and isotropic FBGs, respectively. Figures N.8 (page V.II N-13) and N.10 (page V.II N-14) show the corresponding orthogonal cross sections, the (a) figures along θ_{rot} and the (b) figures along ϕ_{pr}, containing the largest $|\rho_{\text{Int.}}(\theta_{rot}, \phi_{pr})|$, respectively. In the anisotropic FBG case, figure N.7 (page V.II N-13), the largest $|\rho_{\text{Int.}}|$ was negative, where as it was positive for the isotropic FBG in figure N.9 (page V.II N-14).

The absolute value is presented in table N.1(a) (page V.II N-3), as the magnitude, rather than orientation is of relevance. All the polarimeter results presented: figures N.3(c) (page V.II N-10), N.4(c) (page V.II N-11) and $\sigma_{\text{Int.}}$ values are calculated from the application of θ_{rot} and ϕ_{pr} to the polarimeter Stokes vector.

The changes in $\rho_{\text{Int.}}(\theta_{rot})$, figures N.8(a) (page V.II N-13) and N.10(a) (page V.II N-14), exhibit the differences between the anisotropic and isotropic FBGs. The anisotropic FBG has a smoother rise and fall as the rotated axes approach the best alignment.

The isotropic FBG exhibits a flatter approach and steeper fall–off. The flatter approach suggests that the optimum alignment of the axes for correlation may be

[9]One of the motivating observations for this work, was the use of a long section fibre lead to use a laser system on another bench. The fibre lead had two unsupported sections. When the unsupported section nearest the optical bench was rotated slightly counter–clockwise it resulted in the laser signal spiralling from the $-S_3$ hemisphere to the $+S_3$ hemisphere in an $+S_1 \rightarrow +S_2 \rightarrow -S_1 \rightarrow -S_2$ direction.

The movement about the Poincaré sphere could be undone by rotating the lead clockwise. Movements of the fibre lead introduced rotation and phase retardation of an otherwise stable laser, causing some fluctuation on the SpectroBragg.

less as the isotropic FBG has a smaller difference between the orthogonal SOPs.

The changes in $\rho_{\text{Int.}}(\theta_{rot})$, figures N.8(b) (page V.II N-13) and N.10(b) (page V.II N-14) suggest that the fibre lead between the polarimeter and the SpectroBragg, which would have been unchanged between the isotropic and anisotropic FBGs experiments, introduced a phase retardation so as to produce elliptically polarised light.

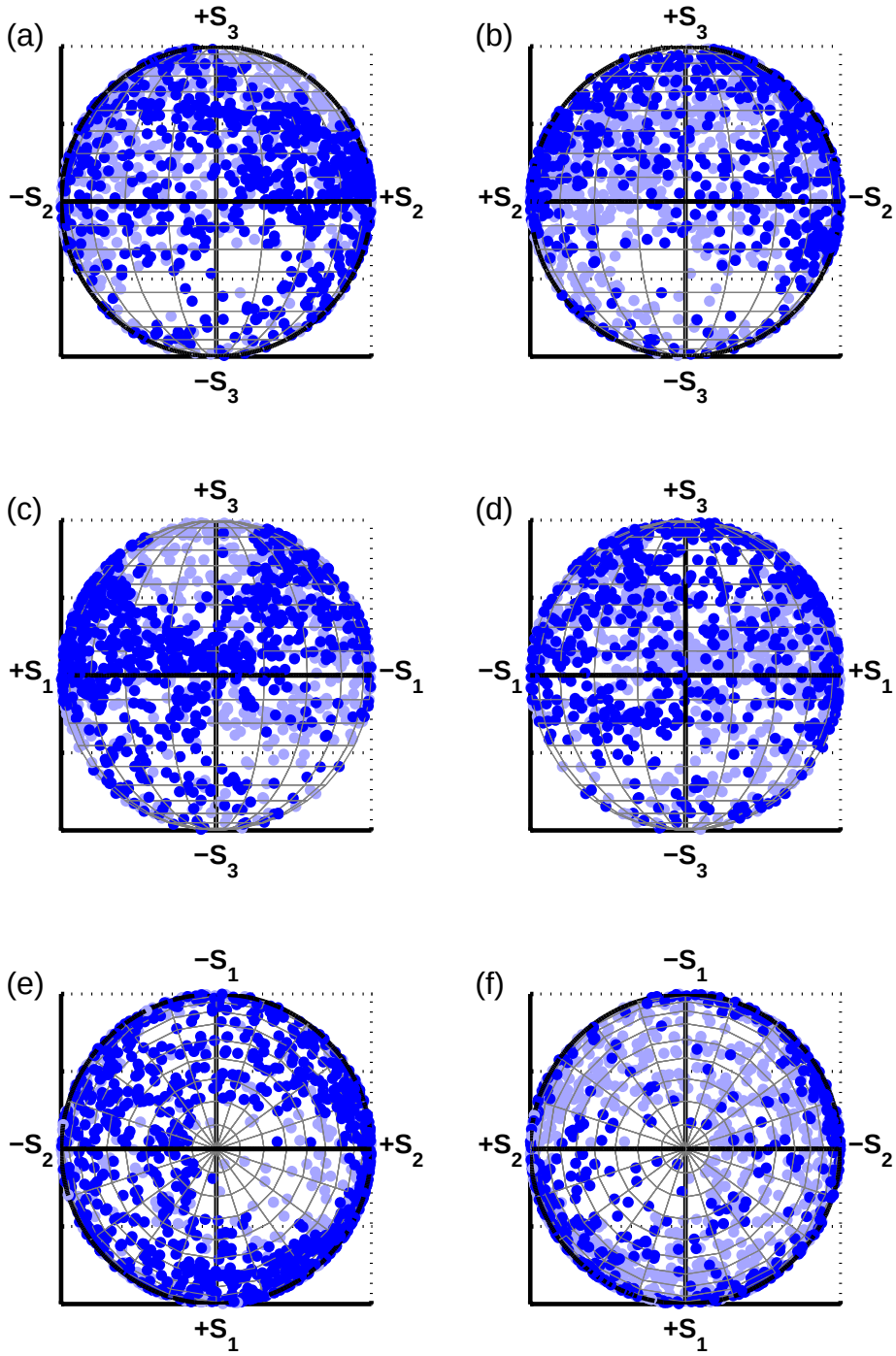

Figure N.1: Poincaré sphere projections of anisotropic FBG data showing: **(a)** S_2 V. S_3 along S_1 to $-S_1$; **(b)** S_2 V. S_3 along $-S_1$ to S_1; **(c)** S_1 V. S_3 along S_2 to $-S_2$; **(d)** S_1 V. S_3 along $-S_2$ to S_2 ;**(e)** S_2 V. S_1 along S_3 to $-S_3$; and **(f)** S_2 V. S_1 along $-S_3$ to S_3.

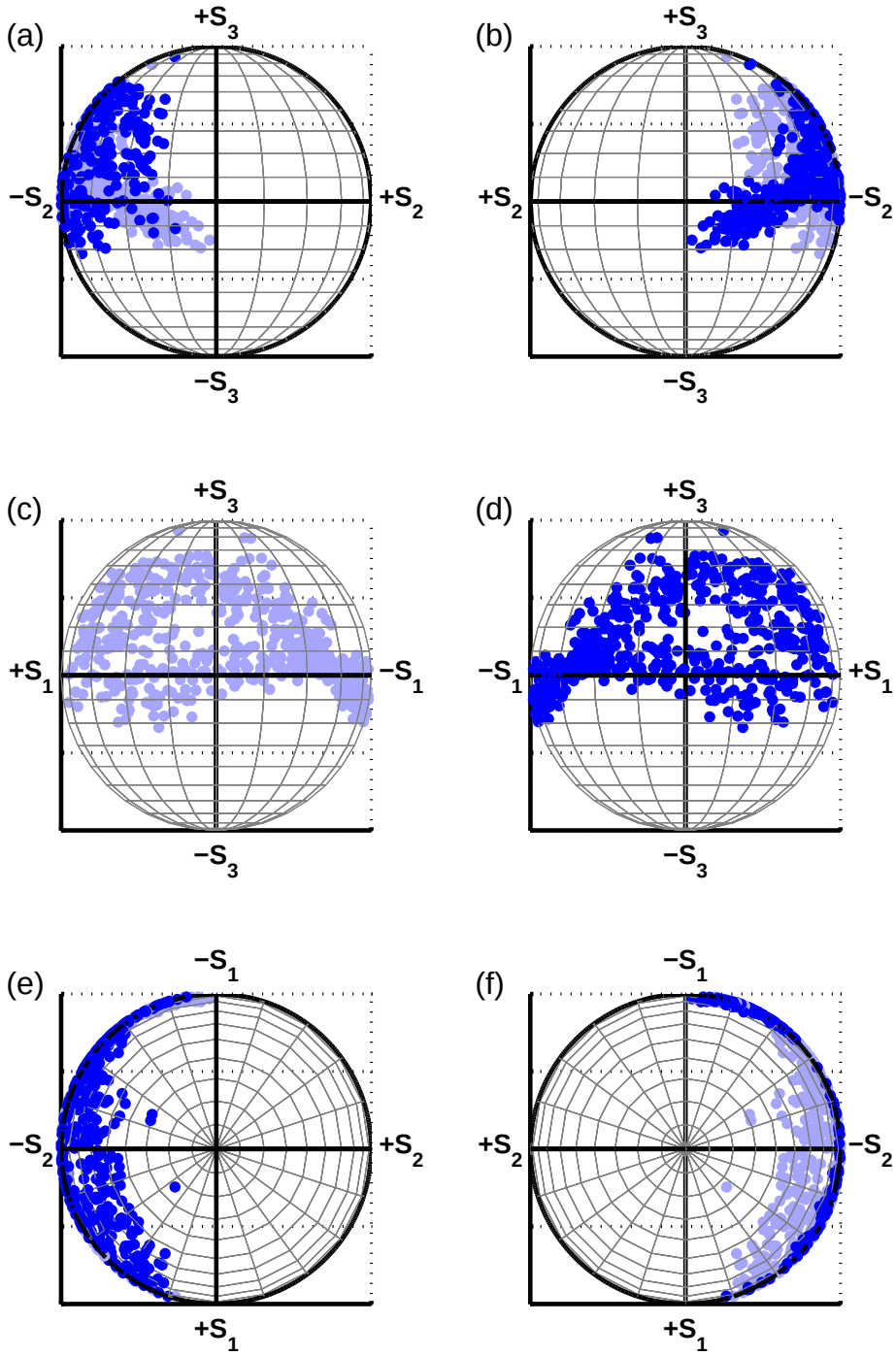

Figure N.2: Poincaré sphere projections of isotropic FBG data showing: **(a)** S_2 V. S_3 along S_1 to $-S_1$; **(b)** S_2 V. S_3 along $-S_1$ to S_1; **(c)** S_1 V. S_3 along S_2 to $-S_2$; **(d)** S_1 V. S_3 along $-S_2$ to S_2 ;**(e)** S_2 V. S_1 along S_3 to $-S_3$; and **(f)** S_2 V. S_1 along $-S_3$ to S_3.

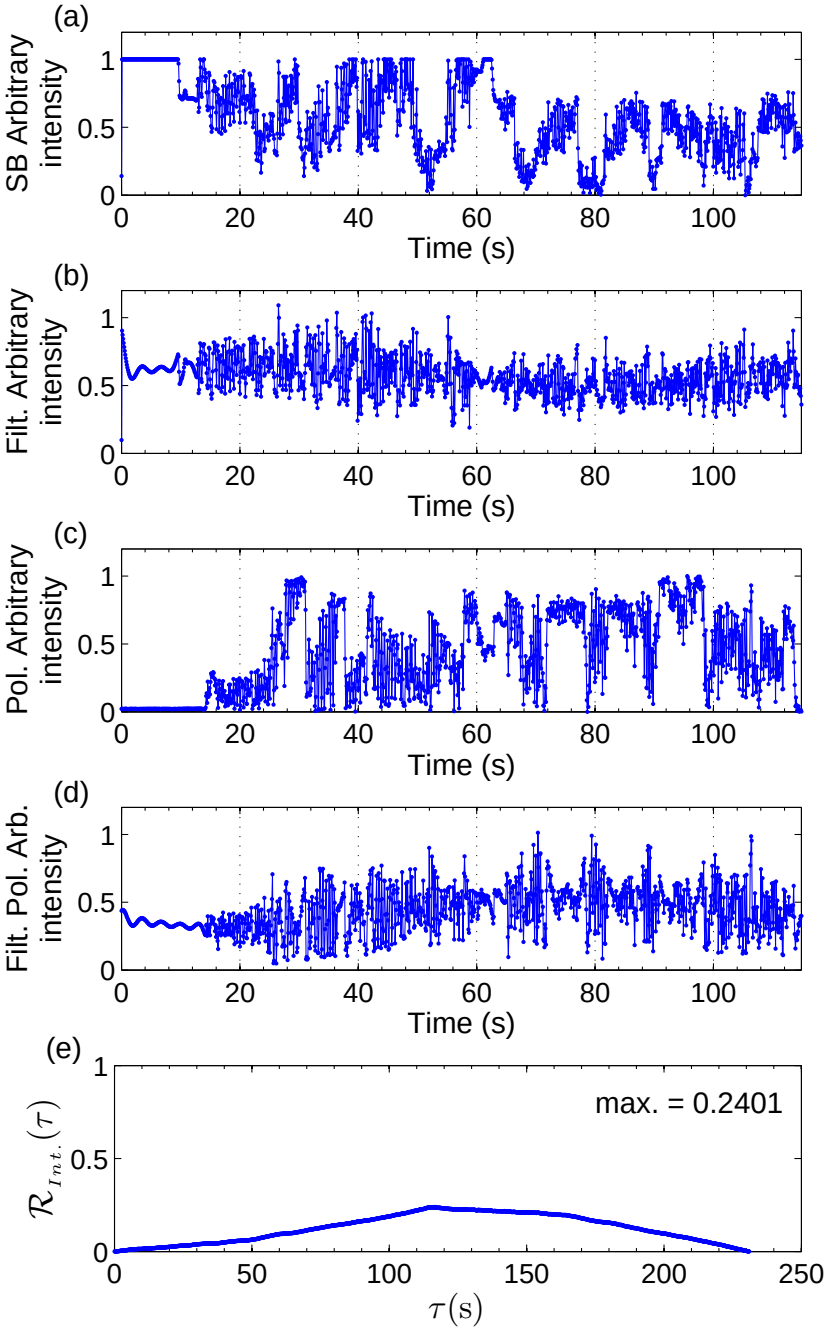

Figure N.3: Plot of anisotropic FBG data showing **(a)** the data captured on the SpectroBragg; **(b)** the FFT filtered SpectroBragg data; **(c)** the calculated ideal SpectroBragg intensity from the polarimeter data, using a rotation angle of 116°; and **(e)** the cross–correlation, $\mathcal{R}_{\text{Int.}}$, of (b) & (d).

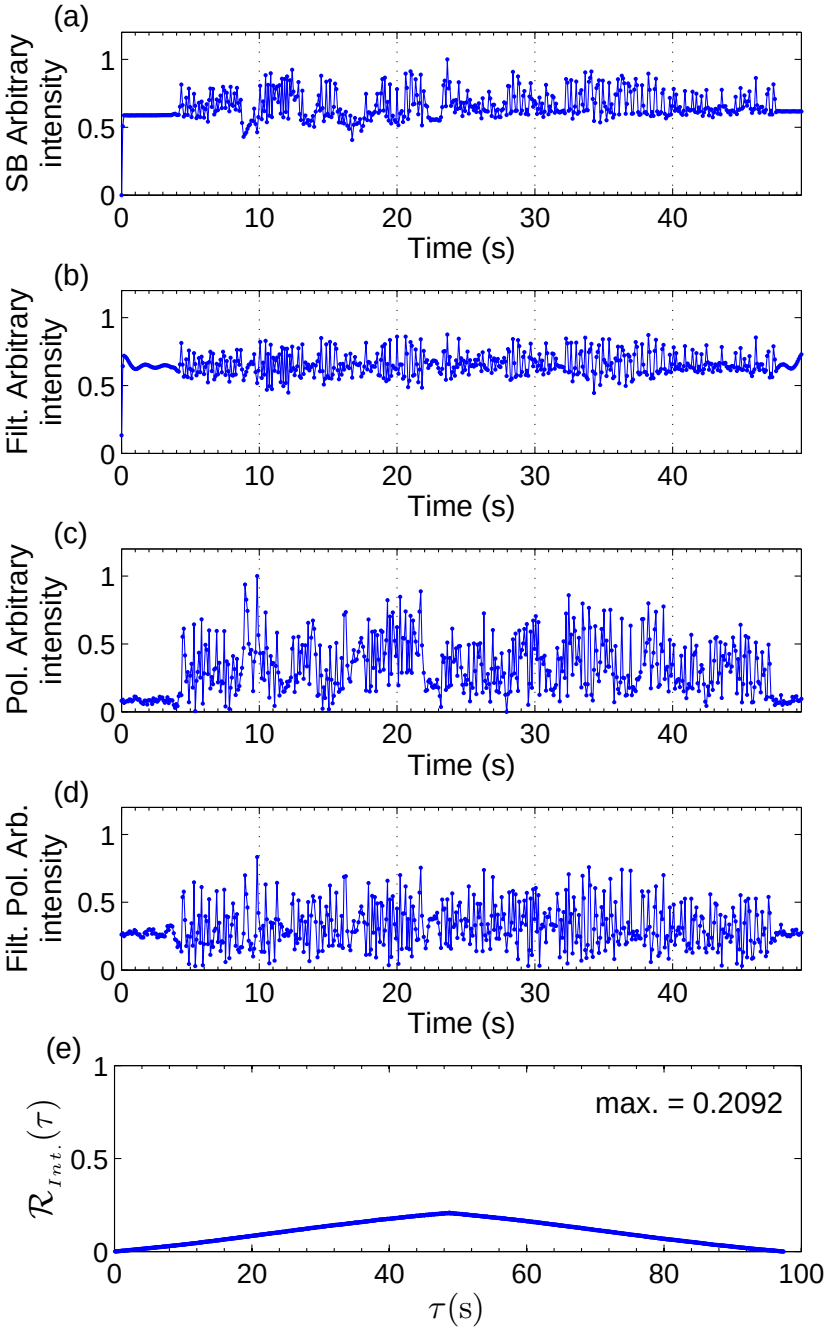

Figure N.4: Plot of isotropic FBG data showing **(a)** the data captured on the SpectroBragg; **(b)** the FFT filtered SpectroBragg data; **(c)** the calculated ideal SpectroBragg intensity from the polarimeter data, using a rotation angle of 26°; and **(e)** the cross–correlation, $\mathcal{R}_{\text{Int.}}$, of (b) & (d).

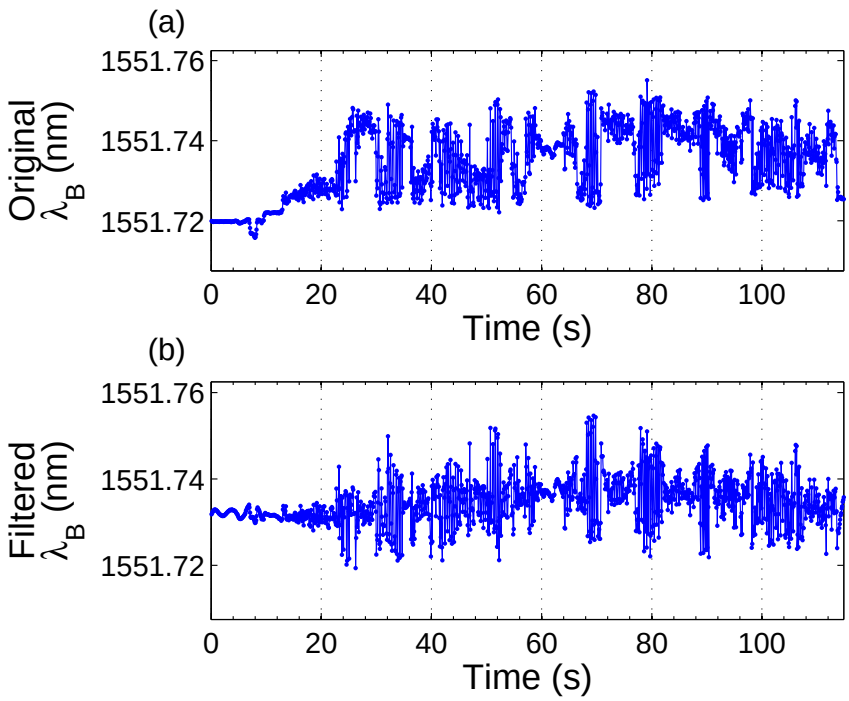

Figure N.5: Plot of **(a)** centroid determined λ_B for the anisotropic FBG data showing; **(b)** the centroid determined λ_B from the FFT filtered SpectroBragg data.

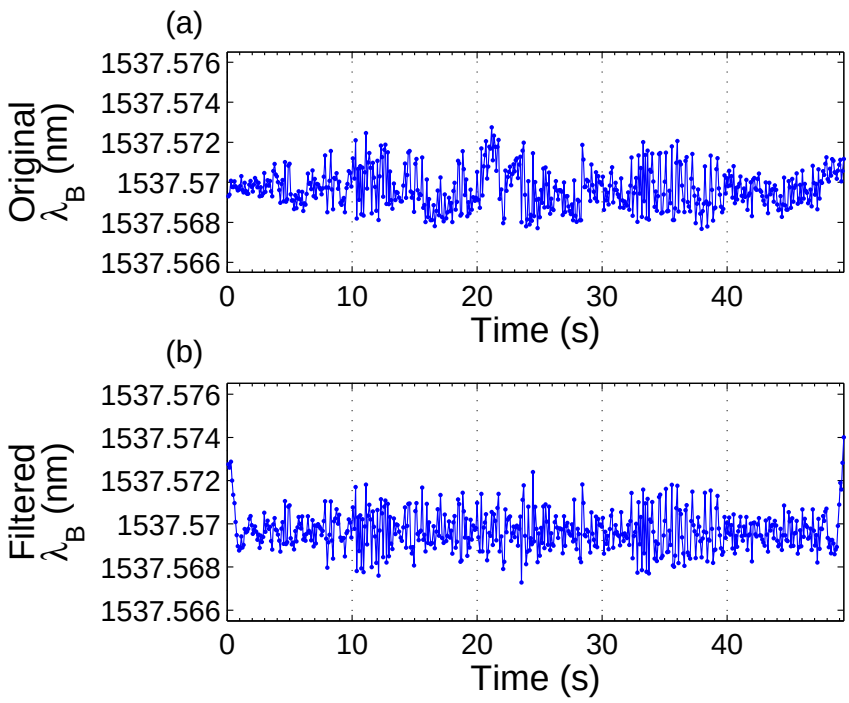

Figure N.6: Plot of **(a)** centroid determined λ_B for the anisotropic FBG data showing; **(b)** the centroid determined λ_B from the FFT filtered SpectroBragg data.

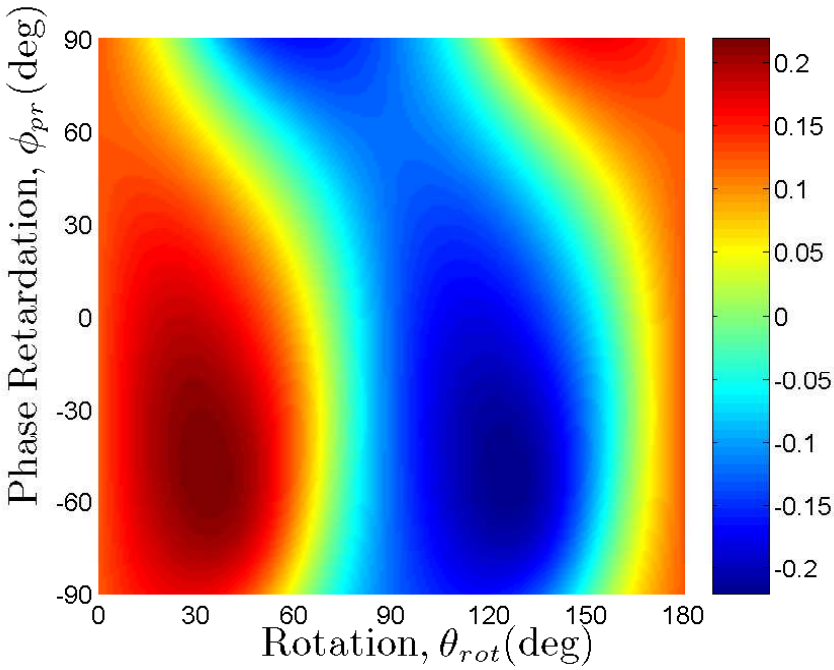

Figure N.7: Plot of changing correlation coefficient $\rho_{\text{Int.}}(\theta_{rot}, \phi_{pr})$ for axes rotation $\theta_{rot} = 0 \ldots 180°$ and phase retardation $\phi_{pr} = -90 \ldots 90°$ obtained for idealised SpectroBragg Mueller matrix for anisotropic FBG data.

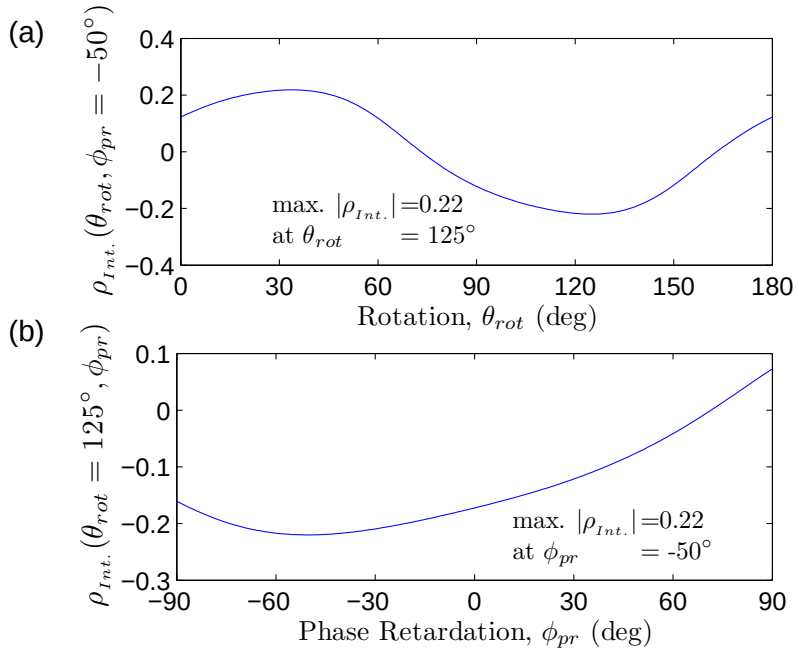

Figure N.8: Cross–sectional plots of figure N.7 which contain the largest value for the correlation coefficient $\rho_{\text{Int.}}(\theta_{rot}, \phi_{pr})$, (a) constant phase retardation ϕ_{pr} and (b) showing constant rotation θ_{rot}.

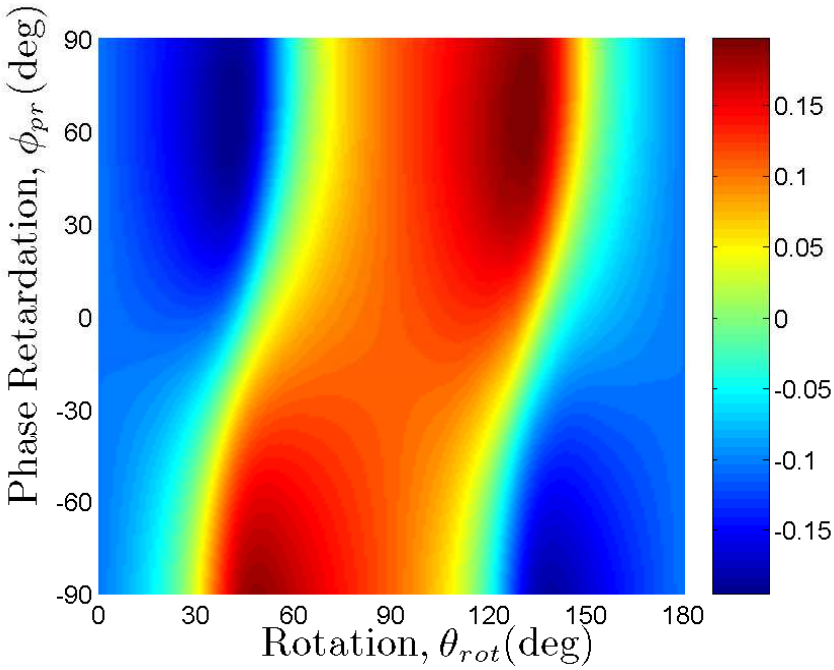

Figure N.9: Plot of changing correlation coefficient $\rho_{\text{Int.}}(\theta_{rot}, \phi_{pr})$ for axes rotation $\theta_{rot} = 0 \ldots 180°$ and phase retardation $\phi_{pr} = -90 \ldots 90°$ obtained for idealised SpectroBragg Mueller matrix for isotropic FBG data.

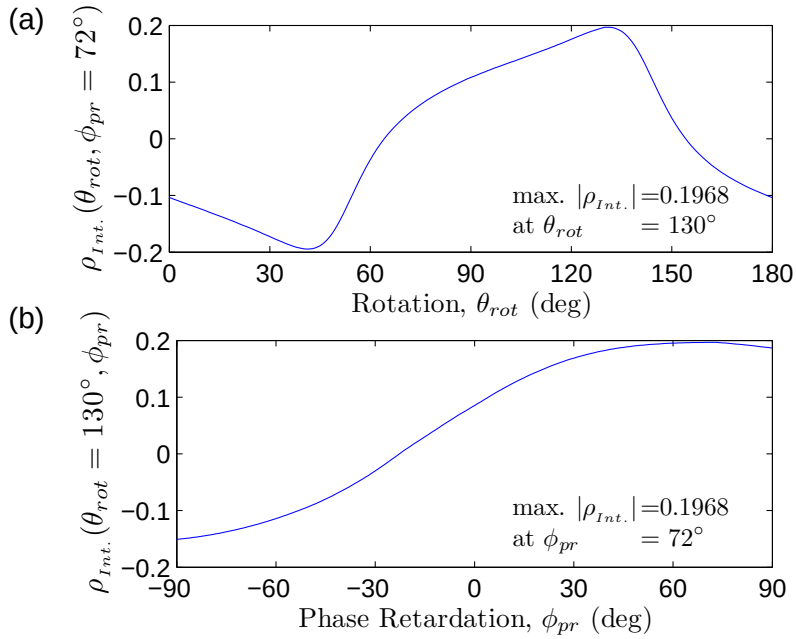

Figure N.10: Cross–sectional plots of figure N.9 which contain the largest value for the correlation coefficient $\rho_{\text{Int.}}(\theta_{rot}, \phi_{pr})$, (a) constant phase retardation ϕ_{pr} and (b) showing constant rotation θ_{rot}.

N.2 Lyot depolariser

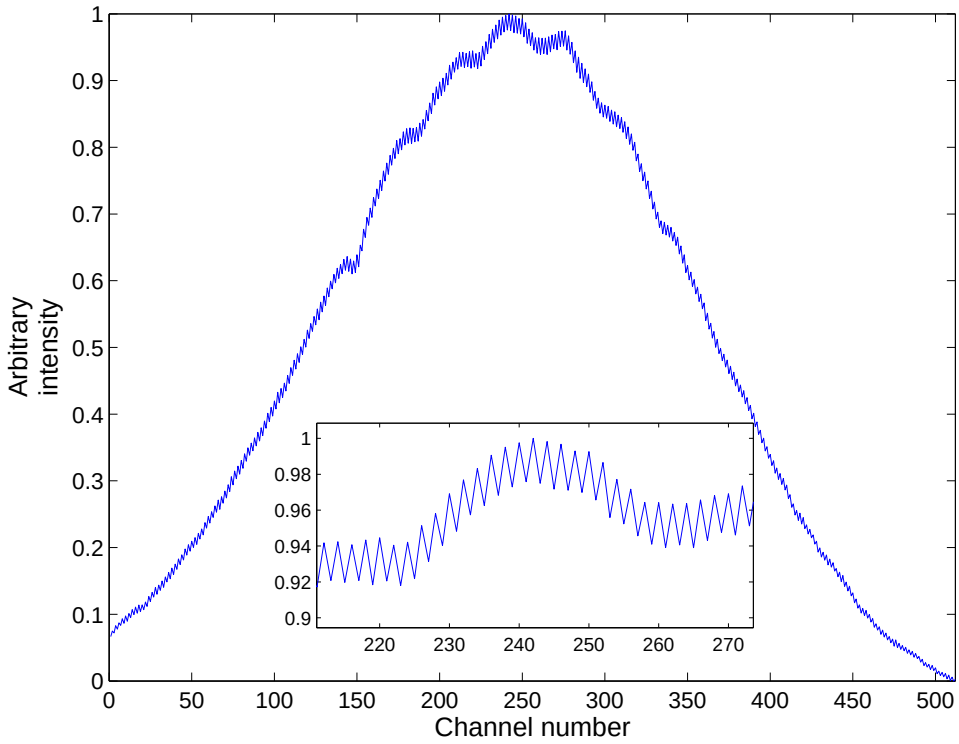

Figure N.11: Channelled spectrum produced by full SLED spectrum through the Lyot depolariser onto the SpectroBragg, with magnified view inset.

The Lyot depolariser, §5.3.2.1 (page V.I - 230), required broadband illumination ($> 8\,\mathrm{nm}$) to produce a depolarised signal. The spectrum from the FBG did not meet this requirement, and so the Lyot depolariser did not effectively depolarise the signal on the SpectroBragg. An added complication for Lyot depolarisation was that the depolariser needed to have as its design spectrum the smaller value of either the FBG (or other signal) bandwidth, or the bandwidth illuminating a single detector element. As the bandwidth of the FBG was $\sim 1\,\mathrm{nm}$ and the spectral bandwidth on a single diode of the InGaAs array was $\sim 137\,\mathrm{pm}$, the Lyot would need to have depolarised at least $\sim 137\,\mathrm{pm}$, i.e.[10] $3\ell \geq 60\,\mathrm{m}$, for a signal not to exhibit polarisation artefacts.

Figure N.11 shows the channelled spectrum which arises from the two sequential stationary Mach–Zehnder interferometers made by the Lyot sections when the full bandwidth of the SLED is captured by the SpectroBragg[11]

There are two oscillations visible on the profile in figure N.11. A long and short term modulation of the spectral intensity, with the longer modulation of greater am-

[10] See §5.2.1.1, equation (5.2) (page V.I - 219).

[11] The signal from the full SLED was depolarised when observed by the polarising beam–splitter/ balanced receiver, as the whole spectrum was captured by one detector.

plitude. The amplitude of the short term modulation is over an order of magnitude greater than the minor DC offsets between the interleaved 256 diode arrays in the 512 diode array. The short term modulation is therefore not an inherent artefact from the array but a modulation arising from the Lyot depolariser.

Quantity	FBG				Control		Lyot	
(a) $\rho_{\text{Int.}}$	Aniso.			$\lvert\rho_{\text{Int.}}\rvert$	0.22	(0.28)	0.36	(0.62)
				θ_{rot}	125°		18°	
				ϕ_{pr}	−50°		−28°	
	Iso.			$\lvert\rho_{\text{Int.}}\rvert$	0.20	(0.18)	0.23	(0.47)
				θ_{rot}	130°		52°	
				ϕ_{pr}	72°		−4°	
(b) $\sigma_{\text{Int.}}$ (pm)	Aniso.	SB.	w. ΔSOP		0.25	(0.56)	0.32	(0.42)
			background		0.07	(0.03)	0.02	(0.0005)
		Pol.	w. ΔSOP		0.38	(0.56)	0.46	(0.61)
			background		0.04	(0.03)	0.02	(0.01)
	Iso.	SB.	w. ΔSOP		0.13	(0.18)	0.25	(0.35)
			background		0.03	(0.001)	0.05	(0.002)
		Pol.	w. ΔSOP		0.50	(0.55)	0.25	(0.26)
			background		0.07	(0.18)	0.08	(0.11)
(c) σ_{λ_B} (pm)	Aniso.		w. ΔSOP		5.80	(7.41)	47.55	(59.11)
			background		0.25	(0.07)	3.48	(0.06)
	Iso.		w. ΔSOP		0.88	(1.05)	2.86	(3.42)
			background		0.88	(0.28)	0.23	(0.21)
(d) $\lvert\rho_{\lambda_B}\rvert$	Aniso.				0.24	(0.40)	0.69	(0.75)
	Iso.				0.46	(0.46)	0.12	(0.16)

Table N.2: Lyot depolariser approach summary of **(a)** correlation coefficient, $\rho_{\text{Int.}}$, values for correlation between captured SpectroBragg intensity and calculated S_{SB}; **(b)** the FFT filtered and unfiltered (in parentheses) normalised standard deviations, $\sigma_{\text{Int.}}$, for both SpectroBragg and polarimeter data. The values are for the data with applied SOP changes and without applied SOP changes (i.e. background); **(c)** the FFT filtered and unfiltered (in parentheses) standard deviation of centroid calculated wavelength, σ_{λ_B}, for the anisotropic and isotropic FBGs; **(d)** the SpectroBragg intensity–centroid λ_B correlation coefficient, ρ_{λ_B}, as a measure of intensity pattern's influence on λ_B.

The FBG Lyot depolarisation results are tabulated in table N.2 along with the control experiment of no depolarisation scheme. The presentation follows the outline introduced in the *control experiment* discussion, §N.1 (page V.II N-2). Table N.2(a) (page V.II N-16) shows the correlation coefficients, $\rho_{\text{Int.}}$.

The anisotropic and isotropic FBG SOPs recorded by the polarimeter are shown in figures N.12 (page V.II N-19) and N.13 (page V.II N-20), respectively. The anisotropic FBG coverage shows a large difference from that achieved for the control experiment, figure N.5 (page V.II N-12). The origin of the difference is unknown, as the same FC/APC rotations were used and the fibre leads up to the polarimeter should not have moved.

The Lyot depolariser used provided worse performance than the control experiment. As the Lyot depolariser required a broader bandwidth than an FBG provided in order to be effective[12], the changes in SOP were converted into phase noise at the same frequency. The value of $\rho_{\text{Int.}}$ is $\sim$ 164% the control experiment value for the anisotropic FBG. The isotropic FBG $\rho_{\text{Int.}}$ is $\sim$ 115% the control experiment value and $\sim$ 105% the anisotropic FBG $\rho_{\text{Int.}}$ for the control experiment. As the FFT filtering of the data was undertaken to pass the SOP changes, the Lyot depolariser's conversion of the applied SOP changes to phase noise provides a stronger correlation than the control experiment.

Table N.2(b) (page V.II N-16) on shows the $\sigma_{\text{Int.}}$ values. Both the anisotropic and isotropic FBG values are larger than the corresponding control experiment values, by $\sim$ 128% and $\sim$ 192%, respectively. This can be explained by the larger changes in intensity achieved by interferometrically coupled phase noise arising from the applied SOP changes.

Table N.2(c) (page V.II N-16) shows the centroid calculated values of σ_{λ_B}. Under applied SOP changes Lyot depolariser produced oscillations in the centroid calculated wavelength an order of magnitude greater than the control or other depolarisation schemes for the anisotropic FBG. Additionally, the unfiltered background σ_{λ_B} values indicate that the experimental conditions were equivalent to the control case.

Table N.2(c) (page V.II N-16) shows the SpectroBragg λ_B–intensity correlation coefficients. The signals are more significantly corrected for both the unfiltered and FFT filtered Lyot SpectroBragg data compared to the control experiment.

Initial work for this thesis began with the construction of the SpectroBragg and then the strain characterisation of the anisotropic FBG. The Lyot depolariser was examined for the strain characterisation work, but was rejected as the performance of the SpectroBragg deteriorated. The strain characterisation work would not have subjected the FBG signal to the SOP changes applied in this work, however, the effective coupling of SOP and phase changes into channelled spectra noise decreased the SpectroBragg performance.

Figures N.14 (page V.II N-21) to N.17 (page V.II N-23) show the data used

[12]The full SLED bandwidth was passed through the Lyot onto a polarising beam–splitter and balanced detector. In this case, where the full spectrum and the detector's spectral window exceeded the minimum bandwidth of the Lyot, the signal was effectively depolarised.

in these calculations. Figures N.14(a) (page V.II N-21) and N.14(c) (page V.II N-21) show the data captured by the SpectroBragg and polarimeter, respectively. Figures N.14(b) (page V.II N-21) and N.14(d) (page V.II N-21) show the filtered SpectroBragg and polarimeter data, respectively. On casual visual inspection, the FFT filtering appears to have had minimal effect.

Figure N.14(e) (page V.II N-21) shows the cross–correlation, $\mathcal{R}_{\text{Int.}}$, of N.14(b) (page V.II N-21) & N.14(d) (page V.II N-21). Despite the visibly identifiable distinct SOP changes[13] figure N.14(e) (page V.II N-21) is smaller than the corresponding control experiment figure N.3(b) (page V.II N-10). These three changes correspond to the FC/APC connector being rotated in the three orthogonal directions. The polarimeter and SpectroBragg have the three distinct changes, but respond differently, hence, the lowering of the correlation. A possible explanation is that the different SOPs had the effect of appearing as different phase differences after passing through the Lyot depolariser.

The corresponding isotropic FBG figure, figure N.15 (page V.II N-22), similarly has distinct SOP changes[14], albeit if not as obvious. The responses of the polarimeter and SpectroBragg are not as distinctly different and so the correlation is improved over that of the anisotropic FBG correlation.

Figures N.16 (page V.II N-23) and N.17 (page V.II N-23) show the centroid calculated wavelength, λ_B, for the anisotropic and isotropic FBGs respectively. The (a) figures show the unfiltered λ_Bs and the (b) figures show the FFT filtered λ_Bs. As mentioned previously in the discussion of table N.2(c) (page V.II N-16), the oscillations are an order of magnitude greater than for the corresponding control experiment for the anisotropic FBG. The combination of SOP and phase changes introduced by the Lyot depolariser degrade the SpectroBragg performance in monitoring effectively static FBG spectra.

Figures N.18 (page V.II N-24) and N.20 (page V.II N-25) show the correlation coefficient, $\rho_{\text{Int.}}$, as a function of changing θ_{rot} and ϕ_{pr}. Figures N.19 (page V.II N-24) and N.21 (page V.II N-25) show the orthogonal cross sections, the (a) figures along θ_{rot} and the (b) figures along ϕ_{pr}, containing the largest $|\rho_{\text{Int.}}(\theta_{rot}, \phi_{pr})|$ used in these calculations.

[13]The three distinct SOP changes are 3 . . . 23 s, 24 . . . 34 s and 35 . . . 45 s.
[14]The three distinct SOP changes are 2 . . . 20 s, 21 . . . 30 s and 31 . . . 60 s.

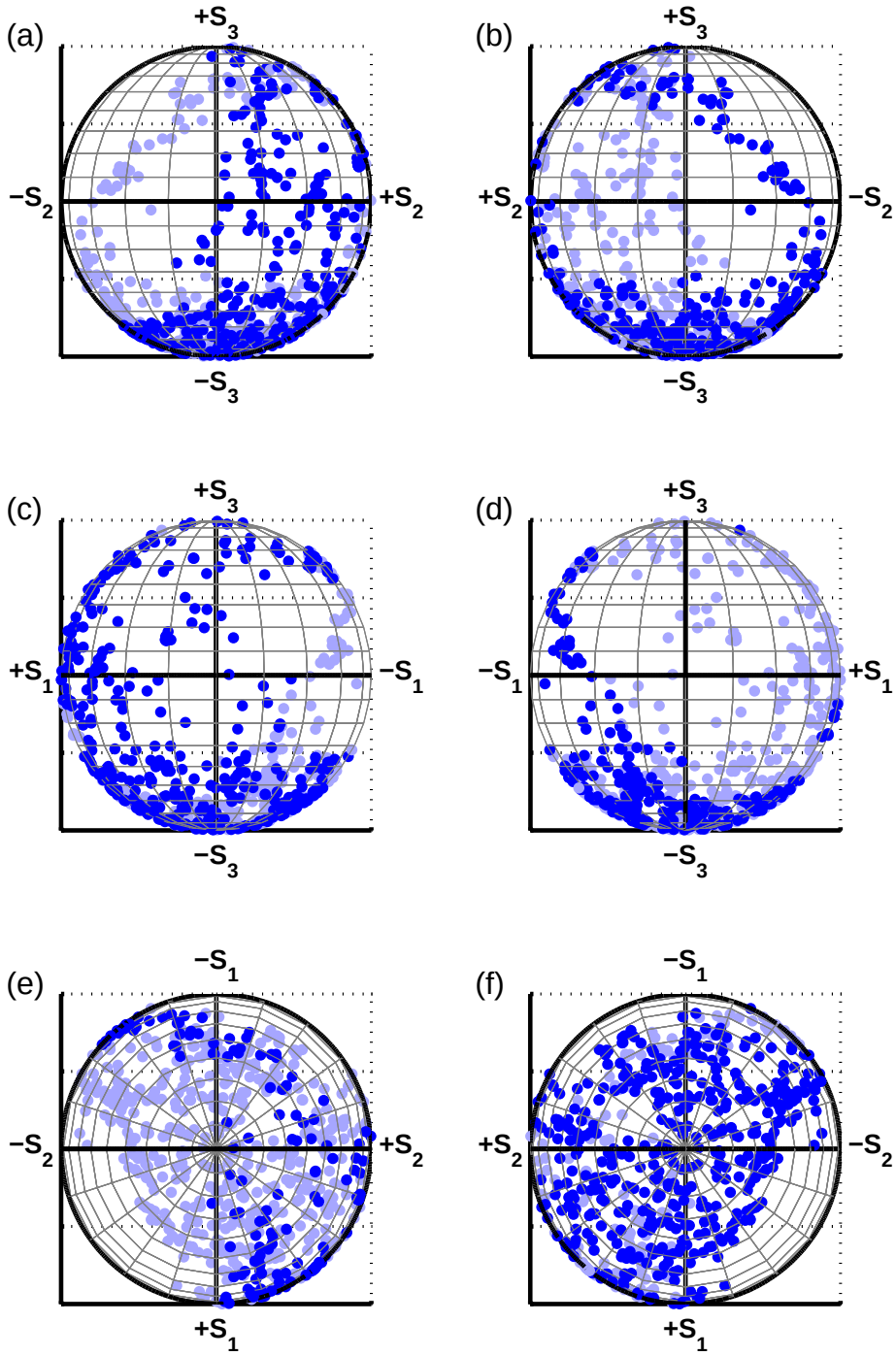

Figure N.12: Poincaré sphere projections of anisotropic FBG data showing: **(a)** S_2 V. S_3 along S_1 to $-S_1$; **(b)** S_2 V. S_3 along $-S_1$ to S_1; **(c)** S_1 V. S_3 along S_2 to $-S_2$; **(d)** S_1 V. S_3 along $-S_2$ to S_2 ;**(e)** S_2 V. S_1 along S_3 to $-S_3$; and **(f)** S_2 V. S_1 along $-S_3$ to S_3.

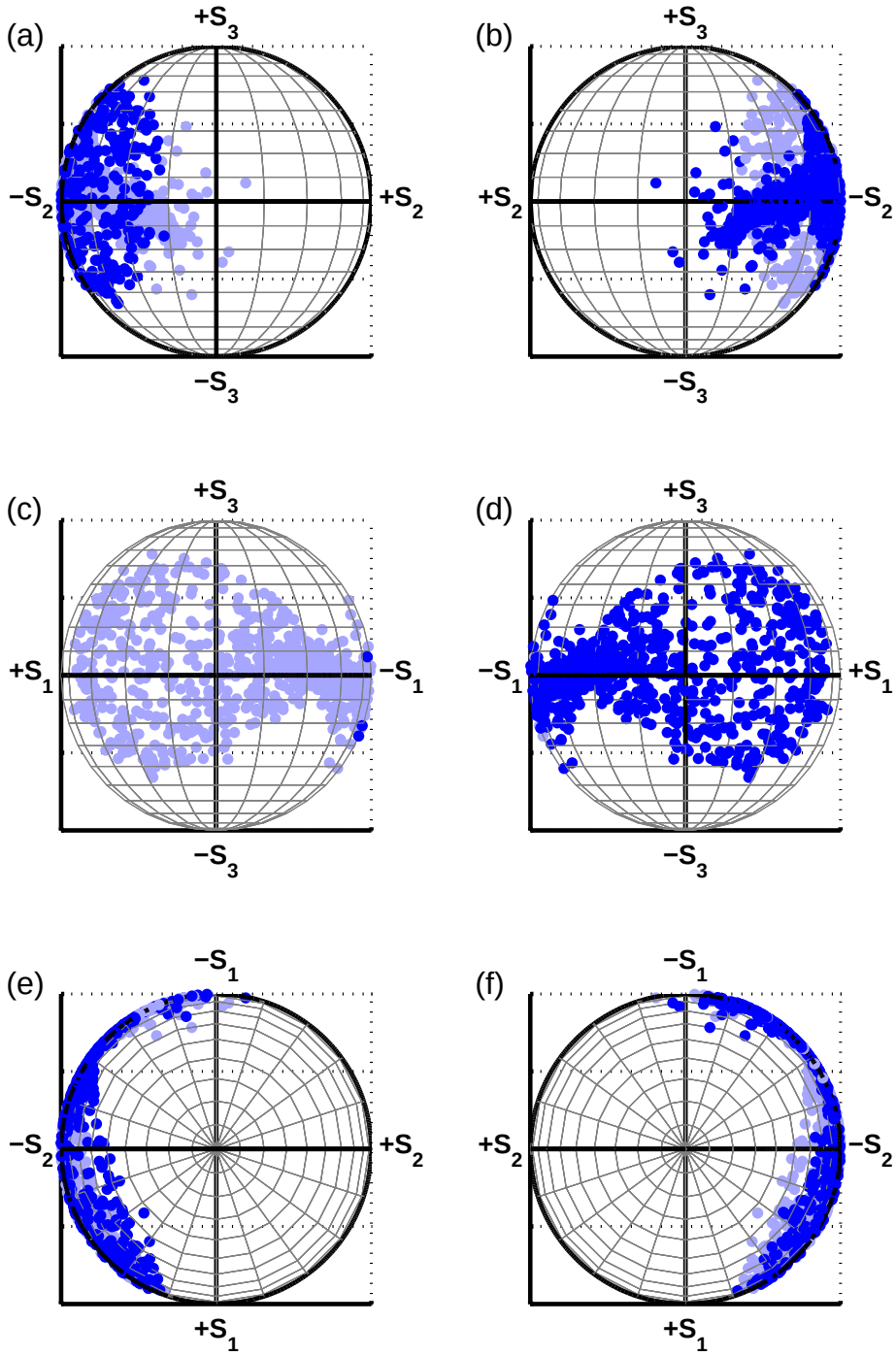

Figure N.13: Poincaré sphere projections of isotropic FBG data showing: **(a)** S_2 V. S_3 along S_1 to $-S_1$; **(b)** S_2 V. S_3 along $-S_1$ to S_1; **(c)** S_1 V. S_3 along S_2 to $-S_2$; **(d)** S_1 V. S_3 along $-S_2$ to S_2 ;**(e)** S_2 V. S_1 along S_3 to $-S_3$; and **(f)** S_2 V. S_1 along $-S_3$ to S_3.

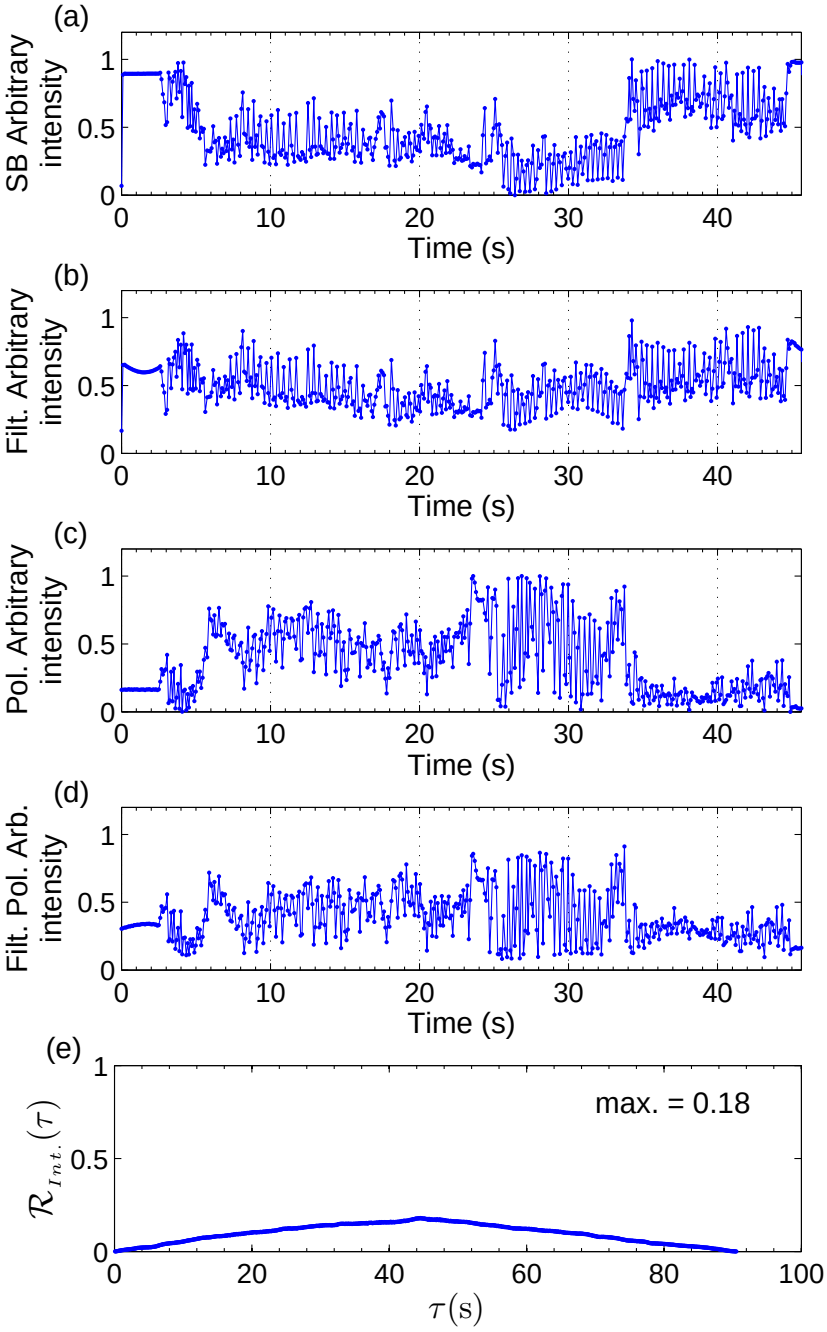

Figure N.14: Plot of anisotropic FBG data showing **(a)** the data captured on the SpectroBragg; **(b)** the FFT filtered SpectroBragg data; **(c)** the calculated ideal SpectroBragg intensity from the polarimeter data, using a rotation angle of 7°; and **(d)** the cross–correlation, $\mathcal{R}_{\text{Int.}}$, of (b) & (c) for Lyot depolariser.

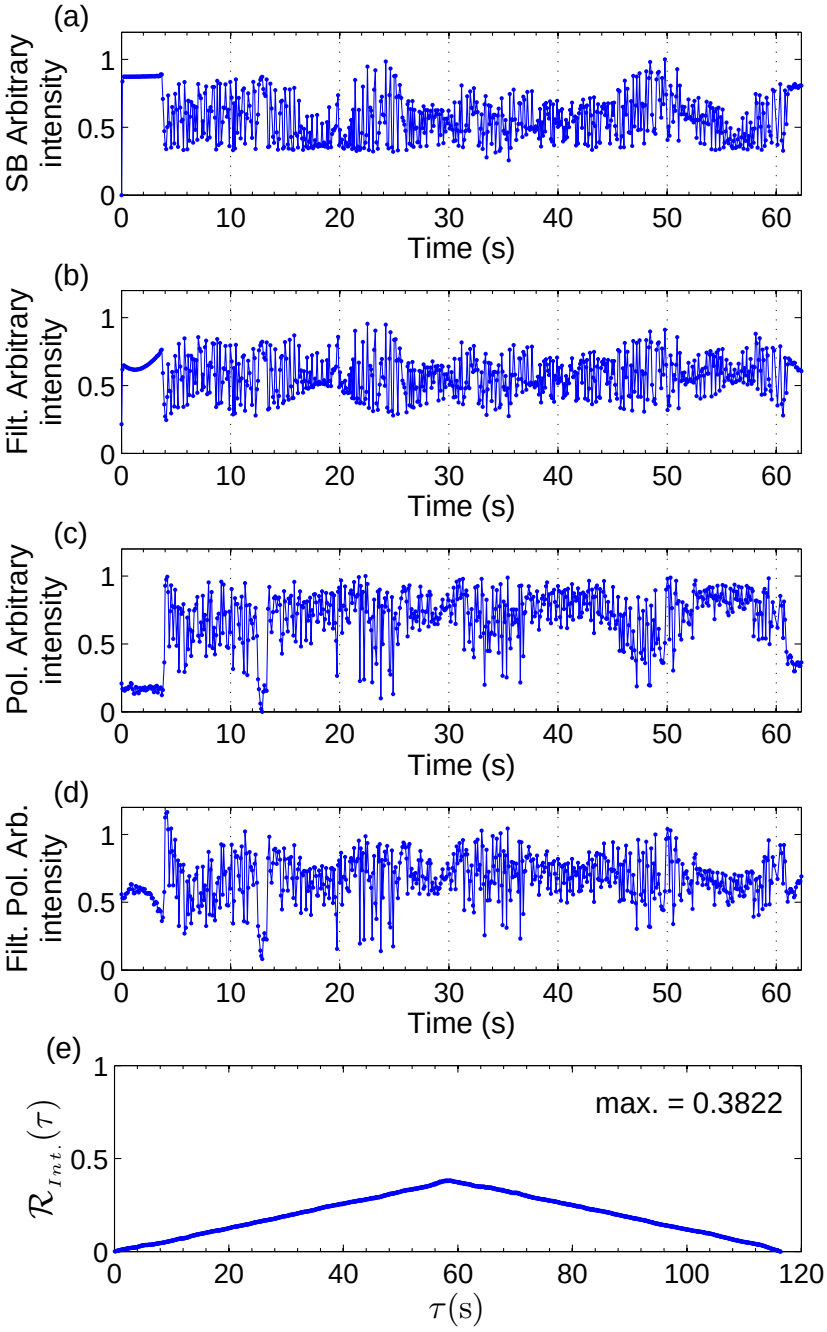

Figure N.15: Plot of isotropic FBG data showing **(a)** the data captured on the SpectroBragg; **(b)** the FFT filtered SpectroBragg data; **(c)** the calculated ideal SpectroBragg intensity from the polarimeter data, using a rotation angle of 49°; and **(d)** the cross–correlation, $\mathcal{R}_{\text{Int.}}$, of (b) & (c) for Lyot depolariser.

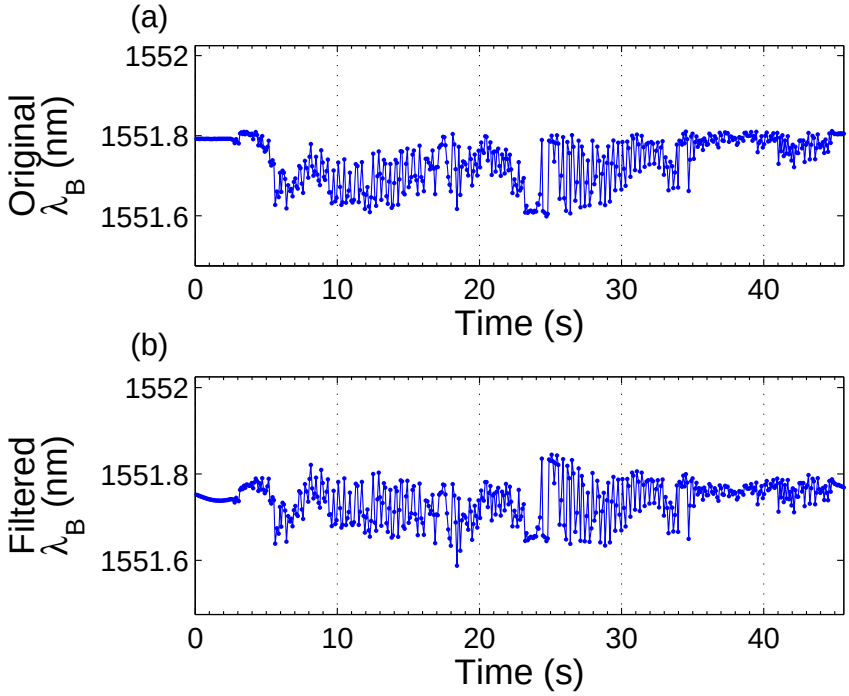

Figure N.16: Plot of **(a)** centroid determined λ_B for the anisotropic FBG data showing; **(b)** the centroid determined λ_B from the FFT filtered SpectroBragg data.

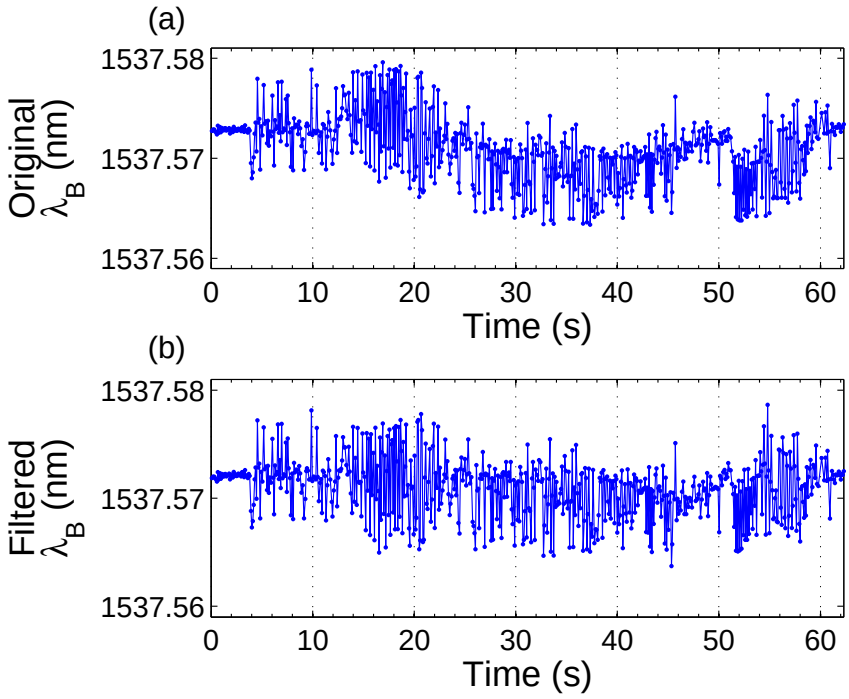

Figure N.17: Plot of **(a)** centroid determined λ_B for the anisotropic FBG data showing; **(b)** the centroid determined λ_B from the FFT filtered SpectroBragg data.

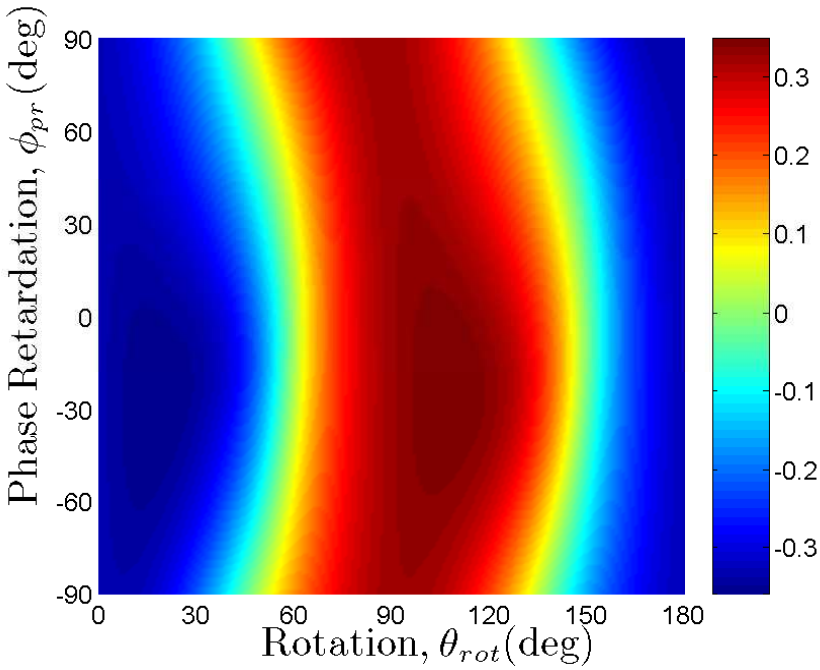

Figure N.18: Plot of changing correlation coefficient $\rho_{\text{Int.}}(\theta_{rot}, \phi_{pr})$ for axes rotation $\theta_{rot} = 0 \ldots 180°$ and phase retardation $\phi_{pr} = -90 \ldots 90°$ obtained for idealised SpectroBragg Mueller matrix for anisotropic FBG data.

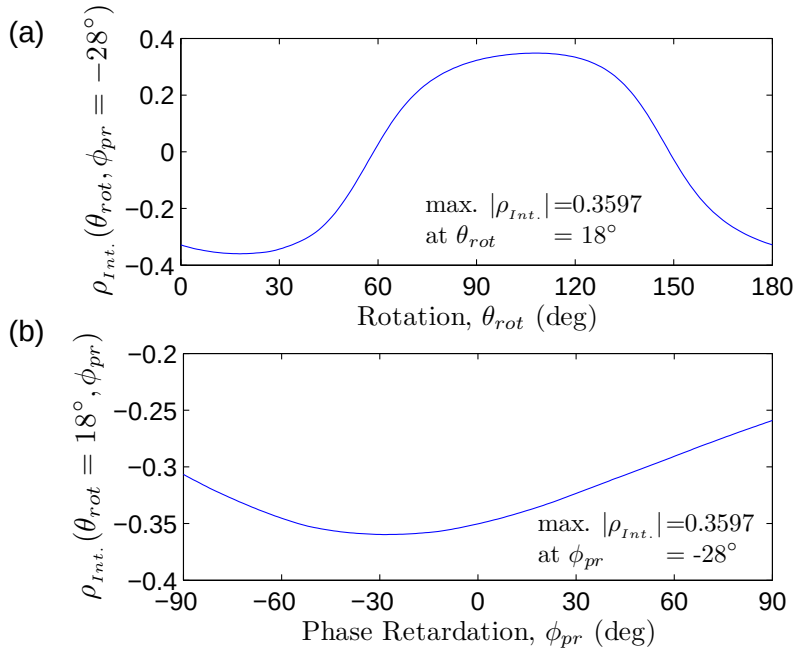

Figure N.19: Cross–sectional plots of figure N.18 which contain the largest value for the correlation coefficient $\rho_{\text{Int.}}(\theta_{rot}, \phi_{pr})$, (a) constant phase retardation ϕ_{pr} and (b) showing constant rotation θ_{rot}.

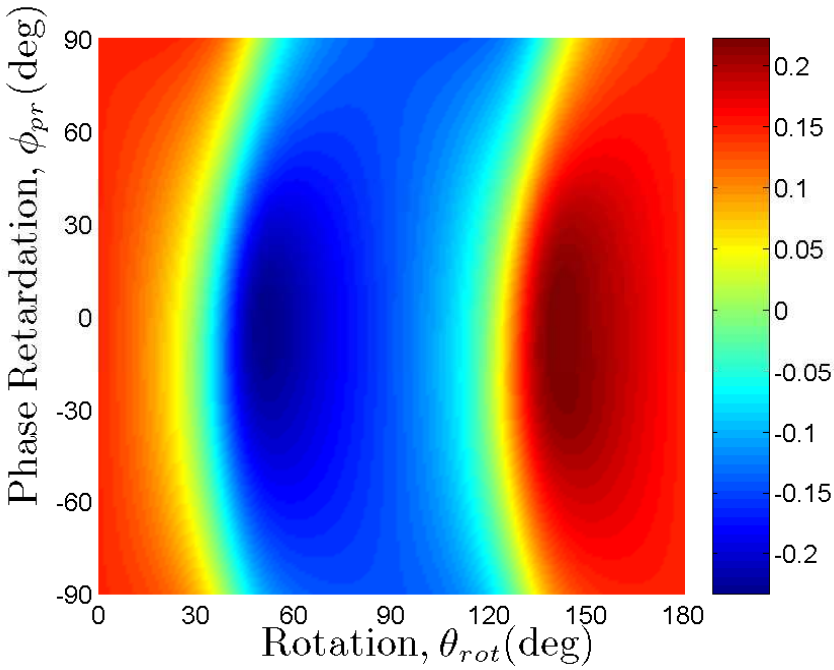

Figure N.20: Plot of changing correlation coefficient $\rho_{\text{Int.}}(\theta_{rot}, \phi_{pr})$ for axes rotation $\theta_{rot} = 0 \ldots 180°$ and phase retardation $\phi_{pr} = -90 \ldots 90°$ obtained for idealised SpectroBragg Mueller matrix for isotropic FBG.

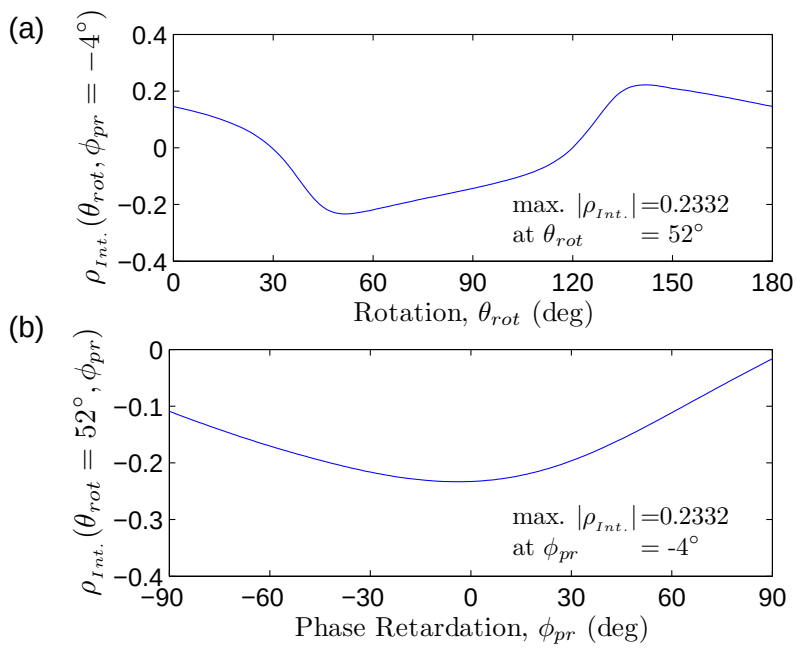

Figure N.21: Cross–sectional plots of figure N.20 which contain the largest value for the correlation coefficient $\rho_{\text{Int.}}(\theta_{rot}, \phi_{pr})$, (a) constant phase retardation ϕ_{pr} and (b) showing constant rotation θ_{rot}.

N.3 Lefèvre SOP fixer

The intention of the Lefèvre polarisation controller approach, §5.3.2.3 (page V.I - 230), and the Circulator/Faraday mirror approach, §5.3.2.4 (page V.I - 232), was to fix the output SOP from an arbitrary input SOP while retaining as much of the power of the input signal at the output as possible.

This would be achieved by converting orthogonal SOPs into one fixed SOP, and incoherently recombining at the output to recover half the full input power in a fixed SOP. Connection losses and the use of a combining of a 2×1 coupler[15] result in less than 50% throughput at best.

The all–fibre polarisation controller [1], the Lefèvre polarisation controller, may be configured to behave as a half–waveplate. When linearly polarised light from an arm of the polarising beam–splitter passes through the Lefèvre polarisation controller configured as a half–waveplate, the SOP is rotated to its orthogonal SOP.

The basic concept of the work reported here was developed by Takada *et al.* [2], who employed free space optical components with a length of fibre as a delay line to depolarise a signal into equal orthogonal output intensities and by Tateda *et al.* [3], who evaluated the performance of polarisation fixers. This was the first approach tested for polarisation mitigation, due to the availability of components.

The apparatus demonstrated that the ODL vibrations were too severe when the stationary Mach–Zehnder interferometer was notionally balanced, and that the performance from the system under test was at best equivalent to the uncorrected polarisation changes or, more frequently, worse as it added phase noise from acoustic sources. The ODL was particularly responsive to acoustic noise, particularly the lower–frequency noise. Placing the ODL on or in foam to dampen acoustic oscillations achieved little in terms of interferometrically coupled noise reduction.

The unbalanced stationary Mach–Zehnder interferometer from [2] produced better results. An improvement in all four quantities was achieved in comparison to the control experiment for the anisotropic FBG, as shown in table N.3.

and σ_{λ_B} were

Figures N.22 (page V.II N-31) and N.23 (page V.II N-32) show the Poincaré sphere plots for the anisotropic and isotropic FBGs, respectively. The anisotropic FBG coverage is close to the control experiment coverage, figure N.1 (page V.II N-8). However, the isotropic FBG coverage differs substantially from the other isotropic FBG Poincaré sphere plots. The pattern is as a ring as opposed to the more bow–tie patterns of the other sets. The difference can be seen in comparing the isotropic FBG azimuthal equidistant plot, figure N.57 (page V.II N-62), in §N.6 (page V.II N-59).

[15] 2×1 couplers are 2×2 couplers with one output port truncated within the packaging.

Quantity	FBG			Control		Lefèvre cont.	
(a) $\rho_{\text{Int.}}$	Aniso.		$\lvert\rho_{\text{Int.}}\rvert$	0.22	(0.28)	0.14	(0.09)
			θ_{rot}	125°		35°	
			ϕ_{pr}	−50°		8°	
	Iso.		$\lvert\rho_{\text{Int.}}\rvert$	0.20	(0.18)	0.21	(0.35)
			θ_{rot}	130°		128°	
			ϕ_{pr}	72°		−45°	
(b) $\sigma_{\text{Int.}}$ (pm)	Aniso.	SB.	w. ΔSOP	0.25	(0.56)	0.06	(0.09)
			background	0.07	(0.03)	0.0066	(0.0066)
		Pol.	w. ΔSOP	0.38	(0.56)	0.40	(0.60)
			background	0.04	(0.03)	0.0304	(0.0159)
	Iso.	SB.	w. ΔSOP	0.13	(0.18)	0.06	(0.09)
			background	0.03	(0.001)	0.0083	(0.0083)
		Pol.	w. ΔSOP	0.50	(0.55)	0.30	(0.36)
			background	0.07	(0.18)	0.0139	(0.0261)
(c) σ_{λ_B} (pm)	Aniso.		w. ΔSOP	5.80	(7.41)	1.84	(2.41)
			background	0.25	(0.07)	1.46	(2.94)
	Iso.		w. ΔSOP	0.88	(1.05)	0.91	(1.40)
			background	0.88	(0.28)	0.43	(0.60)
(d) $\lvert\rho_{\lambda_B}\rvert$	Aniso.			0.24	(0.40)	0.11	(0.08)
	Iso.			0.46	(0.46)	0.69	(0.80)

Table N.3: Lefèvre controller mitigation approach summary of **(a)** correlation coefficient, $\rho_{\text{Int.}}$, values for correlation between captured SpectroBragg intensity and calculated S_{SB}; **(b)** the FFT filtered and unfiltered (in parentheses) normalised standard deviations, $\sigma_{\text{Int.}}$, for both SpectroBragg and polarimeter data. The values are for the data with applied SOP changes and without applied SOP changes (i.e. background); **(c)** the FFT filtered and unfiltered (in parentheses) standard deviation of centroid calculated wavelength, σ_{λ_B}, for the anisotropic and isotropic FBGs; **(d)** the SpectroBragg intensity–centroid λ_B correlation coefficient, ρ_{λ_B}, as a measure of intensity pattern's influence on λ_B.

The source or means by which this change in coverage was achieved is unknown[16]. As for the reduced anisotropic FBG coverage in the Lyot depolariser experiment, figure N.12 (page V.II N-19), the same FC/APC rotations were applied, and movements of the fibre to the polarimeter would have been negligible.

The improvement in the anisotropic FBG $\rho_{\text{Int.}}$ value ($\sim 64\%$) can be seen from figures N.24(a) (page V.II N-33) to N.24(d) (page V.II N-33). The profiles of both the unfiltered and filtered polarimeter and SpectroBragg only appear to show distinct SOP changes at $2 \ldots 17$ s, where as the unfiltered polarimeter data only suggests another separation at $\sim$ 66s. This may be as a result of the fibre loop holders not being at the optimum angle. As the oscillations approached a minimum, further adjustments to achieve improved behaviour became progressively difficult to observe.

The isotropic FBG $\rho_{\text{Int.}}$ value ($\sim 105\%$) is not improved over the control experiment value. The reason can be seen in figure N.25 (page V.II N-34). The three distinct SOP changes are visible on figures N.25(a) (page V.II N-34) to N.25(d) (page V.II N-34), at $2 \ldots 14$ m, $14 \ldots 38$ m and $38 \ldots 46$ m. As for the anisotropic FBG, the profiles of the first distinct SOP changes are best preserved from polarimeter to SpectroBragg. As the SOP changes were applied in the same order for each experiment, it is likely that the SOPs produced at this time were the least corrected SOPs through the apparatus.

The next distinct SOP change is the most corrected initially. It is likely that the FC/APC connector was not kept perfectly orthogonal to the other positions during the full rotation of the connector, hence the rising oscillation. A similar deterioration is observed in the third distinct SOP change.

The anisotropic FBG $\sigma_{\text{Int.}}$ value is the lowest of all the approaches tested, at $\sim 24\%$ of the control experiment value. The corresponding Polarimeter $\sigma_{\text{Int.}}$ value is almost identical to the control experiment value ($\sim 105\%$). Despite the almost unchanged isotropic FBG $\rho_{\text{Int.}}$ value compared to the control experiment, the isotropic FBG $\sigma_{\text{Int.}}$ value ($\sim 46\%$) is reduced.

The FFT filtered anisotropic σ_{λ_B} value is $\sim 32\%$ the control experiment value, and from figure N.26 (page V.II N-35) it can be seen that this was, in part still due to unfiltered noise. The σ_{λ_B} value is not much larger than the background σ_{λ_B} value, despite the large number of outliers.

Changes to the SOP stop at $\sim$ 100 s in figures N.24(a) (page V.II N-33) to N.24(d) (page V.II N-33), yet the oscillation from $\sim$ 104 s in figures N.26(a) (page V.II N-35) & N.26(b) (page V.II N-35) continue. The oscillations are of the same amplitude as the rest of the oscillations in the dataset, but less noisy, yet do not correspond to applied SOP changes. These non–SOP changes are similar to the

[16] A possible source is non–diametrically oriented 'SOP–holes' [4], or forbidden SOPS, if their overlap is then allowed, as in that the overlapped forbidden zones cancel each other out.

interferometrically coupled acoustic noise shown in figure 5.19(a) (page V.I - 244), and may indicate that the FFT filtering was not sufficient.

The background σ_{λ_B} values are reduced by the FFT filtering for both FBGs, but, again, the oscillations after ~ 100 s distort the anisotropic FBG results. That the λ_B signal noise is reduced suggests that the noise was not polarisation linked, but interferometrically coupled noise.

The isotropic σ_{λ_B} value is $\sim 103\%$ the control experiment value. Figure N.27 (page V.II N-35) shows the centroid calculated λ_B for the isotropic FBG. As for figure N.25 (page V.II N-34), the three distinct SOP changes can be observed in figure N.26 (page V.II N-35), in addition to an oscillation after SOP changes were stopped, at ~ 47 s. Again, this oscillation is not very different from the preceding range of SOP changes. It is possible that the acoustic noise coupled into the ODL was sufficient to move periodically the OPD back into a coherent range, and hence introduce interference into the SpectroBragg results.

However, the presence of the same oscillations in the polarimeter and SpectroBragg data, as represented by $\rho_{\text{Int.}}$ makes it unlikely that the source is acoustic noise coupled into the ODL. The narrower spectral profile of the isotropic FBG may have necessitated a larger OPD than the spectrally broader anisotropic FBG, but this effect is unlikely to account for the magnitude of the change between the anisotropic and isotropic FBGs. Unfortunately it was not possible to repeat the experiment by the time this effect was noticed.

The anisotropic FBG ρ_{λ_B} value ($\sim 46\%$) is an improvement over the control experiment value, but may be larger than possibly achievable as a result of the unfiltered oscillations discussed. The isotropic FBG ρ_{λ_B} value ($\sim 150\%$) indicates that the intensity changes are strongly correlated with the centroid calculated λ_B value. Any improvement in the isotropic FBG intensity parameters should improve the λ_B values. Figures N.28 (page V.II N-36) and N.30 (page V.II N-37) show the correlation coefficient, $\rho_{\text{Int.}}$, as a function of changing θ_{rot} and ϕ_{pr}. Figures N.29 (page V.II N-36) and N.31 (page V.II N-37) show the orthogonal cross sections, the (a) figures along θ_{rot} and the (b) figures along ϕ_{pr}, containing the largest $|\rho_{\text{Int.}}(\theta_{rot}, \phi_{pr})|$.

Despite the improvement achieved, the apparatus was prone to several problems. The Lefèvre polarisation controllers were difficult to maintain in a given configuration, with the fibre loop holders parallel to the bench prone to suddenly falling to rest upon the bench, unless supported. It was not possible to tighten the loop holder in place and consequently they may have moved imperceptibly during the experiment if the support was not placed perfectly.

They also required considerable effort to align so as to produce the half–waveplate effect. In particular, it was difficult to make adjustments to the orientation of the paddles when the oscillations became less evident on screen. Consequently,

a more stable, less manually intensive and easier to use version was sought: the circulator/Faraday mirror approach discussed next.

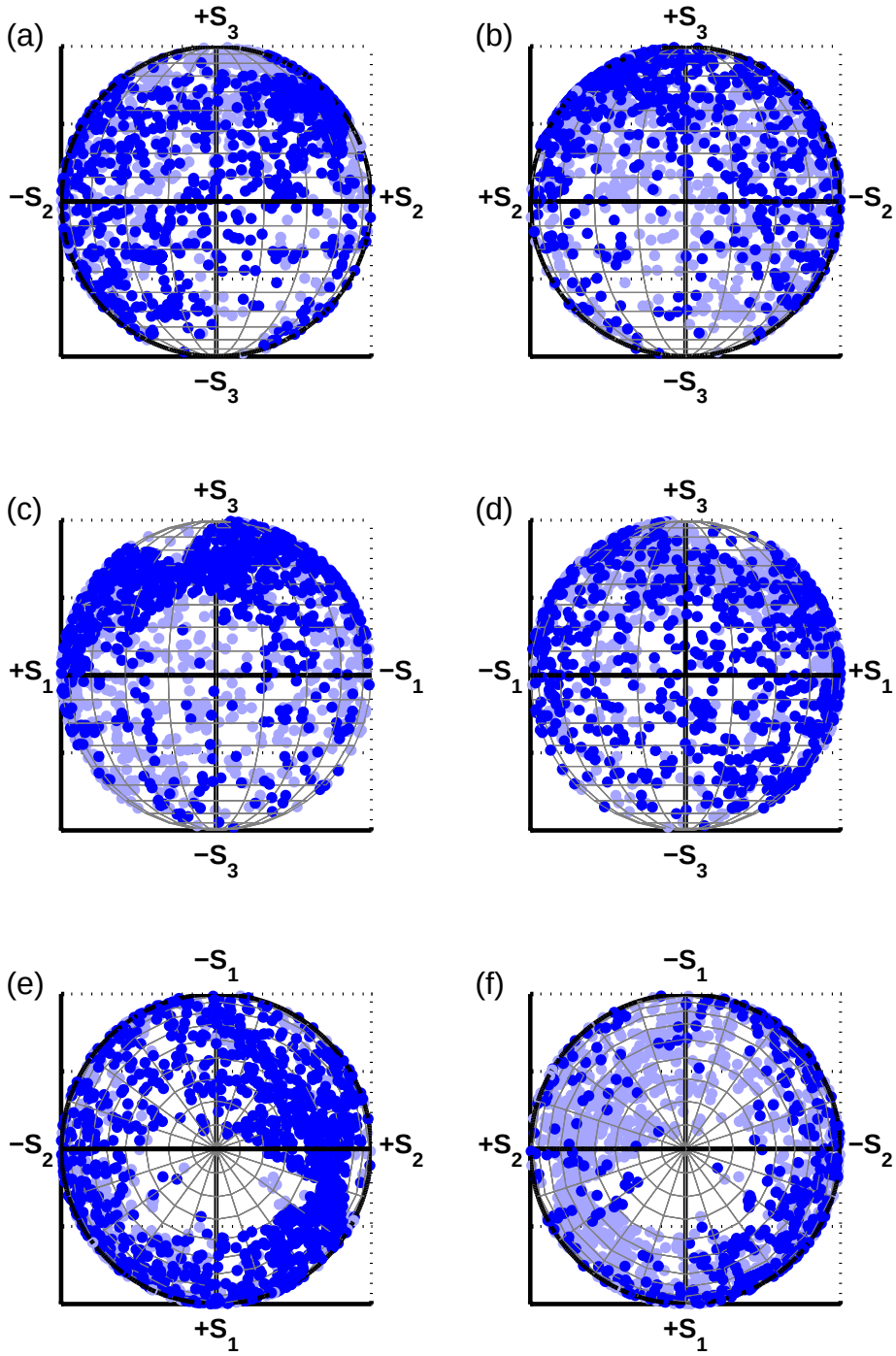

Figure N.22: Poincaré sphere projections of anisotropic FBG data showing: **(a)** S_2 V. S_3 along S_1 to $-S_1$; **(b)** S_2 V. S_3 along $-S_1$ to S_1; **(c)** S_1 V. S_3 along S_2 to $-S_2$; **(d)** S_1 V. S_3 along $-S_2$ to S_2 ;**(e)** S_2 V. S_1 along S_3 to $-S_3$; and **(f)** S_2 V. S_1 along $-S_3$ to S_3.

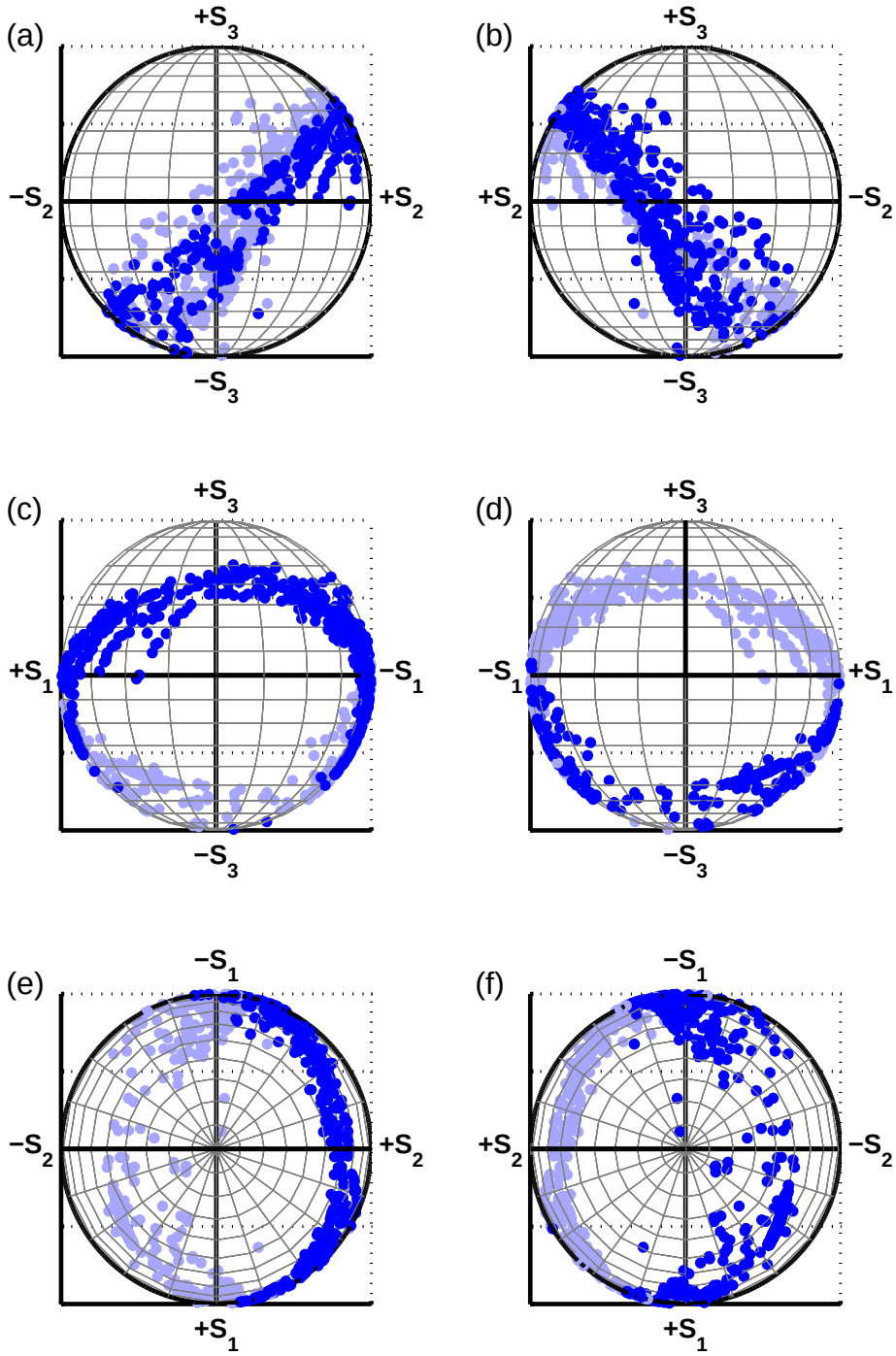

Figure N.23: Poincaré sphere projections of isotropic FBG data showing: **(a)** S_2 V. S_3 along S_1 to $-S_1$; **(b)** S_2 V. S_3 along $-S_1$ to S_1; **(c)** S_1 V. S_3 along S_2 to $-S_2$; **(d)** S_1 V. S_3 along $-S_2$ to S_2 ;**(e)** S_2 V. S_1 along S_3 to $-S_3$; and **(f)** S_2 V. S_1 along $-S_3$ to S_3.

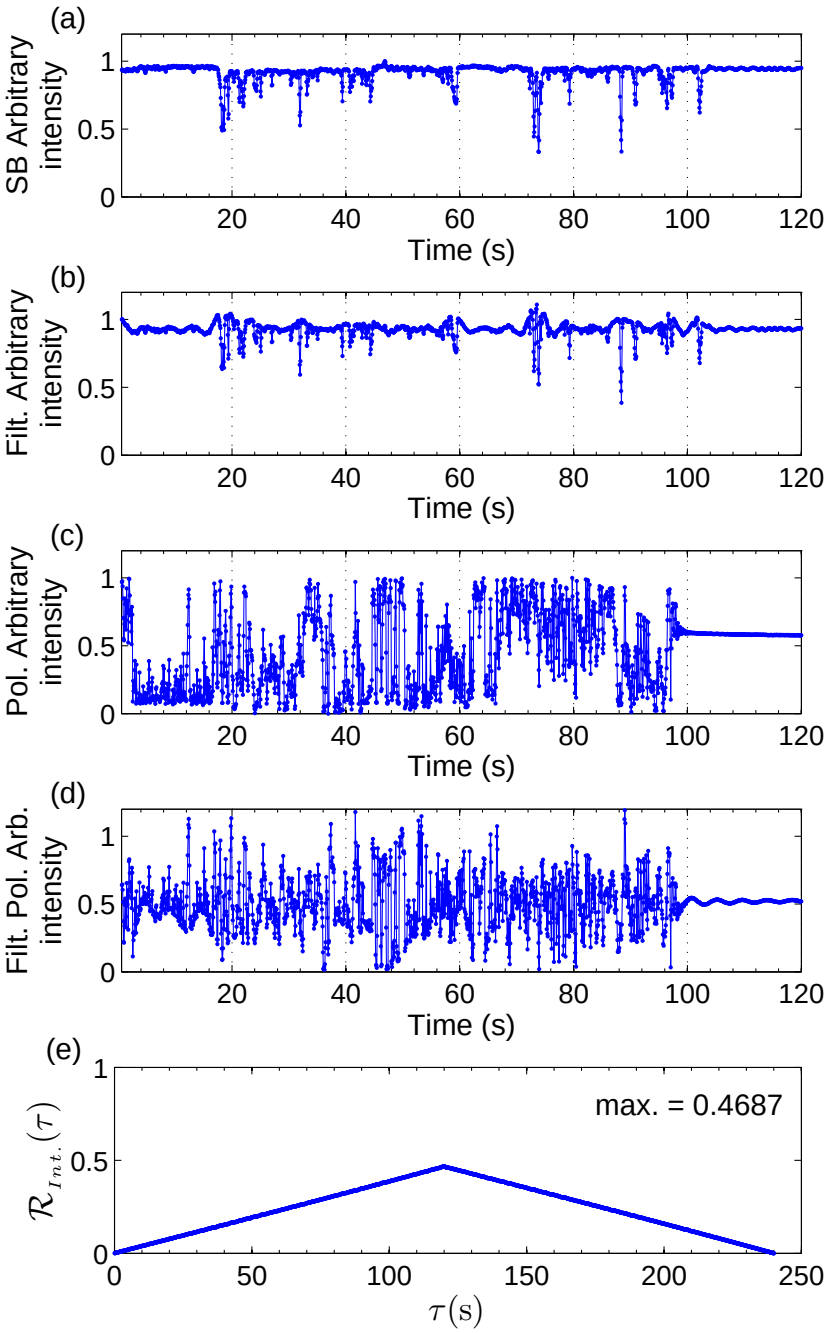

Figure N.24: Plot of anisotropic FBG data showing **(a)** the data captured on the SpectroBragg; **(b)** the FFT filtered SpectroBragg data; **(c)** the calculated ideal SpectroBragg intensity from the polarimeter data, using a rotation angle of 118°; and **(d)** the cross–correlation, $\mathcal{R}_{\text{Int.}}$, of (b) & (c) for Lefèvre controller approach.

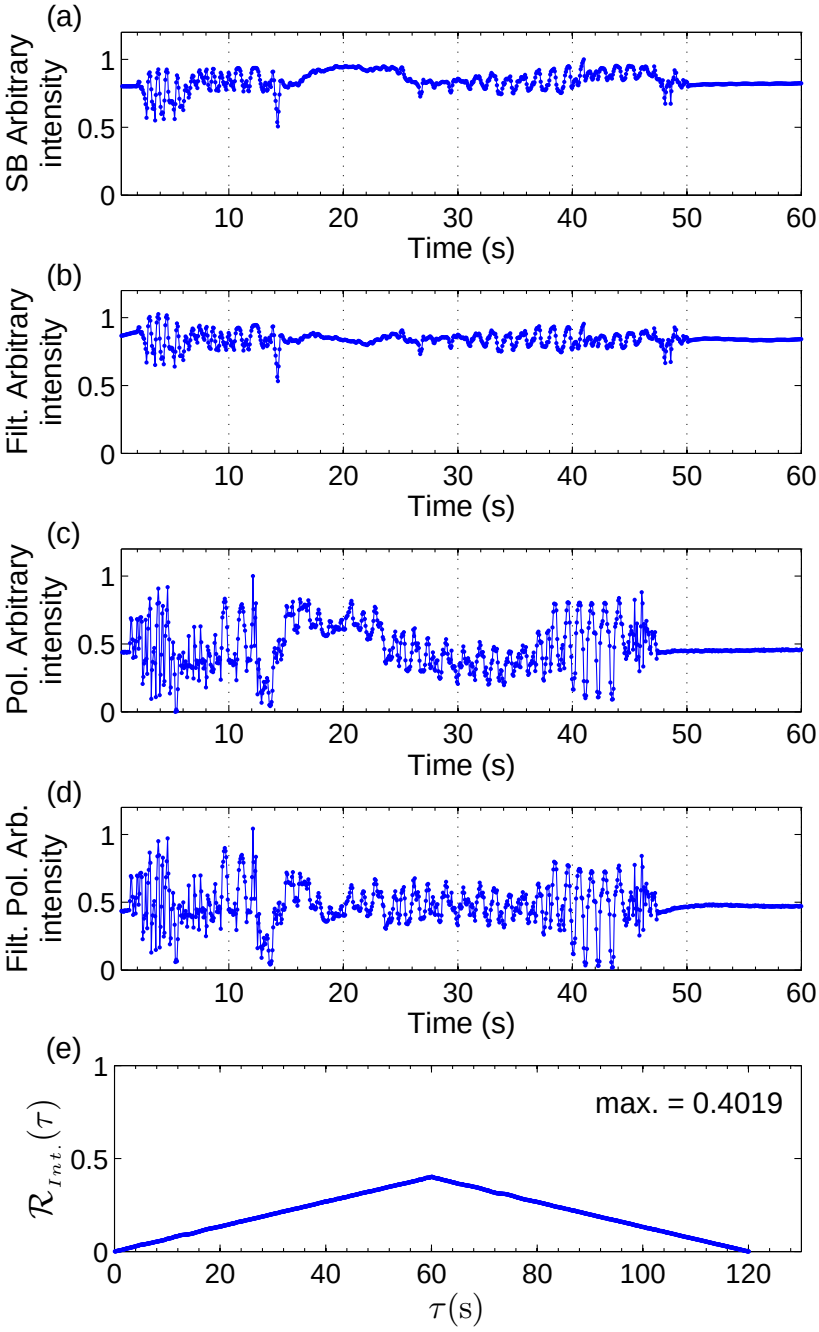

Figure N.25: Plot of isotropic FBG data showing **(a)** the data captured on the SpectroBragg; **(b)** the FFT filtered SpectroBragg data; **(c)** the calculated ideal SpectroBragg intensity from the polarimeter data, using a rotation angle of 16°; and **(d)** the cross–correlation, $\mathcal{R}_{\text{Int.}}$, of (b) & (c) for Lefèvre controller approach.

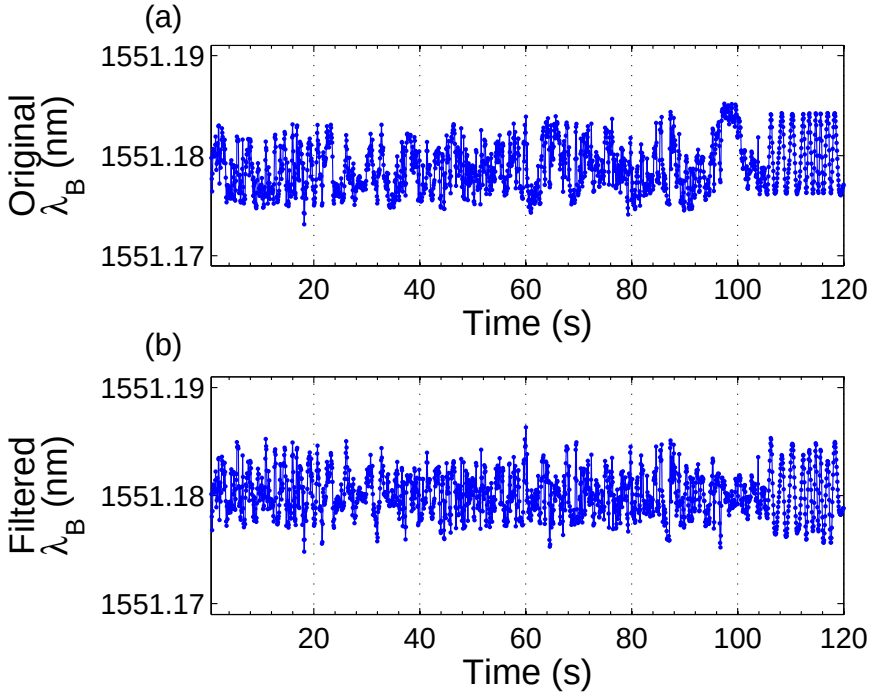

Figure N.26: Plot of **(a)** centroid determined λ_B for the anisotropic FBG data showing; **(b)** the centroid determined λ_B from the FFT filtered SpectroBragg data.

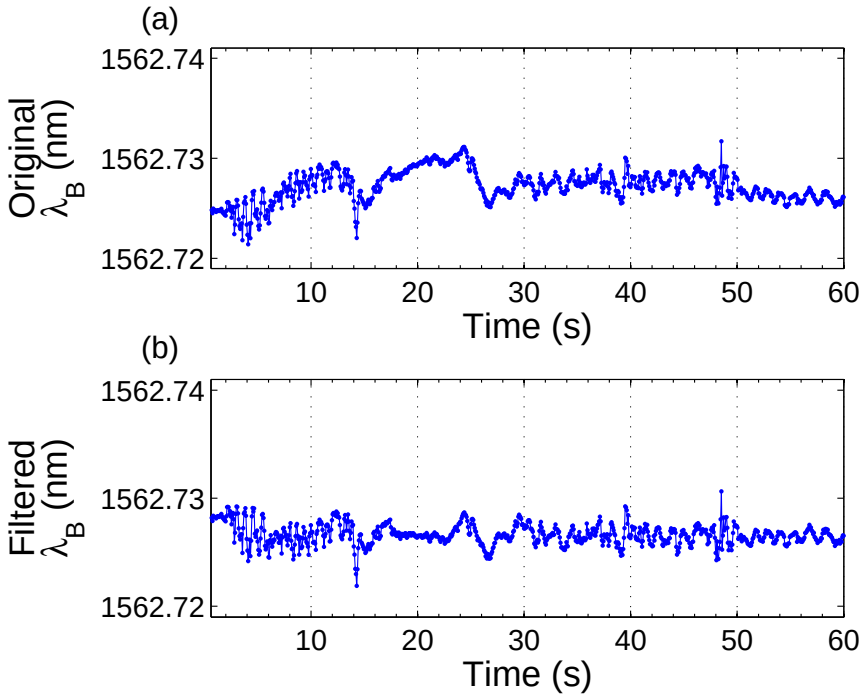

Figure N.27: Plot of **(a)** centroid determined λ_B for the anisotropic FBG data showing; **(b)** the centroid determined λ_B from the FFT filtered SpectroBragg data.

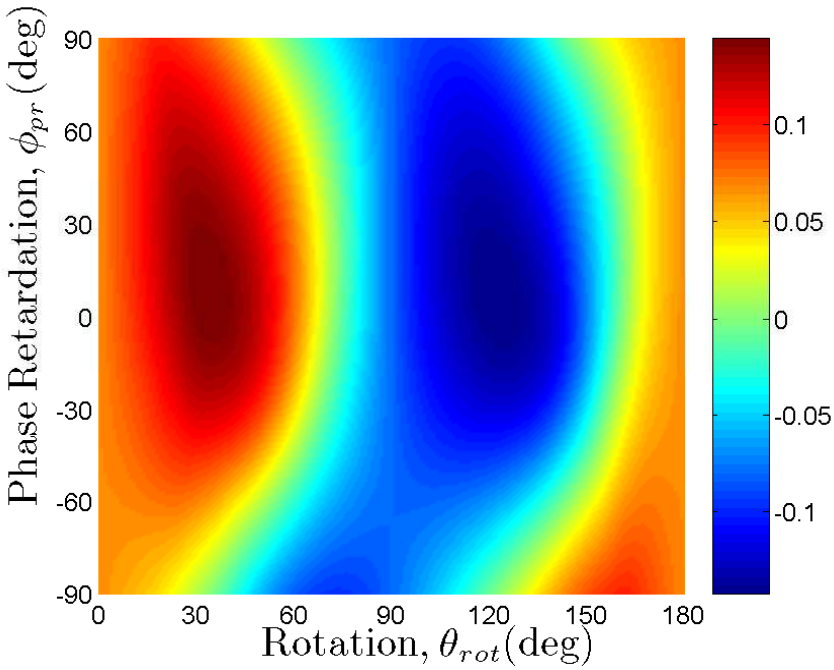

Figure N.28: Plot of changing correlation coefficient $\rho_{\text{Int.}}(\theta_{rot}, \phi_{pr})$ for axes rotation $\theta_{rot} = 0 \ldots 180°$ and phase retardation $\phi_{pr} = -90 \ldots 90°$ obtained for idealised SpectroBragg Mueller matrix for anisotropic FBG.

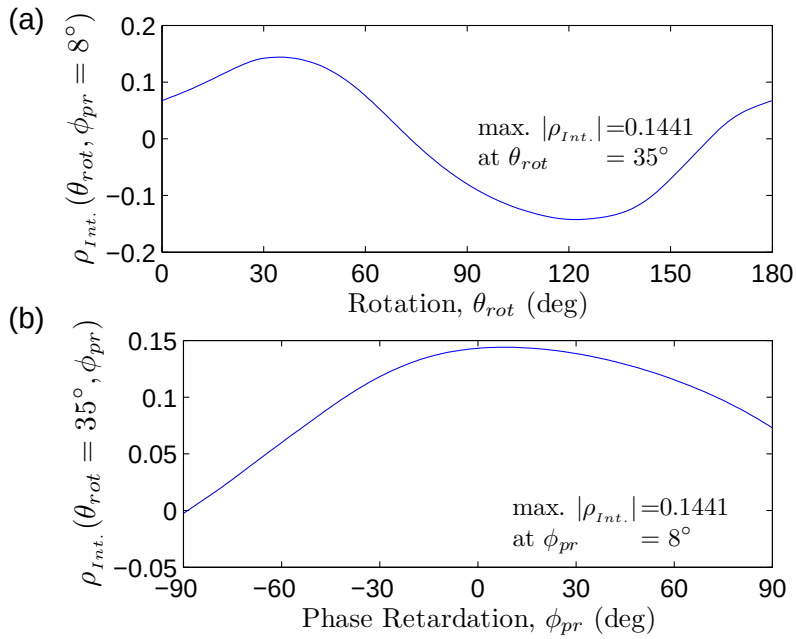

Figure N.29: Cross–sectional plots of figure N.28 which contain the largest value for the correlation coefficient $\rho_{\text{Int.}}(\theta_{rot}, \phi_{pr})$, (a) constant phase retardation ϕ_{pr} and (b) showing constant rotation θ_{rot}.

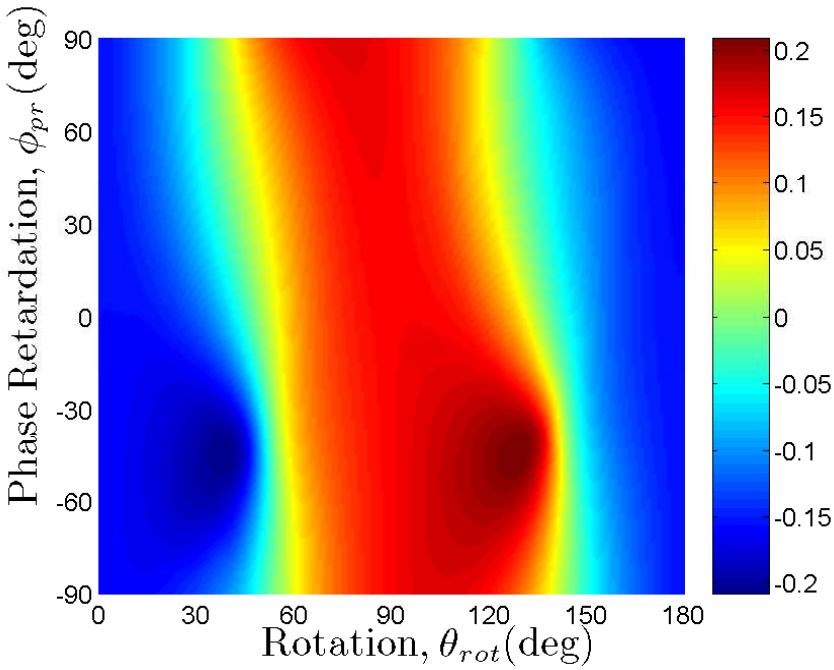

Figure N.30: Plot of changing correlation coefficient $\rho_{\text{Int.}}(\theta_{rot}, \phi_{pr})$ for axes rotation $\theta_{rot} = 0 \ldots 180°$ and phase retardation $\phi_{pr} = -90 \ldots 90°$ obtained for idealised SpectroBragg Mueller matrix for isotropic FBG.

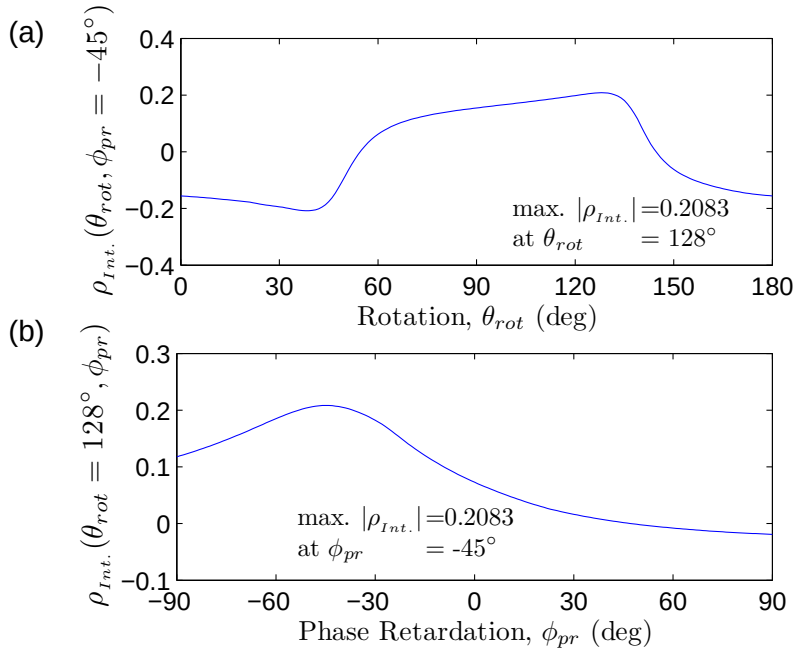

Figure N.31: Cross–sectional plots of figure N.30 which contain the largest value for the correlation coefficient $\rho_{\text{Int.}}(\theta_{rot}, \phi_{pr})$, (a) constant phase retardation ϕ_{pr} and (b) showing constant rotation θ_{rot}.

N.4 Circulator/Faraday mirror SOP fixer

The circulator/Faraday mirror approach, §5.3.2.3 (page V.I - 230), was, in intention, the same optical configuration as described in §N.3 (page V.II N-26). In place of a Lefèvre polarisation controller half–waveplate, a Faraday mirror and a circulator are used. The Faraday mirror rotates the SOP to its orthogonal SOP, and the circulator allows the completion of the stationary Mach–Zehnder interferometer arm.

The circulator/Faraday mirror approach is mechanically more stable and is easier to assemble than the Lefèvre polarisation controller approach of §N.3 (page V.II N-26). However, twists or bends in the circulator or the recombining 50:50 Y–coupler, may introduce further, unwanted rotation and/or phase retardation to the Faraday mirror reflected SOP. Additionally, the circulator was not made of PMF, and twists and bends may have altered the SOP before it was recombined at the 50:50 Y–coupler.

This may have produced an inferior performance to the Lefèvre controller experiment as, in the case of further changes to the SOP, the Lefèvre controller may be configured to produce an effectively orthogonal SOP at the Y–coupler by observing the output, whereas the fixed Faraday mirror would produce lower performance.

The isotropic FBG exhibits the same bow–tie Poincaré sphere pattern, shown in figure N.33 (page V.II N-42), as the control experiment. The anisotropic FBG changing SOPs do not cover the entire Poincaré sphere, figure N.32 (page V.II N-41), and have an appearance closer to the isotropic FBG Poincaré sphere figures' bow–tie pattern. An explanation for this is not apparent, as the Lefèvre controller would have been replaced by the circulator/Faraday mirror, leaving the components from the FBGs to the polarimeter untouched.

A weak π–rotation symmetry about the centre is observed, where the SOP populated regions mirror the SOP unpopulated regions along the S_1S_3 plane. As the greater coverage of the anisotropic FBG SOPs improved the polarisation mitigation values over the isotropic FBG values for the Lefèvre controller, the reduced coverage of the anisotropic FBGs for the circulator/Faraday mirror would be expected to exhibit an intermediate level of performance.

The correlation coefficient, $\rho_{\text{Int.}}$, obtained in table N.4(a) (page V.II N-40) obtained is unchanged from the control experiment for the anisotropic FBG. The value is similar to the isotropic FBG values for the other polarisation mitigation approaches, but nearly an order of magnitude lower ($\sim 15\%$) for the isotropic FBG value. The similarity of figures N.34(b) (page V.II N-43) & N.34(d) (page V.II N-43) accounts for the anisotropic FBG correlation coefficient. The three distinct SOP changes are evident in figure N.34(b) (page V.II N-43) at $20\ldots38$ s, $38\ldots52$ s and $52\ldots68$ s. The SOP changes at $20\ldots38$ s are better mitigated on figures N.34(b)

(page V.II N-43) and N.36(b) (page V.II N-45), which shows the centroid calculated wavelength, λ_B, from the SpectroBragg data.

The SpectroBragg $\sigma_{\text{Int.}}$ value is smaller than the control experiment value ($\sim$ 60%) but larger than the Lefèvre controller value ($\sim$ 250%). The corresponding Polarimeter $\sigma_{\text{Int.}}$ value is $\sim$ 160% the control and Lefèvre controller values, despite the reduced coverage of the Poincaré sphere. The similarity of figures N.34(b) (page V.II N-43) and N.36(b) (page V.II N-45) account for the relatively large correlation coefficient between the SpectroBragg intensity and centroid ρ_{λ_B}.

The isotropic FBG $\sigma_{\text{Int.}}$ value is $\sim$ 292% the control experiment value. The low $\rho_{\text{Int.}}$ value indicates that the intensity pattern at the Polarimeter, which has a $\sigma_{\text{Int.}}$ value 44% of the control experiment, does not follow the applied SOP changes. The possible changes in the 'orthogonal' SOPs after the circulator/Faraday mirror in the combining Y–coupler arms are a likely source of this $\sim$ 292% value of $\sigma_{\text{Int.}}$.

The anisotropic FBG centroid calculated σ_{λ_B} value is smaller than the control experiment value ($\sim$ 57%) but larger than the Lefèvre controller value ($\sim$ 179%), with the ρ_{λ_B} value larger than both the control experiment ($\sim$ 154%) and Lefèvre controller ($\sim$ 336%) values.

The σ_{λ_B} value for the background level is over three times larger then the control experiment, but σ_{λ_B} value for the applied changes is $\sim$ 57% that of the control experiment. This may be due to unfiltered phase noise remaining in the data. Determining an optimal frequency to filter was complicated by a smoother transition between the high frequency components and the lower frequency components.

The isotropic FBG σ_{λ_B} value is ($\sim$ 402%) the control experiment value, but the ρ_{λ_B} value of 0.74 is the largest of any of the approaches tested and is twice the anisotropic FBG value. The large value indicates that the σ_{λ_B} value is largely following the intensity pattern.

The centroid calculated λ_B values are shown in figure N.37 (page V.II N-45). The large isotropic FBG σ_{λ_B} value may be as a result of the FFT filtering, however the distinction of high and low–frequency components was much more evident, and it is more likely that the apparatus was not maintaining the orthogonal SOPs orientation prior to recombination at the Y–coupler.

Figures N.38 (page V.II N-46) and N.40 (page V.II N-47) show the correlation coefficient, $\rho_{\text{Int.}}$, as a function of changing θ_{rot} and ϕ_{pr}. Figures N.39 (page V.II N-46) and N.41 (page V.II N-47) show the orthogonal cross sections, the (a) figures along θ_{rot} and the (b) figures along ϕ_{pr}, containing the largest $|\rho_{\text{Int.}}(\theta_{rot}, \phi_{pr})|$.

Quantity	FBG			Control		Circ. / FM	
(a) $\rho_{\text{Int.}}$	Aniso.		$\lvert\rho_{\text{Int.}}\rvert$	0.22	(0.28)	0.22	(0.34)
			θ_{rot}	125°		150°	
			ϕ_{pr}	−50°		−73°	
	Iso.		$\lvert\rho_{\text{Int.}}\rvert$	0.20	(0.18)	0.03	(0.08)
			θ_{rot}	130°		128°	
			ϕ_{pr}	72°		−82°	
(b) $\sigma_{\text{Int.}}$ (pm)	Aniso.	SB.	w. ΔSOP	0.25	(0.56)	0.15	(0.25)
			background	0.07	(0.03)	0.0244	(0.0244)
		Pol.	w. ΔSOP	0.38	(0.56)	0.62	(1.02)
			background	0.04	(0.03)	0.1192	(0.0318)
	Iso.	SB.	w. ΔSOP	0.13	(0.18)	0.38	(2.07)
			background	0.03	(0.001)	0.13	(0.05)
		Pol.	w. ΔSOP	0.50	(0.55)	0.22	(0.25)
			background	0.07	(0.18)	0.05	(0.004)
(c) σ_{λ_B} (pm)	Aniso.		w. ΔSOP	5.80	(7.41)	3.30	(4.05)
			background	0.25	(0.07)	0.81	(0.42)
	Iso.		w. ΔSOP	0.88	(1.05)	3.54	(5.11)
			background	0.88	(0.28)	1.28	(0.73)
(d) $\lvert\rho_{\lambda_B}\rvert$	Aniso.			0.24	(0.40)	0.37	(0.38)
	Iso.			0.46	(0.46)	0.74	(0.79)

Table N.4: Circulator/Faraday mirror mitigation approach summary of **(a)** correlation coefficient, $\rho_{\text{Int.}}$, values for correlation between captured Spectro-Bragg intensity and calculated S_{SB}; **(b)** the FFT filtered and unfiltered (in parentheses) normalised standard deviations, $\sigma_{\text{Int.}}$, for both SpectroBragg and polarimeter data. The values are for the data with applied SOP changes and without applied SOP changes (i.e. background); **(c)** the FFT filtered and unfiltered (in parentheses) standard deviation of centroid calculated wavelength, σ_{λ_B}, for the anisotropic and isotropic FBGs; **(d)** the SpectroBragg intensity–centroid λ_B correlation coefficient, ρ_{λ_B}, as a measure of intensity pattern's influence on λ_B.

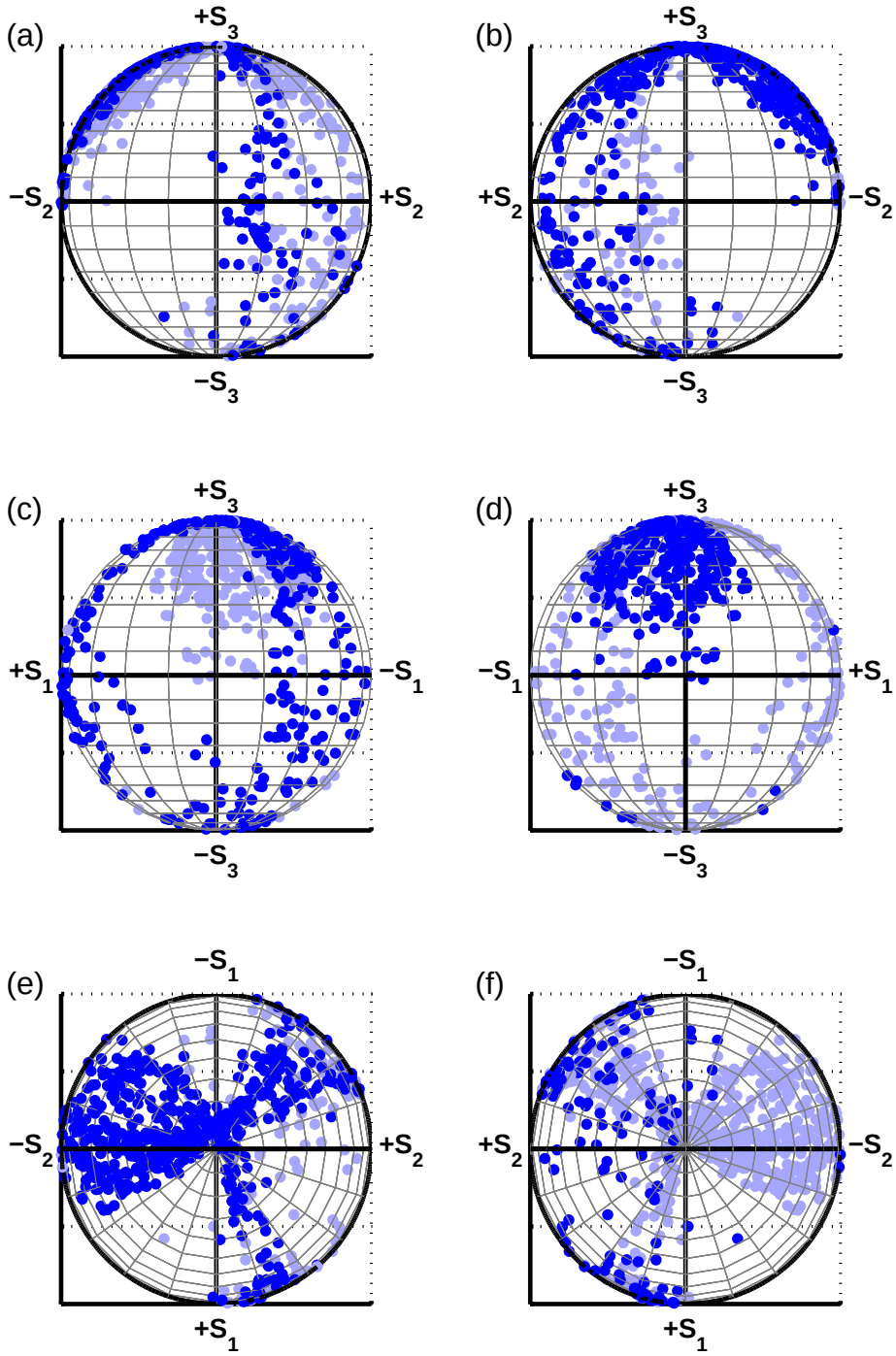

Figure N.32: Poincaré sphere projections of anisotropic FBG data showing: **(a)** S_2 V. S_3 along S_1 to $-S_1$; **(b)** S_2 V. S_3 along $-S_1$ to S_1; **(c)** S_1 V. S_3 along S_2 to $-S_2$; **(d)** S_1 V. S_3 along $-S_2$ to S_2 ;**(e)** S_2 V. S_1 along S_3 to $-S_3$; and **(f)** S_2 V. S_1 along $-S_3$ to S_3.

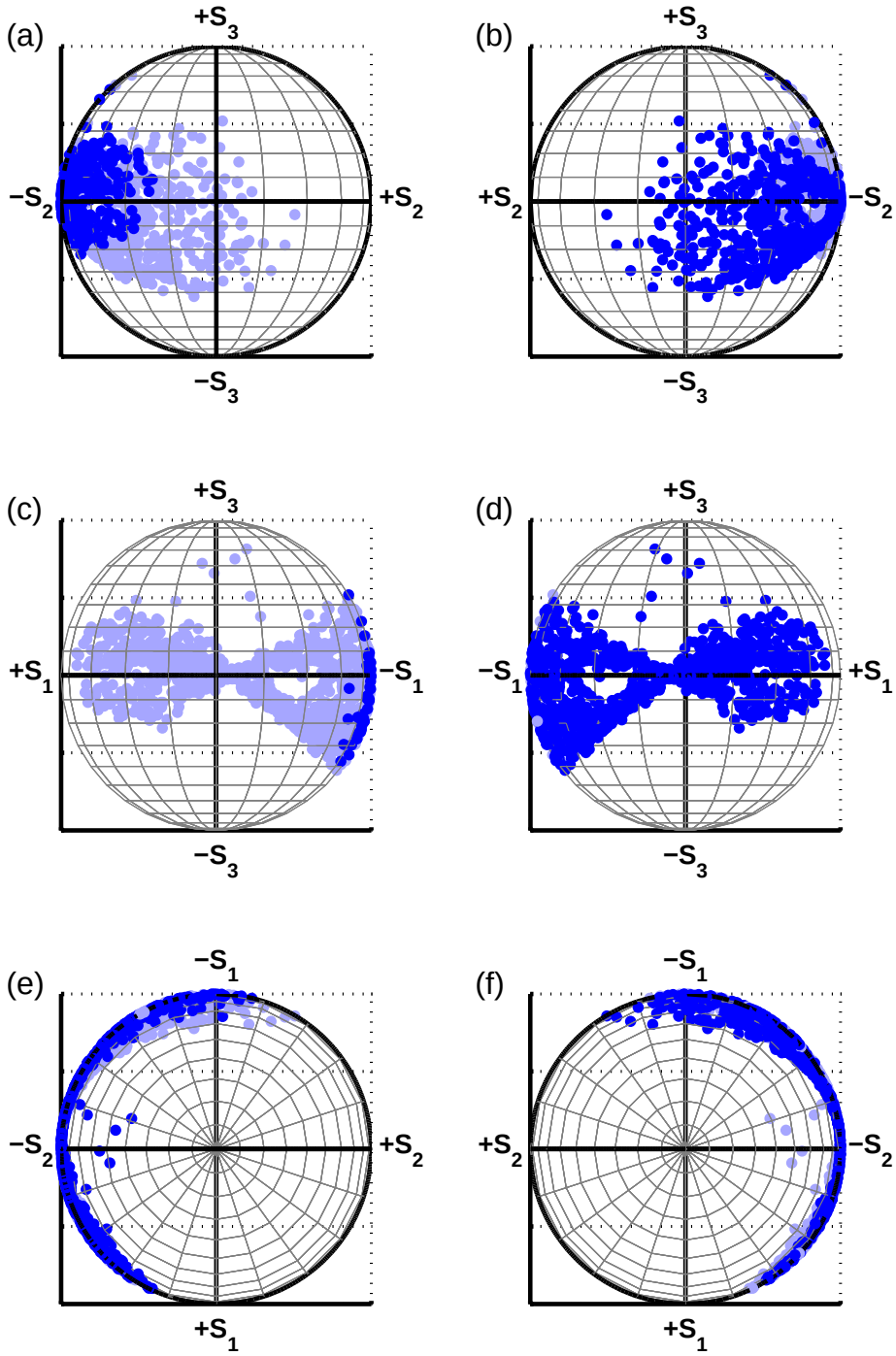

Figure N.33: Poincaré sphere projections of isotropic FBG data showing: **(a)** S_2 V. S_3 along S_1 to $-S_1$; **(b)** S_2 V. S_3 along $-S_1$ to S_1; **(c)** S_1 V. S_3 along S_2 to $-S_2$; **(d)** S_1 V. S_3 along $-S_2$ to S_2 ;**(e)** S_2 V. S_1 along S_3 to $-S_3$; and **(f)** S_2 V. S_1 along $-S_3$ to S_3.

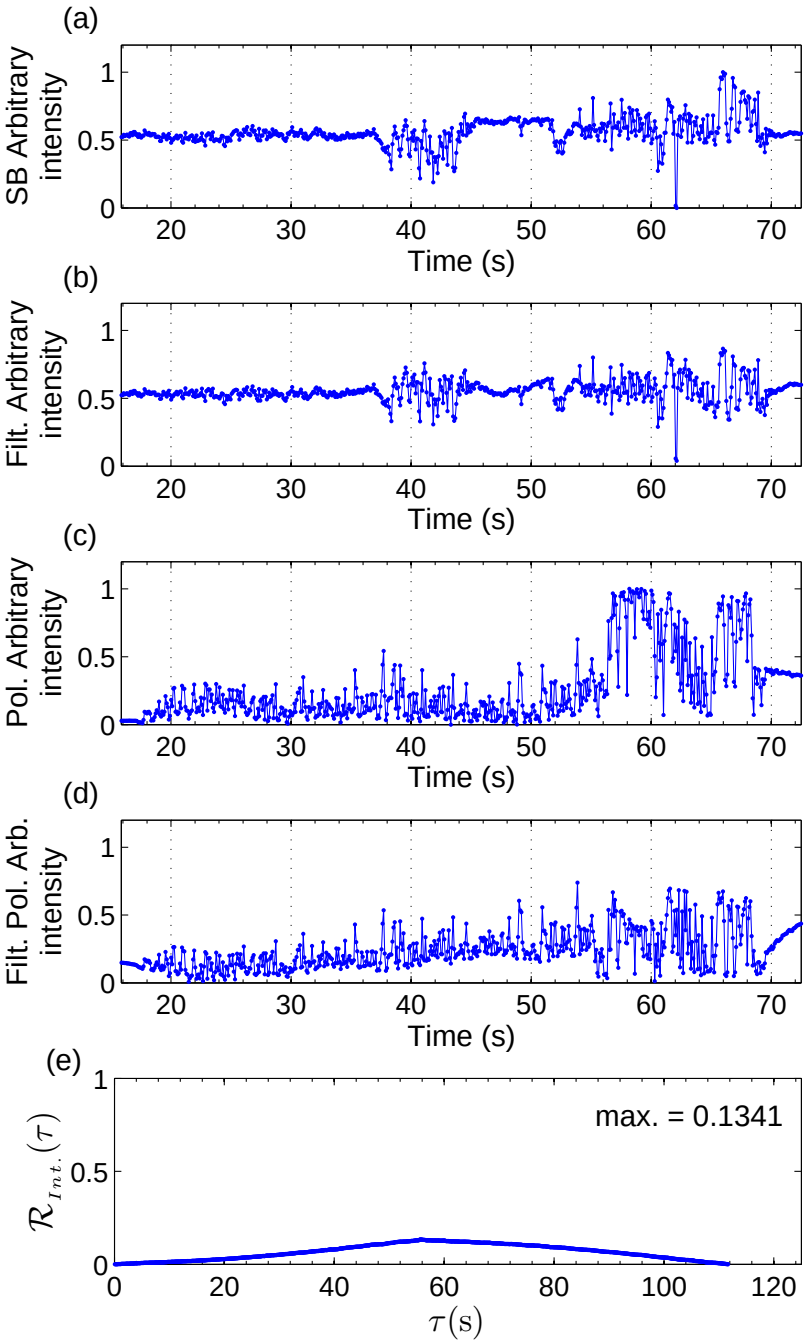

Figure N.34: Plot of anisotropic FBG data showing **(a)** the data captured on the SpectroBragg; **(b)** the FFT filtered SpectroBragg data; **(c)** the calculated ideal SpectroBragg intensity from the polarimeter data, using a rotation angle of 57°; and **(d)** the cross–correlation, $\mathcal{R}_{\text{Int.}}$, of (b) & (c) for Circulator/Faraday mirror approach.

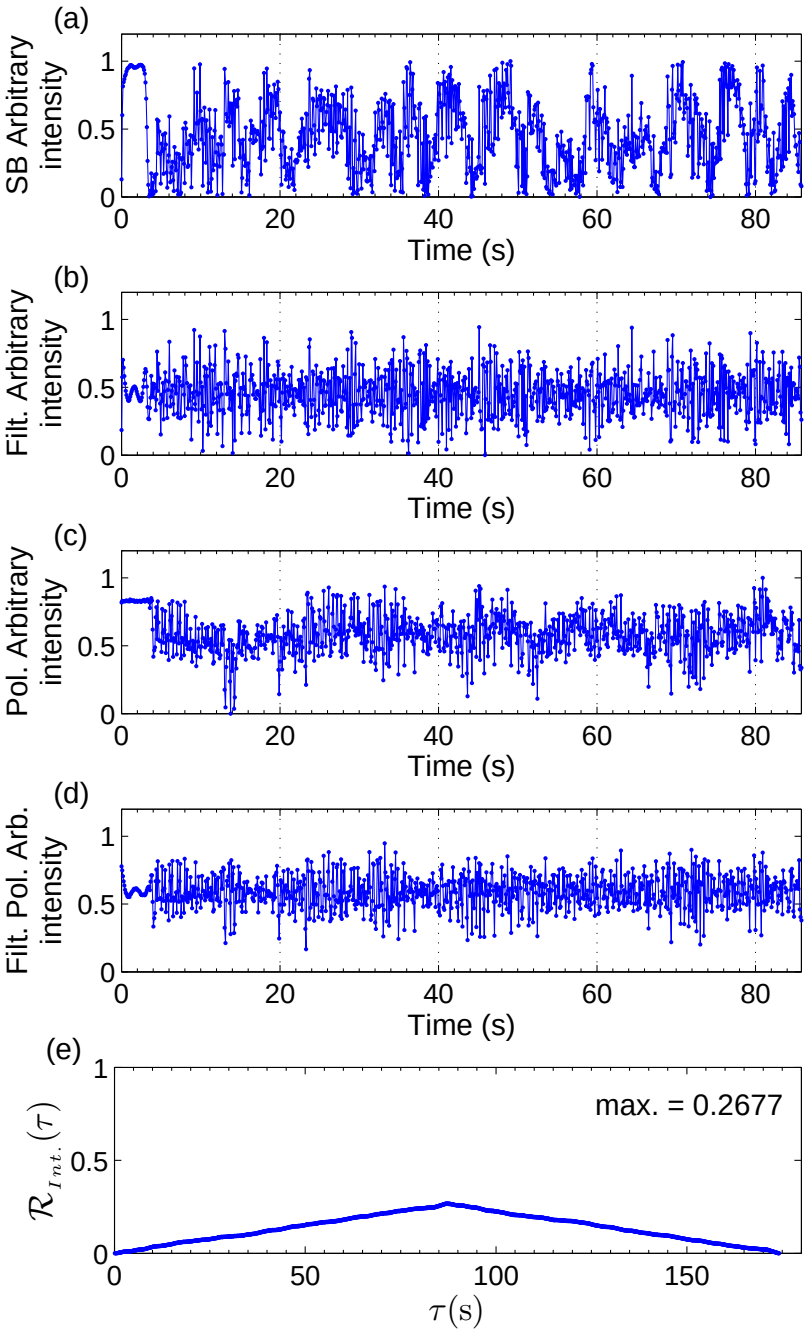

Figure N.35: Plot of isotropic FBG data showing **(a)** the data captured on the SpectroBragg; **(b)** the FFT filtered SpectroBragg data; **(c)** the calculated ideal SpectroBragg intensity from the polarimeter data, using a rotation angle of 120°; and **(d)** the cross–correlation, $\mathcal{R}_{\text{Int.}}$, of (b) & (c) for Circulator/Faraday mirror approach.

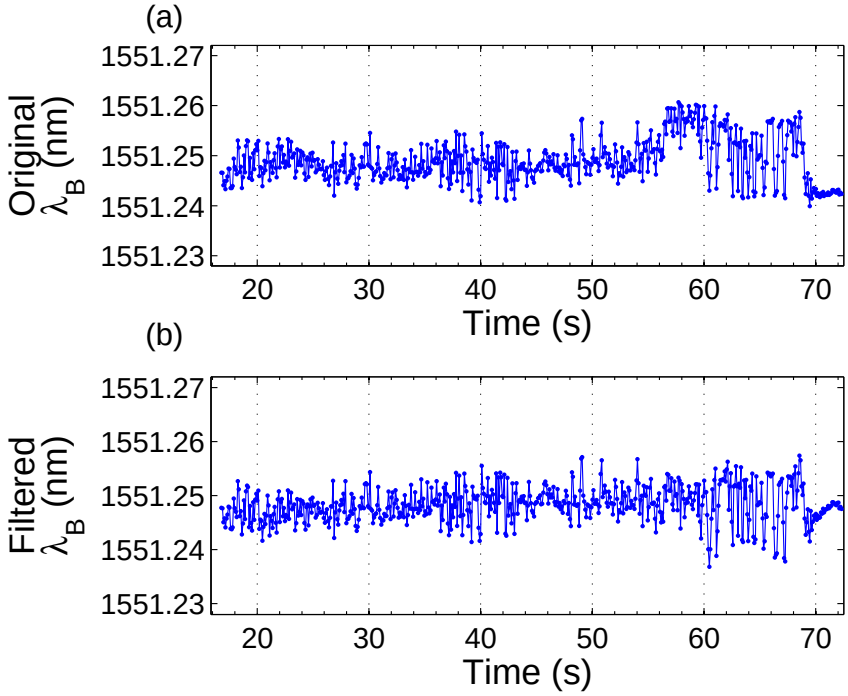

Figure N.36: Plot of **(a)** centroid determined λ_B for the anisotropic FBG data showing; **(b)** the centroid determined λ_B from the FFT filtered SpectroBragg data.

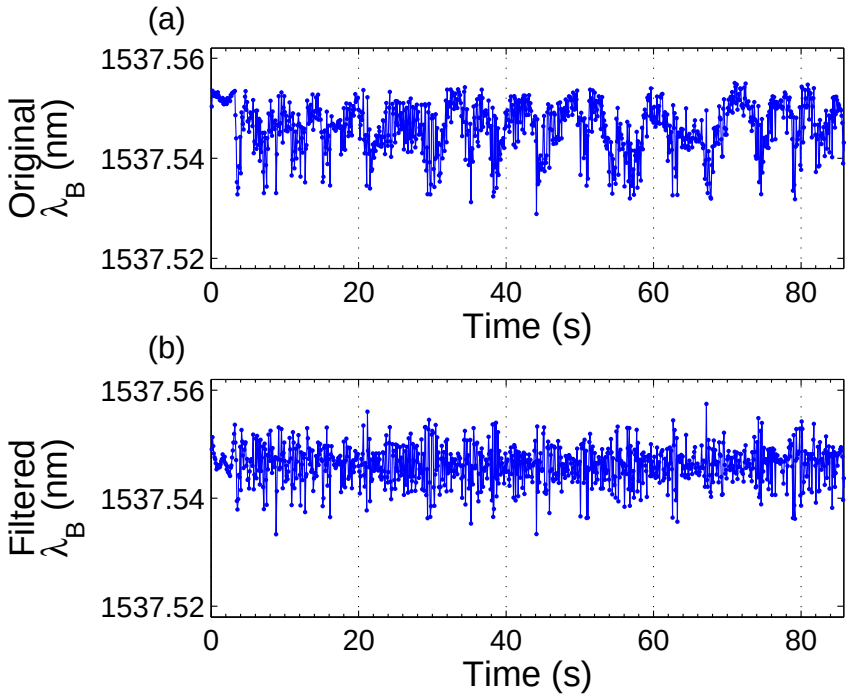

Figure N.37: Plot of **(a)** centroid determined λ_B for the anisotropic FBG data showing; **(b)** the centroid determined λ_B from the FFT filtered SpectroBragg data.

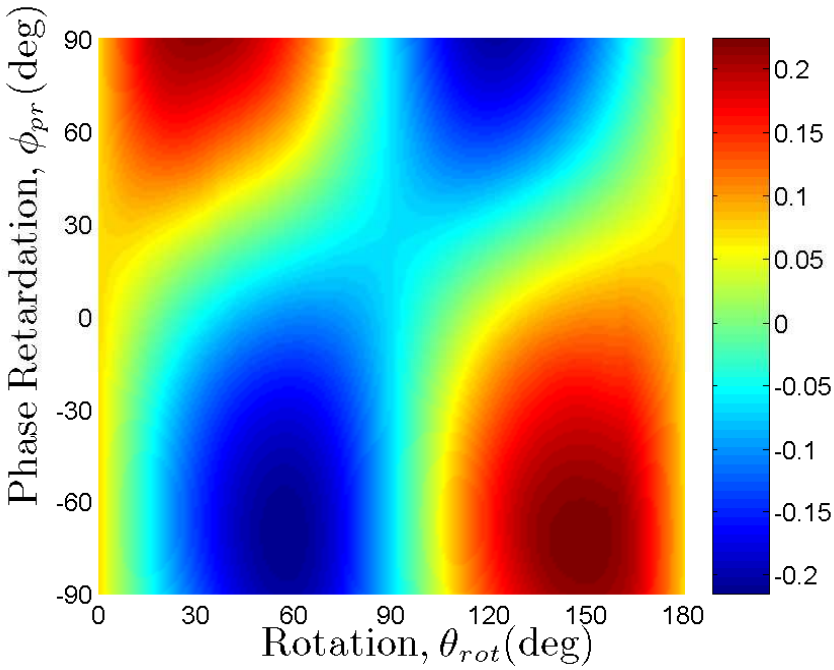

Figure N.38: Plot of changing correlation coefficient $\rho_{\text{Int.}}(\theta_{rot}, \phi_{pr})$ for axes rotation $\theta_{rot} = 0 \ldots 180°$ and phase retardation $\phi_{pr} = -90 \ldots 90°$ obtained for idealised SpectroBragg Mueller matrix for anisotropic FBG.

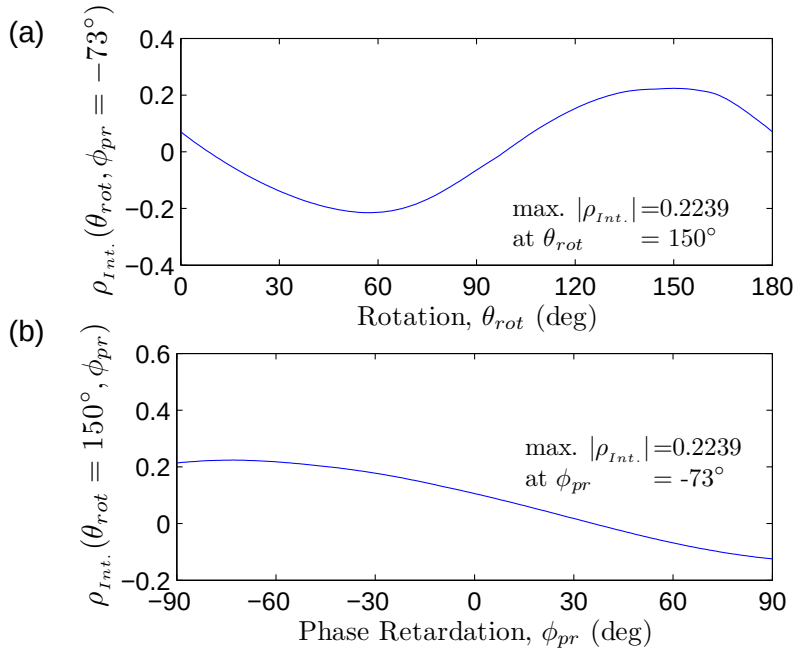

Figure N.39: Cross–sectional plots of figure N.38 which contain the largest value for the correlation coefficient $\rho_{\text{Int.}}(\theta_{rot}, \phi_{pr})$, (a) constant phase retardation ϕ_{pr} and (b) showing constant rotation θ_{rot}.

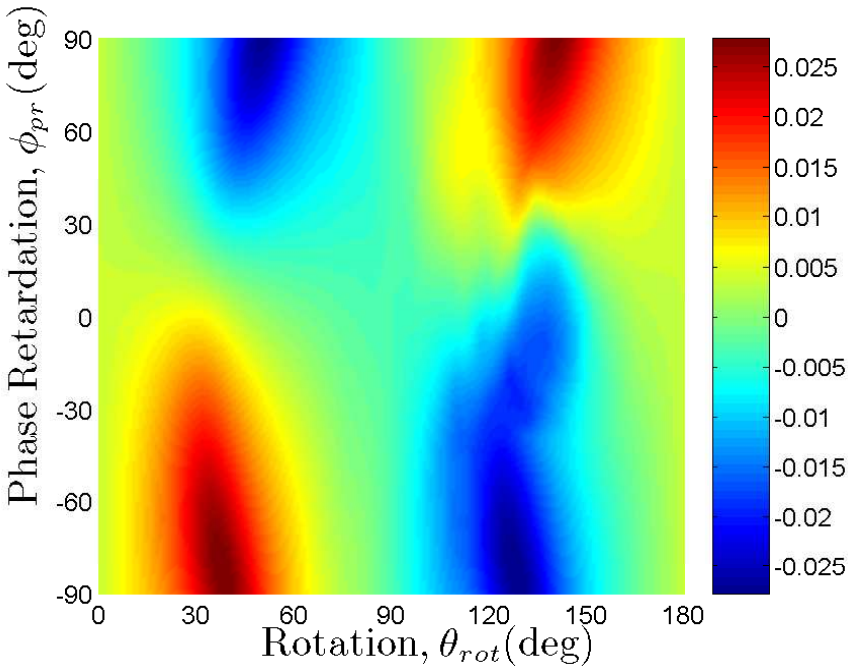

Figure N.40: Plot of changing correlation coefficient $\rho_{\text{Int.}}(\theta_{rot}, \phi_{pr})$ for axes rotation $\theta_{rot} = 0 \ldots 180°$ and phase retardation $\phi_{pr} = -90 \ldots 90°$ obtained for idealised SpectroBragg Mueller matrix for isotropic FBG.

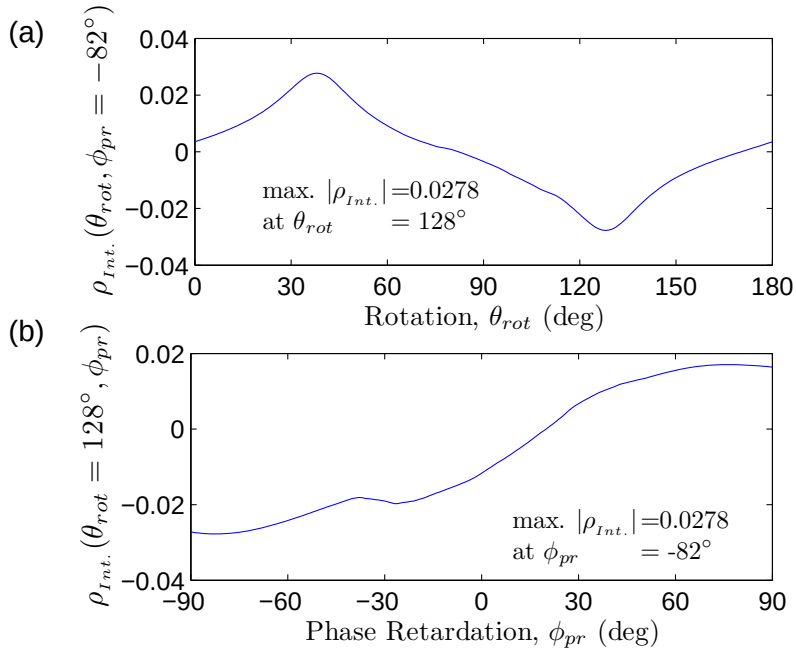

Figure N.41: Cross–sectional plots of figure N.40 which contain the largest value for the correlation coefficient $\rho_{\text{Int.}}(\theta_{rot}, \phi_{pr})$, (a) constant phase retardation ϕ_{pr} and (b) showing constant rotation θ_{rot}.

N.5 PDL balancing

The PDL balancing approach, figure 5.10 (page V.I - 233), uses the matching of losses in both orthogonal SOPs so that the effective signal captured by the SpectroBragg exhibits no change in power levels. This approach departs from the previous devices in that the losses are matched, thus decreasing the intensity throughput to achieve a polarisation mitigation benefit.

The available equipment did not include an attenuator in PMF, and so the ideal version of the Mach–Zehnder in polarisation maintaining construction was not obtained. The PDL matching depolariser proposed by Dong *et al.* [5] was not a broadband device; however, in the experiments performed for this work, the polarisation properties of the polarising beam–splitters and variable attenuator had a small difference from an operating wavelength of 1534 nm to the SpectroBragg centre wavelength of 1550 nm, of the order of $\sim 7\%$. Once the variable attenuator had been configured to provide a suitable level of attenuation, the PDL compensator appeared to suppress SOP changes effectively.

The anisotropic FBG data for the PDL balancing approach does not cover the full Poincaré sphere, figure N.46 (page V.II N-56). The shape of the covered region is closer to a larger version of the bow–tie pattern seen in the isotropic FBG datasets, with the lobes of the edges of the bow beginning to overlap. The isotropic FBG exhibits the same bow–tie structure as the other isotropic FBGs, but rotated on the surface of the Poincaré sphere. Instead of the axis of symmetry being parallel to the S_1S_2 plane (i.e. a rotation), the axis of symmetry is parallel to the S_3 axis (i.e. a phase retardation).

Despite the less than complete anisotropic FBG coverage, the $\rho_{\text{Int.}}$ value is the lowest across all the approaches for the anisotropic FBG data. However, the SpectroBragg and Polarimeter $\sigma_{\text{Int.}}$ values are almost identical to the control experiment values ($\sim 104\%$ & $\sim 103\%$, respectively). Any improvement the PDL balancing approach provides is lost by other means, or more than likely there is only a decorrelation but no reduction in $\sigma_{\text{Int.}}$.

Figures N.44(b) (page V.II N-54) & N.44(d) (page V.II N-54) show the SpectroBragg and calculated polarimeter data which were used to calculate the anisotropic FBG correlation coefficient. Three distinct SOP changes are visible, from 40 . . . 130 s, 160 . . . 340 s and 370 . . . 520 s. The calculated polarimeter SOP changes are of more equal intensity than the equivalent SpectroBragg data.

The anisotropic FBG σ_{λ_B} value from figure N.46 (page V.II N-56) is barely improved over the control experiment. However, the value may have been enlarged by the large departure around 180 s, which corresponds with a low intensity level on the unfiltered SpectroBragg data in figure N.44(a) (page V.II N-54).

The intensity changes during 370 . . . 520 s are slightly less than the previous two distinct SOP changes. The differences between the filtered and unfiltered values suggest that the apparatus admitted phase noise, although the ODL was arranged to unbalance the apparatus. By attenuating both arms to equal intensity, any phase noise would have oscillated between minimum and maximum interference values were it the cause.

Figures N.44(b) (page V.II N-54) and N.44(d) (page V.II N-54) exhibit similar activity, but the correlation coefficient does not reflect this. As the correlation coefficients are low, but the magnitude of the oscillations remains unchanged, the failure to meet the quasi–static PDL requirement and the phase and polarisation–sensitivity of the diffraction grating are likely to be the reason the quoted depolarisation performance was not achieved.

In contrast to the anisotropic FBG, the PDL balancing did not reduce the isotropic FBG $\rho_{\text{Int.}}$ value. The isotropic FBG $\rho_{\text{Int.}}$ exceeds the control experiment value ($\sim 130\%$) and is the largest of the different approaches examined. The SpectroBragg $\sigma_{\text{Int.}}$ values are minimally reduced ($\sim 93\%$) from the control experiment values, figure 5.24 (page V.I - 252), despite the Polarimeter $\sigma_{\text{Int.}}$ value being $\sim 54\%$ that of the control experiment value, figure 5.25 (page V.I - 252).

The isotropic FBG value is larger than the control experiments anisotropic value. The depolarisation was not consistently applied across all SOPs. Comparing figures N.45(b) (page V.II N-55) & N.45(d) (page V.II N-55), two distinct performances can be observed. The oscillation before 130 s has similar features in both N.45(b) (page V.II N-55) & N.45(d) (page V.II N-55), but after 130 s the PDL balanced output from the SpectroBragg is much quieter and does not resemble the corresponding calculated polarimeter data in figure N.45(d) (page V.II N-55). A somewhat similar departure can be seen in figures N.44(b) (page V.II N-54) & N.44(d) (page V.II N-54) for the anisotropic FBG before and after 420 s. It is therefore likely that these corresponded to a set of SOP changes that were more effectively mitigated than the other SOP changes.

For both the SpectroBragg and Polarimeter, the anisotropic & isotropic FBG $\sigma_{\text{Int.}}$ values are approximately equal, indicating that the PDL compensation approach does not reduce the magnitude of the intensity change upon the SpectroBragg signal, even if the absolute intensity level is reduced.

The anisotropic FBG centroid calculated σ_{λ_B} value is a slight improvement over the control experiment value ($\sim 83\%$), as shown in figure 5.26 (page V.I - 254), but is almost totally decorrelated ($\sim 0.4\%$), following the pattern of the corresponding intensity values. The isotropic FBG σ_{λ_B} value is $\sim 176\%$ the control experiment value, with a large correlation $\rho_{\lambda_B} \sim 137\%$ the control experiment value. The corresponding λ_B plot, figure N.47 (page V.II N-56), shows that, although the oscillation

intensity has been reduced, the centroid algorithm has recovered the oscillation.

The presence of the ODL in the system may not have been necessary, and the quoted performance in [5] was not achieved. The ODL was used to ensure that the interferometer was unbalanced.

The differences in performance before and after 130 s in figure N.44(b) (page V.II N-54) may have arisen due to the non–PMF attenuator having a twist or bend. Although the device was unwound and kept straight for the experiment, residual twisting or bending may have rotated the SOPs between the PMF polarising beam–splitters.

Dong *et al.* [5] mention the approach tested here in passing near the end of their paper, suggesting the apparatus as an equivalent arrangement to the apparatus examined in their paper. They do not report results for exactly this apparatus in [5].

The figures N.46 (page V.II N-56) and N.47 (page V.II N-56), along with tables N.5(c) (page V.II N-51) and N.5(d) (page V.II N-51), show that, although the intensity oscillation may be reduced, particularly for the isotropic FBG after time 130 s, the eventual parameter recovered, in this case the SpectroBragg centroid calculated λ_B, may not improve.

Figures N.48 (page V.II N-57) and N.50 (page V.II N-58) show the correlation coefficient, $\rho_{\text{Int.}}$, as a function of changing θ_{rot} and ϕ_{pr}. Figures N.49 (page V.II N-57) and N.51 (page V.II N-58) show the orthogonal cross sections, the (a) figures along θ_{rot} and the (b) figures along ϕ_{pr}, containing the largest $|\rho_{\text{Int.}}(\theta_{rot}, \phi_{pr})|$.

Quantity	FBG			Control	PDL comp.
(a) $\rho_{\text{Int.}}$	Aniso.		$\lvert\rho_{\text{Int.}}\rvert$	0.22 (0.28)	0.10 (0.06)
			θ_{rot}	125°	34°
			ϕ_{pr}	−50°	19°
	Iso.		$\lvert\rho_{\text{Int.}}\rvert$	0.20 (0.18)	0.26 (0.51)
			θ_{rot}	130°	35°
			ϕ_{pr}	72°	−69°
(b) $\sigma_{\text{Int.}}$ (pm)	Aniso.	SB.	w. ΔSOP	0.25 (0.56)	0.26 (0.79)
			background	0.07 (0.03)	0.03 (0.02)
		Pol.	w. ΔSOP	0.38 (0.56)	0.39 (0.76)
			background	0.04 (0.03)	0.36 (0.58)
	Iso.	SB.	w. ΔSOP	0.13 (0.18)	0.12 (0.33)
			background	0.03 (0.001)	0.02 (0.0004)
		Pol.	w. ΔSOP	0.50 (0.55)	0.27 (0.48)
			background	0.07 (0.18)	0.03 (0.002)
(c) σ_{λ_B} (pm)	Aniso.		w. ΔSOP	5.80 (7.41)	4.78 (7.18)
			background	0.25 (0.07)	0.77 (0.70)
	Iso.		w. ΔSOP	0.88 (1.05)	1.55 (2.89)
			background	0.88 (0.28)	0.40 (0.16)
(d) $\lvert\rho_{\lambda_B}\rvert$	Aniso.			0.24 (0.40)	0.001 (0.05)
	Iso.			0.46 (0.46)	0.63 (0.81)

Table N.5: PDL balancing mitigation approach summary of **(a)** correlation coefficient, $\rho_{\text{Int.}}$, values for correlation between captured SpectroBragg intensity and calculated S_{SB}; **(b)** the FFT filtered and unfiltered (in parentheses) normalised standard deviations, $\sigma_{\text{Int.}}$, for both SpectroBragg and polarimeter data. The values are for the data with applied SOP changes and without applied SOP changes (i.e. background); **(c)** the FFT filtered and unfiltered (in parentheses) standard deviation of centroid calculated wavelength, σ_{λ_B}, for the anisotropic and isotropic FBGs; **(d)** the SpectroBragg intensity–centroid λ_B correlation coefficient, ρ_{λ_B}, as a measure of intensity pattern's influence on λ_B.

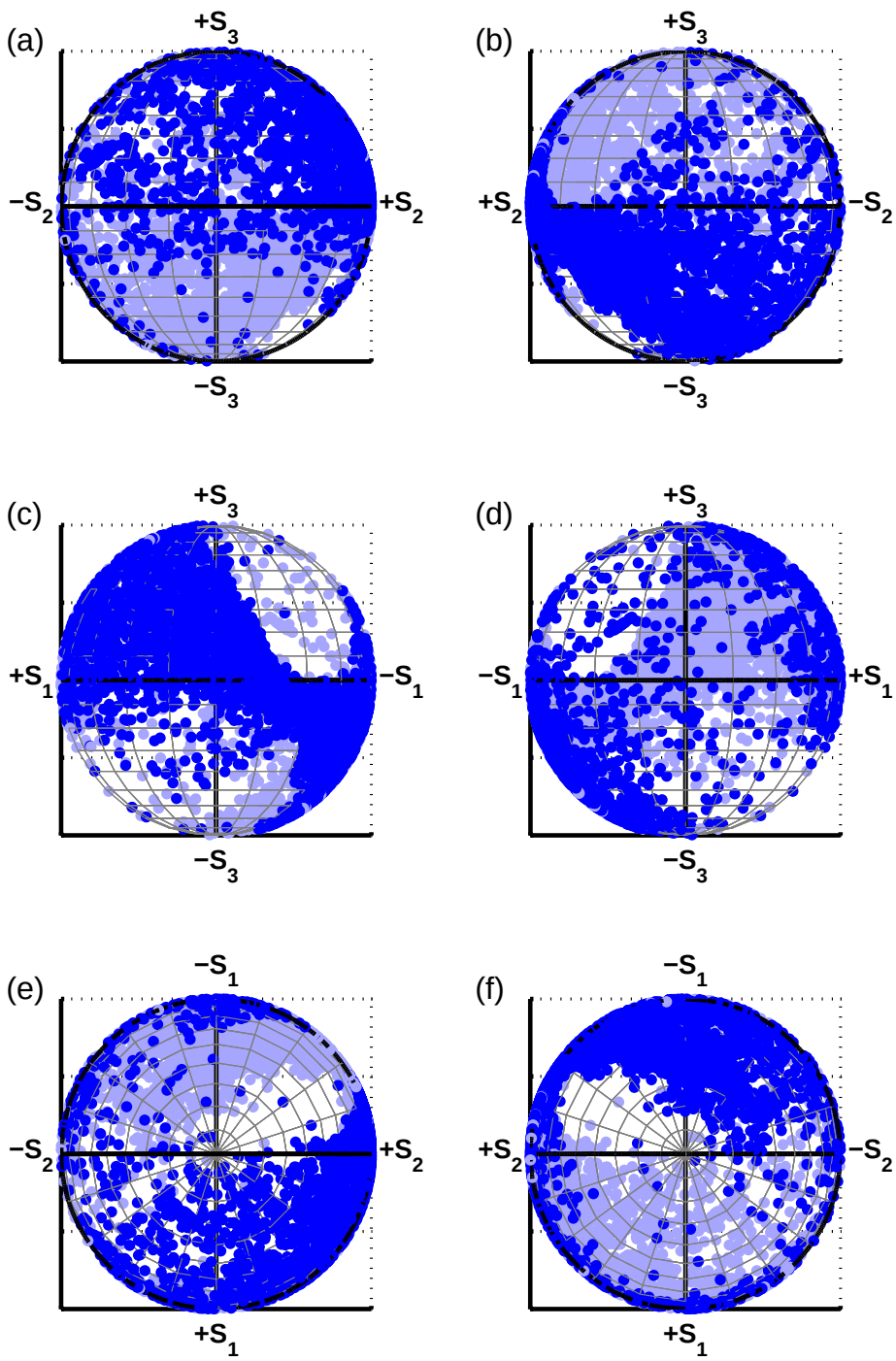

Figure N.42: Poincaré sphere projections of anisotropic FBG data showing: **(a)** S_2 V. S_3 along S_1 to $-S_1$; **(b)** S_2 V. S_3 along $-S_1$ to S_1; **(c)** S_1 V. S_3 along S_2 to $-S_2$; **(d)** S_1 V. S_3 along $-S_2$ to S_2 ;**(e)** S_2 V. S_1 along S_3 to $-S_3$; and **(f)** S_2 V. S_1 along $-S_3$ to S_3.

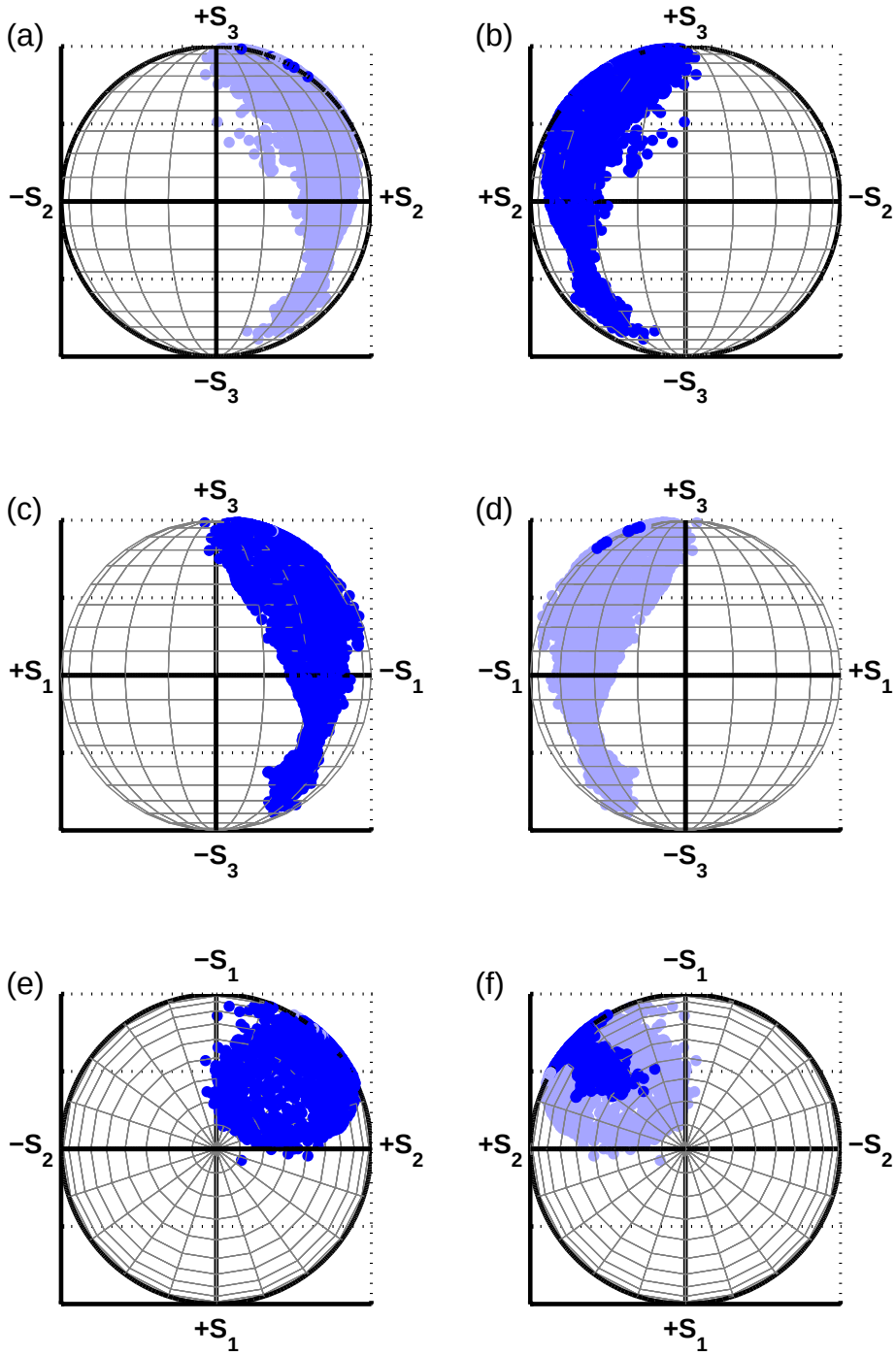

Figure N.43: Poincaré sphere projections of isotropic FBG data showing: **(a)** S_2 V. S_3 along S_1 to $-S_1$; **(b)** S_2 V. S_3 along $-S_1$ to S_1; **(c)** S_1 V. S_3 along S_2 to $-S_2$; **(d)** S_1 V. S_3 along $-S_2$ to S_2 ;**(e)** S_2 V. S_1 along S_3 to $-S_3$; and **(f)** S_2 V. S_1 along $-S_3$ to S_3.

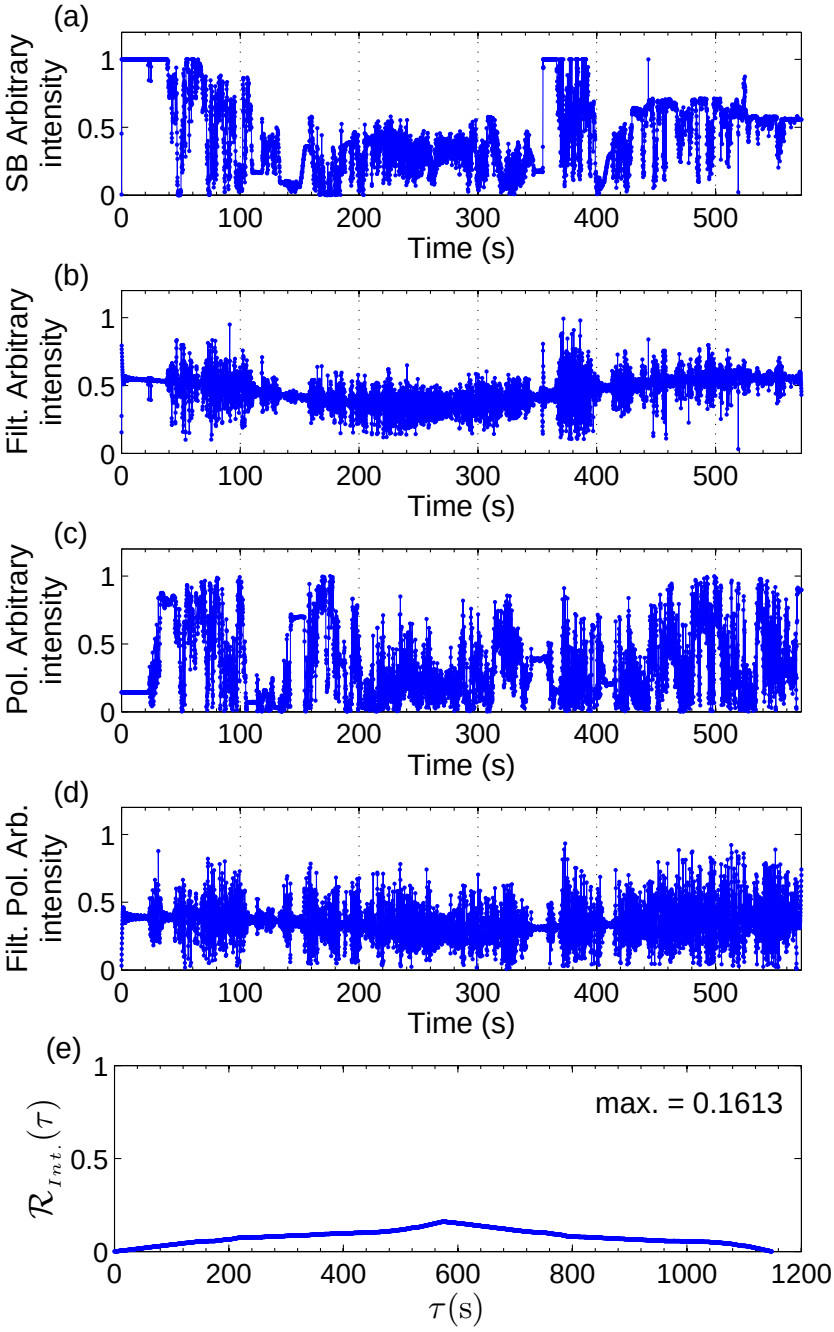

Figure N.44: Plot of anisotropic FBG data showing **(a)** the data captured on the SpectroBragg; **(b)** the FFT filtered SpectroBragg data; **(c)** the calculated ideal SpectroBragg intensity from the polarimeter data, using a rotation angle of 118°; and **(d)** the cross–correlation, $\mathcal{R}_{\text{Int.}}$, of (b) & (c) for PDL compensator.

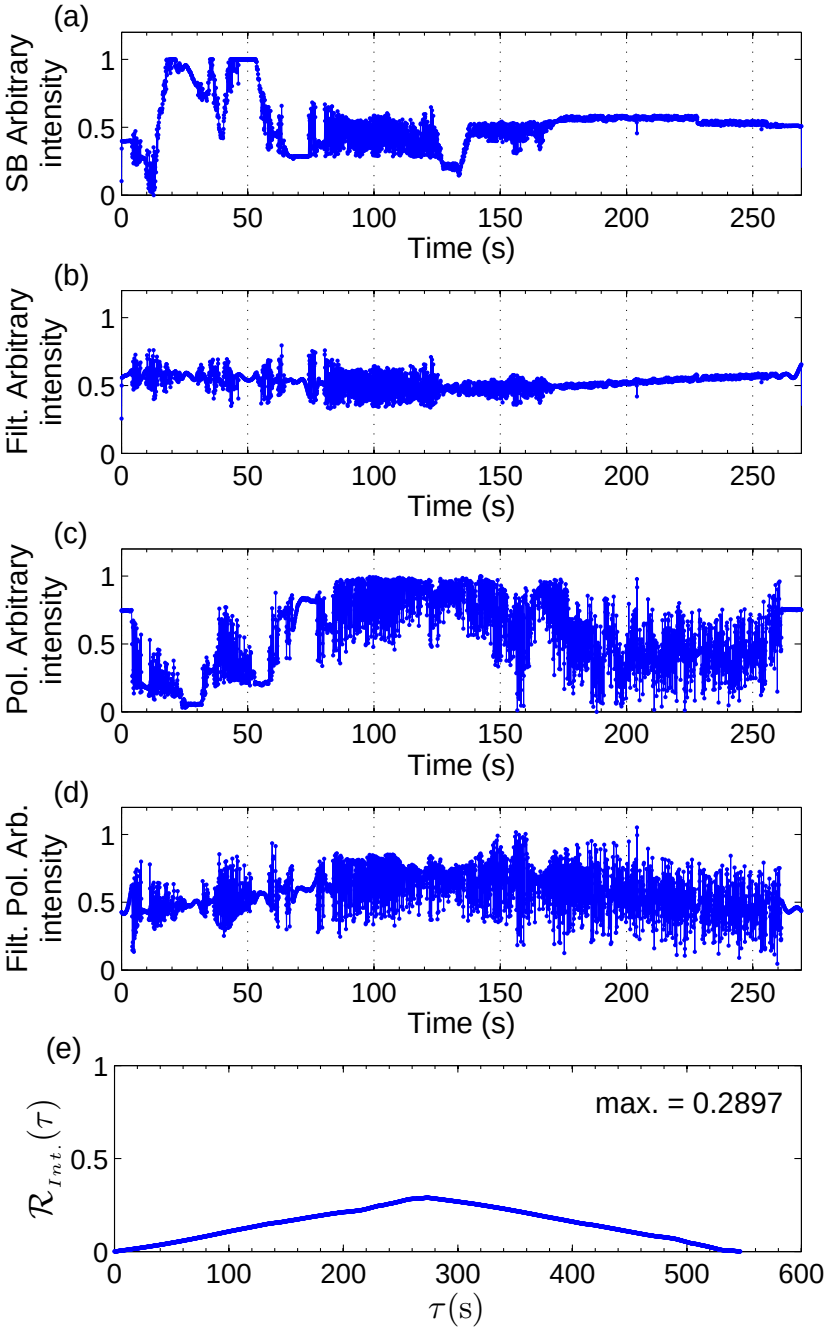

Figure N.45: Plot of isotropic FBG data showing **(a)** the data captured on the SpectroBragg; **(b)** the FFT filtered SpectroBragg data; **(c)** the calculated ideal SpectroBragg intensity from the polarimeter data, using a rotation angle of 61°; and **(d)** the cross–correlation, $\mathcal{R}_{\text{Int.}}$, of (b) & (c) for PDL compensator.

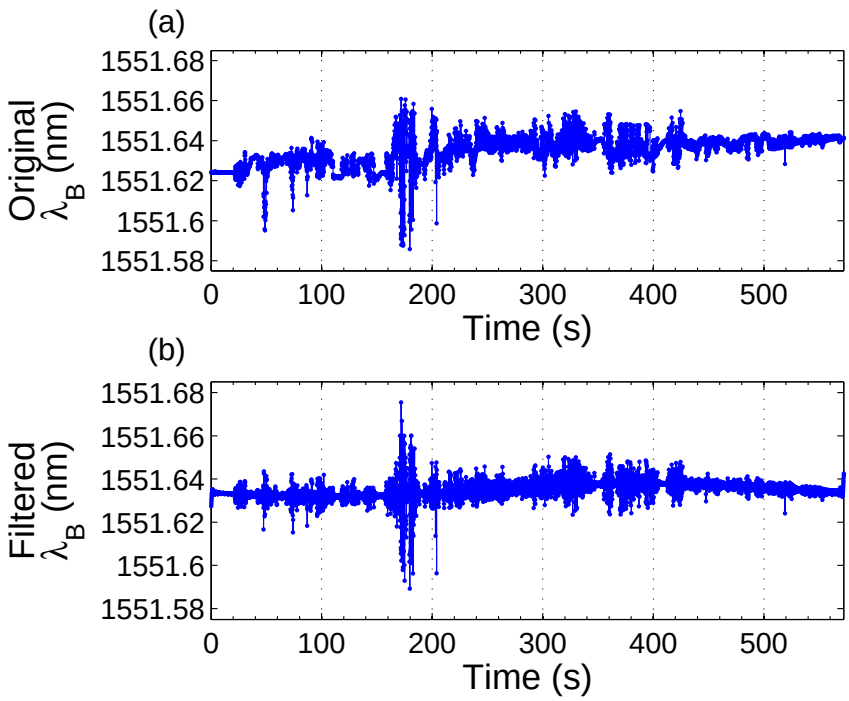

Figure N.46: Plot of **(a)** centroid determined λ_B for the anisotropic FBG data showing; **(b)** the centroid determined λ_B from the FFT filtered SpectroBragg data.

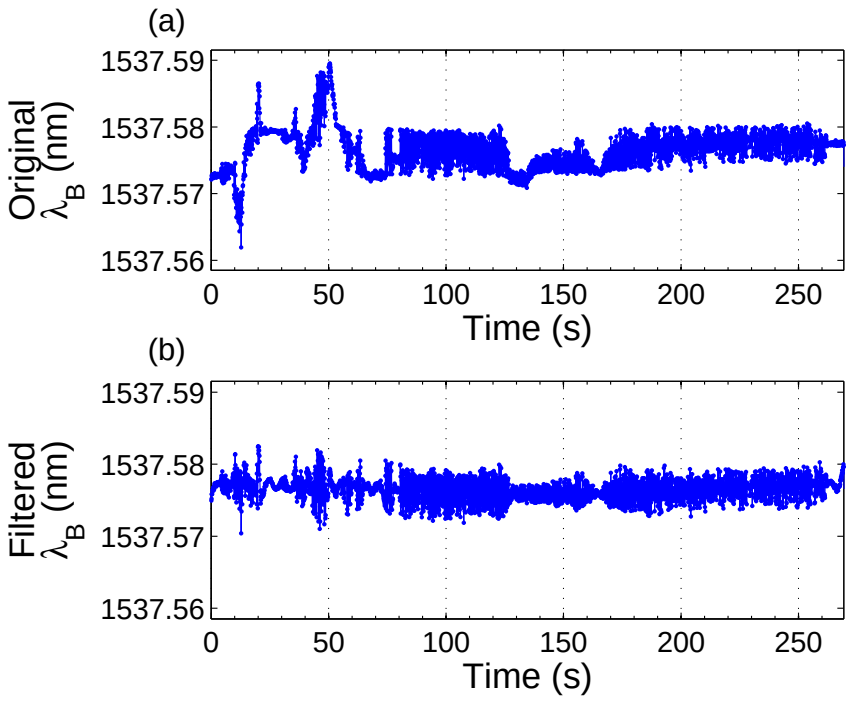

Figure N.47: Plot of **(a)** centroid determined λ_B for the anisotropic FBG data showing; **(b)** the centroid determined λ_B from the FFT filtered SpectroBragg data.

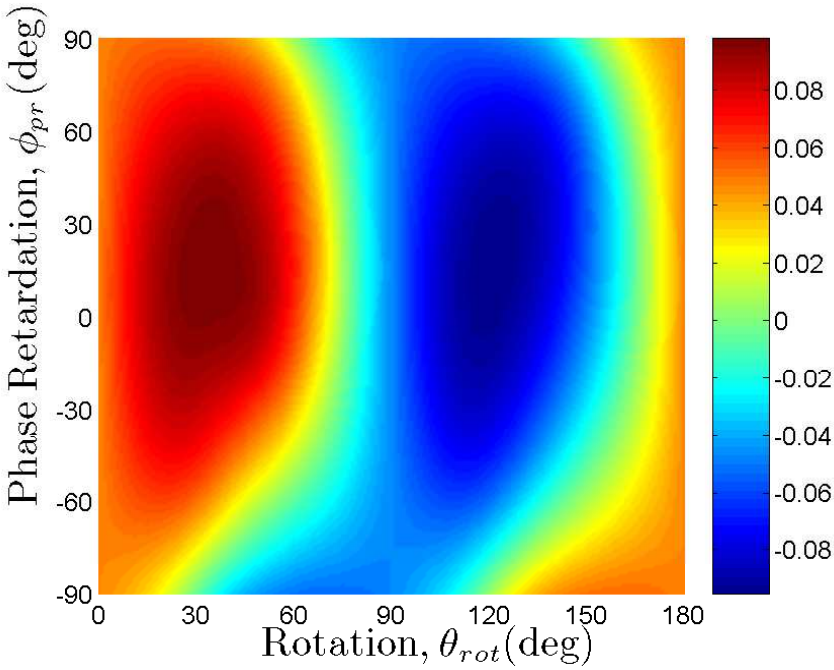

Figure N.48: Plot of changing correlation coefficient $\rho_{\text{Int.}}(\theta_{rot}, \phi_{pr})$ for axes rotation $\theta_{rot} = 0 \ldots 180°$ and phase retardation $\phi_{pr} = -90 \ldots 90°$ obtained for idealised SpectroBragg Mueller matrix for anisotropic FBG.

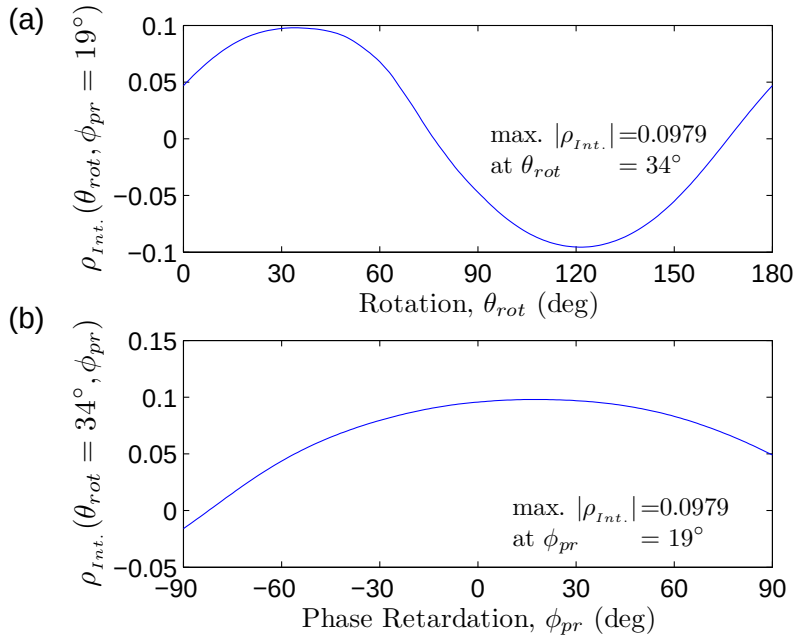

Figure N.49: Cross–sectional plots of figure N.48 which contain the largest value for the correlation coefficient $\rho_{\text{Int.}}(\theta_{rot}, \phi_{pr})$, (a) constant phase retardation ϕ_{pr} and (b) showing constant rotation θ_{rot}.

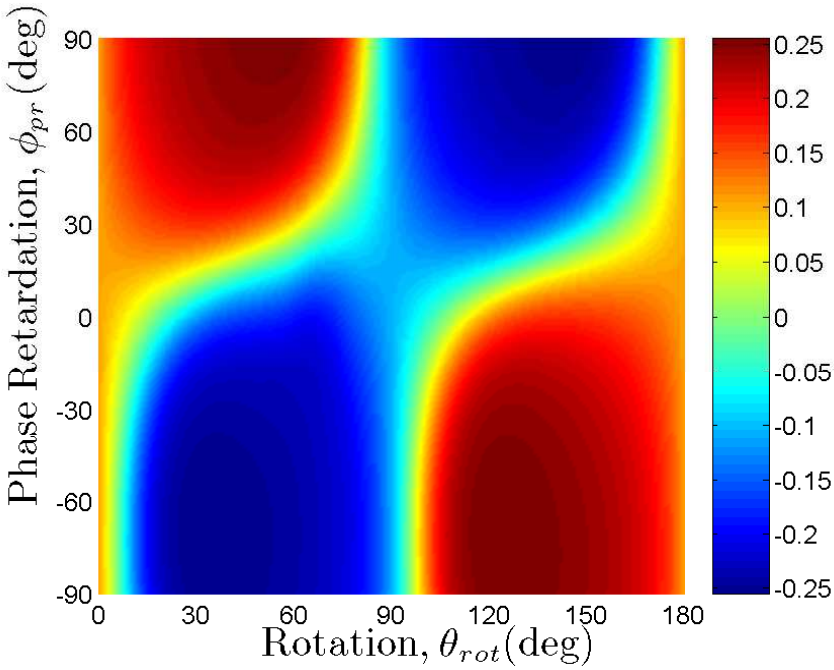

Figure N.50: Plot of changing correlation coefficient $\rho_{\text{Int.}}(\theta_{rot}, \phi_{pr})$ for axes rotation $\theta_{rot} = 0 \ldots 180°$ and phase retardation $\phi_{pr} = -90 \ldots 90°$ obtained for idealised SpectroBragg Mueller matrix for isotropic FBG.

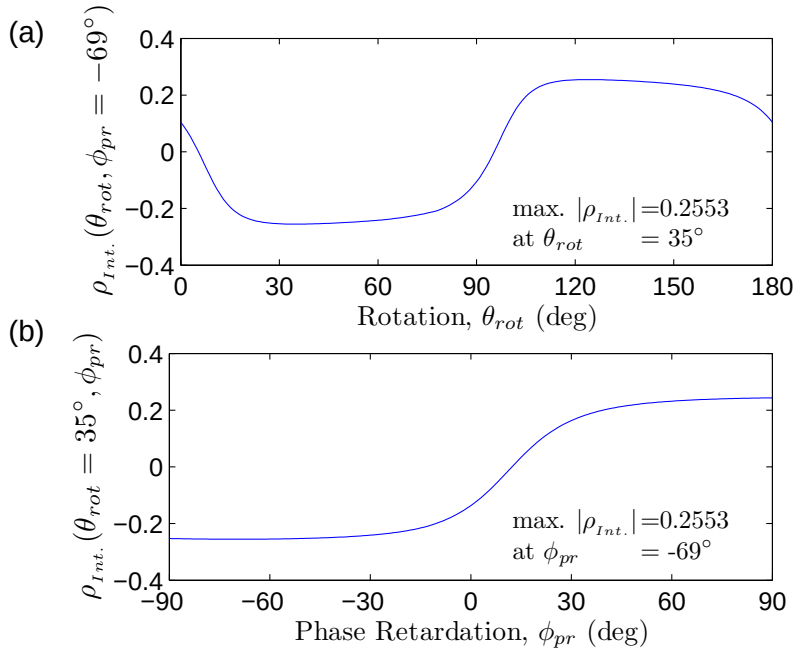

Figure N.51: Cross–sectional plots of figure N.50 which contain the largest value for the correlation coefficient $\rho_{\text{Int.}}(\theta_{rot}, \phi_{pr})$, (a) constant phase retardation ϕ_{pr} and (b) showing constant rotation θ_{rot}.

N.6 Azimuthal Equidistant Projection Figures

The following figures are an alternative visualisation of the Poincaré sphere data shown in the previous sections. They are gathered here to facilitate comparison of the SOP distribution patterns on the Poincaré sphere.

The azimuthal equidistant projection is an origin dependent projection. The angle and distance of all points from the origin are correct from a spherical surface. The origin chosen for these figures is $-S_2$, which conveniently shows the ring pattern of the Lefèvre controller isotropic FBG coverage pattern.

These projections are not area preserving, and so figures N.53 (page V.II N-60) and N.61 (page V.II N-64) should not be interpreted as having different percentages of Poincaré sphere coverage. The projections do allow a look at all the points, and their relationship to each other in one figure, which a two dimensional view of the Poincaré sphere cannot provide.

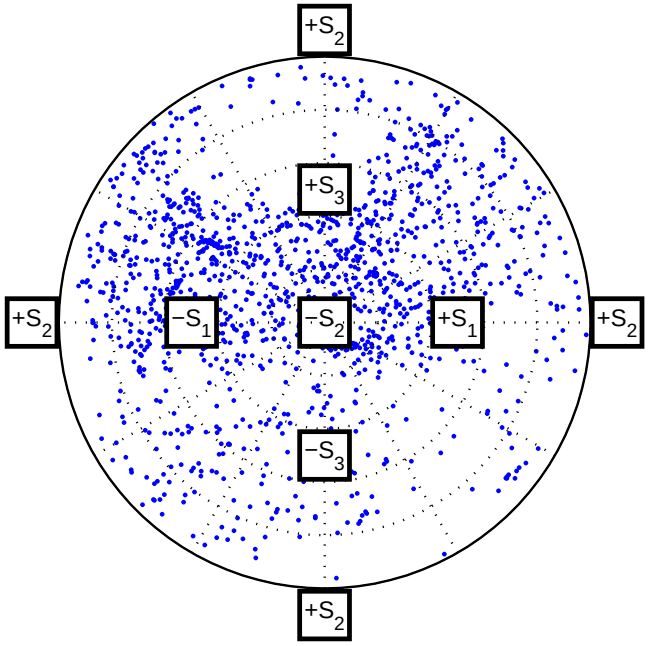

Figure N.52: Control experiment anisotropic FBG Stokes vectors, from figure N.1 (page V.II N-8).

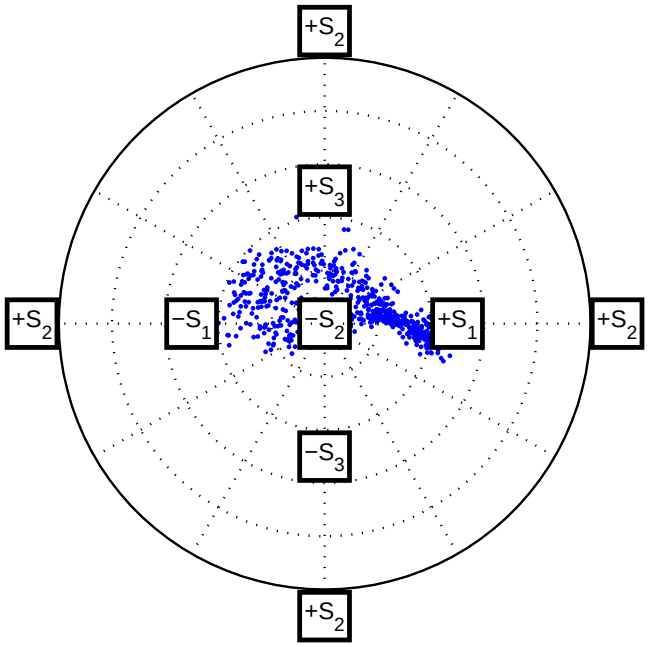

Figure N.53: Control experiment isotropic FBG Stokes vectors, from figure N.2 (page V.II N-9).

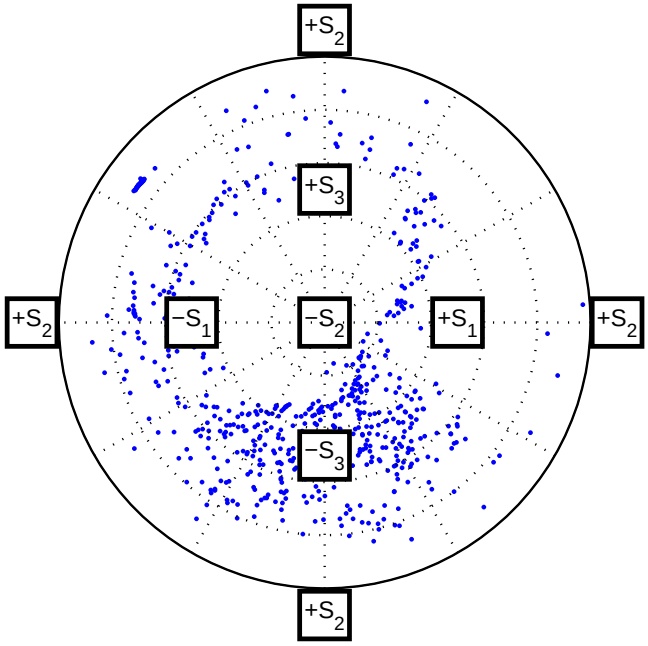

Figure N.54: Lyot depolariser experiment anisotropic FBG Stokes vectors, from figure N.12 (page V.II N-19).

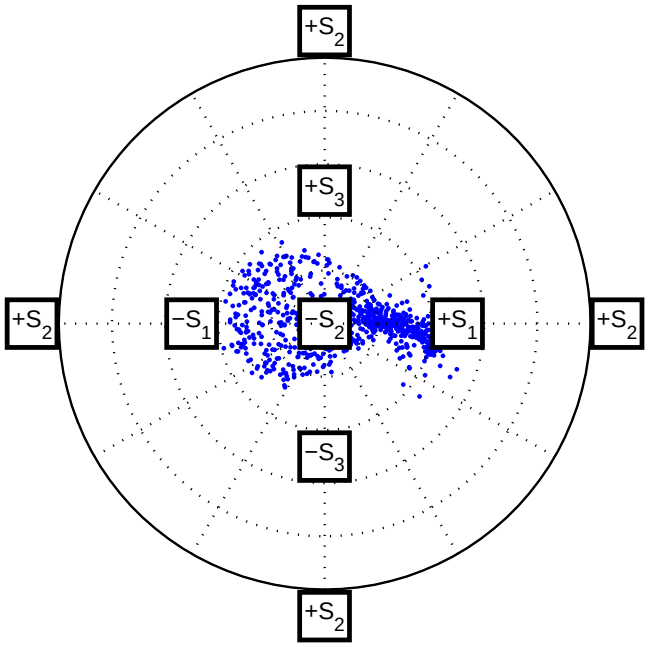

Figure N.55: Lyot depolariser experiment isotropic FBG Stokes vectors, from figure N.13 (page V.II N-20).

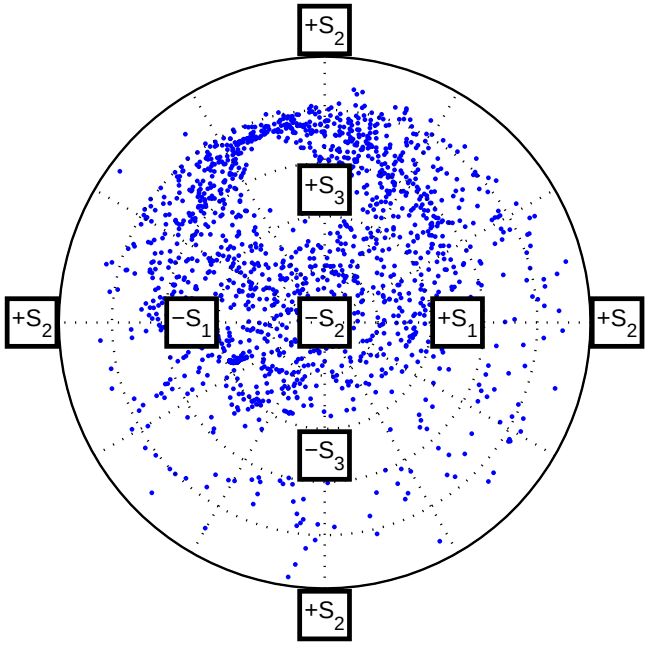

Figure N.56: Lefèvre polarisation controller experiment anisotropic FBG Stokes vectors, from figure N.22 (page V.II N-31).

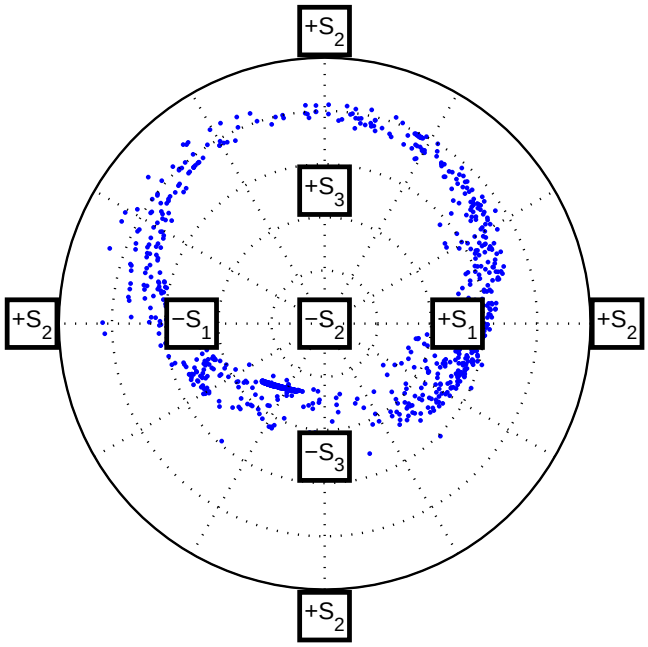

Figure N.57: Lefèvre polarisation controller experiment isotropic FBG Stokes vectors, from figure N.23 (page V.II N-32).

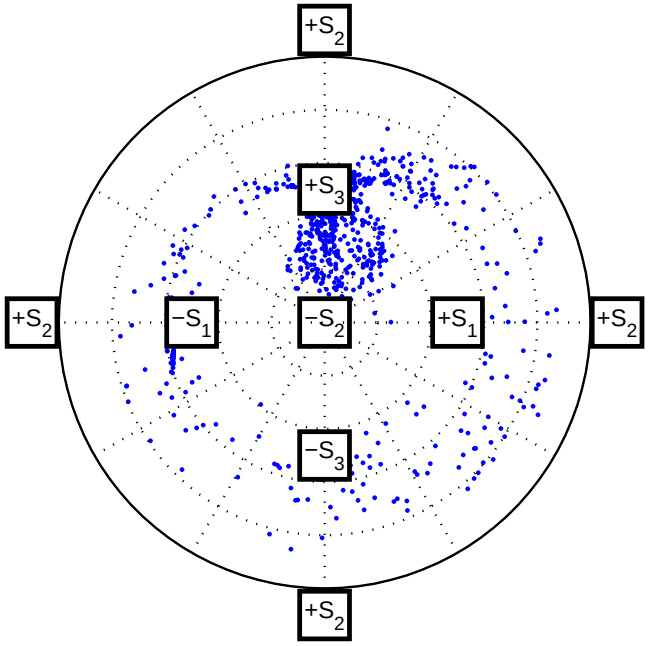

Figure N.58: circulator/Faraday mirror experiment anisotropic FBG Stokes vectors, from figure N.32 (page V.II N-41).

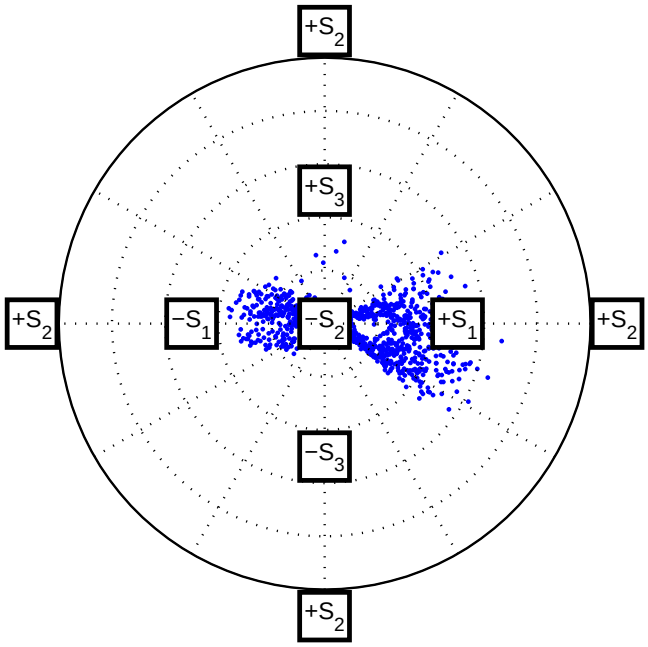

Figure N.59: circulator/Faraday mirror experiment isotropic FBG Stokes vectors, from figure N.33 (page V.II N-42).

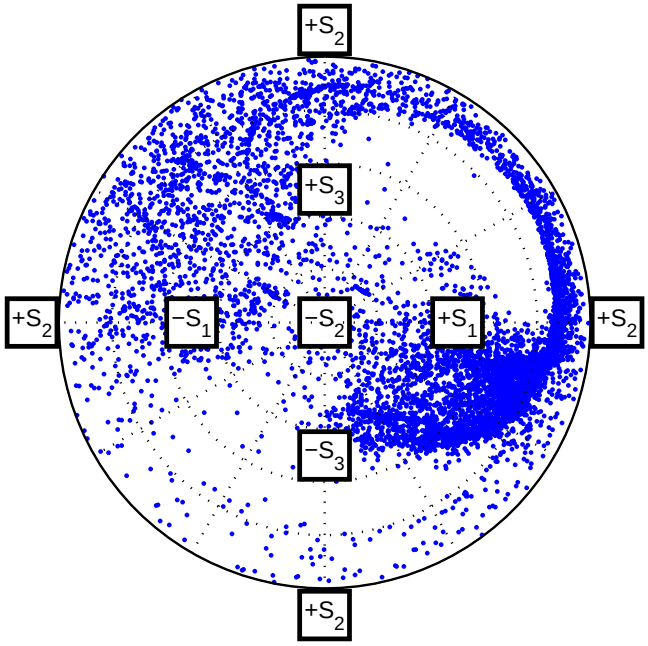

Figure N.60: PDL compensation experiment anisotropic FBG Stokes vectors, from figure N.42 (page V.II N-52).

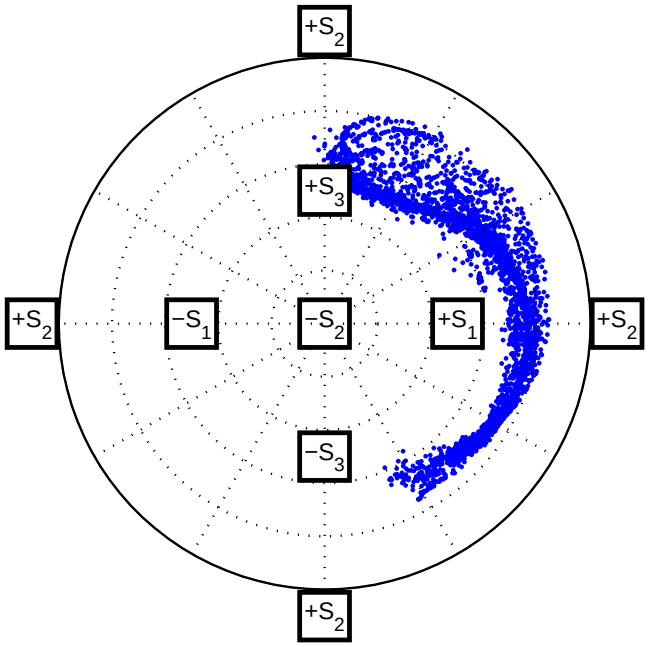

Figure N.61: PDL compensation experiment isotropic FBG Stokes vectors, from figure N.43 (page V.II N-53).

N.7 References

[1] H. C. Lefevre. Single-mode fibre fractional wave devices and polarisation controllers. *Electron. Lett.*, 16(20):778–780, September 1980.

[2] K. Takada, K. Okamoto, and J. Noda. New fiber-optic depolarizer. *J. Lightwave Technol.*, 4(2):213–219, February 1986.

[3] M. Tateda and T. Omatsu. Polarization state fixer composed of passive optical devices. *J. Opt. Soc. Am. A*, 20(2):342–346, February 2003.

[4] Z. Xiao-Guang and Z. Yuan. The number of least degrees of freedom required for a polarization controller to transform any state of polarization to any other output covering the entire Poincaré sphere. *Chinese Phys. B*, 17(7):2509–2513, July 2008.

[5] H. Dong, J. Q. Zhou, M. Yan, P. Shum, L. Ma, Y. D. Gong, and C. Q. Wu. Quasi-monochromatic fiber depolarizer and its application to polarization-dependent loss measurement. *Opt. Lett.*, 31(7):876–878, 2006.

Appendix O

Effect of intensity changes on centroid value

The centroid equation, equation (3.19) (page V.I - 133), is a weighted calculation. The FBG spectral profile, as observed by the SpectroBragg, experienced intensity noise which affected the centroid calculated wavelength by adjusting the weighting. The effect is, consequentially, non–linear.

Mitigating the intensity changes arising from polarisation changes are the focus of chapter 5 (page V.I - 218). In figure O.1(b), with the absence of any mitigation scheme, the intensity changes observed by the SpectroBragg with changes in SOP, figure O.1(b), are shown. The centroid calculated wavelength is shown in figure O.1(c). The mean $\lambda_B = 1551.7\,\text{nm}$ has a standard deviation of 7.3 pm.

Figure O.2(a) shows the normalised intensity[1] values that go into the centroid calculation for the maximum intensity and minimum intensity data[2]. Figure O.2(b) shows the differences in absolute intensity that produce the maximum wavelength changes shown in figure O.1(c).

The correlation[3] of the absolute intensity with the centroid calculated wavelengths λ_B is -0.44. Given the non–linear relationship between the peak intensity and centroid wavelength the mitigation schemes need to reduce this correlation, to reduce the SpectroBragg sensitivity with SOP changes.

[1]The centroid calculation weightings preserved relative to each other. On an absolute scale, the differences are less discernible, while the effective change in λ_B is still the same.

[2]The maximum values are not saturated (clipped) values, as it would appear to be in figure O.2(a). The maximum intensity of the plot was below the saturation level of the array.

[3]Obtained using Matlab routine `corrcoef`.

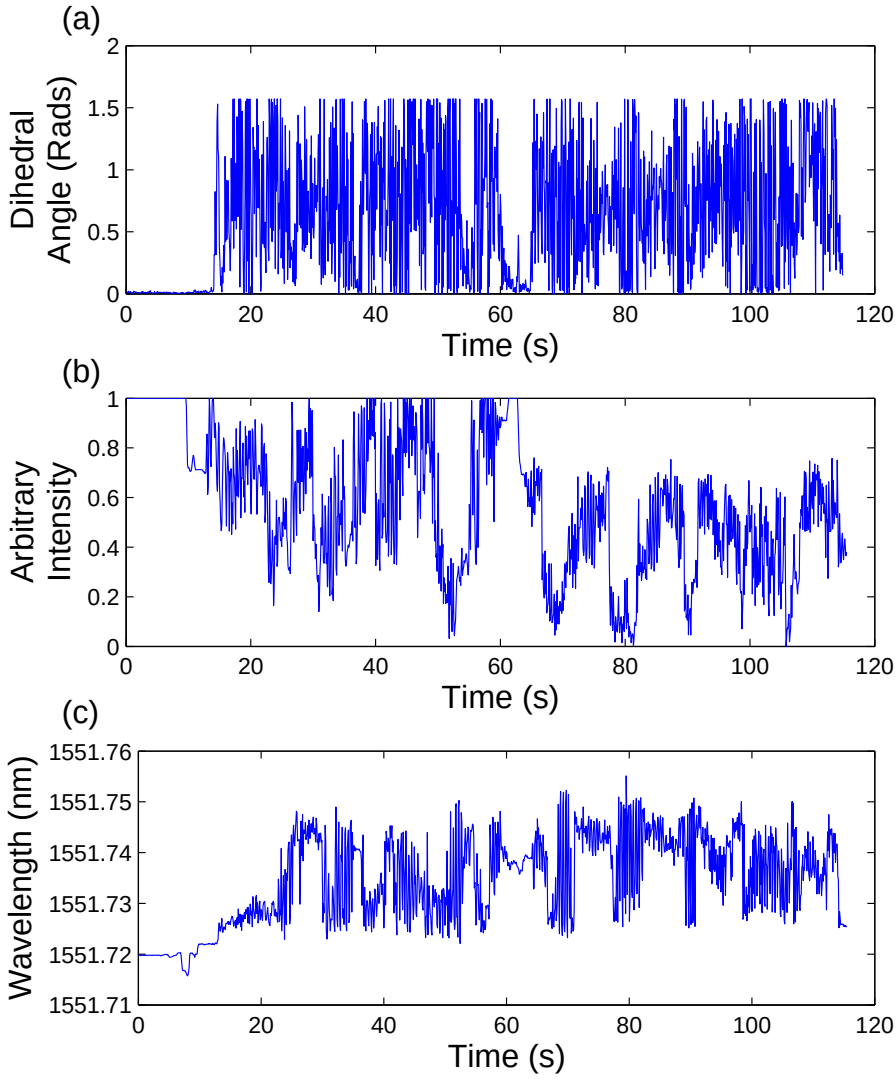

Figure O.1: (a) Dihedral angle between neighbouring SOPs; (b) Intensity observed by SpectroBragg for these changes in SOP; wavelength changes as calculated by centroid calculation for these changes in SOP.

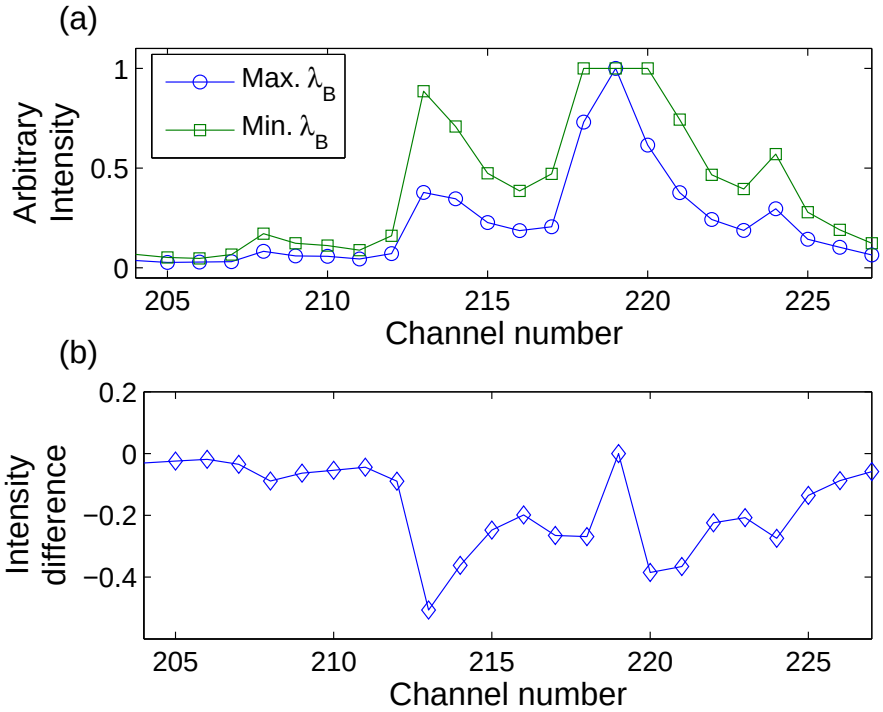

Figure O.2: (a) Normalised plots of the minimum– and maximum–intensity spectral profiles about the centroid calculated λ_B, shown in figure O.1(b); (b) difference between the maximum (blue) and minimum (green) normalised intensity values.

Appendix P

Two–output, π–shifted interferometry

This work uses two–output, π–shifted interferograms, schematically illustrated in figure 2.27 (page V.I - 84). Consequently, $\phi(t)$ cannot be unambiguously determined instantaneously. Wide–sense stationary conditions must be reintroduced. The advantages of using two–output, π–shifted interferometry over single–output interferometry are

- Enhanced (common–mode) noise rejection when two outputs are differenced
- DC level removal when two outputs are differenced
- Maximum visibility, γ, across the full interferogram

The use of the complementary outputs of interferometers to benefit from these advantages has been widely used [1–5]. The two output equations are

$$\begin{aligned} I_0 &= I_{inc}\left[1+\gamma\cos(\phi(t))\right] \\ I_\pi &= I_{inc}\left[1+\gamma\cos(\phi(t)+\pi)\right] \quad = I_{inc}\left[1-\gamma\cos(\phi(t))\right] \end{aligned} \tag{P.1}$$

When captured on a balanced receiver, or differenced in post–processing,

$$\begin{aligned} I_{\pi-shift} &= I_{inc}\left[1+\gamma\cos(\phi(t))\right] - I_{inc}\left[1-\gamma\cos(\phi(t))\right] \\ &= I_{inc}\left[2\gamma\cos(\phi(t))\right] \end{aligned} \tag{P.2}$$

For equal intensities in both interferometer arms, the visibility is constantly $= 1$[1], the maximum. For a single–output interferogram, as the intensity oscillates towards the minimum (particularly for equal intensities in both arms) the captured signal has correspondingly more relative background noise than at the maximum intensity. For constant background noise intensity, the signal–to–noise ratio follows

[1] Assuming no change in the degree of coherence or polarisation between the two beams.

the interferogram intensity. With the two–output, π–shifted interferogram, as one detector goes towards the minimum intensity, the π–shifted interferogram is going towards the maximum intensity on the other detector, $I_{max} = -I_{min}$.

Common–mode noise is rejected, so the impact of Rayleigh scattering induced phase noise is reduced. Using a balanced receiver, the DC level is removed, and so the dynamic range of the data capture system is more effectively used.

The two–output, π–shifted interferogram still requires recalibration. Non–linear movements of the interferometer will produce phase–shifts that need to be recalibrated, or risk being interpreted as spectral features.

P.1 Phase unwrapping

The receivers in the experiment capture the real component of the signal from the interferometer. As we consider that the signal is more accurately described by the analytic signal's complex representation, the real signal necessarily contains only a subset of the information of the analytic signal. The real component does not directly record the phase angle which is expressed in the ratio of the imaginary component, $V^{\Im}$, to the real component, $V^{\Re}$,

$$\Phi(t) = \tan^{-1}\left(\frac{V^{\Im}}{V^{\Re}}\right). \tag{P.3}$$

The problem to be resolved is that the recorded influence of the phase angle on the real signal is wrapped (modulo arithmetic) into the principal values [6], i.e. the interval $(-\pi, \pi]$, as $\sin(\Phi + 2\pi) = sin(\Phi)$, $\forall\, \Phi$.

To attempt to reconstruct the original phase angle is the task of phase unwrapping [7]. The most basic approach is to locate a 'large'[2] discontinuity in the phase and taking it to be the point at which the phase angle has been wrapped into $(-\pi, \pi]$. Depending upon whether the immediately preceding phase angle has been increasing or decreasing, $2m\pi$ or $-2m\pi$ is added to $\Phi(t)$, respectively. m is an integer counter that gets incremented (decremented) for every increasing (decreasing) phase angle wrapping event detected.

Phase angle unwrapping is, in general, a process of determining the least objectionable estimate of how the signal phase angle was wrapped. The 'least objectionable estimate' should minimise the errors that are introduced by the unwrapping process. More elaborate approaches to evaluate the phase changes are compared in [8].

In this work the use of two wavelengths, the signal and reference, which experience the same environmental conditions considerably simplifies the unwrapping

[2] Which turns the problem into defining what is meant by 'large'.

problem. As the non–linearities introduced by the interferometer affect both the reference and signal interferograms at the same time, the phase unwrapping operation will operate equivalently on both reference and signal interferograms.

As such, any phase angle changes of $> 2\pi$, say 4π, that are mistakenly unwrapped as 2π in one interferogram will be similarly unwrapped as 2π in the other. This allows the use of the Matlab routine `unwrap`, which unwraps the phase angle by $\pm 2\pi$ if the phase between consecutive phase elements exceeds $\pm\pi$, respectively. There is no iterative convergence on an improving solution with the `unwrap` command, as it is not required.

The unwrapped phase angle of the reference interferogram is used to recalibrate the reference and signal interferograms, which should have the same interferometer introduced phase discontinuities. This process should modify both signals equivalently, correcting for the non–uniformity of sampling the ideal interferogram. The unwrapped phase angle is used to determine the wavelength via the ratio of the linear fits to the unwrapped phase angles, which divides one unwrapping operation into the other. The division removes the effect of non–perfect phase unwrapping.

P.2 Apodisation or 'windowing' of data

The captured dataset may be considered as a subset of a much larger dataset multiplied with a rectangular [9][3] (or boxcar [10]) function (the window) which effectively isolates the captured data from the rest of the potential whole dataset [11],

$$W_{\text{rect}}(n) = \begin{cases} 1, & 0 \leq n \leq M \\ 0, & \text{otherwise} \end{cases} \tag{P.4}$$

To completely describe a rectangular function requires an infinite number of Fourier frequency terms; conversely, the application of a rectangular window to a dataset introduces high frequency terms into the Fourier transform spectrum. In the recorded data, only frequencies below the Nyquist frequency are captured [12]. When a discrete Fourier transform is taken of a rectangular pulse, frequency terms higher than the Nyquist frequency are aliased and wrapped back into the spectrum [13]. By multiplying the data with the rectangular function, the aliased high frequency components are wrapped back into the spectrum. This will generate spectral components that are convolved with captured spectral components that may overlap to make the actual spectrum unrecoverable.

The purpose of windowing is, by use of an improved window function, to filter

[3] The symbol $\Pi(n)$ to denote the rectangular function [9]. Here $W_{\text{rect}}(n)$ is used for convenience of comparison with the Hamming window, $W_{\text{Hamming}}(n)$.

these high frequency components out to prevent or minimise their presence and hence their convolution with the captured spectrum. The process is the same as apodisation [14, 15] except the result is achieved in the frequency representation as opposed to the spatial or temporal representation.

The application of the improved window modifies the dataset so that instead of the data being multiplied by a rectangular window, the data is multiplied by a window that has fewer spectral components, which are of lower intensity.

Just as with apodisation and the Gibbs phenomenon, by removing the high frequency components, peaks become less spatially confined (as high frequency components define edges) [16]. Spectral features are therefore made to overlap to an extent, and the maximum theoretical FT resolution is diminished. However, the improvement in the spectrum by reducing the aliased frequencies outweighs any information loss due to broadened spectral components.

There are numerous window filters that can be applied. In this work the Hamming filter is applied, using matlab function `hamming`. The Hamming filter is [16]

$$W_{\text{Hamming}}(n) = \begin{cases} 0.54 - 0.46\cos\left(\frac{2\pi n}{M}\right), & 0 \leq n \leq M \\ 0, & \text{otherwise} \end{cases} \tag{P.5}$$

and is illustrated in figure P.1. For comparison the rectangular window of equal width is plotted. The Hamming window produces spectral side–lobe suppression of ~ -40 db relative to the main peak, as shown in figure P.2, which also shows the corresponding spectral response of the rectangular window. It is evident the Hamming window has a wider main lobe, but has significant suppression of adjacent lobes, minimising cross–talk between neighbouring spectral features.

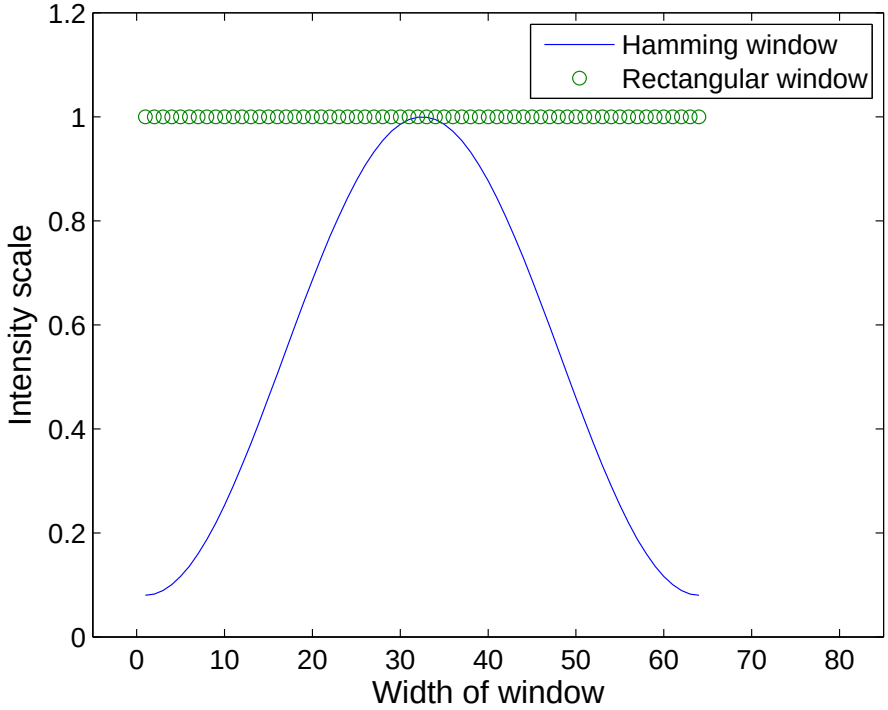

Figure P.1: The Hamming and rectangular windows, multiplying all data in the range by 1.

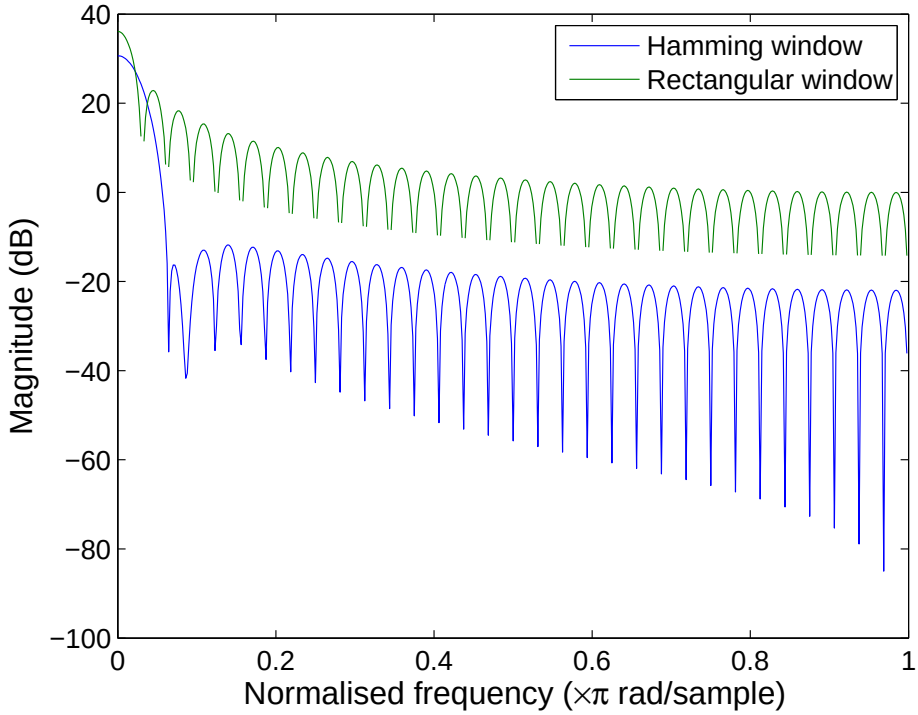

Figure P.2: The semi–log spectral responses of the Hamming and rectangular windows.

P.3 References

[1] W. H. Steel. *Practial two–beam interferometers*, volume 1 of *Interferometry*, chapter 8. Cambridge University Press, Cambridge, 2 edition, 1983. ISBN: 0521311624.

[2] T. F. Zehnpfennig. Method of and apparatus for interferometric background suppression. Patent, December 1978. US 4128337.

[3] R. Vander, S. G. Lipson, and I. Leizerson. Fourier fringe analysis with improved spatial resolution. *Appl. Opt.*, 42(34):6830–6837, 2003.

[4] S.-C. Lin and T. G. Giallorenzi. Sensitivity analysis of the Sagnac-effect optical-fiber ring interferometer. *Appl. Opt.*, 18(6):915–931, 1979.

[5] S. Davis, M. C. Abrams, and J. W. Brault. *Fourier Transform Spectrometry*, chapter 3, pages 29–39. Academic Press, San Diego, 2001. ISBN: 9780120425105.

[6] D. C. Ghiglia and M. D. Pritt. *Two-Dimensional Phase Unwrapping: Theory, Algorithms, and Software*, chapter 1, pages 1–30. John Wiley & Sons, Inc., New York, 1998. ISBN: 0471249351.

[7] D. W. Robinson. *Phase Unwrapping Methods*, chapter 6. Interferogram Analysis: Digital Fringe Pattern Measurement Techniques. IOP Publishing, Ltd., Bristol, 1993. ISBN: 075030197X.

[8] J. R. Fienup. Phase retrieval algorithms: a comparison. *Appl. Opt.*, 21(15):2758–2769, 1982.

[9] R. N. Bracewell. *The Fourier Transform and its Application*, chapter 4, pages 55–73. The McGraw-Hill Companies, Inc., New York, 3rd edition, 1999. ISBN: 0073039381.

[10] L. Mertz. *Transformations in Optics*, chapter 1, pages 1–43. John Wiley & Sons, Inc., New York, 1965.

[11] A. V. Oppenheim, R. W. Schafer, and J. R. Buck. *Discrete-Time Signal Processing*, chapter 10, pages 693–774. Prentice-Hall, Inc., New Jersey, 2 edition, 1999. ISBN: 0137549202.

[12] S. Davis, M. C. Abrams, and J. W. Brault. *Fourier Transform Spectrometry*, chapter 4, pages 41–66. Academic Press, San Diego, 2001. ISBN: 9780120425105.

[13] R. W. Hamming. *Digital Filters*, chapter 3, pages 36–70. Dover Publications, Inc., New York, 3rd edition, 1998. ISBN: 048665088X.

[14] S. Davis, M. C. Abrams, and J. W. Brault. *Fourier Transform Spectrometry*, chapter 6, pages 80–99. Academic Press, San Diego, 2001. ISBN: 9780120425105.

[15] P. Jacquinot and B. Roizen-Dossier. *Apodisation*, volume 3 of *Progress in Optics*, chapter 2. North–Holland Publishing Co., Amsterdam, 1964.

[16] A. V. Oppenheim, R. W. Schafer, and J. R. Buck. *Discrete-Time Signal Processing*, chapter 7, pages 439–540. Prentice-Hall, Inc., New Jersey, 2 edition, 1999. ISBN: 0137549202.

Appendix Q

NewFocus receiver

Q.1 NewFocus receiver repair

During the experiment the 2053's photodiode failed. Without an adequate replacement receiver unit, the failed photodiode was removed and replaced with a *GaP500* photodiode. Performance issues due to the interaction of the original 2053 components with the new photodiode could not be determined, as no model/type specifications for the failed photodiode were available[1], apart from it being InGaAs[2]. It was observed, however, that the sensitivity and noise rejection had improved over the failed diode's past performance when used in the experimental apparatus. The construction is schematically shown in figure Q.1.

Q.2 NewFocus receiver configuration

The two NewFocus receivers were set to operate at the same parameters to provide as close to identical responses as possible. The NewFocus 2117 and 2053 receivers have tuneable bandpass dials to set the upper and lower bounds of the pass band. Receiver gain is set by a dial and switch. For both the 2117 and 2053 the pass band was 10 Hz–10 kHz, and the gain was switched to '×3' and the dial to the maximum '10^4', as shown in figure Q.2, a photograph of the receiver settings. The photodiode in the 2053 single receiver failed during the experimental work, and was replaced with a GAP500 photodiode, as described in appendix Q.1.

[1]The failed photodiode was fixed by epoxy into the supplied FC/PC mounting, hiding any identifying markings.

[2]From *205X series user manual*, New Focus (http://www.newfocus.com/products/documents/manuals/205X_Manual_RevA.pdf).

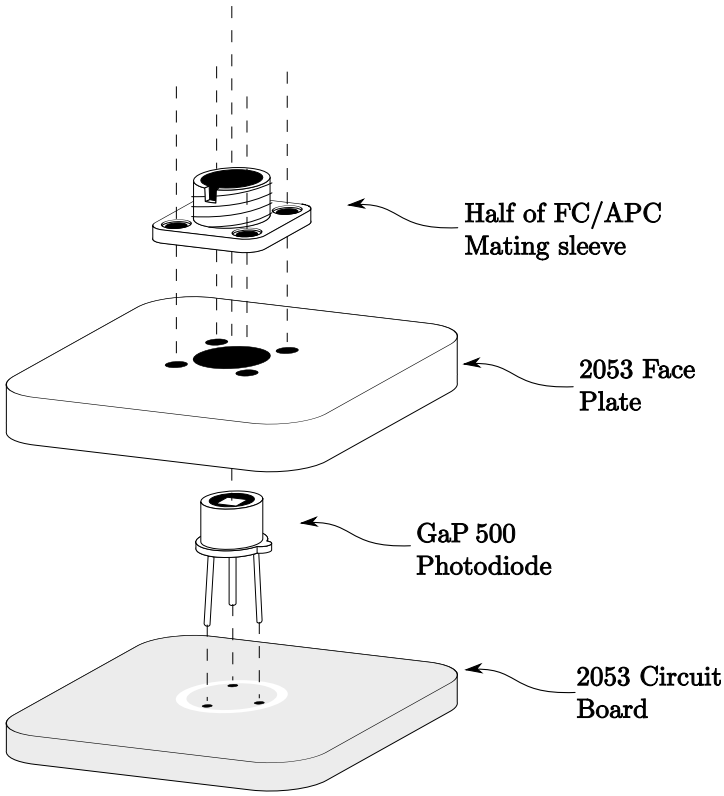

Figure Q.1: Schematic of the modified NewFocus 2053 receiver. The 2053 photodiode failed and was replaced by a GaP500 photodiode. The failed photodiode was fixed with epoxy into the FC/APC connector supplied on the 2053 and so was unusable. The GaP500 photodiode was soldered onto the circuit board as the failed photodiode had been. Half of an FC/APC mating sleeve was used to provide the FC/APC connection, and the photodiode located within the mating sleeve half.

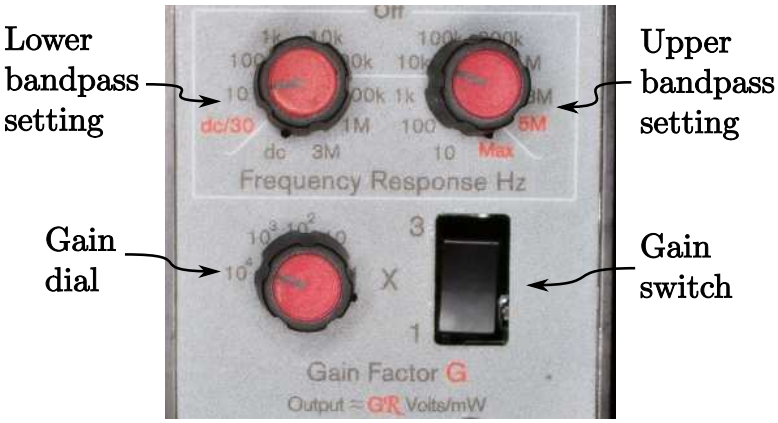

Figure Q.2: Photograph of the NewFocus receiver settings.

Appendix R

Variable and fixed interferogram lengths and window sizes

An automated process was used to recover the interferograms from the captured data. The length of the interferogram changed with the determination of the individual interferograms within the captured data. The noisier the interferogram was, the more difficult the determination of the interferogram edge, and hence the shorter the individual interferogram.

The resulting interferograms were recalibrated as described in §6.4.2 (page V.I - 279). The wavelength value of the sensor was determined using two methods for comparison. First, the centroid peak wavelength approach was used to demonstrate direct use of the spectral features, as described in §6.4.3 (page V.I - 290). The FBG centroid was calculated and corrected for changes in the reference laser centroid.

Secondly, the Hilbert transform technique, HTT, was used to determine the FBG wavelength. The HTT approach is described in §6.4.4 (page V.I - 295). Both techniques require the FBG and laser data to be windowed to select the feature from the combined array.

For the centroid technique a rectangular window was used, as the rectangular window does not alter the weights. For the HTT a Hamming window was used as it apodises the truncated signal. The choice of optimum and suitable window length had to be determined.

For each interferogram, the centroid and HTT were calculated for different window widths. For windows $2n_w + 1$ wide, n_w was varied from 1 to 20.

R.1 Variable interferogram length centroid approach

Each recalibrated interferogram (see §6.4.2 (page V.I - 279)) contained the laser, reference FBG and temperature signal FBG spectra. A rectangular window was

employed to isolate an individual spectral profile. The choice of the optimum width of the window needed to be determined.

Ideally, the window should remove all extraneous noise while retaining all the spectral features. In practice, the presence of noise on the signal limits the determination of what is extraneous. These experiments were performed such that the two–output π–shifted recoverable signal was just above the background noise level. Typically, a sensor system would not be designed to operate at this limit.

To determine the optimum window width, the laser and FBG spectral features were evaluated with varying window widths $= 2n_w + 1$, with n_w from 1 to 20.

Figures R.1 (page V.II R-3) and R.2 (page V.II R-3) show the $n_w = 1$ and $n_w = 20$ rectangular windows respectively. The windowed data are shown with the full interferogram to indicate the overlap that occurs at the larger n_w. For the majority of recovered spectra, the $n_w \geq 2$ range covered the data points of the peak.

The centroid was calculated for each spectral feature and the reference laser wavelength subtracted from the FBG wavelengths as an instrumental calibration. The optimum window width was determined by subtracting the $(n_w + 1)^{\text{th}}$ centroid wavelength from the n_w^{th} centroid wavelength. In the absence of noise, the difference in centroid wavelengths would converge towards zero as the window length, n_w, increased. In the presence of noise, the difference would exhibit a minimum as the contribution of the signal above the noise was reached, and a subsequent rise, as the extraneous noise was added to the calculation.

At each temperature step ~ 26 calculated centroids were averaged to give the final centroid determined wavelength for the spectral feature. Those average wavelengths and associated standard deviations provided a means of comparing the different n_w lengths.

Figures R.3 (page V.II R-4) and R.4 (page V.II R-4) show the differences in the centroid calculated average wavelengths, $\Delta_w \overline{\lambda_B}$, and the associated standard deviations, $\Delta_w \delta_{\lambda_B}$, as a function of n'_w, the index of the differences $\Delta F\left(n'_w\right) = F\left(n_w + 1\right) - F\left(n_w\right)$ for function F. Both the temperature signal (blue) and reference (green) FBGs are plotted. The average value, of all blue and green values at each n'_w, is plotted in red to give an overall trend.

The presence of the neighbouring spectral peaks about the FBGs is evident in the divergence and local minima in the plots. The lowest values are found at the small values of n'_w.

The $n_w = 1$ window length does not cover the full spectral width, as shown in figure R.1 (page V.II R-3). The lowest usable values that cover the spectral features are then $n_w = 2, 3, 4$.

The slope value of the linear fit to the temperature response curve, $\frac{1}{\lambda_B}\frac{\delta\lambda_B}{\delta T}$, of the different n_w are plotted on figure R.5 (page V.II R-5), with the corresponding

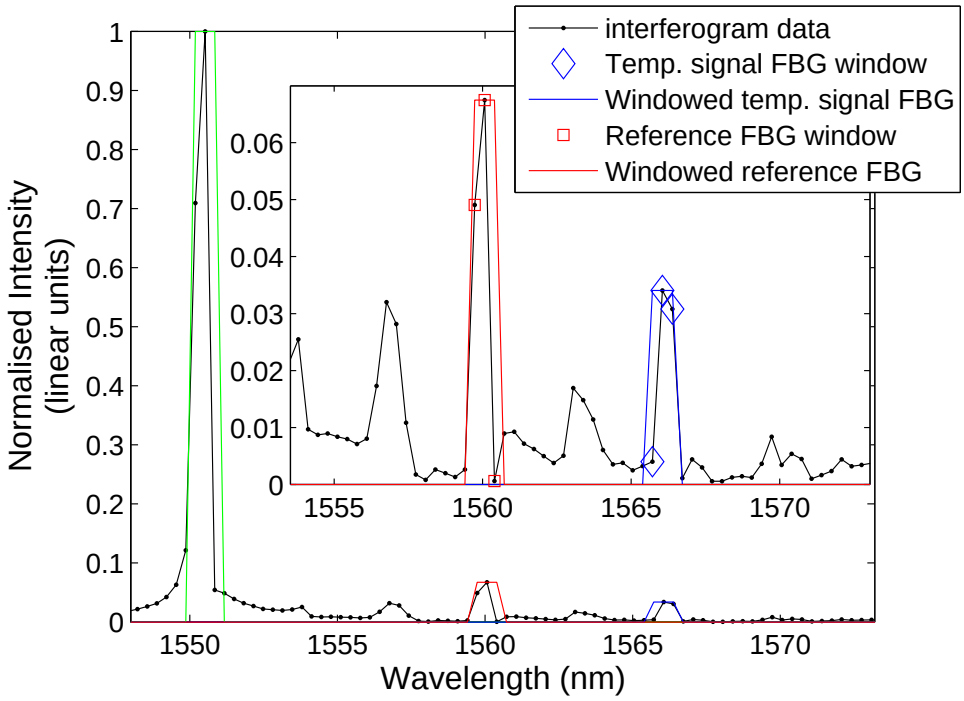

Figure R.1: Centroid rectangular windows for $n_w = 1$, with window length $2n_w + 1$.

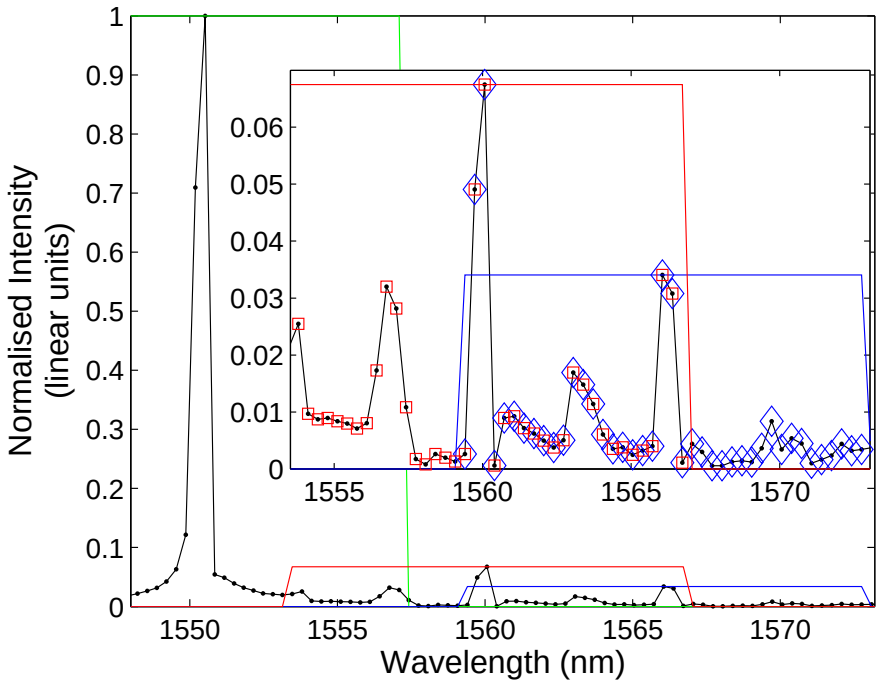

Figure R.2: Centroid rectangular windows for $n_w = 20$, with window length $2n_w + 1$. The legend of figure R.1 applies.

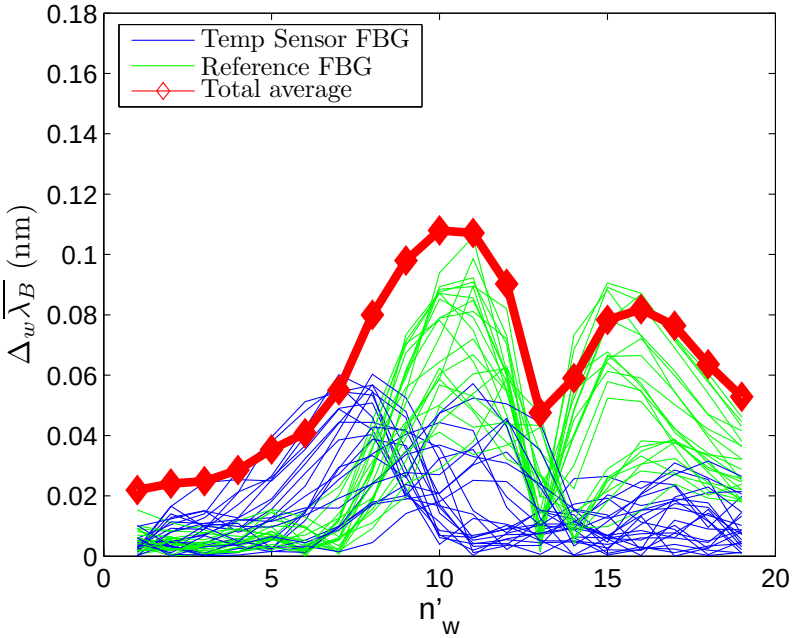

Figure R.3: Overlayed differences in mean centroid determined peak wavelengths, $\Delta_w \overline{\lambda_B}$, as rectangular window width, n_w, is adjusted for temperature sensor and reference FBG. The differences do not converge as the lowest values are at $n'_w = 1:3$.

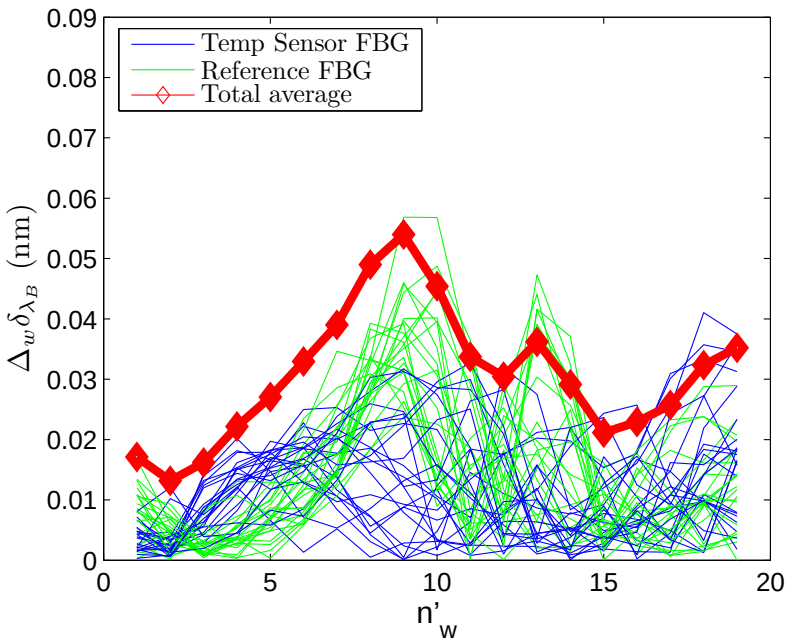

Figure R.4: Overlayed differences in standard deviation of the centroid determined peak wavelengths, $\Delta_w \delta_{\lambda_B}$, as rectangular window width, n_w, is adjusted for temperature sensor and reference FBG.

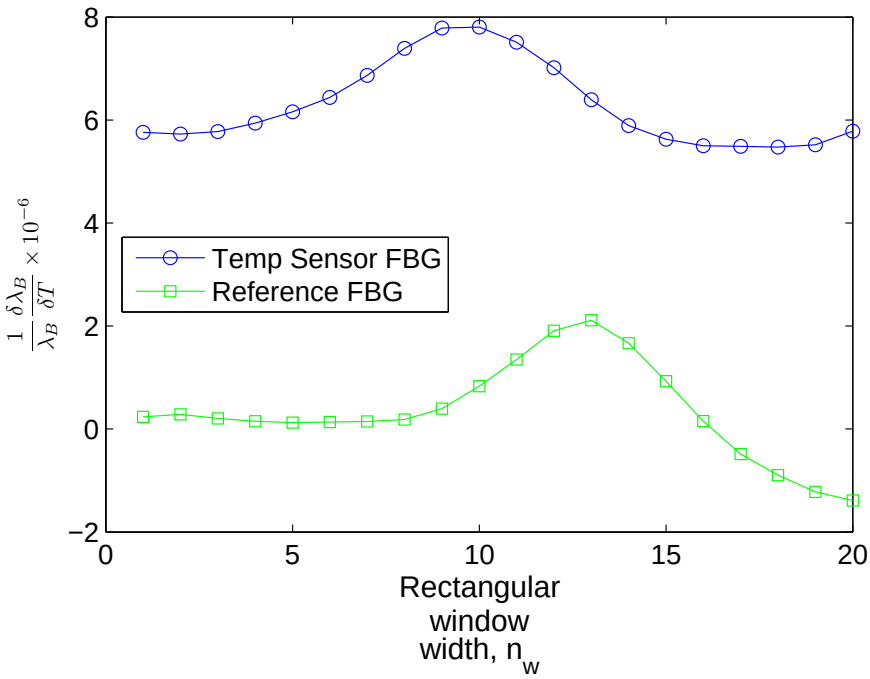

Figure R.5: Linear fit to temperature response slope of temperature signal and reference FBGs as calculated by centroid approach, with rectangular windows of width $2n_w + 1$.

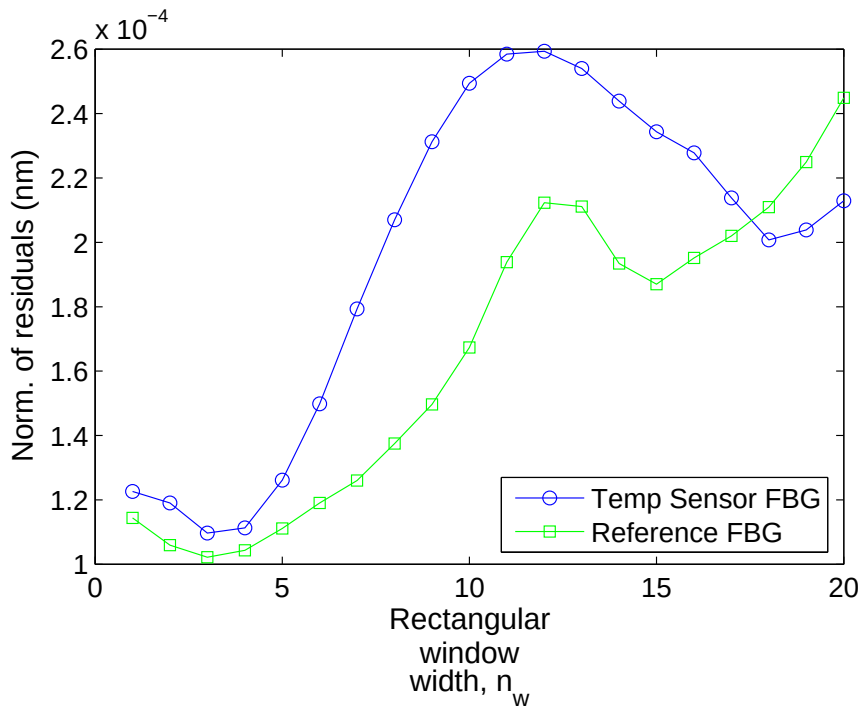

Figure R.6: Residuals to the linear fits to temperature response slope of temperature signal and reference FBGs shown in figure R.5.

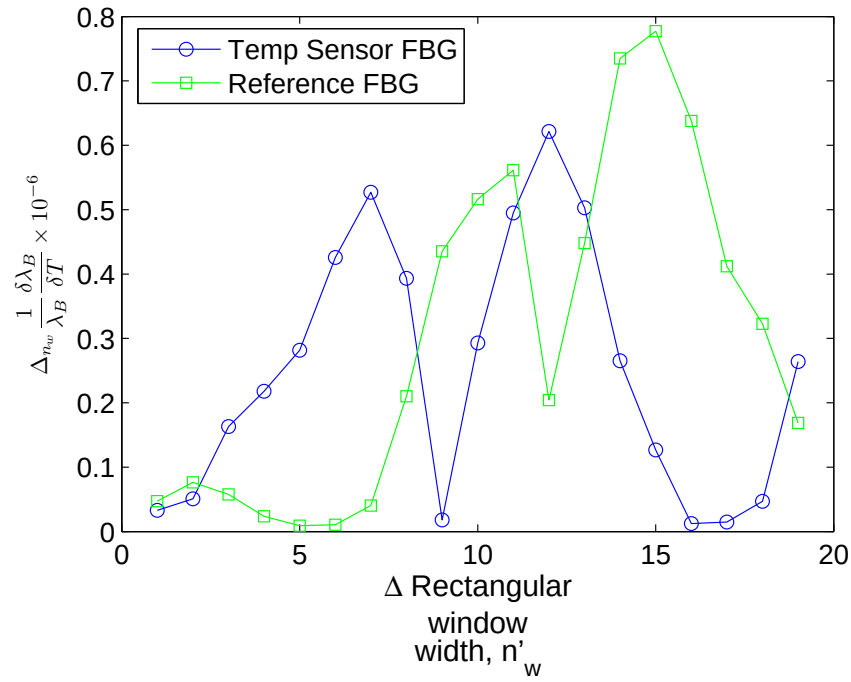

Figure R.7: Differences in linear fit to temperature response slope of temperature signal and reference FBGs as calculated by centroid approach, n'_w changing.

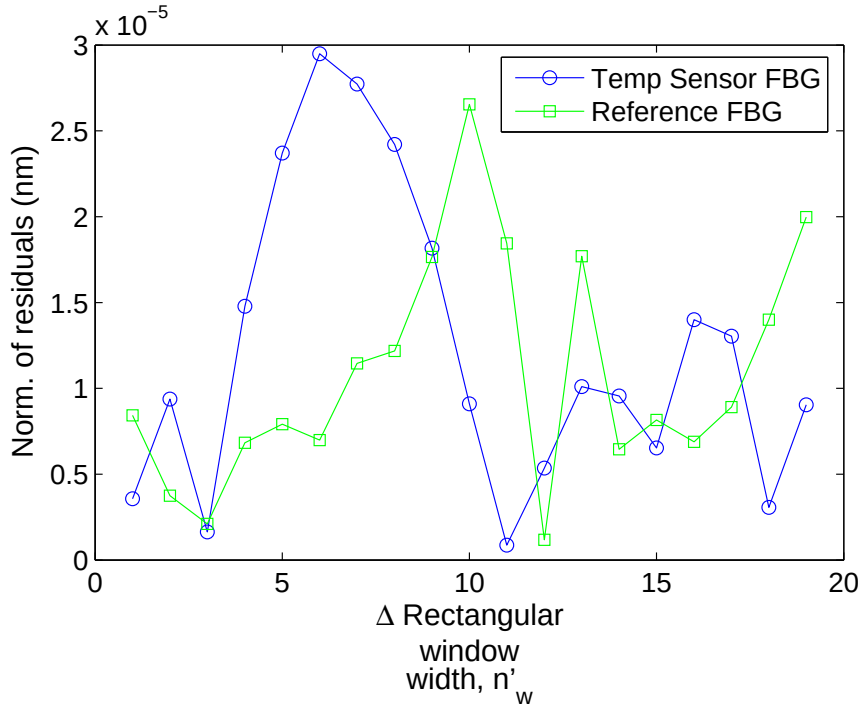

Figure R.8: Differences in the residuals to the linear fits to temperature response slopes of figure R.7.

residuals to those linear fits plotted in figure R.6 (page V.II R-5).

The differences in the linear fits with n'_w provide an alternative means of determining the optimum n_w value. Figures R.7 (page V.II R-6) and R.8 (page V.II R-6) show the differences in the slope values and the residuals to the slope values (figures R.5 (page V.II R-5) and R.6 (page V.II R-5), respectively) as a function of n'_w.

The local minima in the differences in slope at $n'_w = 1, 2$ (figure R.7 (page V.II R-6) and in the difference in residuals at $n'_w = 1, 2, 3$ (figure R.8 (page V.II R-6) again suggest a smaller window size of $n_w = 2, 3, 4$ as providing an optimum value. The lower local minima at other values of n'_w do not coincide for the two FBGs, nor for the differences in slopes and differences in residuals.

R.2 Variable length HTT

For the Hilbert transform technique, HTT, the laser, reference FBG and temperature signal FBG spectral profiles needed to be isolated to determine the ratio of the unwrapped phases (see §6.4.4 (page V.I - 295)). To isolate an individual spectral profile a Hamming window was employed. The choice of the optimum width of the window again needed to be determined. The different shape of the Hamming window to the rectangular window, and the different processing method do not allow the centroid value to be assumed as appropriate.

Again, the optimum window should provide the best signal with effective noise rejection. To determine the optimum window width, the laser and FBG spectral features were evaluated with varying window widths $= 2n_w + 1$, where n_w was changed from 1 to 20.

The centroid's rectangular window, figures R.1 (page V.II R-3) and R.2 (page V.II R-3) show the $n_w = 1$ and $n_w = 20$ Hamming windows respectively. The windowed data are shown with the full interferogram to indicate the overlap that occurs at the larger n_w.

The HTT wavelength was calculated for each laser and FBG wavelength. The HTT incorporates the reference laser through the ratio of the unwrapped phases. Again, the optimum window width was determined by the differences in centroid wavelength with n'_w.

At each temperature step ~ 26 HTT calculated wavelengths were averaged to give the final HTT determined wavelength for the spectral feature.

Figures R.11 (page V.II R-9) and R.12 (page V.II R-9) show the differences in the HTT calculated average wavelengths, $\Delta_w \overline{\lambda_B}$, and the associated standard deviations, $\Delta_w \delta_{\lambda_B}$, as a function of n'_w, where $\Delta F\left(n'_w\right) = F\left(n_w + 1\right) - F\left(n_w\right)$ for function F. Both the temperature signal (blue) and reference (green) FBGs are plotted. The average value at each n'_w is plotted in red, to give an overall trend.

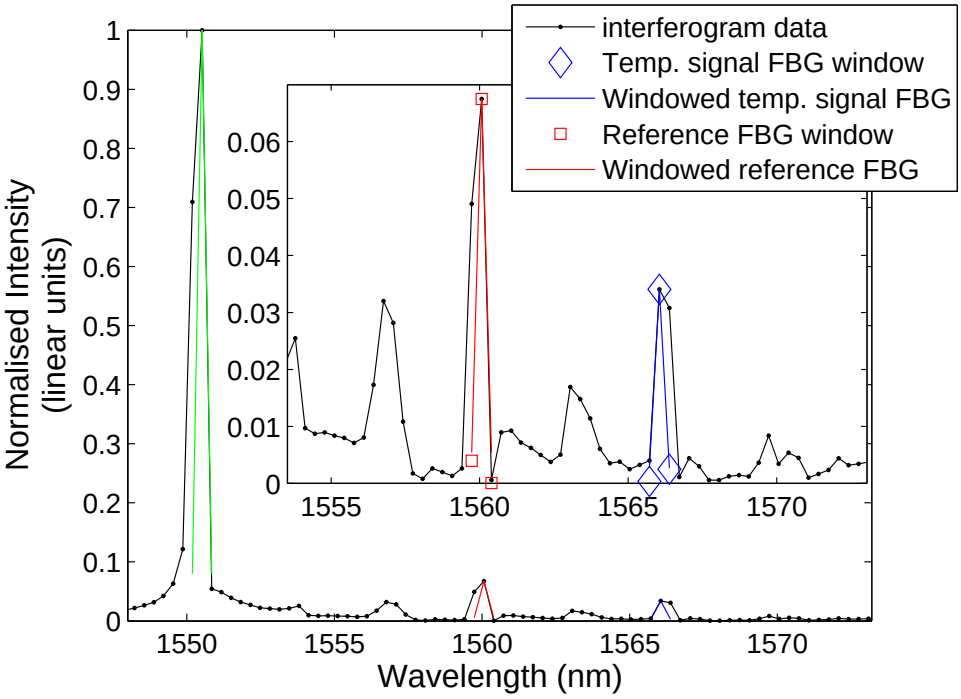

Figure R.9: HTT Hamming windows for $n_w = 1$, with window length $2n_w + 1$.

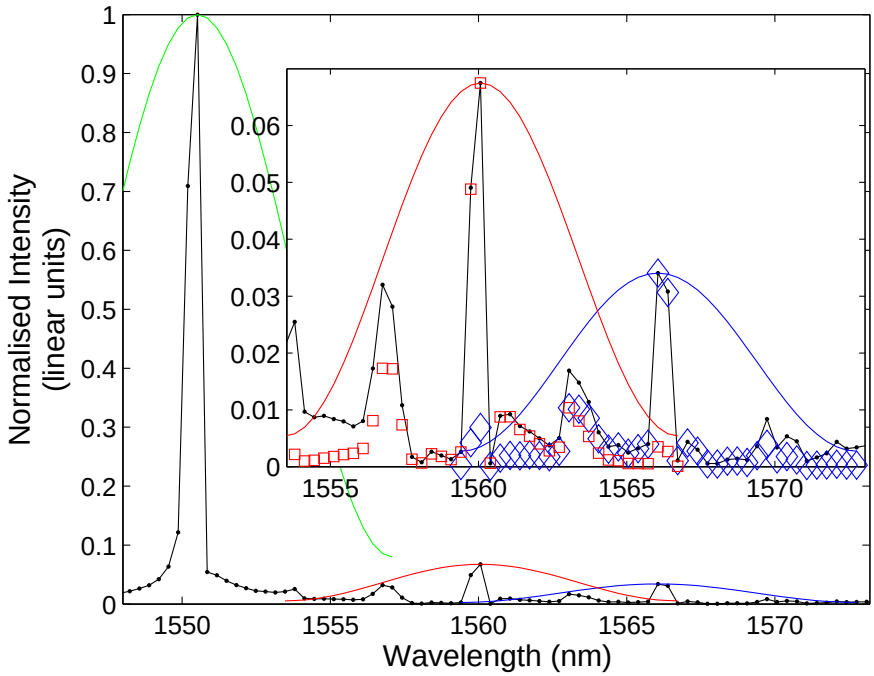

Figure R.10: HTT Hamming windows for $n_w = 20$, with window length $2n_w+1$. The legend of figure R.9 applies.

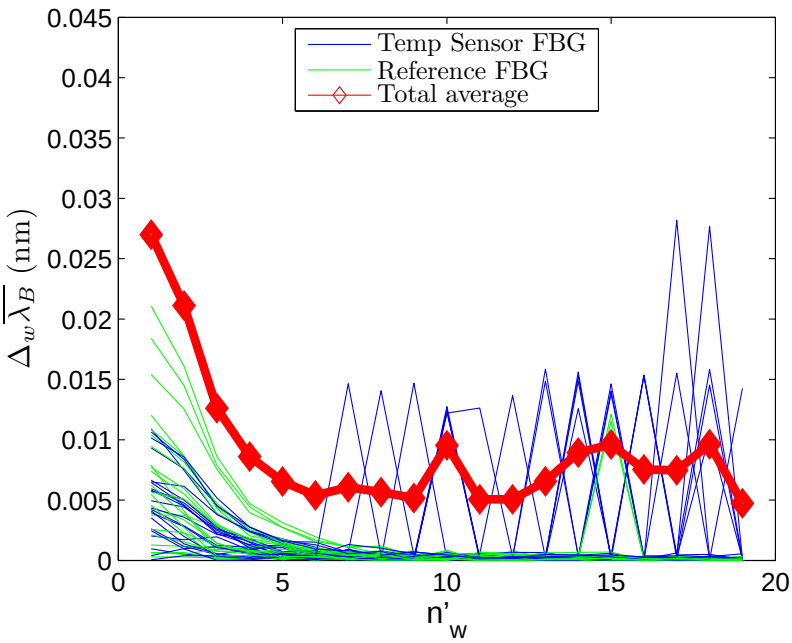

Figure R.11: Overlayed differences in mean HTT determined peak wavelengths, $\Delta_w \overline{\lambda_B}$, as Hamming window width, n_w, is adjusted for temperature sensor and reference FBG.

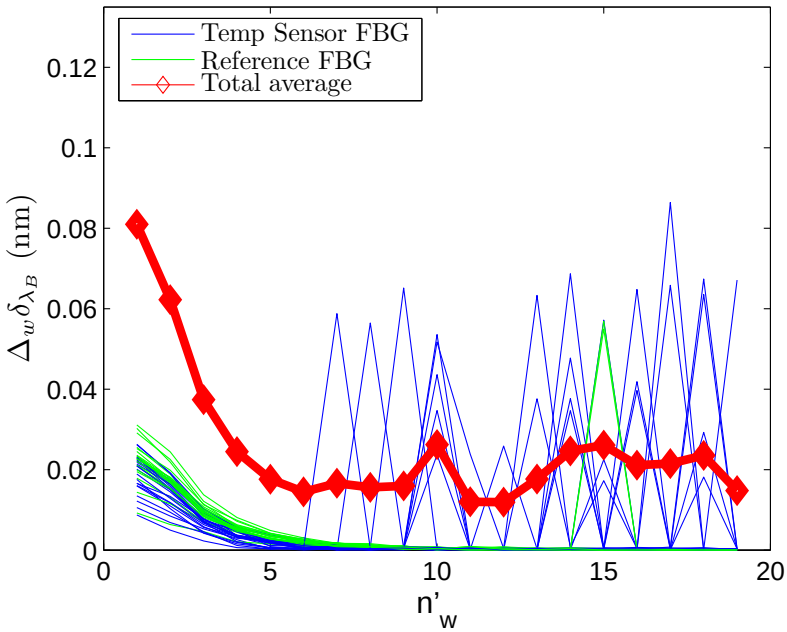

Figure R.12: Overlayed differences in standard deviation of the HTT determined peak wavelengths, $\Delta_w \delta_{\lambda_B}$, as Hamming window width, n_w, is adjusted for temperature sensor and reference FBG.

The plots of the average and the standard deviations show a converging trend until $n'_w = 6$. Thereafter, both the averages and standard deviations exhibit divergences that are approximately of the same magnitude as the initial undersampled value.

It is not evident in these figures that these divergences are not present in all plots. The overlayed plots are not transparent on the figure, and the appearance of the divergence is misleading. This is shown in the overall trend (red) which does not reach the same magnitude. However, the divergences present a limit in terms of magnitude they may diverge by, for a sensor application.

The presence of the neighbouring spectral peaks about the FBGs is less evident in the divergence and local minima in the plots, but still present in the overall trend. The lowest values are at $n_w = 6, 7$. The overall trends in the averages and standard deviations more closely match than do the overall trends for the centroid averages and standard deviations. This may be explained in terms of improved repeatability of the individual measurements going into the averages and standard deviations from the HTT approach, as well as the influence of the change in n_w being more consistent with the HTT approach. It is important to note that, for $n_w = 2, 3, 4$, the overall centroid standard deviation (0.017) is two thirds the overall centroid average (0.026). For $n_w = 6, 7$, the overall HTT standard deviation (0.017) is ~ 2.667 times the overall HTT average (0.006). The larger overall standard deviation indicates that, although the average and standard deviation trends may agree, the spread of the HTT calculated values from the individual interferograms differs more than do the average values.

Again, for comparison, the slope value of the linear fit to the temperature response curve, $\frac{1}{\lambda_B}\frac{\delta\lambda_B}{\delta T}$, of the different n_w are plotted on figure R.13 (page V.II R-11), with the corresponding residuals to those linear fits plotted in figure R.14 (page V.II R-11).

The differences in the linear fits with n'_w provide an alternative means of determining the optimum n_w value. Figures R.15 (page V.II R-12) and R.16 (page V.II R-12) show the differences in the slope values and the residuals to the slope values (figures R.13 (page V.II R-11) and R.14 (page V.II R-11), respectively) as a function of n'_w.

The local minima in the differences in slope at $n'_w = 6$ (figure R.15 (page V.II R-12)) and in the difference in residuals at $n'_w = 6$ for the temperature signal FBG (figure R.16 (page V.II R-12)) agree with the previously determined value of $n_w = 6, 7$ as providing an optimum value. The difference in residuals for the reference FBG (figure R.16 (page V.II R-12)) does not reach a minimum until $n'_w = 16$, i.e. $n_w = 16, 17$. Apart from $n'_w = 15$, the values exhibit a convergence.

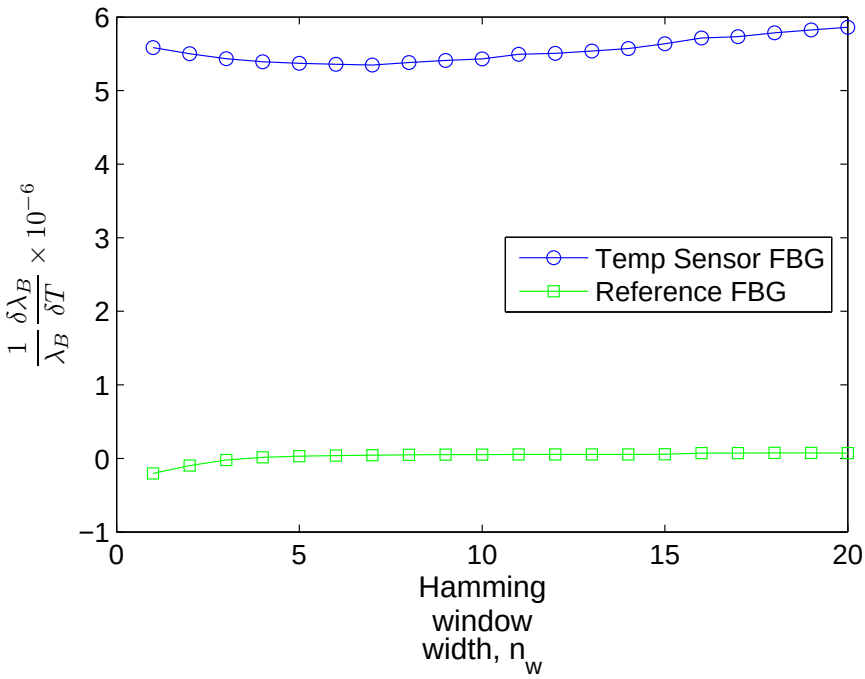

Figure R.13: Linear fit to temperature response slope of temperature signal and reference FBGs as calculated by HTT approach, with Hamming windows of width $2n_w + 1$.

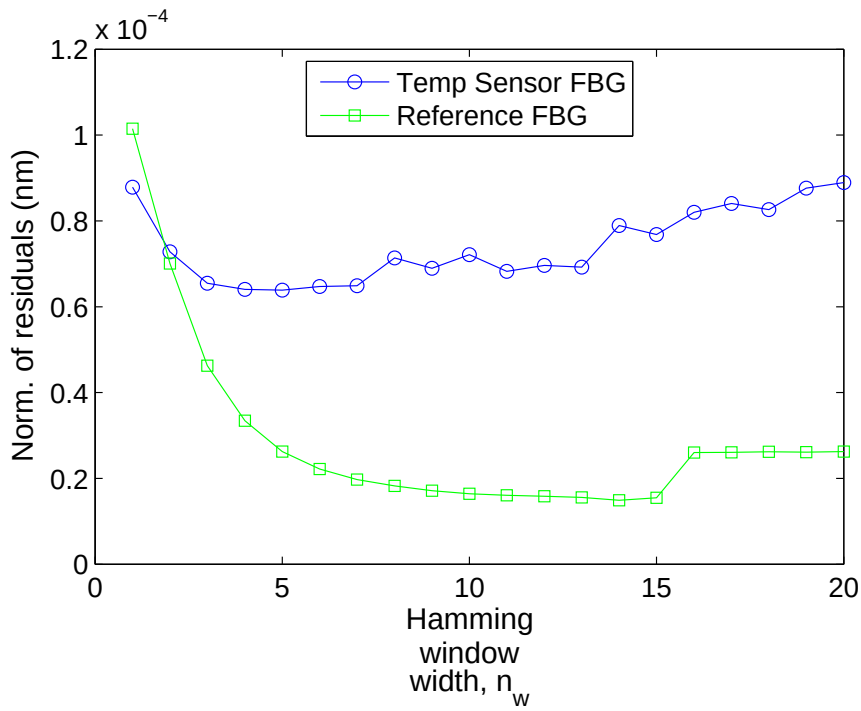

Figure R.14: Residuals to the linear fits to temperature response slope of temperature signal and reference FBGs shown in figure R.13.

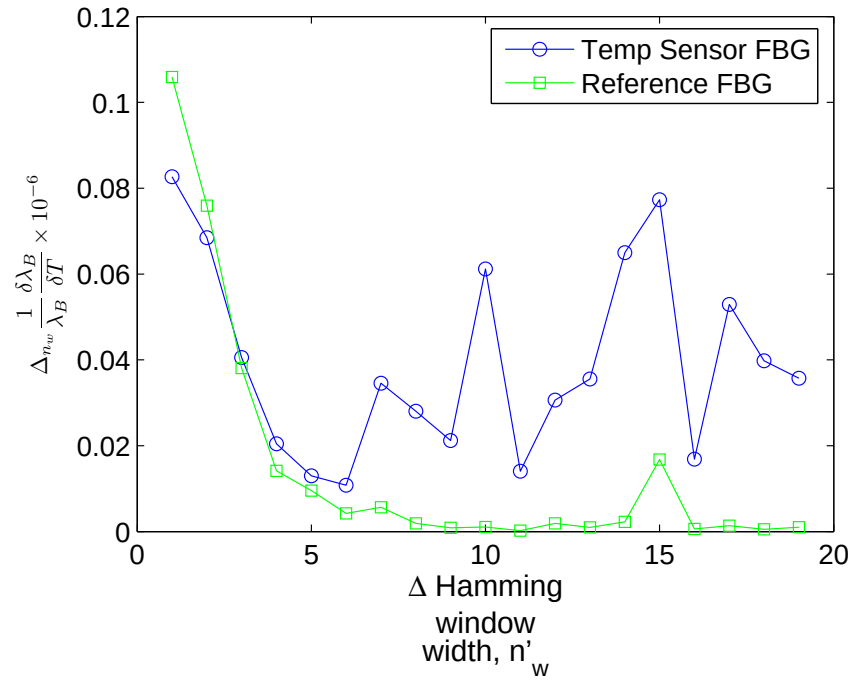

Figure R.15: Differences in linear fit to temperature response slope of temperature signal and reference FBGs as calculated by HTT approach, n'_w changing.

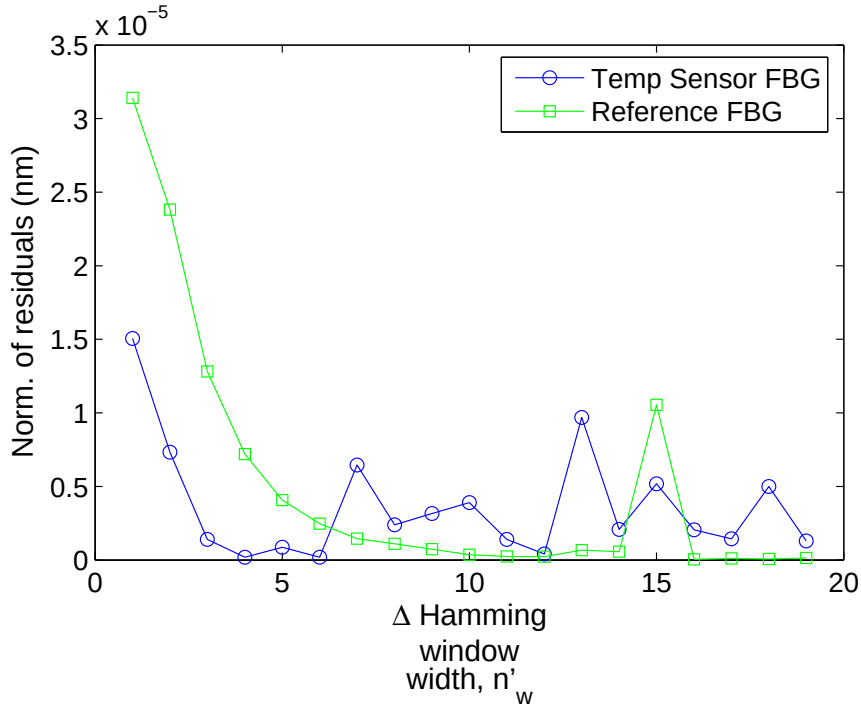

Figure R.16: Differences in the residuals to the linear fits to temperature response slopes of figure R.13.

R.3 Peak Wavelength determination: Centroid approach

As the interferograms varied in length, the spectral range windowed varied as $n_w(0.7 \pm 0.03)$ nm. To determine if the varying effective spectral window adversely affected the calculated values, the interferograms were re–examined with fixed length interferograms.

The length difference between the minimum length (~ 22200) interferogram and the maximum length (~ 23900) interferogram was ~ 1700 data points. Sixteen interferogram lengths, n_i, in steps of 100 data points, were chosen to examine what the influence of changing interferogram length might be. The effective spectral window at each n_i was constant under each n_w, and the centroid wavelength calculated for each n_w and n_i as before.

This generated a large amount of data, with centroid values for 585 individual interferograms over the 22 temperature steps, 20 different n_w values and 16 different n_i values. To present this data clearly and unambiguously presents a challenge with the conflicting requirements of quantity of data and necessary detail. Three visualisations of the data are presented to convey different aspects of these conflicting requirements:

- The individual wavelength–temperature plots are shown with the different n_i plots overlayed, but with the different n_w separated. The differences in n_w are greater than the differences in n_i, and so the data are not presented with n_i separated.
- The discussion follows the form as for the centroid approach in section §R.1 (page V.II R-1):
  - The differences in the average and standard deviations (and the overall trend) are shown for n'_w, the differences with n_w, and then n'_i, the differences with n_i are presented and discussed.
  - Then the slopes and residuals of the linear fits to the temperature response are presented and discussed.

Instead of commenting upon the sixteen individual n_w subfigures, they may be gathered into three groups with similar features. The centroid calculations, figure R.17 (page V.II R-14), show that the smaller window lengths ($n_w = 1 \ldots 3$) produce both smaller standard deviation and closer alignment of the mean values across the different n_i.

The values ($n_w = 4 \ldots 14$) show the increasing standard deviations with changing interferogram length, despite the average value remaining consistent. At the longer

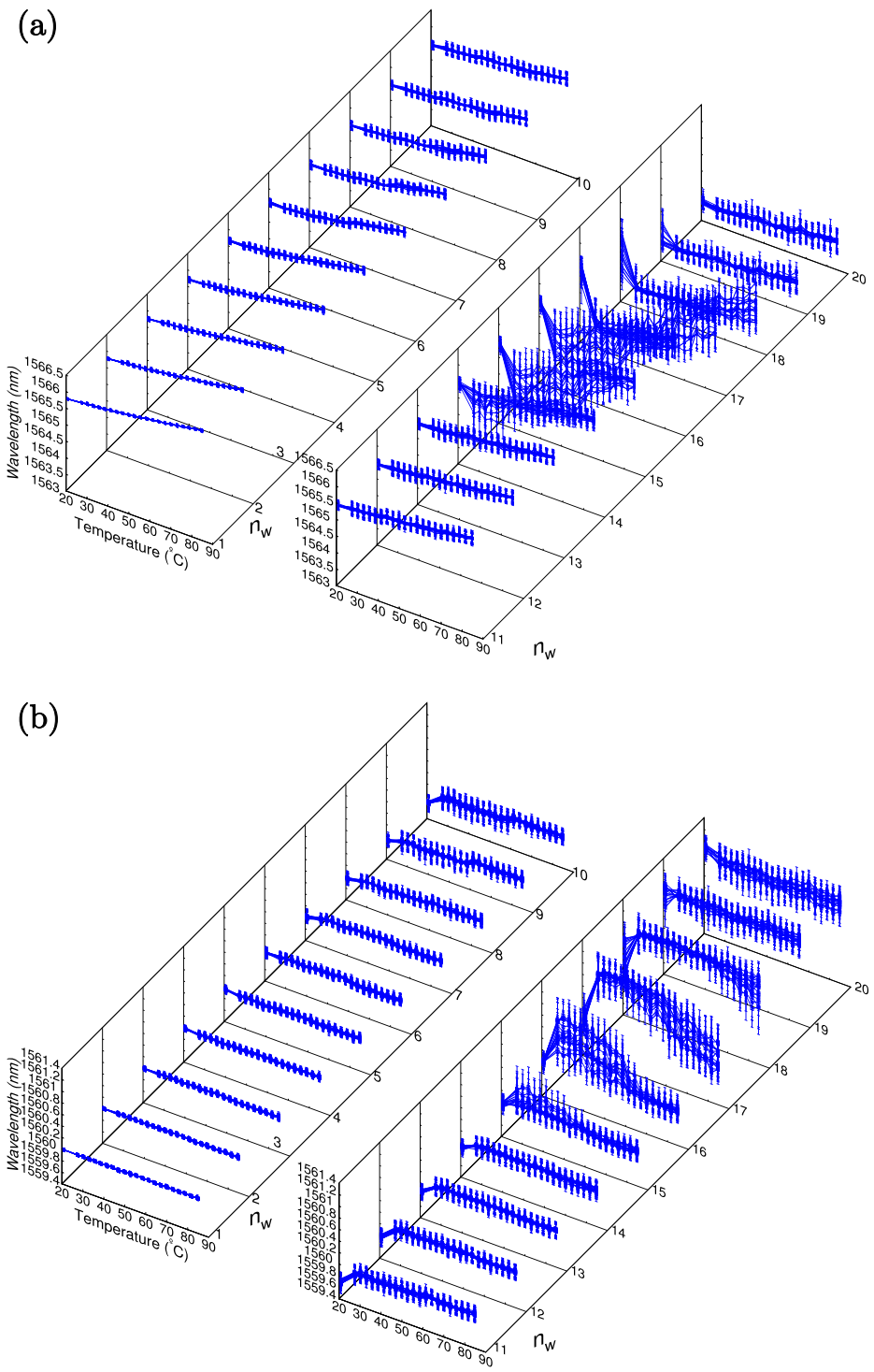

Figure R.17: (a)Temperature signal FBG ($\sim$ 1566 nm) and (b) reference FBG ($\sim$ 1560nm) centroid wavelength against temperature. Different window lengths are overlapped at each interferogram length. The wavelength values have been corrected against the reference laser wavelength.

	Temp. FBG (pm)		Ref. FBG (pm)	
n_w	min.	max.	min.	max.
$1\ldots3$	2.8	15.4	2.2	13.7
$4\ldots14$	8.3	82.6	7.4	38.3
$15\ldots20$	30.9	493.4	22.1	240.7

Table R.1: Averages of centroid calculated mean values across all n_i for the ranges of n_w.

	Temp. FBG (pm)		Ref. FBG (pm)	
n_w	min.	max.	min.	max.
$1\ldots3$	19.4	62.1	16.6	46
$4\ldots14$	61.7	231.3	40.1	159.2
$15\ldots20$	149.2	591.1	113.8	328.2

Table R.2: Standard deviations of centroid calculated mean values across all n_i for the ranges of n_w.

window lengths ($n_w = 15\ldots20$), the other FBG begins to appreciably contribute to the wavelength value and the reference and sensor values drift towards each other and the standard deviations increase.

The minimum and maximum mean and standard deviations of the sixteen different interferogram lengths overlayed for these three regions are listed in table R.1. The corresponding mean and standard deviation values of the overlayed errorbars (i.e. the individual standard deviations) are listed in table R.2.

The influence of the neighbouring FBG is visible at $n_w = 15\ldots20$, and these data are shown for comparison purposes with the later HTT results. The influence of the other FBG also provided confirmation of the approach as indicating influences on the centroid calculation.

To determine which of the 20 window lengths, n_w, and 16 interferogram lengths, n_i, provided a consistent[1] value, the differences between the neighbouring FBG peak wavelengths as n_w and n_i are plotted.

The difference in average λ_B with n_w, $\Delta_w\overline{\lambda_B}$, is plotted in figure R.18 (page V.II R-16), and the associated standard deviations, $\Delta_w\delta_{\lambda_b}$, plotted in figure R.20 (page V.II R-17).

Figures R.19 (page V.II R-16) and R.21 (page V.II R-17) show the average n'_w value of minimum $\Delta_w\overline{\lambda_B}$ and $\Delta_w\delta_{\lambda_b}$ for each temperature step, respectively, along with the distribution of those minimum positions to one standard deviation.

Figure R.18 (page V.II R-16) has the lowest values in the $n'_w = 1\ldots3$ range. The corresponding values on figure R.20 (page V.II R-17) are similarly low. Values

[1] A consistent value indicates a value minimally independent of changes in window or interferogram length.

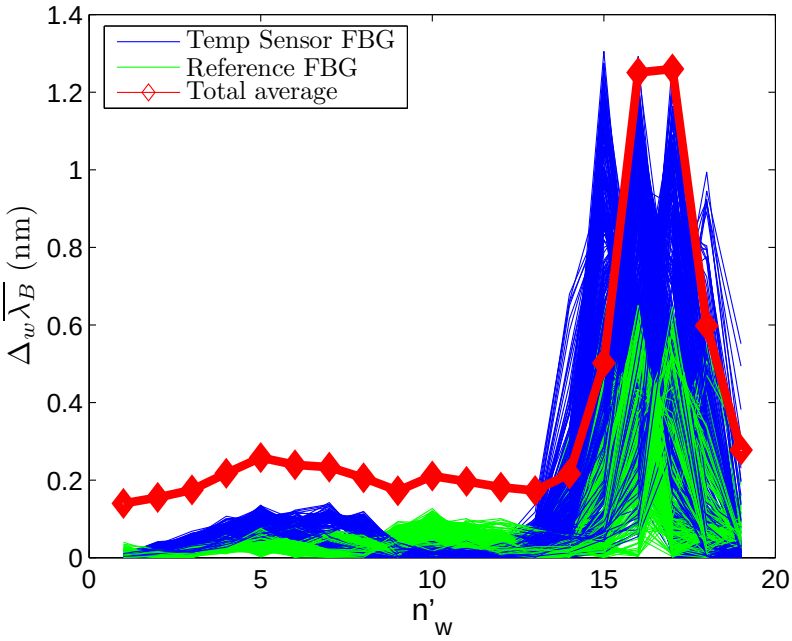

Figure R.18: Overlayed differences in mean centroid determined peak wavelengths, $\Delta_w\overline{\lambda_B}$, as rectangular window width, n_w, is adjusted for temperature sensor and reference FBG. The differences do not converge as the lowest values are at $n'_w = 1 \ldots 3$.

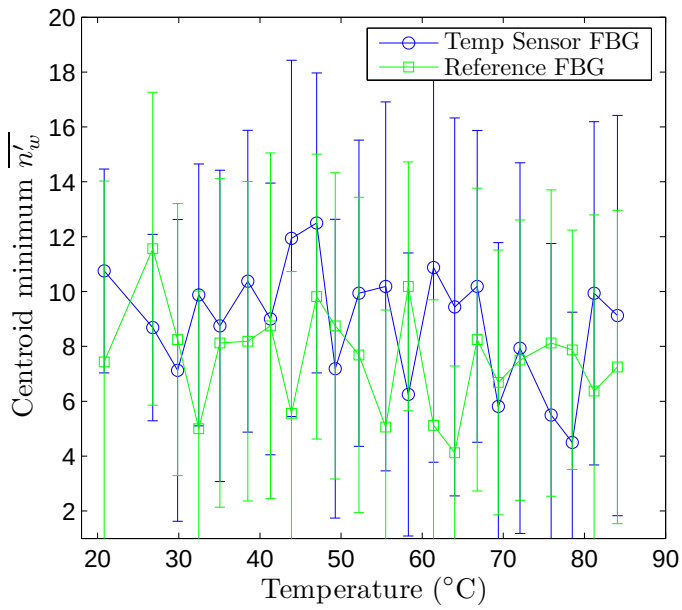

Figure R.19: The n'_w position at which a minimum centroid determined $\Delta_w\overline{\lambda_B}$ is obtained for each temperature step. The average values are 8.9 ± 5.93 and 7.53 ± 5.49 for the temperature sensor and reference FBGs, respectively.

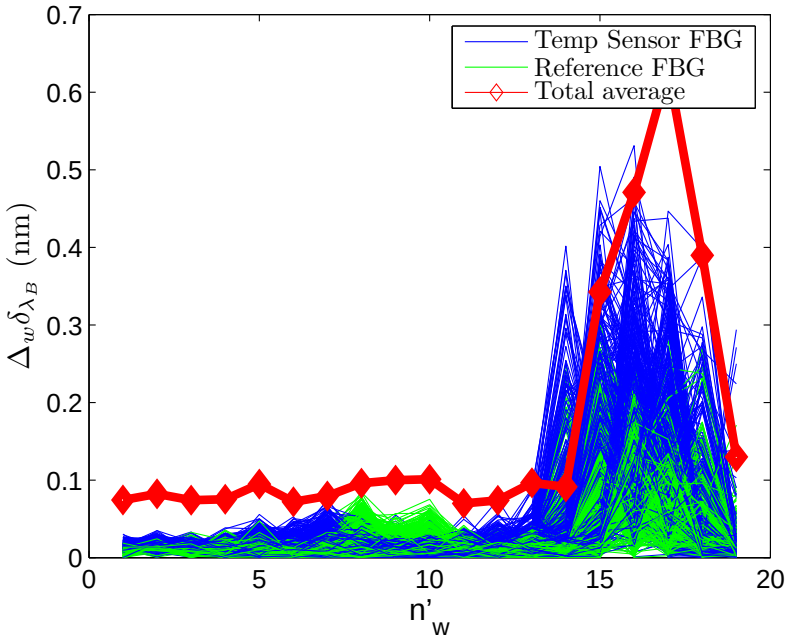

Figure R.20: Overlayed differences in standard deviation of the centroid determined peak wavelengths, $\Delta_w \delta_{\lambda_B}$, as rectangular window width, n_w, is adjusted for temperature sensor and reference FBG. The differences do not converge as the lowest values are at $n'_w = 1 \ldots 3$.

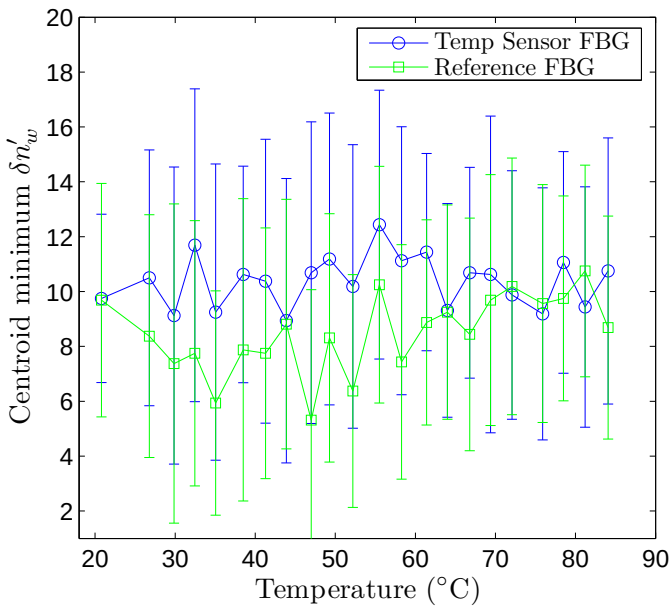

Figure R.21: The n'_w position at which a minimum centroid determined $\Delta_w \delta_{\lambda_B}$ is obtained for each temperature step. The average values are 10.38 ± 4.63 and 8.47 ± 4.56 for the temperature sensor and reference FBGs, respectively.

	Ref. FBG	Temp. FBG
$\overline{n'_w}$	8.9 ± 5.93	7.53 ± 5.49
$\overline{n'_i}$	3.98 ± 4.26	4.15 ± 4.03

Table R.3: Mean values of temperature sensor and reference FBGs with changing n'_w and n'_i from figures R.19 (page V.II R-16) and R.23 (page V.II R-19), respectively.

	Ref. FBG	Temp. FBG
$\delta n'_w$	10.3 ± 4.63	8.47 ± 4.56
$\delta n'_i$	9.64 ± 8.37	9.85 ± 8.33

Table R.4: Mean values of temperature sensor and reference FBGs with changing n'_w and n'_i from figures R.21 (page V.II R-17) and R.25 (page V.II R-20), respectively.

of $n'_w = 2, 3$ correspond to $n_w = 2, 3, 4$, just as in the variable interferogram length situation.

The difference in average λ_B with n_i, $\Delta_i\overline{\lambda_B}$, is plotted in figure R.22 (page V.II R-19), and the associated standard deviations, $\Delta_i\delta_{\lambda_b}$, plotted in figure R.24 (page V.II R-20).

Figures R.23 (page V.II R-19) and R.25 (page V.II R-20) show the average n'_i value of minimum $\Delta_i\overline{\lambda_B}$ and $\Delta_i\delta_{\lambda_b}$ for each temperature step, respectively, along with the distribution of those minimum positions to one standard deviation.

The mean values of the n'_w and n'_i centroid minima of figures R.19 (page V.II R-16) and R.23 (page V.II R-19) are tabulated in table R.3 (page V.II R-18). The mean values of the n'_w and n'_i centroid minima of figures R.21 (page V.II R-17) and R.25 (page V.II R-20) are tabulated in table R.4 (page V.II R-18).

Figure R.22 (page V.II R-19) does not visually suggest a lowest value. The *total average*, or trend, (in red) of all the overlayed plots has a minimum value at $n'_i = 16$. The decreasing difference may be a result of the fixed rectangular windows incorporating less of the total spectrum, and therefore being comparatively more similar with n'_i. Figure R.24 (page V.II R-20) does not present an obvious choice of optimum n_i, and provides motivation for alternate visualisations of the data.

The need to determine an optimum n_i motivated the next alternative visualisation attempted. The normalised slope of the linear fit to the temperature response was calculated for each $n_w = 1 \ldots 20$ and $n_i = 1 \ldots 16$, and plotted as a false–colour surface. Figures R.26 (page V.II R-21) and R.27 (page V.II R-21) show the normalised slopes of the linear fits to the data in figures R.17(a) & (b) (page V.II R-14), the temperature signal FBG and reference FBG, respectively.

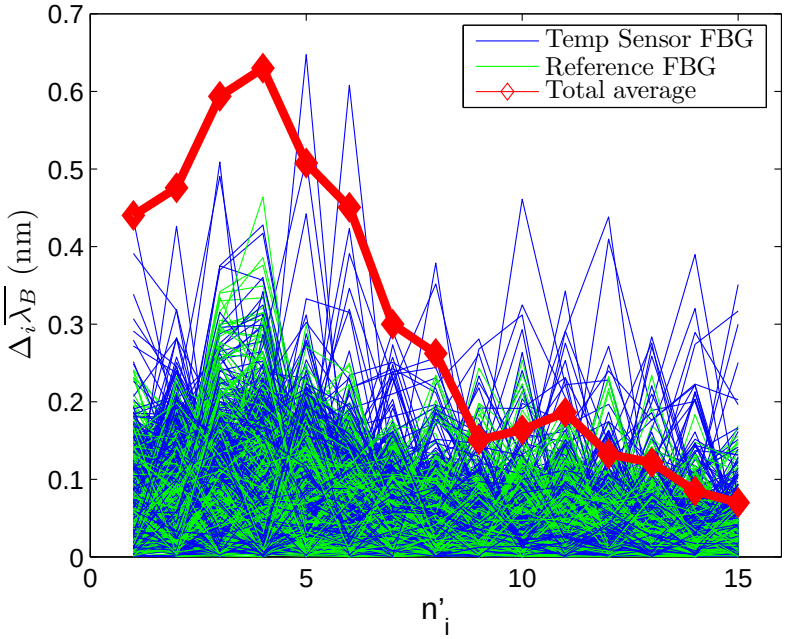

Figure R.22: Overlayed differences in mean centroid determined peak wavelengths, $\Delta_i\overline{\lambda_B}$, as rectangular window width, n_i, is adjusted for temperature sensor and reference FBG.

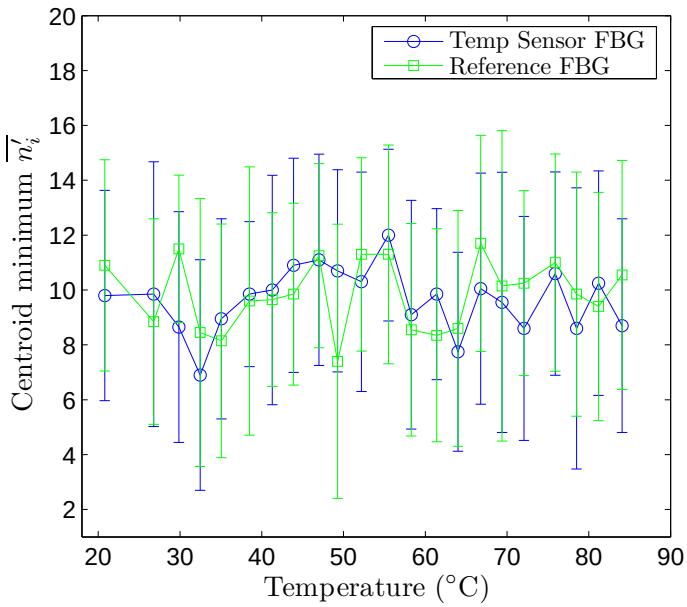

Figure R.23: The n_i' position at which a minimum centroid determined $\Delta_i\overline{\lambda_B}$ is obtained for each temperature step. The average values are 9.64 ± 3.98 and 9.85 ± 4.15 for the temperature sensor and reference FBGs, respectively.

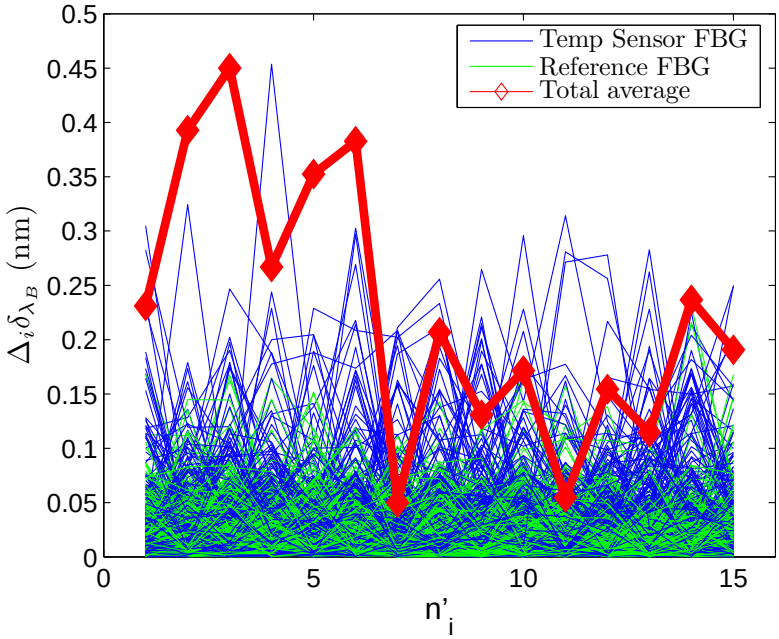

Figure R.24: Overlayed differences in standard deviation of the centroid determined peak wavelengths, $\Delta_i\delta_{\lambda_B}$, as rectangular window width, n_i, is adjusted for temperature sensor and reference FBG.

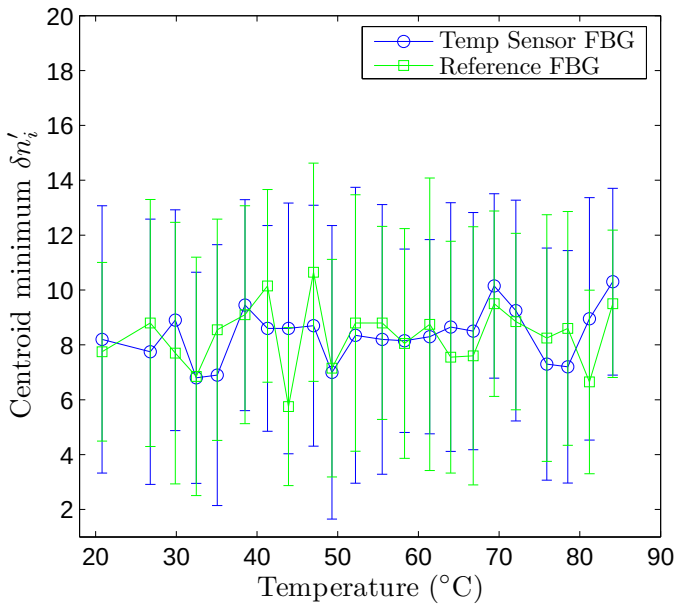

Figure R.25: The n_i' position at which a minimum centroid determined $\Delta_i\delta_{\lambda_B}$ is obtained for each temperature step. The average values are 8.37 ± 4.26 and 8.33 ± 4.03 for the temperature sensor and reference FBGs, respectively.

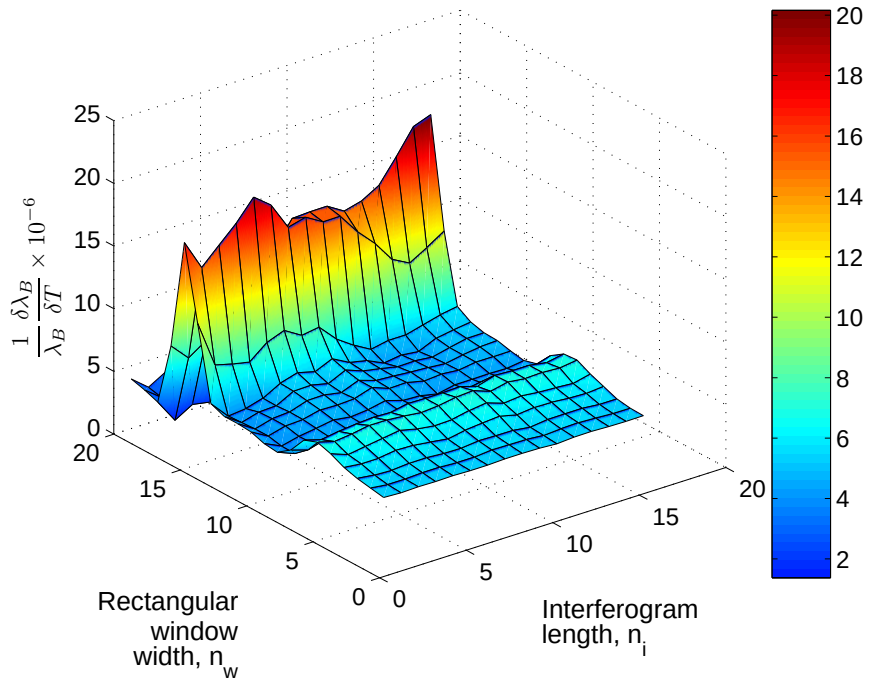

Figure R.26: Linear fit to temperature response slope of temperature signal FBG as calculated by centroid approach, with rectangular windows of width $2n_w + 1$ and interferogram length step n_i.

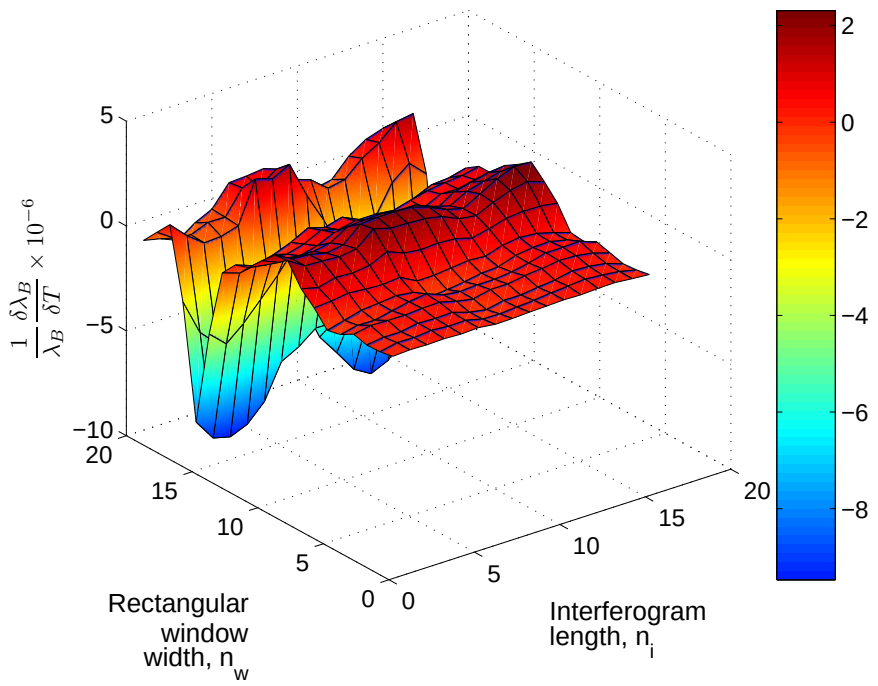

Figure R.27: Linear fit to temperature response slope of reference FBG as calculated by centroid approach, with rectangular windows for $2n_w + 1$ and interferogram length step n_i.

The slopes of the linear fits illustrate the changes that happen with the window length and with interferogram length. Figures R.26 (page V.II R-21) and R.27 (page V.II R-21) are given the false colours to emphasise the changes, although intersection of the black lines marks the slope data point. The presence of the adjacent peaks, and in particular the FBG peaks, is evident in the oscillation with increasing n_w. The values $n_w = 2, 3, 4$ are, once more, optimum.

Figures R.28 (page V.II R-23) and R.29 (page V.II R-23) show the corresponding residuals to the linear fits shown in figures R.26 (page V.II R-21) and R.27 (page V.II R-21), respectively. The change in window length n_w results in greater changes than change in the length of the interferograms n_i. The residuals give a comparative indication of how closely the data match the linear fit.

Figure R.32 (page V.II R-25) shows the n_i temperature response slope values for the temperature sensor FBG for $n_w = 2, 3, 4$. The corresponding reference FBG differences are shown in figure R.33 (page V.II R-25). The same oscillations are seen in the HTT obtained temperature response slope values, on figures R.45 (page V.II R-37) to R.52 (page V.II R-42). As different lengths of the same signal are used, the oscillation is likely to be introduced in the signal processing prior to the centroid/HTT calculations. This might arise during the recalibration process. It is unlikely to be additional spectral content as the change in length is approximately 0.5% per n_i, and is averaged over the ~ 26 interferograms at each temperature step.

The reference FBG slope should be close to zero as the FBG was not actively heated and was, ideally, only monitoring the laboratory temperature. The changes introduced by varying n_i are smaller than for n_w and less easily attributable[2] to side structures. An oscillation is evident as n_i' increases. The oscillation is present and even more noticeable in the HTT figures, R.45 (page V.II R-37) and R.46 (page V.II R-37). This oscillation prevents the selection of an optimum n_i value. The value of the thermal response depends upon the interferogram length, n_i, chosen. The values for $n_w = 2, 3, 4$ are tabulated against each n_i in tables R.5 (page V.II R-27) and R.6 (page V.II R-27), for the temperature signal and reference FBGs.

The errorbars are smaller than for the variable interferogram length plots, figures 6.20 (page V.I - 292) and 6.21 (page V.I - 292), as they traverse the range of different n_i. This is shown in figures R.34 (page V.II R-28) and R.35 (page V.II R-29) for the temperature signal and reference FBGs. The (a) subfigures are reproductions of 6.20 (page V.I - 292) and 6.21 (page V.I - 292), for comparison. The (b) and (c) subfigures show the $n_i = 5$ and $n_i = 7$ plots, respectively. The $n_w = 2$ blue line in the (a) subfigures is reproduced as a black line in the (b) and (c) subfigures as a visual

[2]The changes with n_i illustrated provide a source for the standard deviations shown in the variable length case reported. The values at a given n_w are sampled from the surface R.26 (page V.II R-21) according to the length of the interferogram, for each individual wavelength calculated.

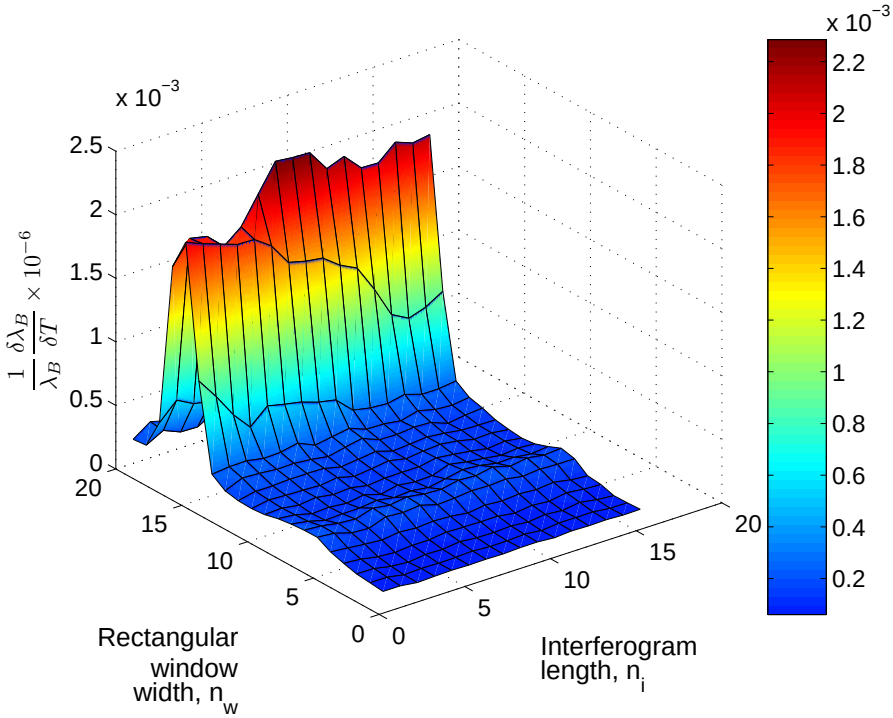

Figure R.28: Residuals to the linear fits to temperature response slope of signal FBG shown in figure R.26 (page V.II R-21).

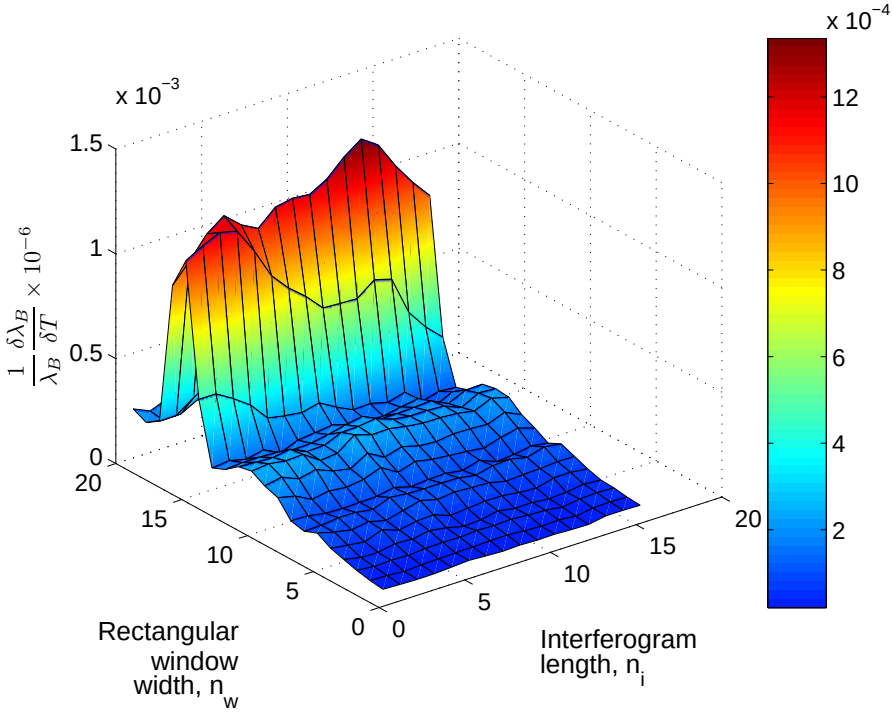

Figure R.29: Residuals to the linear fits to temperature response slope of reference FBG shown in figure R.27 (page V.II R-21).

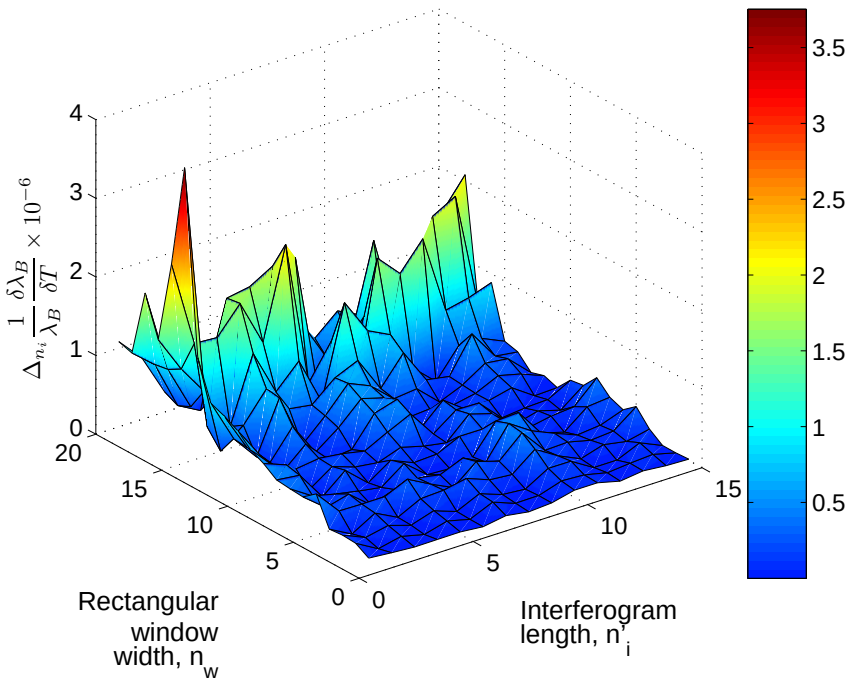

Figure R.30: Differences along n_i of slopes the linear fits to temperature response slope of temperature signal FBG shown in figure R.26 (page V.II R-21).

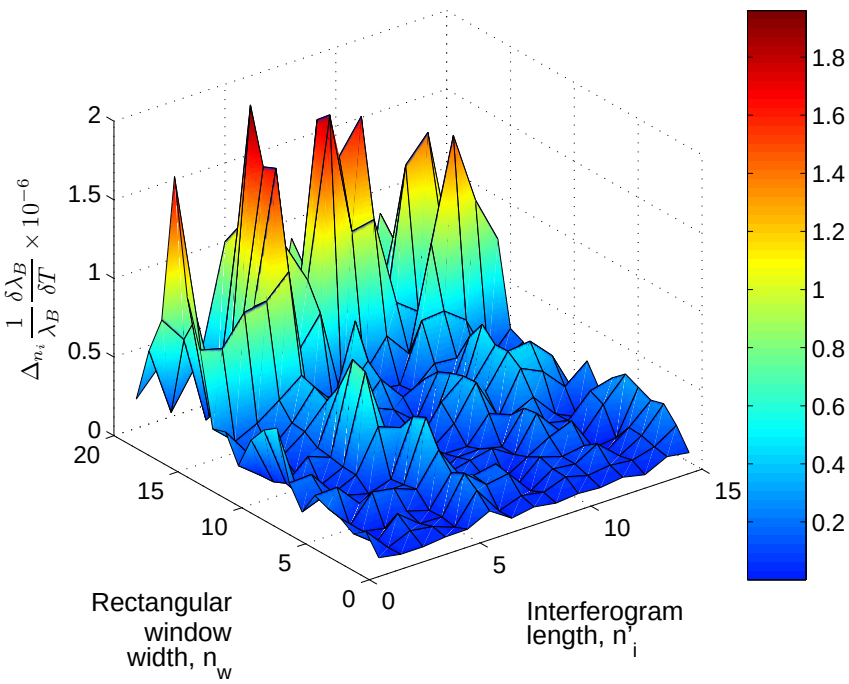

Figure R.31: Differences along n_i of slopes the linear fits to temperature response slope of reference FBG shown in figure R.27 (page V.II R-21).

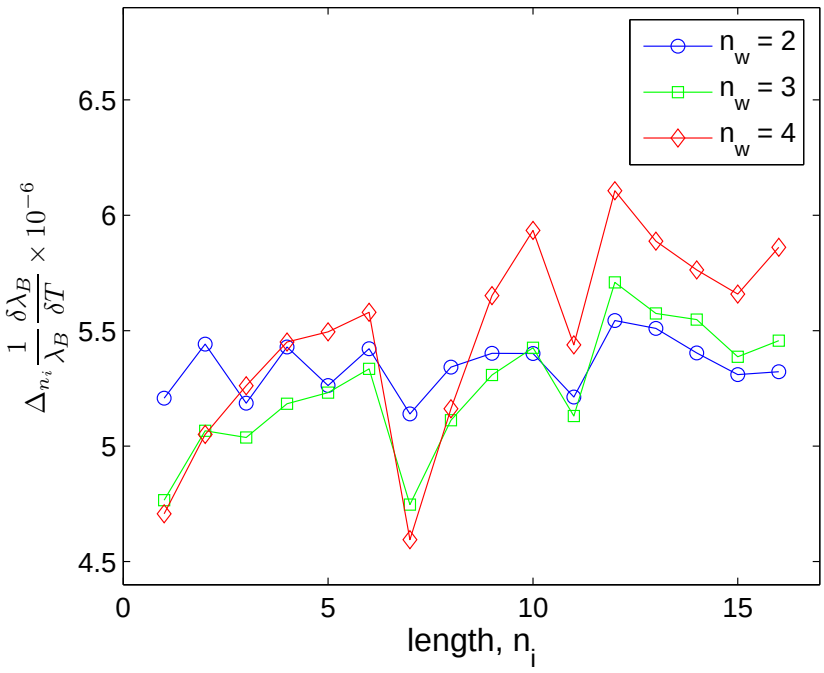

Figure R.32: Temperature signal FBG values of $n_w = 2, 3, 4$ from R.26 (page V.II R-21) indicating oscillation.

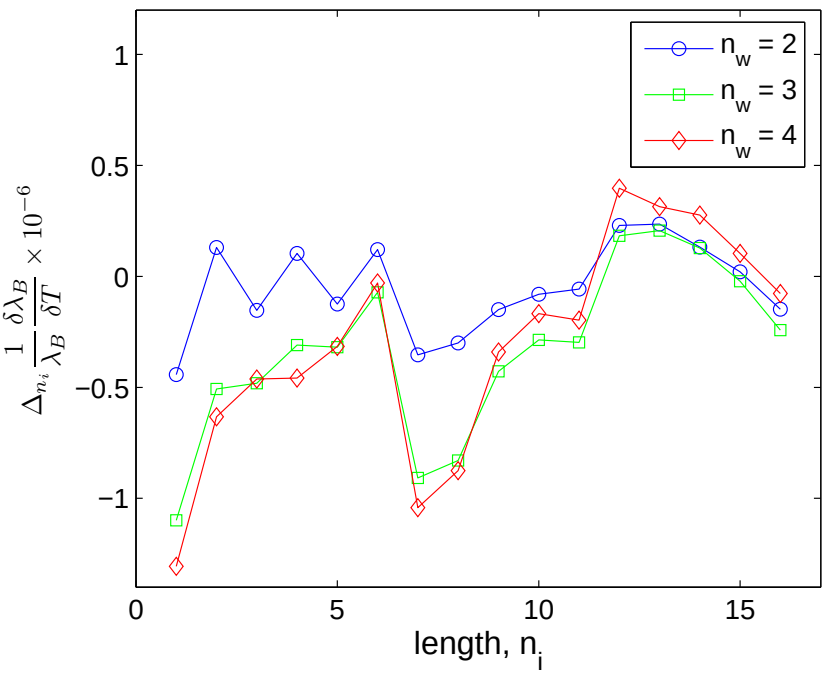

Figure R.33: Reference FBG values of $n_w = 2, 3, 4$ from R.27 (page V.II R-21) indicating oscillation.

aid. The values $n_i = 5$ and $n_i = 7$ were chosen as examples of the upper and lower oscillation values on figures R.32 (page V.II R-25) and R.33 (page V.II R-25). After table 6.4 (page V.I - 291), the slope values for the figures R.34 (page V.II R-28) and R.35 (page V.II R-29) are listed in tables R.5 (page V.II R-27) and R.6 (page V.II R-27), respectively. Note, that these are the same n_w and n_i temperature signal and reference slope values (residuals) shown in figures R.26 (page V.II R-21) and R.27 (page V.II R-21) (R.28 (page V.II R-23) and R.29 (page V.II R-23)), respectively.

As the oscillation of the temperature signal and reference FBGs differs, figures R.32 (page V.II R-25) and R.33 (page V.II R-25), the correction of temperature signal FBG against the reference FBG also contains an oscillation dependent upon n_i. The maximum and minimum differences between FBG temperature response slope values are $6.1 \times 10^{-6}\,{}^{\circ}\mathrm{C}^{-1}$ and $4.6 \times 10^{-6}\,{}^{\circ}\mathrm{C}^{-1}$, respectively.

n_i	n_w 2	3	4
1	5.58 (0.09)	5.77 (0.10)	6.08 (0.13)
2	5.41 (0.09)	5.59 (0.10)	5.91 (0.12)
3	5.41 (0.07)	5.53 (0.08)	5.92 (0.09)
4	5.48 (0.07)	5.65 (0.06)	6.10 (0.08)
5	5.48 (0.07)	5.67 (0.08)	6.07 (0.10)
6	5.40 (0.07)	5.56 (0.08)	5.89 (0.10)
7	5.40 (0.08)	5.54 (0.09)	5.70 (0.11)
8	5.53 (0.07)	5.69 (0.08)	5.95 (0.11)
9	5.51 (0.07)	5.65 (0.08)	6.09 (0.11)
10	5.48 (0.08)	5.63 (0.08)	6.20 (0.11)
11	5.37 (0.06)	5.45 (0.07)	5.86 (0.08)
12	5.47 (0.08)	5.63 (0.09)	6.02 (0.10)
13	5.50 (0.08)	5.64 (0.08)	5.99 (0.09)
14	5.44 (0.08)	5.65 (0.10)	5.88 (0.11)
15	5.36 (0.06)	5.51 (0.07)	5.82 (0.10)
16	5.35 (0.06)	5.52 (0.06)	5.94 (0.09)

Table R.5: Temperature sensor FBG centroid approach calculated slopes, $\frac{1}{\lambda_B}\frac{\partial \lambda_B}{\partial T} \times 10^{-6}$ °C^{-1}, for $n_w = 2, 3, 4$ for each n_i, with norm of residuals (nm) in parenthesis.

n_i	n_w 2	3	4
1	-0.07 (0.04)	-0.09 (0.05)	0.07 (0.07)
2	0.09 (0.03)	0.02 (0.04)	0.23 (0.05)
3	0.07 (0.02)	0.01 (0.04)	0.20 (0.05)
4	0.15 (0.03)	0.16 (0.04)	0.20 (0.06)
5	0.09 (0.03)	0.12 (0.05)	0.26 (0.06)
6	0.10 (0.03)	0.15 (0.05)	0.29 (0.07)
7	-0.09 (0.04)	-0.11 (0.05)	0.07 (0.06)
8	-0.11 (0.04)	-0.25 (0.05)	-0.08 (0.04)
9	-0.04 (0.04)	-0.09 (0.05)	0.10 (0.04)
10	0.0029 (0.03)	-0.08 (0.06)	0.10 (0.06)
11	0.10 (0.03)	0.02 (0.05)	0.23 (0.05)
12	0.15 (0.03)	0.10 (0.04)	0.31 (0.05)
13	0.23 (0.02)	0.27 (0.03)	0.42 (0.04)
14	0.17 (0.04)	0.23 (0.05)	0.39 (0.04)
15	0.07 (0.04)	0.10 (0.05)	0.26 (0.06)
16	-0.12 (0.04)	-0.18 (0.05)	0.0048 (0.05)

Table R.6: Reference FBG centroid approach calculated slopes, $\frac{1}{\lambda_B}\frac{\partial \lambda_B}{\partial T} \times 10^{-6}$°C^{-1}, for $n_w = 2, 3, 4$ for each n_i, with norm of residuals (nm) in parenthesis.

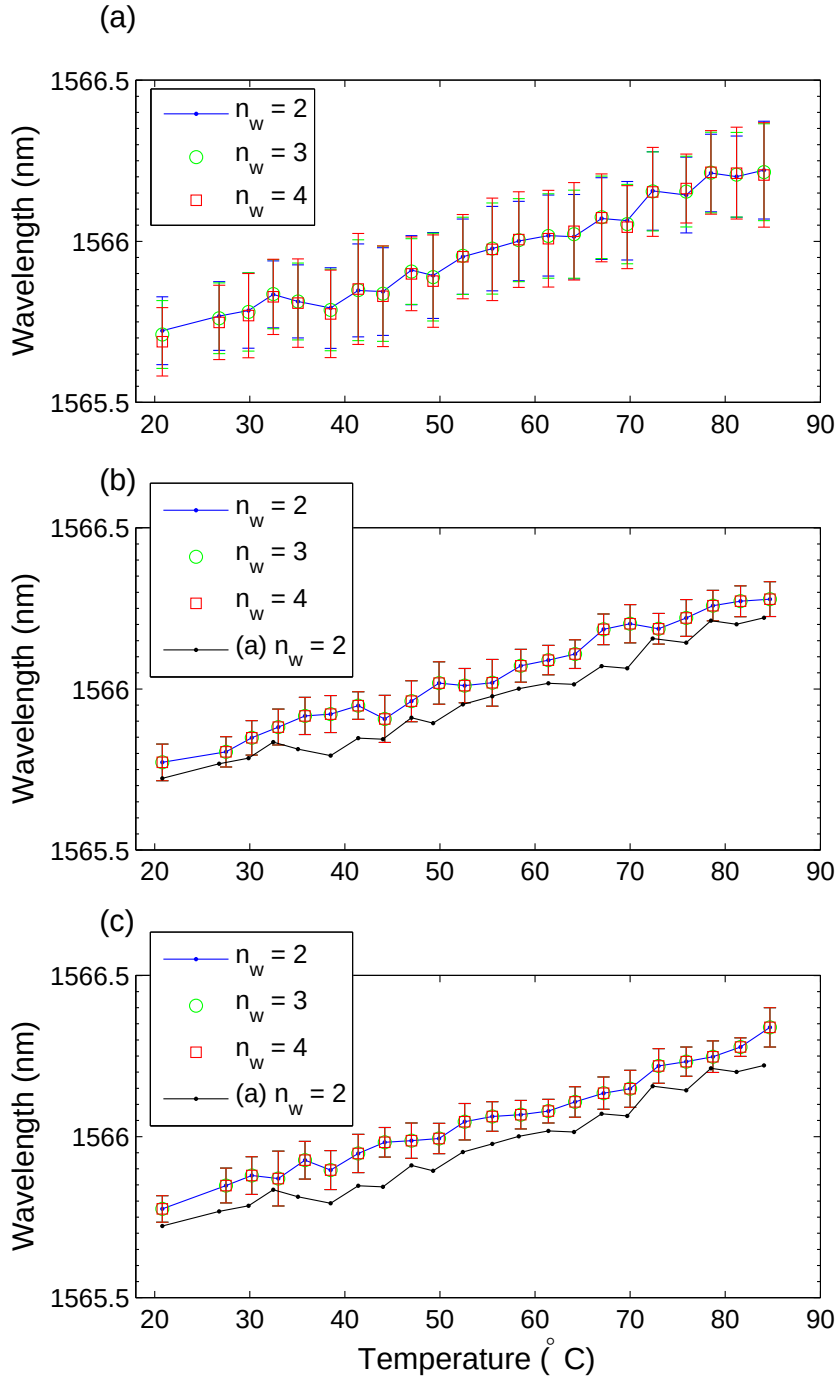

Figure R.34: (a) Temperature signal FBG values of $n_w = 2, 3, 4$ from figure 6.20 (page V.I - 292); (b) corresponding temperature signal FBG values for $n_i = 5$ (lower n_i) ; (c) corresponding temperature signal FBG values for $n_i = 7$ (upper n_i).

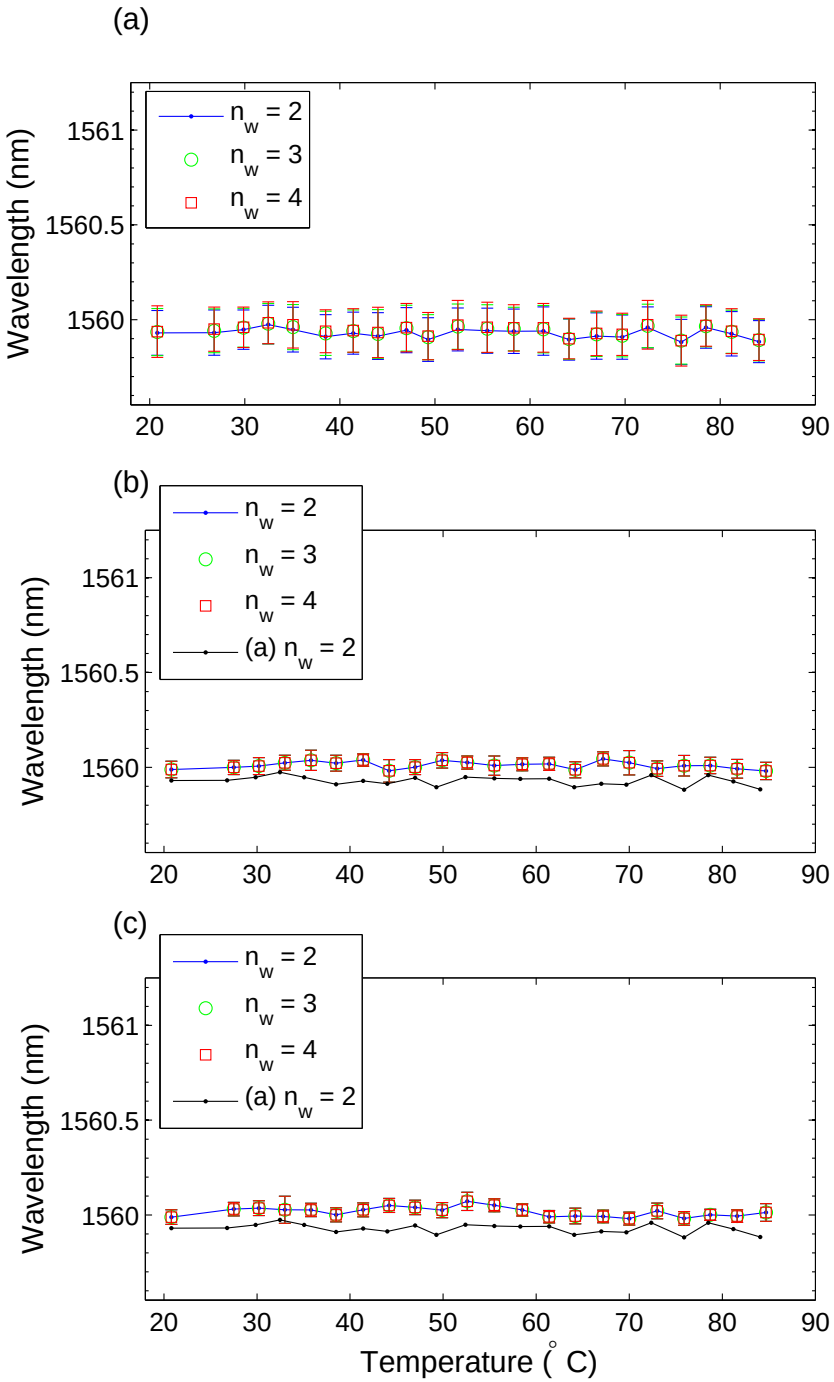

Figure R.35: (a) Reference FBG values of $n_w = 2, 3, 4$ from figure 6.21 (page V.I - 292); (b) corresponding reference FBG values for $n_i = 5$ (lower n_i) ; (c) corresponding reference FBG values for $n_i = 7$ (upper n_i).

	Temp. FBG (pm)		Ref. FBG (pm)	
n_w	min.	max.	min.	max.
1 : 3	3.7	56.2	2.3	45.5
4 : 14	1.1	6.8	0.9	5.7
15 : 20	1.2	2.1	0.9	13.6

Table R.7: Averages of HTT calculated mean values across all n_i for the ranges of n_w.

R.4 Peak wavelength determination: HTT approach

As for the centroid approach, the optimum Hamming window width needed to be determined which admitted the maximum signal information and the minimum noise for the HTT approach.

The HTT approach calculated temperature response slopes, figure R.36 (page V.II R-31), show that the HTT approach is, in comparison to the centroid calculation, less sensitive to the longer window lengths $n_w = 4 \ldots 17$ than to the shorter window lengths ($n_w = 1 \ldots 3$). This can be understood as a result of the shape of the Hamming window against the rectangular window. For shorter window lengths, the spectrum of the FBG is modified. Depending upon which data point the window is centred at, the eventual slope will alter, hence the large values and changes in value at the shorter window size.

The reduced influence of the neighbouring FBG is observed at the larger window sizes $n_w = 18 \ldots 20$) in the increased standard deviations. The changes are noticeably smaller than for the centroid approach. The minimum and maximum standard deviations (vertical errorbars) of the sixteen different interferogram lengths overlayed for these three regions are listed in table R.7. The corresponding mean value of the overlayed errorbars (i.e. the individual standard deviations) are listed in table R.8 (page V.II R-34).

Similarly, the average and standard deviations exhibit smaller changes using the HTT approach, compared to the centroid approach.

As for the centroid approach, figures R.37 (page V.II R-32) and R.39 (page V.II R-33) show the values of the mean HTT determined peak wavelengths, $\Delta_w \overline{\lambda_B}$, and corresponding standard deviations, $\Delta_w \delta_{\lambda_B}$, with increasing n'_w, respectively. The n'_w position of the corresponding minimum HTT determined value is plotted in figures R.38 (page V.II R-32) and R.40 (page V.II R-33), respectively.

The optimum values of $n_w = 12, 13, 14$ do not agree with the optimum value obtained from the variable interferogram length analysis, $n_w = 6, 7$ (figures R.11

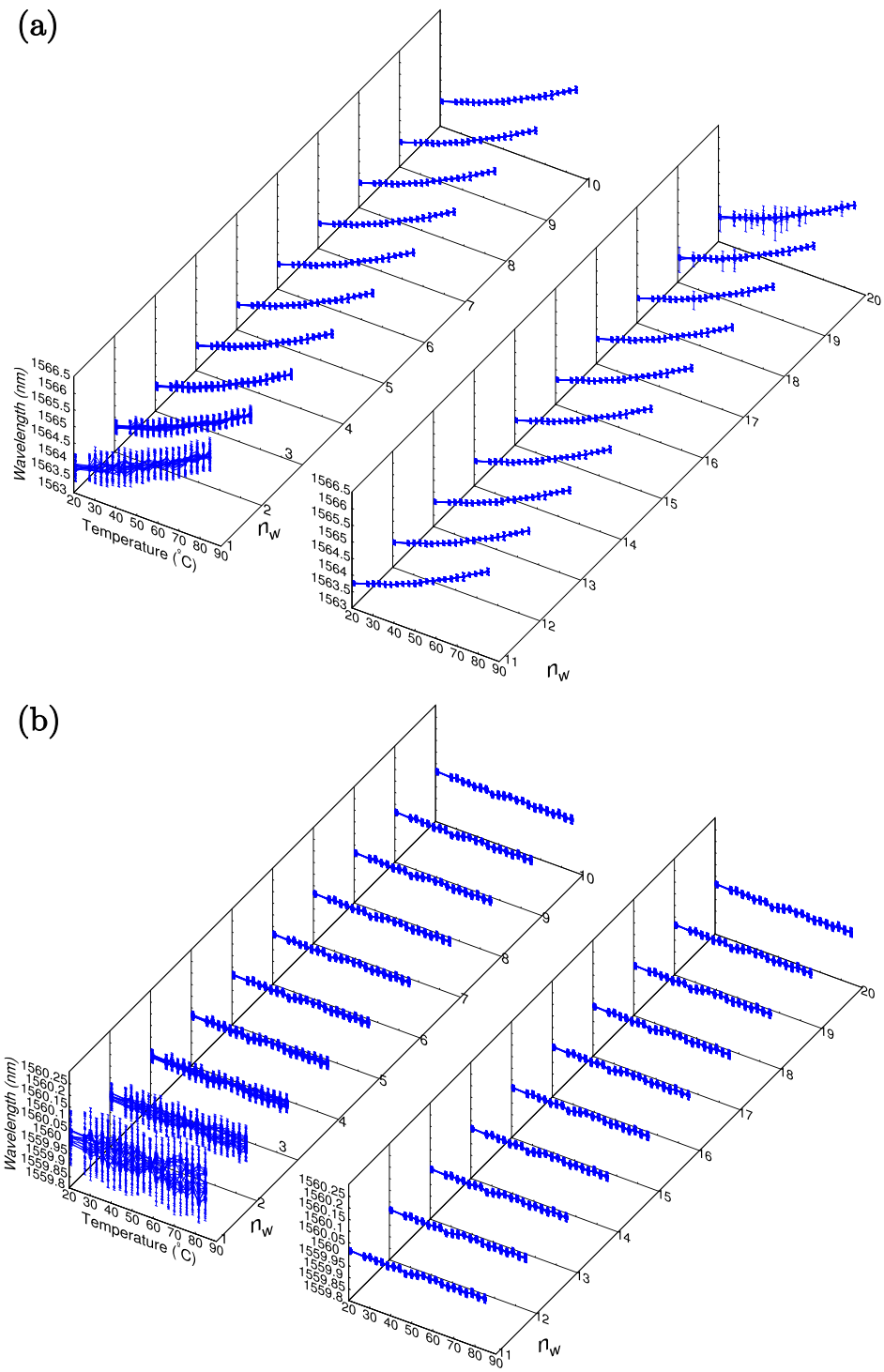

Figure R.36: (a) Temperature signal FBG ($\sim$ 1566 nm) and (b) reference FBG ($\sim$ 1560 nm) HTT wavelength against temperature. Different window lengths are overlapped at each interferogram length. The wavelength values have been corrected against the reference laser wavelength.

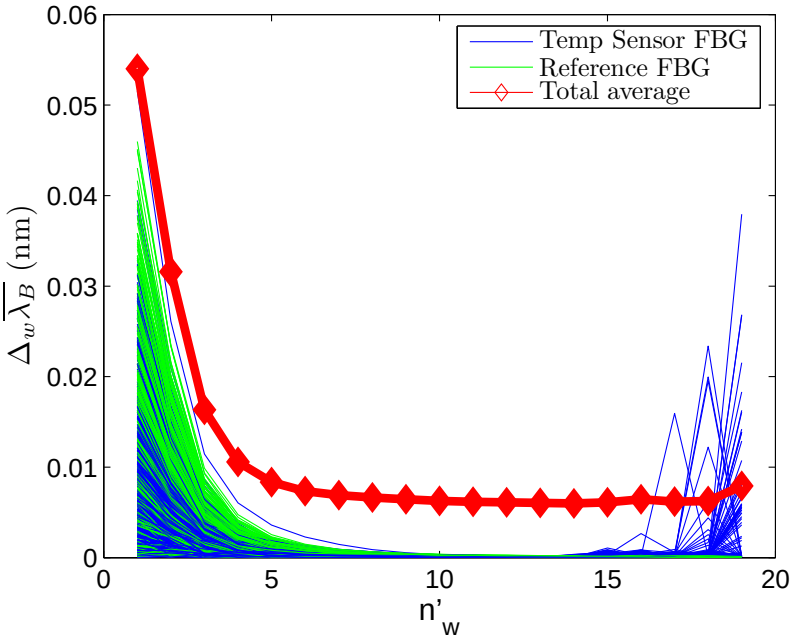

Figure R.37: Overlayed differences in mean HTT determined peak wavelengths, $\Delta_w\overline{\lambda_B}$, as Hamming window width, n_w, is adjusted for temperature sensor and reference FBG. The differences converge until the other FBG begins to enter the window.

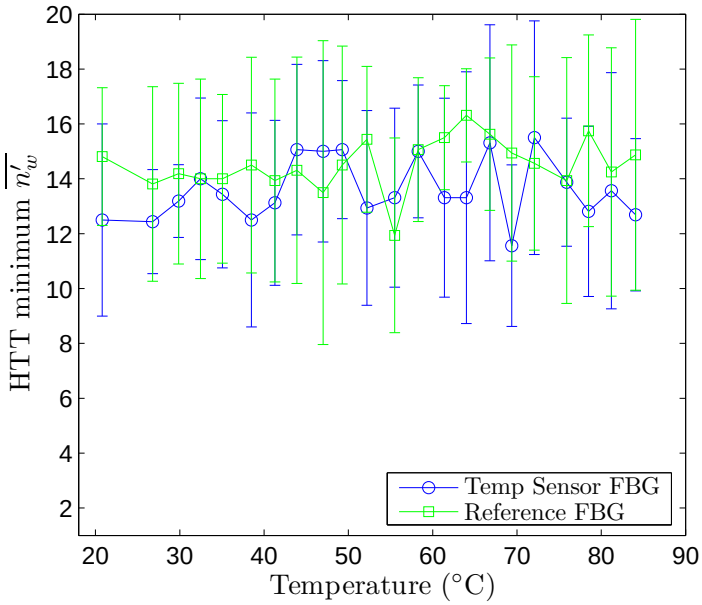

Figure R.38: The n'_w position at which a minimum HTT determined $\Delta_w\overline{\lambda_B}$ is obtained for each temperature step. The average values are 13.61 ± 3.27 and 14.53 ± 3.57 for the temperature sensor and reference FBGs, respectively.

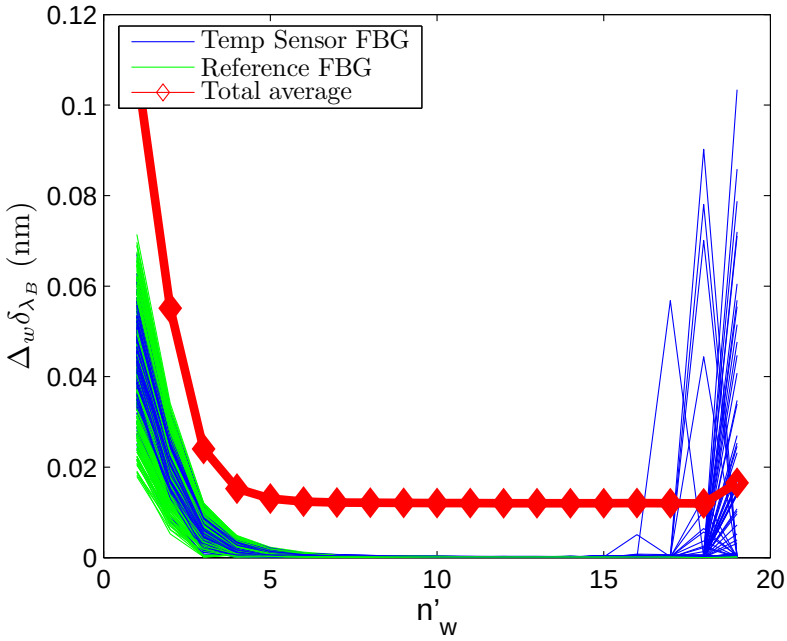

Figure R.39: Overlayed differences in standard deviation of the HTT determined peak wavelengths, $\Delta_w \delta_{\lambda_B}$, as Hamming window width, n_w, is adjusted for temperature sensor and reference FBG. The differences converge until the other FBG begins to enter the window.

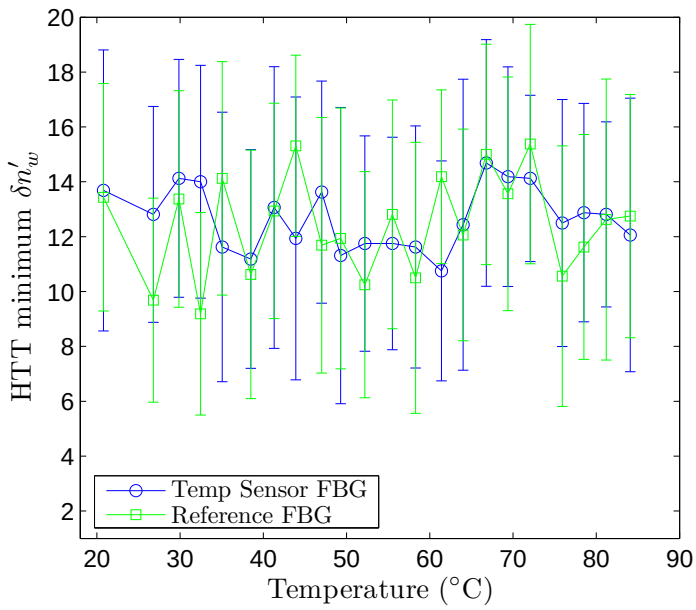

Figure R.40: The n'_w position at which a minimum HTT determined $\Delta_w \delta_{\lambda_B}$ is obtained for each temperature step. The average values are 12.68 ± 4.39 and 12.44 ± 4.42 for the temperature sensor and reference FBGs, respectively.

	Temp. FBG (pm)		Ref. FBG (pm)	
n_w	min.	max.	min.	max.
1 : 3	20.8	96.1	24	101.6
4 : 14	10.9	19	12.5	33.8
15 : 20	11	17.1	13.1	37.4

Table R.8: Standard deviations of HTT calculated mean values across all n_i for the ranges of n_w.

(page V.II R-9) and R.12 (page V.II R-9)). For the variable interferogram length analysis, the value of $n'_w = 6$ was the lowest value that did not have occasional noisy departures. However, ignoring these departures, the values at $n_w = 11, 12, 13$ would be lower than $n_w = 6, 7$, agreeing with the values from the present analysis.

The source of the noisy departures is likely to be the oscillation observed in the centroid determined slope value as n_i was changed. As for the centroid approach, an optimum value of n_i is sought next.

Figures R.41 (page V.II R-35) and R.43 (page V.II R-36) show the values of the mean HTT determined peak wavelengths, $\Delta_i\overline{\lambda_B}$, and corresponding standard deviations, $\Delta_i\delta_{\lambda_B}$, with increasing n'_i, respectively. The n'_i position of the corresponding minimum HTT determined value is plotted in figures R.42 (page V.II R-35) and R.44 (page V.II R-36), respectively.

The mean values of the n'_w and n'_i HTT determined minima of figures R.38 (page V.II R-32) and R.42 (page V.II R-35) are tabulated in table R.9 (page V.II R-38). The mean values of the n'_w and n'_i HTT determined minima of figures R.40 (page V.II R-33) and R.44 (page V.II R-36) are tabulated in table R.10 (page V.II R-38).

Again, an optimum n_i is not easily chosen. Unlike the centroid approach situation, the values of n_i do not have a clear trend. The scale of $\Delta_i\overline{\lambda_B}$ on figure R.41 (page V.II R-35) is approximately one seventh the scale on the corresponding centroid approach figure R.22 (page V.II R-19), and the scale of figure R.43 (page V.II R-36) approximately one fourth the scale on the corresponding centroid approach figure R.24 (page V.II R-20). This agrees with the overall improvement in noise reduction obtained from the HTT approach.

As for the centroid approach, alternative visualisations of the data were examined. Taking the slope of the linear fit to the temperature response slope and the norm of the residuals, the value of the slope can be plotted for each of the different interferogram lengths and window lengths. The plot of the norm of the residuals[3] of the linear fit can provide a measure of the overall closeness of the fit to the data.

Figures R.45 (page V.II R-37) and R.46 (page V.II R-37) show the normalised

[3]The Euclidean length of the residual vector.

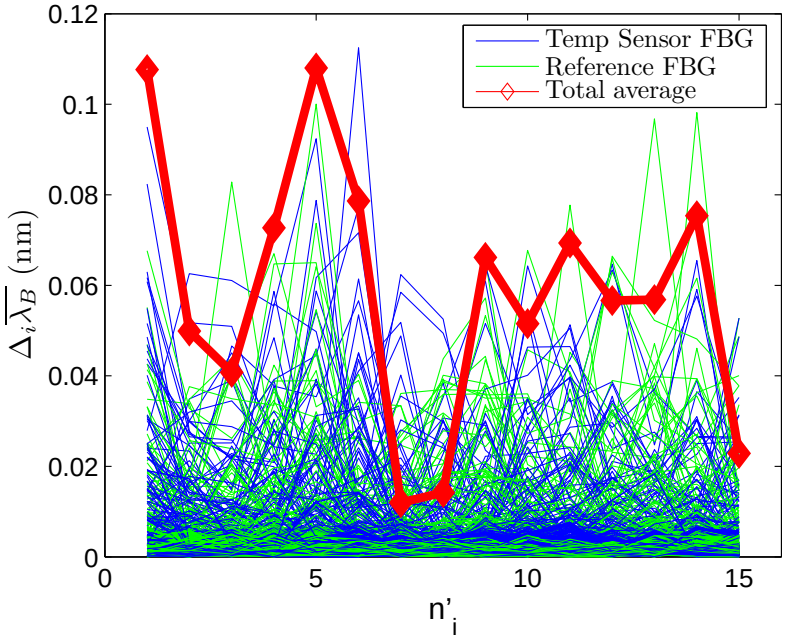

Figure R.41: Overlayed differences in mean HTT determined peak wavelengths, $\Delta_i\overline{\lambda_B}$, as interferogram length, n_i, is adjusted for temperature sensor and reference FBG. The differences show no convergence but a weak periodic oscillation.

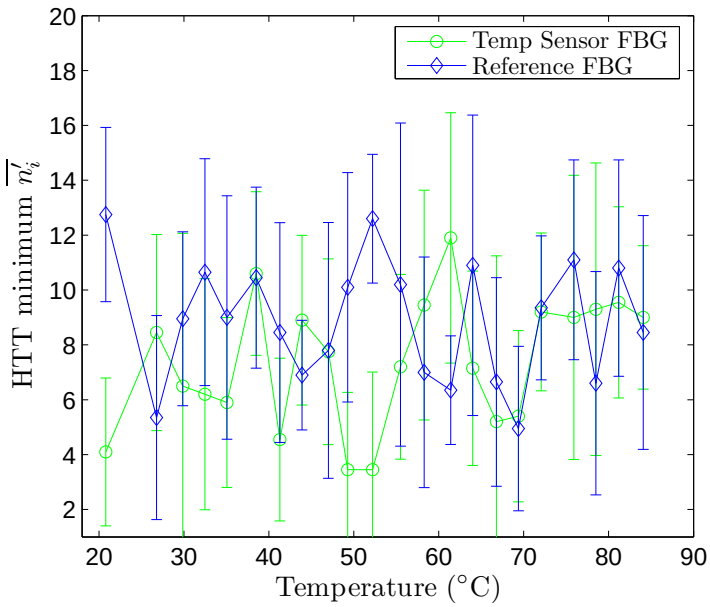

Figure R.42: The n_i' position at which a minimum HTT determined $\Delta_i\overline{\lambda_B}$ is obtained for each temperature step. The average values are 8.88 ± 4.35 and 7.37 ± 4.45 for the temperature sensor and reference FBGs, respectively.

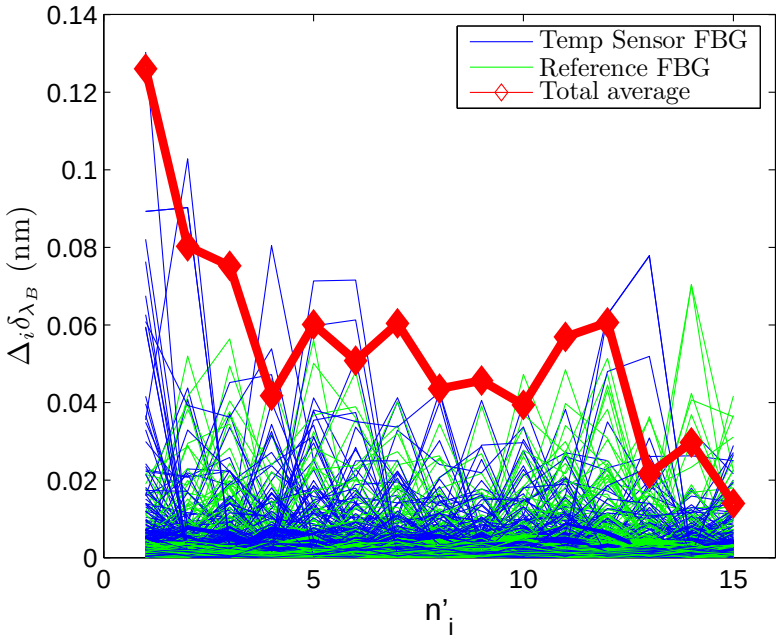

Figure R.43: Overlayed differences in standard deviation of the HTT determined peak wavelengths, $\Delta_i\delta_{\lambda_B}$, as interferogram length, n_i, is adjusted for temperature sensor and reference FBG. The differences show no obvious convergence.

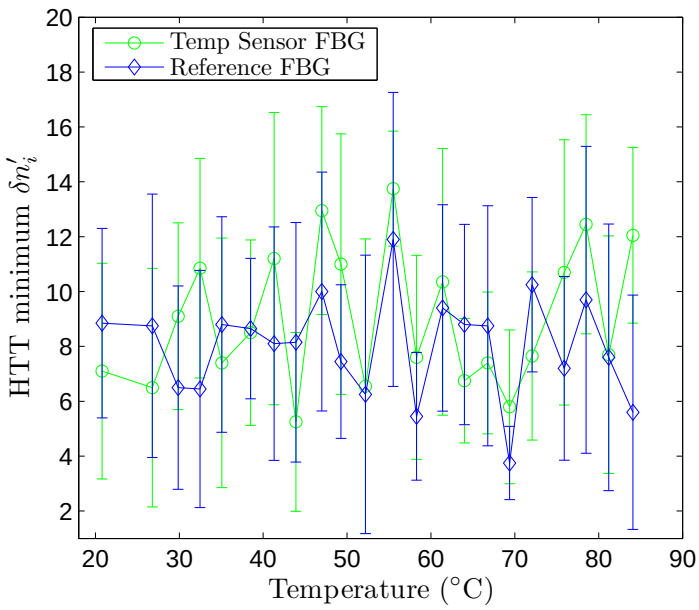

Figure R.44: The n_i' position at which a minimum HTT determined $\Delta_i\delta_{\lambda_B}$ is obtained for each temperature step. The average values are 8.02 ± 4.35 and 9.03 ± 4.48 for the temperature sensor and reference FBGs, respectively.

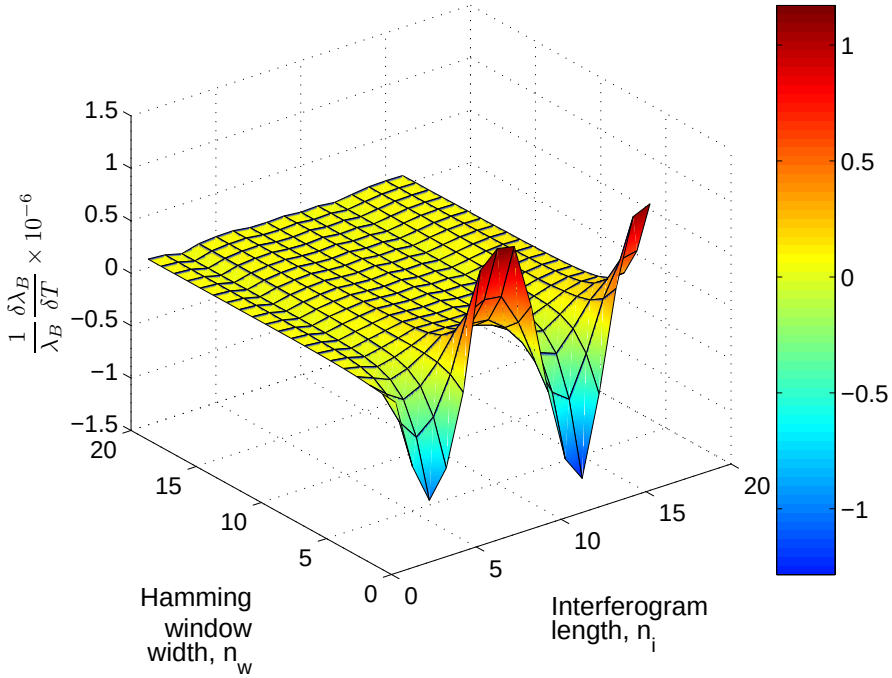

Figure R.45: Linear fit to temperature response slope of temperature signal FBG as calculated by HTT approach, with rectangular windows of width $2n_w+1$ and interferogram length step n_i.

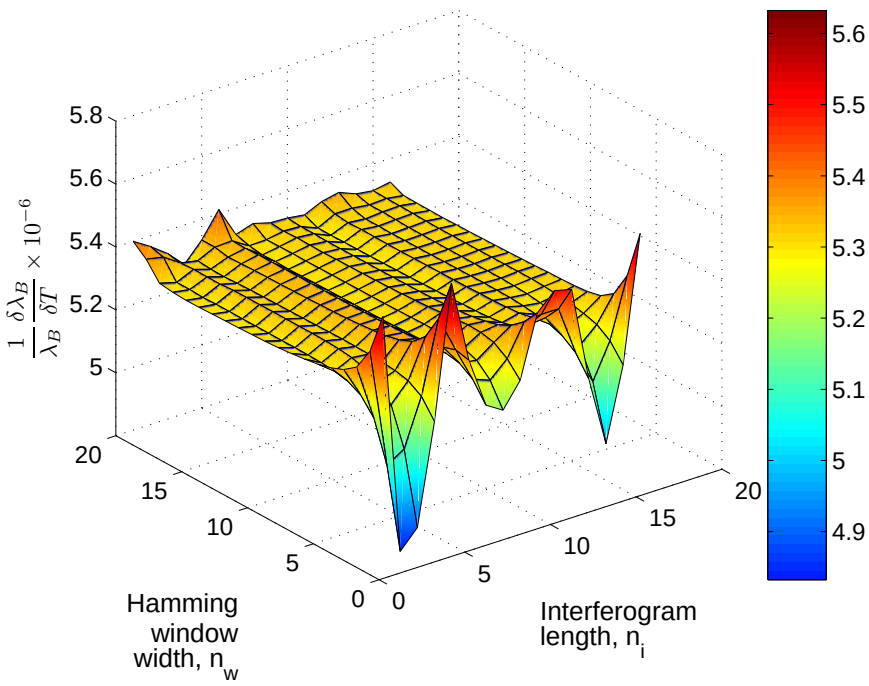

Figure R.46: Linear fit to temperature response slope of reference FBG as calculated by HTT approach, with rectangular windows for $2n_w+1$ and interferogram length step n_i.

	Ref. FBG	Temp. FBG
$\overline{n'_w}$	13.61 ± 3.27	14.53 ± 3.57
$\overline{n'_i}$	4.35 ± 4.35	4.45 ± 4.48

Table R.9: Mean values of temperature sensor and reference FBGs with changing n'_w and n'_i from figures R.37 (page V.II R-32) and R.41 (page V.II R-35), respectively.

	Ref. FBG	Temp. FBG
$\delta n'_w$	12.68 ± 4.39	12.44 ± 4.42
$\delta n'_i$	8.88 ± 8.02	7.37 ± 9.03

Table R.10: Mean values of temperature sensor and reference FBGs with changing n'_w and n'_i from figures R.39 (page V.II R-33) and R.43 (page V.II R-36), respectively.

slopes of the linear fits to the data in figures R.36(a) & (b) (page V.II R-31), the temperature signal FBG and reference FBG, respectively.

The undersampled FBG peak (from a too–short Hamming window length) dominates figures R.45 (page V.II R-37) and R.46 (page V.II R-37), as in figure R.37 (page V.II R-32). The presence of the adjacent peaks, are not as evident as for the centroid approach, figures R.28 (page V.II R-23) and R.29 (page V.II R-23), respectively. The other FBG peak, is evident in the oscillation at $n_w = 19, 20$ on figure R.45 (page V.II R-37). The values $n_w = 12, 13, 14$ are, once more, optimum.

The oscillation along n_i is more evident in figures R.45 (page V.II R-37) and R.46 (page V.II R-37) than from the centroid approach in figures R.28 (page V.II R-23) and R.29 (page V.II R-23). The oscillation is observed across the different n_w values in both figures R.45 (page V.II R-37) and R.46 (page V.II R-37), with changes in n_w scaling it.

The oscillation is, once more, not the same for the two FBG, suggesting that if it is a processing artefact, it depends upon the data passing through the processing. The largest HTT approach oscillations are at $n_w = 1 \ldots 3$, which are plotted in figures R.53 (page V.II R-43) and R.54 (page V.II R-43) for the temperature signal and reference FBGs, respectively. Also plotted are the $n_w = 14$ value for comparison and the average value of all n_i over $n_w = 13, 14, 15$. The value $n_i = 4$, 5.308×10^{-6} °C^{-1}, is the only value that is simultaneously close to the average, 5.311×10^{-6} °C^{-1}, for both the temperature signal and reference FBGs. This is not a reason to choose $n_i = 4$, but is the closest experimentally obtained value to the average value of the oscillation for both FBGs.

The values of the slopes plotted in figures R.45 (page V.II R-37) and R.46 (page

V.II R-37), and their associated residuals, for $n_w = 13, 14, 15$ are listed in tables R.11 (page V.II R-39) and R.12 (page V.II R-44), respectively. The maximum and minimum values for the temperature response slope are 5.34×10^{-6} °C^{-1} and 5.29×10^{-6} °C^{-1}, respectively.

n_i	n_w		
	13	14	15
1	5.308 (0.069)	5.307 (0.069)	5.306 (0.069)
2	5.297 (0.070)	5.297 (0.070)	5.297 (0.069)
3	5.325 (0.068)	5.325 (0.068)	5.324 (0.068)
4	5.309 (0.070)	5.308 (0.070)	5.307 (0.070)
5	5.332 (0.068)	5.331 (0.068)	5.330 (0.068)
6	5.339 (0.069)	5.339 (0.069)	5.339 (0.069)
7	5.300 (0.069)	5.299 (0.069)	5.299 (0.069)
8	5.308 (0.070)	5.308 (0.070)	5.307 (0.070)
9	5.318 (0.067)	5.318 (0.067)	5.317 (0.067)
10	5.312 (0.070)	5.312 (0.070)	5.312 (0.070)
11	5.293 (0.065)	5.292 (0.066)	5.292 (0.066)
12	5.313 (0.069)	5.313 (0.070)	5.313 (0.070)
13	5.308 (0.066)	5.307 (0.066)	5.307 (0.066)
14	5.307 (0.070)	5.308 (0.070)	5.308 (0.070)
15	5.310 (0.071)	5.310 (0.071)	5.310 (0.071)
16	5.306 (0.069)	5.305 (0.069)	5.305 (0.069)

Table R.11: Temperature sensor FBG HTT approach calculated slopes, $\frac{1}{\lambda_B}\frac{\partial \lambda_B}{\partial T} \times 10^{-6}$ °C^{-1}, for $n_w = 2, 3, 4$ for each n_i, with norm of residuals (nm) in parenthesis.

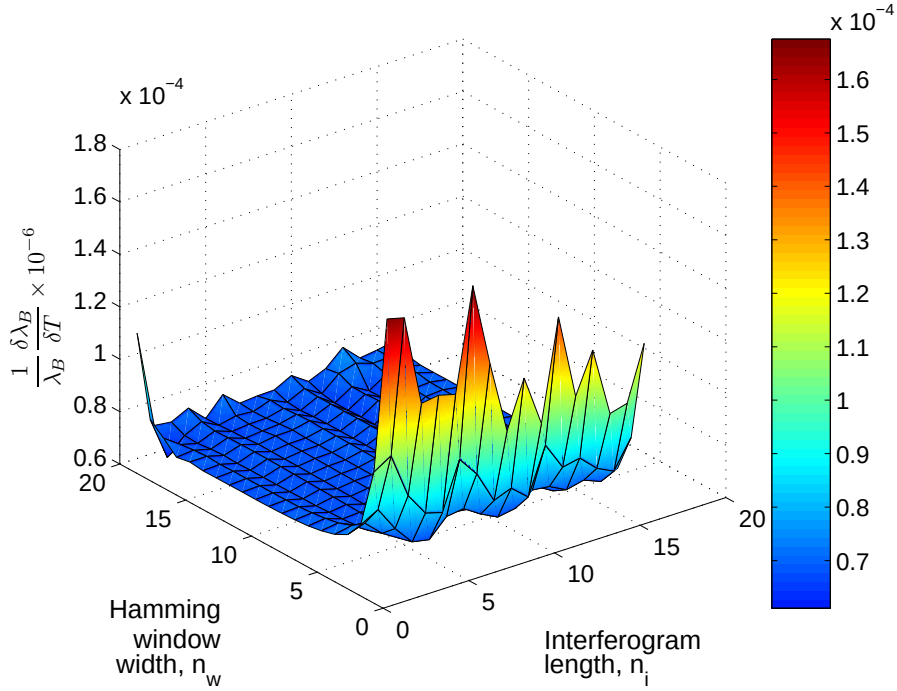

Figure R.47: Residuals to the linear fits to temperature response slope of signal FBG shown in figure R.45 (page V.II R-37).

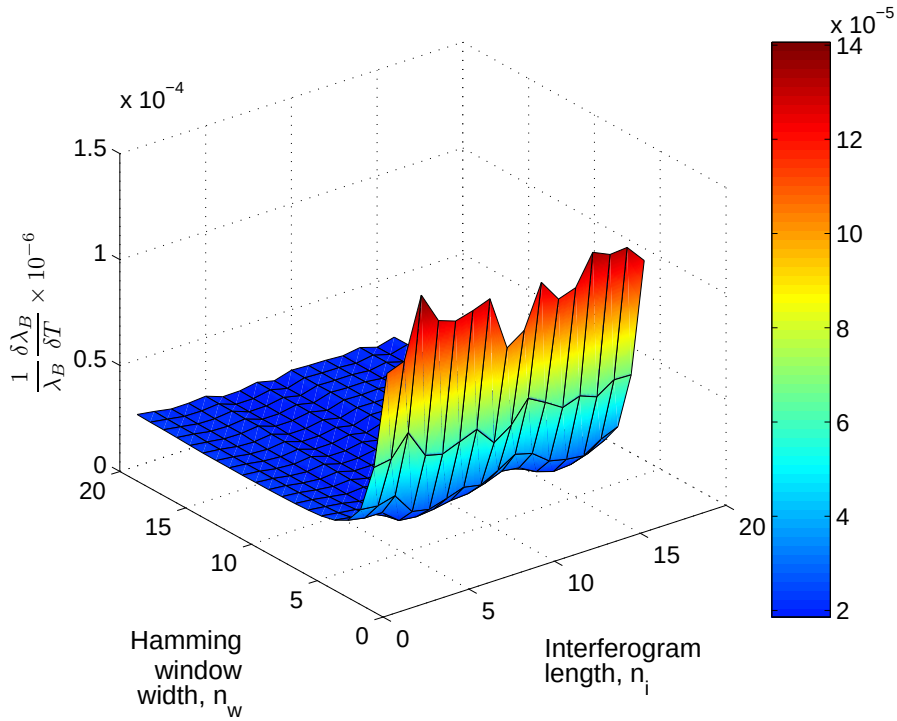

Figure R.48: Residuals to the linear fits to temperature response slope of reference FBG shown in figure R.46 (page V.II R-37).

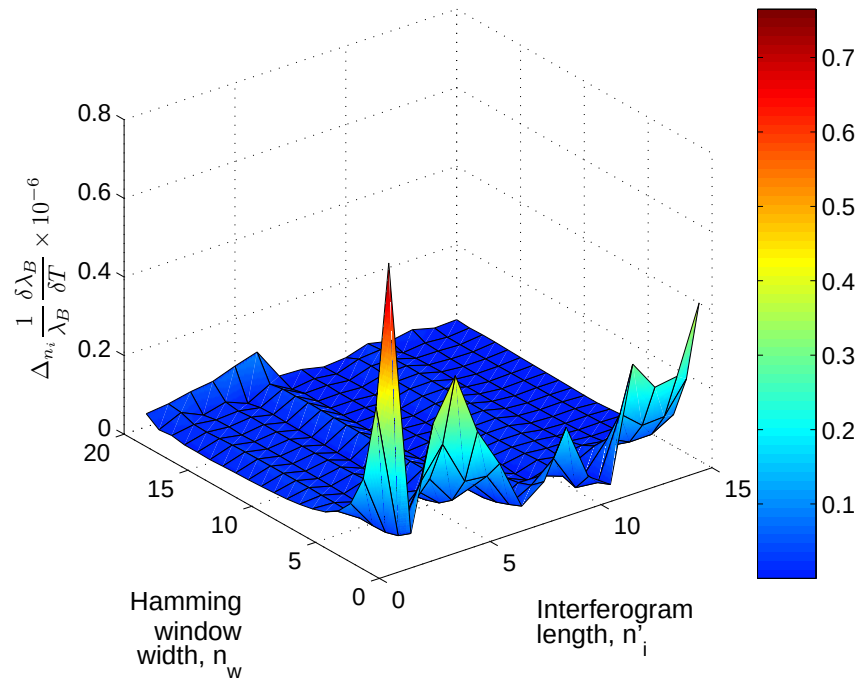

Figure R.49: Differences along n_i of slopes the linear fits to temperature response slope of temperature signal FBG shown in figure R.45 (page V.II R-37).

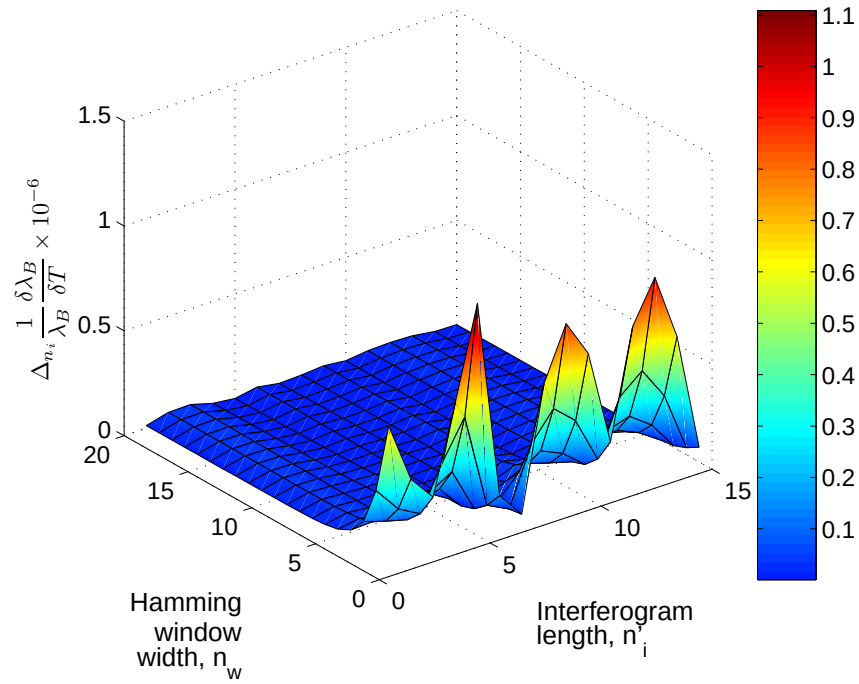

Figure R.50: Differences along n_i of slopes the linear fits to temperature response slope of reference FBG shown in figure R.46 (page V.II R-37).

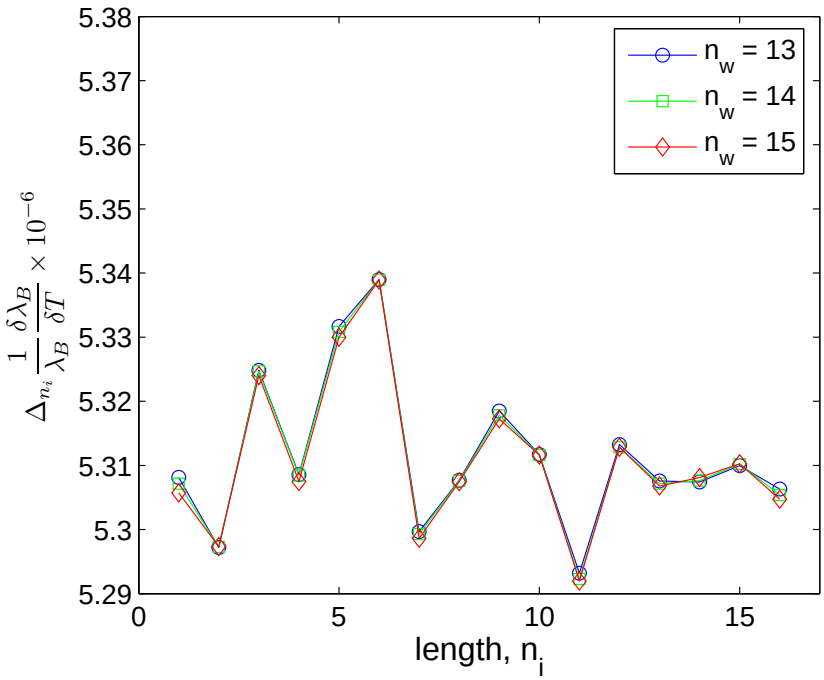

Figure R.51: Temperature signal FBG values of $n_w = 13, 14, 15$ from R.45 (page V.II R-37) indicating oscillation.

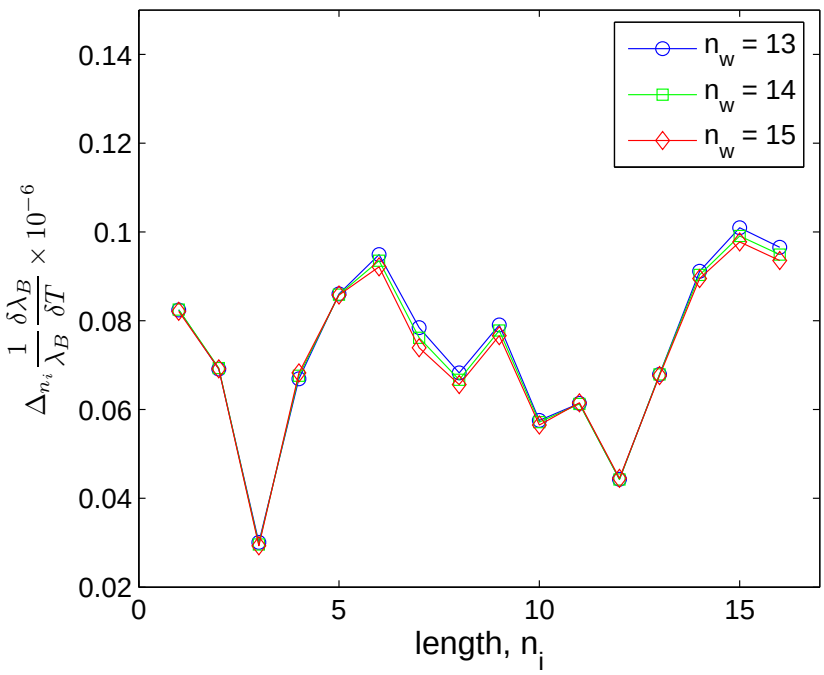

Figure R.52: Reference FBG values of $n_w = 13, 14, 15$ from R.46 (page V.II R-37) indicating oscillation.

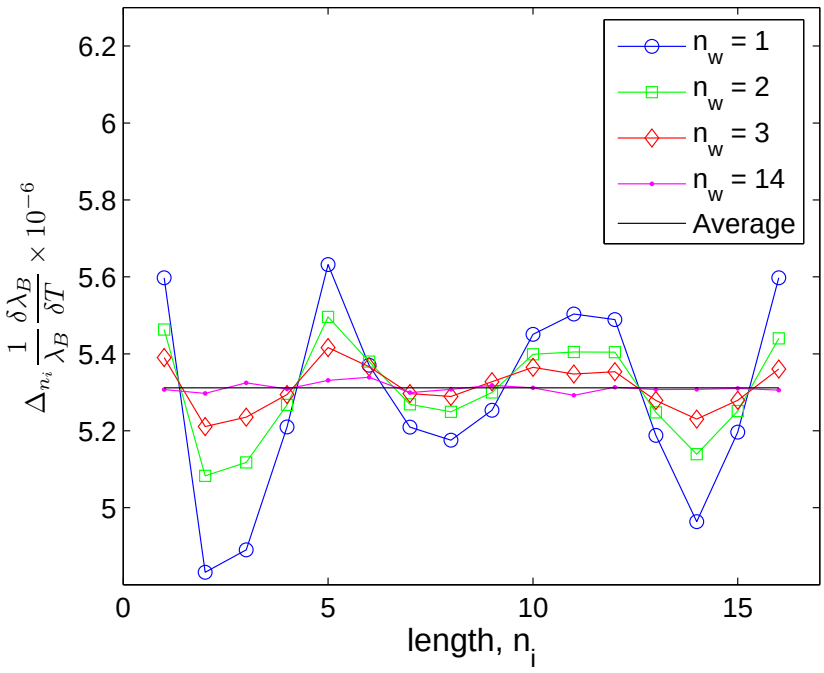

Figure R.53: Temperature signal FBG values of $n_w = 1, 2, 3$ and the average value from $n_w = 13, 14, 15$.

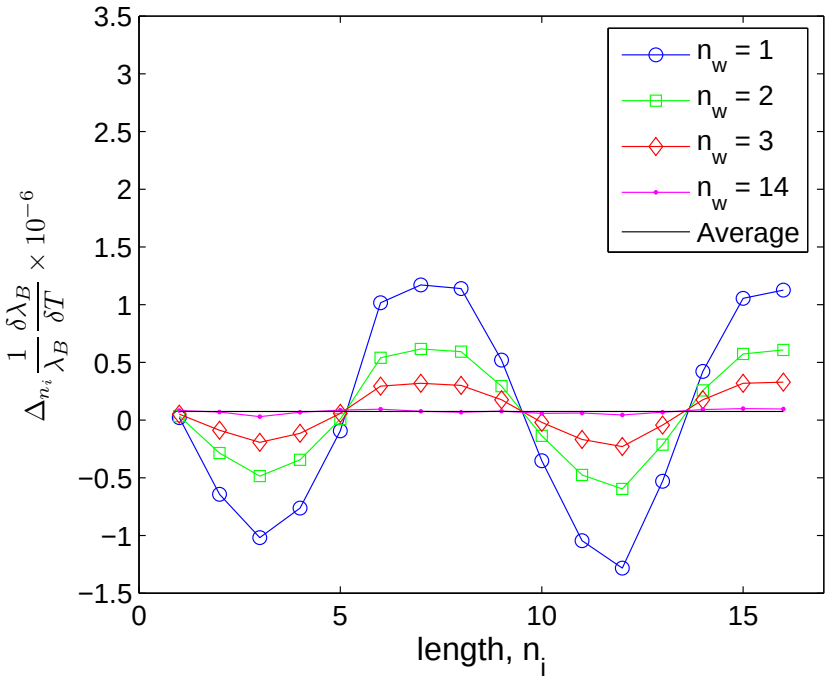

Figure R.54: Reference FBG values of $n_w = 1, 2, 3$ and the average value from $n_w = 13, 14, 15$.

n_i	n_w		
	13	14	15
1	0.082 (0.023)	0.083 (0.023)	0.082 (0.023)
2	0.069 (0.022)	0.069 (0.022)	0.069 (0.022)
3	0.030 (0.021)	0.030 (0.021)	0.029 (0.021)
4	0.067 (0.020)	0.068 (0.021)	0.068 (0.021)
5	0.086 (0.021)	0.086 (0.021)	0.086 (0.022)
6	0.095 (0.019)	0.094 (0.019)	0.092 (0.019)
7	0.078 (0.019)	0.076 (0.019)	0.074 (0.019)
8	0.068 (0.020)	0.067 (0.020)	0.066 (0.020)
9	0.079 (0.019)	0.078 (0.019)	0.077 (0.019)
10	0.058 (0.021)	0.057 (0.021)	0.057 (0.021)
11	0.061 (0.021)	0.061 (0.021)	0.062 (0.021)
12	0.044 (0.021)	0.044 (0.021)	0.045 (0.021)
13	0.068 (0.020)	0.068 (0.020)	0.068 (0.020)
14	0.091 (0.021)	0.090 (0.021)	0.090 (0.022)
15	0.101 (0.019)	0.099 (0.019)	0.098 (0.019)
16	0.097 (0.021)	0.095 (0.021)	0.094 (0.021)

Table R.12: Reference FBG HTT approach calculated slopes, $\frac{1}{\lambda_B}\frac{\partial \lambda_B}{\partial T} \times 10^{-6}{}^{\circ}\mathrm{C}^{-1}$, for $n_w = 2, 3, 4$ for each n_i, with norm of residuals (nm) in parenthesis.

		n_w
Variable	Centroid	$2, 3, 4$
	HTT	$6, 7$
Fixed	Centroid	$2, 3, 4$
	HTT	$13, 14, 15$

Table R.13: Optimum n_w values for the centroid and HTT approaches, for both the variable and fixed interferogram length cases.

		n_i
Fixed	Centroid	5
	HTT	4

Table R.14: Selected n_i values for the centroid and HTT approaches, based upon minimum difference from average across all n_w and n_i.

R.5 Summary

As the material presented in this appendix is quite lengthy, a summary of the results is useful. The recalibrated π–shifted interferogram data were examined using variable length interferograms and the centroid algorithm and the Hilbert transform technique were used to recover the wavelength of both temperature signal and reference FBGs.

The centroid calculation employed a rectangular window to isolate spectral features, as the rectangular window does not alter the weighting of the spectral components. The HTT approach employed a Hamming window to isolate the spectral features, as the Hamming window apodises Fourier transform introduced side–lobes.

The use of a fixed–width window with varying interferogram length resulted in a different spectral range being windowed. When the same recalibrated π–shifted interferogram data were examined using fixed length interferograms, a reduction in the standard deviation of the temperature response slope values was observed.

To investigate if there was an interferogram length/window length combination which provided the lowest standard deviation, the interferogram data were examined by taking different fixed length interferograms with different window widths. The changes in interferogram length were indexed with n_i and the changes in window length indexed with n_w.

The optimum values of n_w are listed in table R.13 (page V.II R-45). These are the same for the centroid approach, but differ for the HTT approach. Both the variable and fixed interferogram length HTT approaches are likely to have had convergence minima at $n_w = 13, 14, 15$, however the presence of noise at these n_w for the variable interferogram length case led to the conservative choice of $n_w = 6, 7$.

Determining the optimum n_i for the fixed interferogram length case was more difficult. No convergence was observed and alternative visualisations of the data

showed a variation or oscillation. Consequently, the temperature response slope to be ultimately reported depended upon the value of n_i selected. In order to present a value for comparison, the average of the oscillation was chosen. The n_i which had the minimum difference from the average was used as representative data of the average value. Table R.14 (page V.II R-45) lists the n_i chosen for the centroid and HTT approaches.